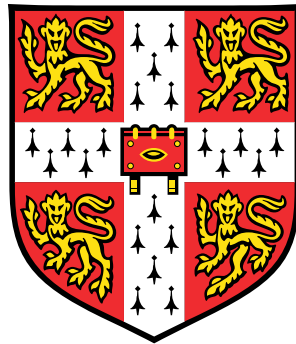


On entropic and compositional sound and its sources



Jocelino A. da R. B. Rodrigues

Department of Engineering
University of Cambridge

This dissertation is submitted for the degree of
Doctor of Philosophy

Dedico esta tese à minha família – pelo apoio incondicional.
I dedicate this thesis to my family – for their unwavering support.

Declaration

I hereby declare that except where specific reference is made to the work of others, the contents of this dissertation are original and have not been submitted in whole or in part for consideration for any other degree or qualification in this, or any other university. This dissertation is my own work and contains nothing which is the outcome of work done in collaboration with others, except as specified in the text and Acknowledgements. This dissertation contains fewer than 65,000 words including appendices, bibliography, footnotes, tables and equations and has fewer than 150 figures.

Jocelino A. da R. B. Rodrigues
May 2021

Abstract

On entropic and compositional sound and its sources

Jocelino A. da R. B. Rodrigues

Combustion noise is relevant to current aviation, rocket, and ground-based gas turbine engines, as it contributes to environmental noise pollution and can trigger thermoacoustic instabilities. These consequences are particularly prevalent in lean, premixed, prevaporised combustors, which are designed to reduce nitrous oxide (NO_x) emissions. As a result, there is a need to better understand the mechanisms that drive sound generation in such systems.

There are two components to combustion noise: direct noise – generated by the unsteady heat release of a flame – and indirect noise – produced by the acceleration of entropic, vortical, or compositional inhomogeneities. Separation of the respective contributions has proven to be complex to achieve in real engines – for this purpose, model experiments have been developed. These are non-reacting experiments that use unsteady, synthetic perturbations to emulate the fundamental physics of combustion acoustics processes and provide clear data for comparison with theory. Indirect noise models have been theorised for compositional perturbations and experimental validation has been provided via the measurement of acoustic waves (i.e. the output), while assuming a constant compositional perturbation (i.e. the input).

This thesis follows on from such experiments by simultaneously measuring both acoustic and compositional waves in a model setup, making use of numerical, analytical, and experimental studies. It first builds upon a previous model experiment through a numerical investigation on the generation, mixing, and convection of entropic and compositional waves generated by heat addition and gas injection. The computed temperature and mass fraction fields are compared with experimental results and inform the design of a new model setup – the Canonical Wave Rig (CWR).

The CWR is then used to study direct and indirect noise under simplified, well-controlled conditions. Subsonic and sonic (choked) conditions are investigated for a convergent-divergent nozzle. Acoustic, entropic, and compositional perturbations are

generated via the co-flow injection of air or methane into a low Mach number mean flow of air. Spontaneous Raman spectroscopy (1.5 kHz) is employed for the time-resolved measurement of the local concentration upstream of the nozzle.

Single pulse experiments in the infra-sound range are used to validate the derived analytical model for direct noise due to co-flow injection. The measurement of non-reverberated indirect noise is made for the first time and is contrasted with results obtained via dereverberation (i.e. removing the effect of pressure build up due to acoustic reflections). Indirect noise transfer functions are calculated using the acoustic and compositional measurements, and issues pertaining to the methods applied are highlighted. Lastly, the pulse burst injection of methane at frequencies up to 250 Hz is presented. The goal of these experiments is to provide data at more realistic frequencies and amplitudes.

Publications

Journal articles

- De Domenico, F., Rolland, E. O., **Rodrigues, J.**, Magri, L., Hochgreb, S. (2021) ‘Compositional and entropic indirect noise generated in subsonic non-isentropic nozzles’, *Journal of Fluid Mechanics* **910**, A5.
- **Rodrigues, J.**, Busseti, A., Hochgreb, S. (2020) ‘Numerical investigation on the generation, mixing and convection of entropic and compositional waves in a flow duct’, *Journal of Sound and Vibration*, **472**, 115155.

Conference proceedings

- **Rodrigues, J.**, Noh, D., Navarro-Martinez, S., Hochgreb, S., Jones, W. P. (2018) ‘Large Eddy Simulations of the dispersion and dissipation of injected compositional inhomogeneities in the Cambridge Wave Generator’, *12th International ERCOFTAC Symposium on Engineering Turbulence Modelling and Measurements*, Montpellier, France.
- **Rodrigues, J.**, Rolland, E. O., De Domenico, F., Hochgreb, S. (2017) ‘Computational Investigation Of Direct Noise Generated By Synthetic Hot Spots In A Duct’, *24th International Congress on Sound and Vibration*, London, UK.

In preparation

- **Rodrigues, J.**, Weller, L., De Domenico, F., Hochgreb, S., ‘On direct and indirect noise: measurement of acoustic, entropic, and compositional waves in a model thermoacoustic system’.

- **Rodrigues, J.**, Weller, L., De Domenico, F., Hochgreb, S., ‘High-frequency measurement of concentration in an isothermal methane–air gas mixture using spontaneous Raman spectroscopy’.
- **Rodrigues, J.**, Yong, K. J., Meindl, M., Polifke, W., Hochgreb, S., ‘Acoustic response of perforated plate and nozzle geometries at high Mach number conditions’.

Acknowledgements

I feel very fortunate to have had the opportunity to undertake my doctorate at Cambridge. During this time, I faced many challenges and hurdles, lived through a few ups and downs, both academic and personal – but I will always be grateful for this unique experience. It is undeniable that this degree would not have been the same without the support, patience, and kindness of many people over the past years. I would like to take this opportunity to acknowledge them.

Thank you to my supervisor, Prof. Simone Hochgreb, for giving me the opportunity to undertake this challenging research project. Under her tutelage, I have learnt a lot about academia and engineering research, and, over the course of my PhD, I feel I have grown immensely – for that, I am eternally grateful. Thank you to my advisor, Prof. Matthew Juniper, for his wisdom and support, as well as for leading the thermoacoustics coffees and kindly inviting me to poker nights at his Trinity office. I am also extremely grateful to the funding bodies that made the completion of my doctorate possible, namely the Engineering and Physical Sciences Research Council (EPSRC), the School of Technology (Qualcomm Scholarship), and Rolls-Royce (a kind mention to Marco Zedda and Prof. Epaminondas Mastorakos). A special thank you to Churchill College for the support provided throughout my whole PhD.

Thank you to my group colleagues Dr. Lee Weller, Dr. Francesca De Domenico, Dr. Erwan Rolland, and Andrea Busseti. Without them, this work would not have been possible. To Lee, for the support and advice provided over the last three years of my PhD. His infectious desire to learn and constant lightheartedness in lab are truly inspiring. I learnt a great deal by working with him and deeply appreciate the time and effort he invested in the work presented here. To Francesca, for her kindness, patience, and availability. Her understanding of indirect noise has been a source of countless conversations during my PhD and her constructive inputs on this work have been incredibly helpful. To Erwan, for showing me the ropes in lab and lending me his ears during (and after) his time in the office. His valuable comments and contributions are very much appreciated. To Andrea, for his contributions to the numerical investigation and incessant desire to learn.

To the Hopkinson Lab and the Engineering Department. Thank you to those who shared their knowledge with me and contributed to my PhD in many different ways. In no particular order: Brian, Francesco, Pedro, Luca, Luming, Robert, James, Andrea, Zhi, Andrej, Steve, Patton, Aaron, Christian, Jose, Hans, Nick, Jack, Max, Fiona, Petr, Filip, Jenna, Pau, Savvas, Ingrid, Michael, Hassan, Dante, and many others. Thank you to Peter Benie for his kind support and availability to assist me whenever I was faced with computer-related problems. To John Hazlewood for helping me resolve the (many) issues that arose with acoustics equipment. To the technicians in both workshops – Roy, Alistair, Mark, Ken, John, Barney, Rob, and others – for assisting me with my design and manufacturing needs. The experiments in this thesis would not have been possible without their work.

Thank you to Kah Joon Yong, Maximilian Meindl, and Prof. Wolfgang Polifke at the Technical University of Munich (TUM) for the collaboration and for providing numerical data for this thesis.

Thanks to everyone outside of lab who helped me maintain a balanced and social life. To all the people who contributed to the music in my life. To the friends I made at CUAFC. To the friends I made at Churchill College – Miguel, Andy, Hanna, Alex, and many others – thank you for some memorable times! To Rufat for being a great thesis-writing pal during my last sprint towards the finish line. I am especially grateful to my good friends and former housemates Hannah, Karen, Tom, Victor, Jacques, and Jill for their love and support. I couldn't have asked for kinder people to live with during my time at Cambridge and will forever cherish the memories we share.

Finally, I would like to thank my family from the bottom of my heart. I would not have made it through the PhD without them. To my loving parents, Edith and Jocelino, for their patience; always available for a phone call to listen to my woes and give me their opinion (whether or not I want to hear it). To my sister, Beatriz, for her kindness, and my cousin, Joana, for her support. To my tante & marraine Felisbela, oncle Daniel, cousine Mathilde, et cousin & filleul, Thomas. To my late grandfather, Virgílio, and grandmother, Albertina, whom I lost at the start and end of my PhD, respectively, and whom I deeply miss – *saudade*.

Sic itur ad astra

Table of contents

List of figures	xix
List of tables	xxxiii
Nomenclature	xxxv
1 Introduction	1
1.1 Motivation	2
1.1.1 Thermoacoustic instabilities	2
1.1.2 The pollution problem	4
1.1.3 Combustion noise	7
1.2 Thesis outline	9
2 State of the art	11
2.1 Theory of combustion noise	12
2.1.1 Governing equations	12
2.1.2 Decomposition and evolution of disturbances	13
2.1.3 Canonical mode coupling	15
2.2 Analytical modelling of direct and indirect noise	17
2.2.1 Review	17
2.2.2 Theoretical framework	21
2.2.3 Compact wave source	22
2.2.4 Reverberation	28
2.3 Experimental investigations on indirect noise	29
2.3.1 Commercial engines	29
2.3.2 Lab-scale combustors	30
2.3.3 Model setups	33
2.4 Summary	40

3	Numerical simulations: inhomogeneities in a flow duct	41
3.1	Motivation and objectives	42
3.2	Experimental details	44
3.3	Numerical methodology	47
3.3.1	Governing equations	47
3.3.2	General solver details	47
3.3.3	Gas injection	48
3.3.4	Heat addition	51
3.4	Results	55
3.4.1	Gas injection	55
3.4.2	Heat addition	59
3.4.3	Comparison of scalar perturbations	63
3.5	Summary	64
4	Experimental methods	67
4.1	Motivation and objectives	68
4.2	The Canonical Wave Rig: a model thermoacoustic system	70
4.2.1	Inlet: perforated plate	71
4.2.2	Outlet: convergent-divergent nozzle	73
4.2.3	Pseudo-anechoic tube	74
4.2.4	Gas injection system	75
4.2.5	Acoustic pressure measurements	79
4.2.6	Mean flow properties	80
4.3	Raman spectroscopy: time-resolved concentration measurements	82
4.3.1	Background	82
4.3.2	Setup	84
4.3.3	Data processing	87
4.3.4	Potential factors affecting the Raman signal	89
4.3.5	Calibration	94
4.3.6	Temporal resolution	95
4.3.7	Translation to compositional wave amplitude	98
4.4	Summary	100

5	Direct & indirect noise experiments I: single pulse injection	103
5.1	Motivation and objectives	104
5.2	Test cases	105
5.3	Non-reverberating system	106
5.3.1	Setup and methodology	106
5.3.2	Direct noise waves	108
5.3.3	System characterisation	114
5.3.4	Indirect noise waves	119
5.4	Reverberating system	122
5.4.1	Setup and methodology	122
5.4.2	Pressure perturbations	122
5.4.3	Dereverberation	127
5.5	Indirect noise quantification: a comparative study	128
5.6	Indirect-to-direct noise ratios	130
5.7	Time-resolved entropic and compositional wave measurement	132
5.7.1	Calibration curves	132
5.7.2	Results	133
5.8	Entropic and compositional nozzle transfer functions	136
5.9	Summary	138
6	Direct & indirect noise experiments II: pulse burst injection	141
6.1	Motivation and objectives	142
6.2	Test cases	144
6.3	High frequency system characterisation	145
6.3.1	Experiments: multi-microphone method	145
6.3.2	Numerical investigation: RANS/LNSE	149
6.3.3	Results	151
6.4	Reverberating system	154
6.4.1	Setup and methodology	154
6.4.2	Pressure perturbations	154
6.5	Time-resolved entropic and compositional wave measurement	155
6.5.1	Calibration curves	156
6.5.2	Results	157
6.6	Frequency content	158
6.7	Source identification	161
6.8	Summary	164

7	Final remarks	167
7.1	Conclusions	168
7.1.1	Numerical simulations	168
7.1.2	Phase-locked measurement of acoustic & compositional waves . .	169
7.2	Future work	172
7.2.1	Data analysis	172
7.2.2	Numerical simulations	172
7.2.3	Experimental studies	174
7.2.4	Analytical modelling	175
	References	177
	Appendix A Derivations	203
A.1	Entropic wave amplitude	204
A.2	Compact wave source	209
A.2.1	Linearisation and normalisation	210
A.2.2	Resulting jump conditions	213
	Appendix B Additional details on Raman spectroscopy	217
B.1	Probe volume	218
B.1.1	Confocal theory	218
B.1.2	Limit cases	219
B.2	Full calibration dataset	220
B.3	Error analysis	222

List of figures

1.1	The Wright Flyer takes off for the first time (Dec. 17 th , 1903).	1
1.2	Combustion instability damage: (a) rocket engine injector (Rocket Engine Testing Facility, NASA, 1957) ²⁶⁰ and (b) combustion chamber liner ¹⁹⁰ . . .	3
1.3	Summary of primary engine noise sources ⁶⁸ and greenhouse gas emissions ⁸¹ . Inspired by Dowling and Mahmoudi ⁶⁸	4
1.4	Environmental pollution from commercial aviation: (a) air pollution – CO ₂ and NO _x emissions. Global data (1964–2018) from Lee et al. ¹⁸⁰ , adapted from Ritchie ²⁷⁵ . European data (1990–2018) from European Union Aviation Safety Agency ⁸⁷ ; (b) noise pollution – turbojet engine noise sources during approach conditions. Data from Safran Aircraft Engines (previously Snecma), adapted from Dowling and Mahmoudi ⁶⁸ . . .	5
1.5	Schematic of the GE Rich-Quench-Lean (RQL-2) gas turbine combustor ⁹⁰ . Inspired by Magri et al. ²⁰⁵	8
2.1	Compact wave source: added fluxes (mass φ'_m , momentum φ'_M , energy φ'_e , and mixture fraction φ'_Z) and generated waves (acoustic π_d^\pm , entropic σ , and compositional ξ).	23
2.2	Effect of reverberation on upstream-travelling π_d^- and downstream-travelling π_d^+ direct noise waves where L is the system length, and R_i and R_o are the inlet and outlet reflection coefficients, respectively.	28
3.1	Experimental setup for the LITGS (top) ⁶⁵ and thermocouple (bottom) ⁶² measurements with (a) mass flow controller, (b) fast response solenoid valve and (c) heating grid. The probe locations are identified for each experimental campaign (\bullet). All dimensions in mm.	45
3.2	Probe volume schematic.	46

3.3	Meshes for the full (top) and reduced (bottom) configurations used in the gas injection cases (x - y midplane). Planar symmetry is assumed. Figures scaled axially by a factor of 0.33. Dimensions in mm.	50
3.4	(a) Current delivered to grid driving system (—); (b) modelled power input (---) and convected power (—) for case 8 ($\bar{u} = 2.56 \text{ m s}^{-1}$). Heat addition from $t = 0$ to 0.2 s.	52
3.5	Numerical schematic (top) and mesh (bottom) used in the heat addition cases (x - y midplane). Rotational symmetry is assumed – shown is the modelled 2.5° segment (z - y plane). Heating grid modelled as volume with length of 10 mm. Dimensions in mm.	53
3.6	Evolution of the compositional and entropic wave amplitude distribution for argon (top) and helium (bottom) on the x - y midplane (left) and x - z midplane (right). Probe volume schematics are shown to scale (based on Figs. 3.1 and 3.2): $x_1 = 0.13 \text{ m}$, $x_2 = 0.21 \text{ m}$, $x_3 = 0.29 \text{ m}$, $x_4 = 0.37 \text{ m}$ and $x_5 = 0.45 \text{ m}$ downstream of the injection location. Figures scaled axially by a factor of 0.5. Injection from $t = 0$ to 200 ms.	56
3.7	Evolution of the centreline compositional and entropic perturbations downstream of the injection location for argon (top) and helium (bottom). Injection from $t = 0$ to 0.2 s.	57
3.8	Time series of the centreline compositional and entropic perturbations for argon and helium at $x_1 = 0.13 \text{ m}$, $x_2 = 0.21 \text{ m}$, $x_3 = 0.29 \text{ m}$, $x_4 = 0.37 \text{ m}$ and $x_5 = 0.45 \text{ m}$ downstream of the injection location. Comparison between experimental data using LITGS phase-averaged from 30 shots (\bullet) ⁶⁵ and the numerical results using URANS: centreline point (—), probe volume average (—) and cross-sectional area average (—).	58
3.9	Evolution of the entropic wave amplitude distribution on the x - y midplane for case 1 (left) and case 8 (right) ($\xi = 0$). Part of the upstream section has been omitted; 1.68 m of the duct is shown. Probe locations shown to scale: $x_G = 0.04 \text{ m}$, $x_S = 0.36 \text{ m}$, and $x_L = 1.4 \text{ m}$ downstream of the heating grid. Figures scaled axially by a factor of 0.4. Heat addition from $t = 0$ to 200 ms.	60
3.10	Evolution of the centreline entropic perturbations downstream of the heating grid for cases 1, 3, 6 and 8 ($\xi = 0$). Heat addition from $t = 0$ to 0.2 s.	61

- 3.11 Time series of the centreline entropic perturbations ($\xi = 0$): (a) comparison between experiments using thermocouples (TC) (---) and numerical results using URANS for test cases 1, 3, 6 and 8 at $x_G = 0.04$ m (—), $x_S = 0.4$ m (—) and $x_L = 1.4$ m (—) downstream of the heating grid; (b) comparison between TC and URANS results for case 1 with LITGS (•) results phase-averaged from 30 shots⁶⁵; (c) comparison between TC and URANS results for case 1 using the heat transfer boundary condition (— $h_\infty = 25$ W m⁻² K⁻¹ and — $h_\infty = 2$ W m⁻² K⁻¹). 62
- 3.12 Centreline entropic perturbations as a function of time (shifted for each probe location and normalised by the respective bulk convective time). Comparison between experiments using LITGS (•) for the gas injection cases and thermocouples (---) for the heat addition (left) and numerical results using URANS (—) (right). For heat addition, case 1 ($\bar{u} = 0.88$ m s⁻¹) is shown. 64
- 4.1 General setup of the modular Canonical Wave Rig (CWR). Note: in the experimental campaigns presented, only one injection tube is inserted at a time – all three are shown here solely for visual purposes. Lengths are not to scale. 70
- 4.2 Perforated plate inlet: (a) upstream view of plate in the CWR, (b) upstream view of plate and (c) side view of plate. 71
- 4.3 CAD rendering of air flow through the perforated plate assuming a turbulent cone half-angle of 12°: (a) isometric view with bulk jet exit velocity \bar{u}_0 and Mach number \bar{M}_0 of jet as a function of mean flow rate \bar{m} ; (b) decay of normalised bulk axial jet velocity \bar{u}_j/\bar{u}_0 as a function of perforated plate hole diameter d_{pp} ²⁶³. 72
- 4.4 Convergent-divergent nozzle used in the Canonical Wave Rig (CWR). . . 73
- 4.5 Measured direct noise pressure fluctuations due to air injection $\pi_d^+ \bar{\gamma} \bar{p}$ and reflected waves $(R_{o1} \pi_d^+ + R_{i1} \pi_d^-) \bar{\gamma} \bar{p}$ demonstrating the effectiveness of the pseudo-anechoic tube ($L_a = 30$ m) in creating time separation. 74
- 4.6 Injection system: (a) upstream view inside the CWR and (b) side view showing the high-speed valve and the direction of the injected flow. . . . 76
- 4.7 Circuit diagram with flow lines for mean and injected flows: (1) gas cylinders (air or methane), (2) manual valve, (3) pressure regulator, (4) pressure gauge, (5) mass flow meter, (6) solenoid valve, (7) air filter regulator with pressure gauge, and (8) mass flow controller. 77

4.8	Pulse width modulation (PWM) used in the energy saving circuit for a high frequency injection test case (2 ms pulse, 12.5% holding voltage): output voltage (—) and average voltage (---).	78
4.9	Example of acoustic pressure signal post-processing: raw signals from 100 pulses (—), phase-averaged signal over 100 pulses (—), and phase-averaged and filtered signal (—).	79
4.10	Evaluation of mean flow properties as a function of flow rate: (a) upstream pressure \bar{p}_1 (with choking flow rate \bar{m}_c and choked flow region highlighted), (b) downstream pressure \bar{p}_2 , (c) upstream bulk velocity \bar{u}_1 and Mach number \bar{M}_1 (with choked flow region highlighted), and (d) upstream Reynolds number Re (with laminar, transitional and turbulent flow regimes highlighted ²⁷³).	80
4.11	General comparison of estimated acoustic He and convective St non-dimensional frequencies for gas turbines and experiments presented in this thesis.	81
4.12	Diagram of the Rayleigh and Raman (Stokes and anti-Stokes) scattering processes. Conservation of angular frequency is depicted where subscripts $(\cdot)_{sc}$, $(\cdot)_{mol}$, $(\cdot)_p$ refer to the scattered light, the molecule vibration, and the incident photon, respectively. Inspired by Jones et al. ¹⁶³ and Smith and Dent ²⁹⁸	83
4.13	Schematic of the spontaneous Raman spectroscopy system. The main components of the system are: (1) achromatic doublet lens ($\varnothing = 25.4$ mm, $f = 100$ mm), (2) achromatic doublet lens ($\varnothing = 25.4$ mm, $f = 50$ mm), (3) mounted pinhole ($\varnothing = 25.4$ mm, 25 μm), (4) achromatic doublet lens ($\varnothing = 25.4$ mm, $f = 50$ mm), (5) 532 nm single-notch filter ($\varnothing = 25.4$ mm), (6) beam trap, (7) long-pass 532 nm dichroic beamsplitter ($\varnothing = 25.4$ mm), (8) achromatic doublet lens ($\varnothing = 50.8$ mm, $f = 100$ mm), (9) photodiode array (PDA) detector. Also included: (a) timings of the camera-intensifier-laser system, (b) measured laser pulse energies as a function of repetition rate ¹⁹⁵ and (c) confocal volume schematic (oblate ellipsoid) assuming a spherically Gaussian beam. Dimensions not to scale.	85
4.14	Energy-normalised counts C (—) and averaged counts \bar{C} (—). Case presented is for a methane–air mixture ($Y_{\text{CH}_4} = 20\%$) where $N_s = 1450$ shots, $G = 55\%$, and $\bar{p} = 101,325$ Pa.	88

- 4.15 (a) Averaged counts for the full signal (\bar{C}_S —) and for the fitted background signal (\bar{C}_B - - -); (b) background-subtracted averaged counts ($\bar{C}_{S'}$ —) and integrated counts ($\bar{C}_{S'_{N_2}}$ and $\bar{C}_{S'_{CH_4}}$) for the two molecules of interest. Case presented is for a methane-air mixture ($Y_{CH_4} = 20\%$) where $N_s = 1450$ shots, $G = 55\%$, and $\bar{p} = 101,325$ Pa. 89
- 4.16 Integrated counts for N_2 ($\bar{C}_{S'_{N_2}}$) as a function of mean flow rate \bar{m} of air for different intensifier gains G (● 40%, ● 50%, ● 60%) at $\bar{p} = 101,325$ Pa. 90
- 4.17 Integrated counts with atmospheric value subtracted for N_2 ($\bar{C}_{S'_{N_2}}^{atm}$) as a function of mean pressure \bar{p} (bottom axis) and concentration (top axis) with linear fits for different intensifier gains G (● 40%, ● 50%, ● 60%) where the standard deviation is shown ($\pm 1\sigma$). 91
- 4.18 Integrated counts for the two molecules of interest as a function of intensifier gain G : (a) N_2 ($\bar{C}_{S'_{N_2}}$) and (b) CH_4 ($\bar{C}_{S'_{CH_4}}$) with exponential fits for different methane mass fractions Y_{CH_4} (● 0%, ● 10%, ● 20%, ● 30%, ● 40%, ● 50%, ● 100%). Data points which fall outside the exponential fits are caused by camera saturation. 92
- 4.19 Averaged counts for air flow with (—) and without (—) quartz where $N_s = 1450$ shots and $G = 55\%$: (a) full signals and (b) background-subtracted signals. 93
- 4.20 Cycle-averaged laser pulses for single-pulsed and dual-pulsed mode excitation. 93
- 4.21 Averaged counts for mean flow ($Y_{CH_4} = 10\%$) with laser in single-pulsed (—) and dual-pulsed mode (—) where $N_s = 1450$ shots and $G = 55\%$: (a) full signals and (b) background-subtracted signals. 94
- 4.22 Calibration curves for (a) N_2 and (b) CH_4 at $\bar{p} = 101,325$ Pa for $G = 55\%$. 95
- 4.23 Time-resolved, cycle-averaged integrated counts for N_2 (—) and CH_4 (—) due to a single pulse, co-flow injection of methane with air mass flow rate \bar{m} of (a) 2.5 g s^{-1} , (b) 6.5 g s^{-1} , and (c) 10.5 g s^{-1} (with nozzle termination). A five point moving average has been used and the standard error is shown ($\pm 1\sigma_{\bar{x}}$). Ten pulses ($N_p = 10$) have been averaged. Intensifier gain $G = 55\%$. 96
- 4.24 For a 9% methane-air mixture: (a) energy-normalised counts C as a function of time and wavenumber; (b) time-resolved integrated counts for N_2 ($\hat{C}_{S'_{N_2}}$) and CH_4 ($\hat{C}_{S'_{CH_4}}$) as a function of time. 97
- 4.25 Original calibration curve (—) and corrected calibration curve scaled by r (⋯) for N_2 (—) and CH_4 (—). 99

- 4.26 Mole X and mass Y fractions for measured (— N_2 , — CH_4) and inferred total (—) due to a single pulse, co-flow injection of methane with air mean flow rate \bar{m} of 11 g s^{-1} for (a) far and (b) close injection locations. Expected total (---) is also included. Ten pulses ($N_p = 10$) have been averaged. Intensifier gain $G = 55\%$ 100
- 5.1 Schematics of setups used for characterisation experiments. For the injection of air, $L_a = L_h$ (30 m) and for the injection of methane, $L_a = 2L_h$ (60 m). 106
- 5.2 Acoustic waves generated by the co-flow injection of air: (a) upstream-travelling direct noise waves π_d^- ; (b) downstream-travelling direct noise waves π_d^+ ; (c) mean perturbation amplitude from experiments (\bullet) with polynomial fit (—) and theoretical model predictions for co-flow injection (---) and cross-flow injection (.....) for both waves; (d) ratio of direct noise waves π_d^-/π_d^+ 108
- 5.3 Acoustic waves generated by the co-flow injection of methane: (a) upstream-travelling direct noise waves π_d^- ; (b) downstream-travelling direct noise waves π_d^+ ; (c) mean perturbation amplitude from experiments (\bullet) with polynomial fit (—) and theoretical model predictions for co-flow injection (---) and cross-flow injection (.....) for both waves; (d) ratio of direct noise waves π_d^-/π_d^+ 109
- 5.4 Co-flow injection of air: (a) polynomial fits for experimental data (—) compared to co-flow theory for π_d^+ (---) and π_d^- (.....) using $d_i = 3.4 \text{ mm}$ for $Y_i = 0.09, 0.10$ and 0.11 ; (b) polynomial fits for experimental data (—) compared to co-flow theory for π_d^+ (---) and π_d^- (.....) using $Y_i = 0.10$ for $d_i = 3.4 \text{ mm}$, $d_i = 2.5 \text{ mm}$ and decreasing $d_i = 3.4 \rightarrow 2.5 \text{ mm}$; (c) ratio of experimental fits for direct noise wave amplitudes π_d^-/π_d^+ (—) compared to co-flow theory using $d_i = 3.4 \text{ mm}$ for $Y_i = 0.09, 0.10$ and 0.11 ; (d) ratio of experimental fits (—) for direct noise wave amplitudes π_d^-/π_d^+ compared to co-flow theory using $Y_i = 0.10$ for $d_i = 3.4 \text{ mm}$, $d_i = 2.5 \text{ mm}$ and decreasing $d_i = 3.4 \rightarrow 2.5 \text{ mm}$ 110

- 5.5 Co-flow injection of methane: (a) polynomial fits for experimental data (—) compared to co-flow theory for π_d^+ (---) and π_d^- (.....) using $d_i = 3.4$ mm for $Y_i = 0.09, 0.10$ and 0.11 ; (b) polynomial fits for experimental data (—) compared to co-flow theory for π_d^+ (---) and π_d^- (.....) using $Y_i = 0.10$ for $d_i = 3.4$ mm, $d_i = 2.5$ mm and decreasing $d_i = 3.4 \rightarrow 2.5$ mm; (c) ratio of experimental fits for direct noise wave amplitudes π_d^-/π_d^+ (—) compared to co-flow theory using $d_i = 3.4$ mm for $Y_i = 0.09, 0.10$ and 0.11 ; (d) ratio of experimental fits (—) for direct noise wave amplitudes π_d^-/π_d^+ compared to co-flow theory using $Y_i = 0.10$ for $d_i = 3.4$ mm, $d_i = 2.5$ mm and decreasing $d_i = 3.4 \rightarrow 2.5$ mm. 111
- 5.6 Co-flow injection of air with constrained $Y_i \pm 0.01$ (---) and unconstrained (---) solutions for co-flow theory predictions: (a) π_d^\pm waves with fit (—); (b) injection mass fraction with assumed experimental set point (—); (c) ratio of waves with fit (—); (d) optimised injection diameter with geometric diameter (—) 112
- 5.7 Co-flow injection of methane with constrained $Y_i \pm 0.01$ (---) and unconstrained (---) solutions for co-flow theory predictions: (a) π_d^\pm waves with fit (—); (b) injection mass fraction with assumed experimental set point (—); (c) ratio of waves with fit (—); (d) optimised injection diameter with geometric diameter (—) 113
- 5.8 Pressure perturbations due to co-flow injection of air using setup A (—) and setup C (.....) for (a) $\bar{m}/\bar{m}_c = 0.25$ and (b) $\bar{m}/\bar{m}_c = 1.1$ with standard deviation ($\pm 1\sigma$) used to compute the inlet's reflection coefficient R_{i1} . . . 114
- 5.9 Inlet reflection coefficient R_{i1} : experiments (\bullet) with standard deviation ($\pm 1\sigma$) and mean (—). 115
- 5.10 Pressure perturbations due to co-flow injection of air using setup A (—) and setup B (.....) for (a, c) $\bar{m}/\bar{m}_c = 0.25$ and (b, d) $\bar{m}/\bar{m}_c = 1.1$ with standard deviation ($\pm 1\sigma$) used to compute the nozzle's upstream reflection R_{o1} and transmission T_{o1} coefficients. 116
- 5.11 Nozzle's acoustic (a) reflection coefficient R_{o1} and (b) transmission coefficient T_{o1} : experiments (\bullet) with standard deviation ($\pm 1\sigma$), polynomial fit (—), scaled polynomial fit (.....), and experimental data from similar nozzle⁶⁴ (\circ). 117

- 5.12 Acoustic waves for (a) test case Air-A-1 ($\bar{m}/\bar{m}_c = 0.25$), (b) test case Air-A-18 ($\bar{m}/\bar{m}_c = 1.1$), (c) test case Air-C-1 ($\bar{m}/\bar{m}_c = 0.25$) and (d) test case Air-C-18 ($\bar{m}/\bar{m}_c = 1.1$), with standard deviation ($\pm 1\sigma$) used to compute the system's acoustic attenuation α . Pressure perturbations at x_1 (—) and x_2 (—) are shown along with predicted p' if there were no attenuation of the waves ($\alpha = 0 \text{ m}^{-1}$). 118
- 5.13 Acoustic attenuation α as a function of normalised mean flow rate \bar{m}/\bar{m}_c : experimental data using test cases Air-A (•) and Air-C (◦) and a linear fit (—). 119
- 5.14 Anechoic subtraction method visualised: test CH₄-B-18 (⋯) minus scaled direct noise signal(s) (—). Resultant indirect acoustic waves (—) due to co-flow injection of methane for $\bar{m}/\bar{m}_c=1.1$ are shown: π_i^- for (a) far and (b) close injection locations; π_i^+ for (c) far and (d) close injection locations. A 15 ms moving average filter has been applied to the indirect noise signals. 120
- 5.15 Indirect noise waves obtained via anechoic subtraction: π_i^\pm for the (a) far and (b) close injection locations. A 15 ms moving average filter has been applied to the signals. 121
- 5.16 CWR setup for the single pulse injection campaign with far ($L_c = 0.55 \text{ m}$) and close ($L_c = 0.11 \text{ m}$) injection locations. The anechoic length is $L_a \simeq 90 \text{ m}$ giving an anechoic time of $\tau_a = 0.5 \text{ s}$. Pressure perturbations are measured by two transducers (one upstream and one downstream of the nozzle). Dimensions not to scale. 122
- 5.17 Upstream (a) and downstream (b) pressure perturbations due to injection at the far location. Colourmaps show methane injection perturbations using linear interpolation to map between different mean flow rates. Data is scaled using a power-law relationship ($y = x^\gamma$, where $\gamma = 0.5$) in order to more easily visualise the lower amplitude perturbations; (b,d) three flow rates from the respective colourmaps (i–iii) are selected for the measurement of methane (—) and scaled air (---) injection pressure perturbations. 123
- 5.18 Upstream (a) and downstream (b) pressure perturbations due to injection at the close location. Colourmaps show methane injection perturbations using linear interpolation to map between different mean flow rates. Data is scaled using a power-law relationship ($y = x^\gamma$, where $\gamma = 0.5$) in order to more easily visualise the lower amplitude perturbations; (i–iii) three flow rates from the respective colourmaps are selected for the measurement of methane (—) and scaled air (---) injection pressure perturbations. . . 125

5.19	Upstream (a) and downstream (b) pressure perturbations at the end of the pulse ($t = 0.05$ s) due to the co-flow injection of methane at the far (—) and close (—) injection locations as a function of normalised mean flow rate \bar{m}/\bar{m}_c	126
5.20	Reverberated indirect noise pressure perturbations obtained by subtracting scaled air signals from methane signals: (a) upstream and (b) downstream of the nozzle.	126
5.21	Indirect noise waves obtained via dereverberation: π_i^\pm for the (a) far and (b) close injection locations. A 15 ms moving average filter has been applied to the signals.	127
5.22	Comparison of indirect wave quantification methods: (a) anechoic subtraction and (b) dereverberation. A 15 ms moving average filter has been used and the subtraction noise appearing before the arrival of the pulses has been filtered out for clarity purposes.	128
5.23	Indirect noise waves: maximum (a) π_i^- and (b) π_i^+ as a function of normalised mass flow rate \bar{m}/\bar{m}_c for far (\circ) and close (\bullet) injection locations. Also included are the best fits for close (—) and far (---) injection results obtained using the anechoic subtraction (—) and dereverberation (—) methods.	129
5.24	Indirect noise waves: (a) integral of π_i^- with respect to time, and (b) integral of π_i^+ with respect to time as a function of normalised mass flow rate \bar{m}/\bar{m}_c for far (\circ) and close (\bullet) injection locations. Included for visualisation purposes are the average integrals for the anechoic subtraction (—) and dereverberation (—) methods.	130
5.25	Indirect-to-direct noise ratios for (a) upstream and (b) downstream chambers for far (\circ) and close (\bullet) injection locations. Included are results obtained via anechoic subtraction (i.e. with anechoic inlet and outlet $R_{i1} = R_{o2} = 0$ condition in §5.3.4 —) and via dereverberation (i.e. with anechoic outlet $R_{o2} = 0$ condition in §5.4.3 —).	132
5.26	Original calibration curve (—) and corrected calibration curves (.....) used to extract species concentration from the time-resolved integrated counts \hat{C} . The nitrogen counts during the unsteady injection experiments were different than during the original calibration. As a result, two corrected calibration curves are needed (one for each injection campaign) obtained using the methodology described in §4.3.7.	133

- 5.27 Raman spectroscopy measurements due to injection at (a) close (—) and far (—) locations for all 18 test cases (10 pulse average for each case); experiments for each injection location were run independently, but the signals have been superimposed for visualisation purposes. Colours are mapped for ξ using a power-law relationship ($y = x^\gamma$ where $\gamma = 0.5$) in order to more easily visualise the lower amplitude wave. Linear interpolation is used to map between different mean flow rates in the y-axis; (b) three flow rates from the colourmap are selected to show the changes in signature for different \bar{m}/\bar{m}_c and a five-point (i.e. 3.33 ms) moving average is used; included is the area-weighted result for the close injection case (—). 134
- 5.28 Computer-aided drawing rendering of the injected jet based on the half-angle of a free jet's turbulent cone ($\theta_{tc} \approx 12^\circ$)^{70,324}: for the close injection location, the probed region (●) is located within the mixing length L_m . The ratio of the injection jet area at the probe location A_j to the duct area A is estimated to be approximately 0.62. 135
- 5.29 Raman measurements: (a) mean peak compositional amplitude ξ and (b) time-integrated compositional amplitude $\frac{1}{t_i} \int \xi dt$ for close (—) and far (—) injection locations with associated entropic wave amplitude as per Eq. (2.46). Also included is the area-weighted close injection result (—). 136
- 5.30 Indirect noise nozzle transfer functions π_i^\pm/ξ (left y-axis) and π_i^\pm/σ (right y-axis) due to injection at close (●) and far (○) locations. Contrasted are results using method 1 – proposed by De Domenico et al.⁶⁴ (—), method 2 – using peak quantities (—), and method 3 – using time-integrated quantities (—). 137
- 6.1 Acoustic pressure field $p' = p'_i + p'_r$ in a cylindrical flow duct with low Mach number mean flow \bar{M} 146
- 6.2 Modified CWR setup used to characterise the inlet (perforated plate) reflection coefficient R_{i1} via the multi-microphone method: sinusoidal excitation is provided by two horn drivers and pressure perturbations are measured using the four pressure transducers highlighted. Lengths not to scale. 148
- 6.3 Reflection coefficient for perforated plate inlet as a function of frequency f for no bias flow ($\bar{m} = 0 \text{ g s}^{-1}$): experimental magnitude $|R_{i1}|$ (○) and phase $\angle R_{i1}$ (○), and numerical magnitude $|R_{i1}|$ (—) and phase $\angle R_{i1}$ (—) computed using the LNSE method (numerical data courtesy of Kah Joon Yong and Maximilian Meindl). 151

- 6.4 Reflection coefficient for perforated plate inlet as a function of frequency f and flow rate \bar{m} measured using multi-microphone method: magnitude $|R|$ (left) and phase $\angle R$ (right). 152
- 6.5 Upstream reflection R_{o1} and transmission T_{o1} coefficients for the convergent-divergent nozzle obtained using a hybrid RANS/LNSE approach (numerical data courtesy of Kah Joon Yong and Maximilian Meindl). Experimental data obtained in §5.3.3 for zero-frequency case (i.e. acoustically compact $He = 0$) is also included for comparison (\circ). 153
- 6.6 CWR setup for the pulse burst injection campaign using the close injection location ($L_c = 0.11$ m). The anechoic length is $L_a \simeq 120$ m giving an anechoic time of $t_a = 0.7$ s. Pressure fluctuations measured by four transducers (two upstream and downstream of the nozzle, respectively). Dimensions not to scale. 154
- 6.7 Acoustic pressure perturbations measured by the two upstream (p'_{11} — and p'_{12} —) and downstream (p'_{21} — and p'_{22} —) transducers due to the co-flow injection of methane at frequency f_i for two mean flow rate limit cases: (a) $\bar{m}/\bar{m}_c = 0.6$ (subsonic nozzle) and (b) $\bar{m}/\bar{m}_c = 1.1$ (sonic/choked nozzle). Anechoic window $\tau_a = 0.7$ s is shown. 155
- 6.8 Original calibration curve (—) and corrected calibration curves (.....) used to extract species concentration from the time-resolved integrated counts \hat{C} . The nitrogen counts during the unsteady injection experiments were different than during the original calibration. As a result, a corrected calibration curve is needed obtained using the methodology described in §4.3.7. The 2 Hz injection case is used to calibrate all the Raman experiments in this chapter. 156
- 6.9 Raman measurements – compositional ξ and entropic σ wave amplitudes due to the co-flow injection of methane at frequency f_i for two mean flow rate limit cases (a) $\bar{m}/\bar{m}_c = 0.6$ (subsonic nozzle) and (b) $\bar{m}/\bar{m}_c = 1.1$ (sonic/choked nozzle). Anechoic window $\tau_a = 0.7$ s is shown with the first 40 ms highlighted in blue. 157
- 6.10 FFT magnitude for normalised air mass flow rate $\bar{m}/\bar{m}_c = 0.6$ (subsonic nozzle): (a) acoustic pressure signals of the two upstream (p'_{11} — and p'_{12} —) and downstream (p'_{21} — and p'_{22} —) transducers; (b) compositional wave amplitude ξ due to methane injection. Signals cut at 0.7 s (anechoic time τ_a). 159

- 6.11 FFT magnitude for normalised air mass flow rate $\bar{m}/\bar{m}_c = 1.1$ (sonic/choked nozzle): (a) acoustic pressure signals of the two upstream (p'_{11} — and p'_{12} —) and downstream (p'_{21} — and p'_{22} —) transducers; (b) compositional wave amplitude ξ due to methane injection. Signals cut at 0.7 s (anechoic time τ_a). 160
- 6.12 Source identification: extracting acoustic wave sources (π_d^\pm, π_i^\pm) from reverberated pressure signals for pulse burst injection frequencies f_i for $\bar{m}/\bar{m}_c = 0.6$ (subsonic nozzle). Included are the downstream-travelling waves π_d^+, π_i^+ (—) and the upstream-travelling waves π_d^-, π_i^- (—). Anechoic window $\tau_a = 0.7$ s is shown with the first 40 ms highlighted in blue. 162
- 6.13 Source identification: extracting acoustic wave sources (π_d^\pm, π_i^\pm) from reverberated pressure signals for pulse burst injection frequencies f_i for $\bar{m}/\bar{m}_c = 1.1$ (sonic/choked nozzle). Included are the downstream-travelling waves π_d^+, π_i^+ (—) and the upstream-travelling waves π_d^-, π_i^- (—). Anechoic window $\tau_a = 0.7$ s is shown with the first 40 ms highlighted in blue. 163
- B.1 Calibration curves for (a) N_2 and (b) CH_4 shows data points for calibration test cases using different mean pressures \bar{p} (1.0–1.5 bar), intensifier gains G (35–70%) and methane mass fractions Y_{CH_4} (● 0%, ● 10%, ● 20%, ● 30%, ● 40%, ● 50%, ● 100%). Error bars show the standard deviation ($\pm 1\sigma$) in the signal for each test case. The region of operation is presented (cases where camera has saturated are not shown) where $EM = 15$ is the intensifier's electron multiplication factor and c_i is the molar concentration of the respective molecule. Lines of best fit (—) use the power-law $y = \beta x^\eta$ where β and η are constants calculated via the sum of squared residuals method for each gas ($\beta_{CH_4} = 4289 \pm 1$, $\eta_{CH_4} = 0.77 \pm 0.02$, $\beta_{N_2} = 673 \pm 2$, $\eta_{N_2} = 0.79 \pm 0.04$). 220

- B.2 Integrated counts for N₂ (●) and CH₄ (●) versus normalised x-axis where EM = 15 is the intensifier's electron multiplication factor, G is the intensifier gain, c_i is the molar concentration and $d\sigma/d\Omega|_i$ is the differential Raman scattering cross section of the respective molecule. Error bars show the standard deviation ($\pm 1\sigma$) in the signal for each test case. The region of operation is presented (cases where camera has saturated are not shown). Data follows a power-law $y = \beta x^\eta$ where β and η are constants calculated via the sum of squared residuals method ($\beta = 1.63 \times 10^{29}$, $\eta = 0.76$) along with the ratio of differential Raman scattering cross section between the two molecules, which is estimated to be $\frac{d\sigma}{d\Omega}|_{\text{CH}_4} / \frac{d\sigma}{d\Omega}|_{\text{N}_2} = 7.9$. This agrees with literature^{57,91,253}. 221
- B.3 Signal-to-background ratio (SBR) for N₂ and CH₄: calibration test cases are shown here (cases where the camera has saturated are not shown) with different mean pressures \bar{p} (1.0–1.5 bar), intensifier gains G (35–70%) and methane mass fractions Y_{CH_4} (● 0%, ● 10%, ● 20%, ● 30%, ● 40%, ● 50%, ● 100%). For cases shown, $\text{SBR}_{\text{CH}_4} > 4$ and $\text{SBR}_{\text{N}_2} < 4$ 222
- B.4 Error analysis for (a) single pulse and (b) pulse burst experiments: (top) mean total mole fraction \bar{X}_{tot} computed across the anechoic window; (middle) mean standard deviation $\bar{\sigma}$ of compositional wave amplitude ξ computed across the anechoic window – calculated by propagating forward the standard deviation of the time-resolved integrated counts \hat{C} ; (bottom) mean standard error $\bar{\sigma}_{\bar{x}}$ of compositional wave amplitude ξ computed across the anechoic window – calculated by propagating forward the standard error of the time-resolved integrated counts \hat{C} 223

List of tables

2.1	Summary of compact wave sources. For gas injection, it is assumed the injected gas and mean flow air are at the same temperature ($T_i = \bar{T}$) and that the pressure is equilibrated at the injection plane ($p_i = \bar{p}$).	27
2.2	Summary of model experiments in literature presented in chronological order. From left to right: first author, year of publication, unsteady synthetic source type (temperature T' , vorticity Ω' , composition Y'), approximate maximum absolute entropic wave amplitude σ_{\max} , source identification method used (TC: thermocouple sensor; PIV: Particle Image Velocimetry; LITGS: Laser-Induced Thermal Grating Spectroscopy; BOS: Background-Oriented Schlieren; APs: aerodynamic probes, including pneumatic probes, five-hole probes, aerodynamic pressure probes, and total pressure probes; Sp. Raman: spontaneous Raman spectroscopy), nozzle flow condition \bar{M} (subsonic/choked/supersonic), and measurement of pressure fluctuations p' (upstream/downstream of acceleration region).	39
3.1	Estimated injected mass flow rate (\dot{m}_i), Reynolds number (Re_i), Mach number (M_i), jet-to-crossflow momentum flux ratio (J), molecular weight (W), density ratio ($\rho_i/\bar{\rho}$), entropic-compositional coupling term defined by Eq. (2.46) ($\Delta s/\bar{c}_p$), dynamic viscosity (μ), and laminar and turbulent Schmidt numbers (Sc_l, Sc_t) for each gas at $T = 293$ K ¹⁰⁸ . The mean flow rate of air is $\bar{m} = 1.57$ g s ⁻¹ ($\bar{u} = 0.92$ m s ⁻¹ , $Re = 2580$) for all cases. For air, $\mu = 18.3$ μ Pa s and $Pr = 0.7$	49
3.2	Summary of test cases: bulk flow velocity \bar{u} , Reynolds number Re , bulk power factor b , maximum heat transferred to air $\dot{Q}_{c_{\max}}$, and time constant τ_w . Transient factor $a = 1.50$ for all cases.	53
4.1	Canonical waves generated due to the injection of air or methane ²⁷⁸	75

5.1	Experimental test conditions: primary mass flow rate \bar{m} , approximate bulk throat Mach number \bar{M}_t , injected mass flow rate of methane \dot{m}_i , estimated methane bulk injection velocity \bar{u}_{i,CH_4} , upstream mean pressure \bar{p}_1 , upstream Mach number \bar{M}_1 , downstream mean pressure \bar{p}_2 , downstream Mach number \bar{M}_2 , upstream bulk flow velocity \bar{u}_1 , and upstream Reynolds number Re	105
5.2	System and source characterisation test cases and measured variables. Each setup was used at every flow rate (18 cases, from 2.5 to 11 g s ⁻¹ in 0.5 g s ⁻¹ increments) for the co-flow injection of the two gases (air or methane). Methane experiments using setup B were run for two convective lengths (close and far injections – see Fig. 5.16).	107
5.3	Summary of indirect-to-direct noise ratios for different cases: fully reverberating bicameral system ²⁷⁸ , partially non-reverberating bicameral system (i.e. non-reverberating upstream (US) or downstream (DS) chambers with anechoic inlet or outlet, respectively), and fully non-reverberating bicameral system (non-reverberating upstream and downstream chambers with anechoic inlet and outlet).	131
6.1	Experimental test conditions: injection frequency f_i , maximum estimated Helmholtz number He , primary mass flow rate \bar{m} , estimated injection mass fraction of methane Y_i , estimated injected mass flow of methane \dot{m}_i , and number of pulses during anechoic window.	144
7.1	Summary of one-dimensional models for acoustically compact or non-compact, isentropic or non-isentropic regions of flow acceleration subject to linear or non-linear acoustic π , entropic σ , compositional ξ , or vortical Ω perturbations. The first published journal papers are referenced; for full list of works, see the literature review presented in §2.2.1. Empty table cells represent gaps in current literature.	176
B.1	Raman spectroscopy setup: beam diameter d , numerical aperture NA, resolution in x - y plane δ_{xy} , resolution in z plane δ_z , confocal volume V_{con} , and illumination volume V_{ill}	219

Nomenclature

Roman Symbols

a	transient multiplier factor
A	cross-sectional area
b	bulk power factor
c	speed of sound or molar concentration
c_p	specific heat capacity at constant pressure
C_{raw}	raw counts
C	energy normalised counts
\bar{C}	summed counts
$\bar{\bar{C}}$	integrated counts
\hat{C}	time-resolved integrated counts
e	specific energy
E	energy
f	frequency or focal length
G	intensifier gain
g	Gibbs free energy
h	specific enthalpy or heat transfer coefficient
He	Helmholtz number

I	signal intensity
j^H	heat flux
j^M	mass diffusion flux
J	jet-to-crossflow momentum flux ratio
k	angular wavenumber or turbulent kinetic energy
L	length
\dot{m}	mass flow rate
M	Mach number
n	refractive index
N_s	number of shots
N_p	number of injected pulses
N_b	number of injected pulse bursts
p	pressure
P	power
Pr	Prandtl number
\dot{Q}	power or heat transfer rate
r	radius or calibration scaling factor
R	acoustic reflection coefficient or specific gas constant
\mathcal{R}_u	universal gas constant
$\tilde{\mathcal{R}}$	reverberation transfer function
Re	Reynolds number
s	specific entropy
Sc	Schmidt number
\dot{S}_q	volumetric source term

t	time
T	acoustic transmission coefficient or temperature
\bar{T}	transmissive transfer function
t_p	pulse duration
t_t	transient current surge duration
u	velocity
V	volume or voltage
\mathcal{V}	time-integrated voltage
\dot{w}	rate of chemical production/consumption
W	molecular weight or molar mass
X	mole fraction
Y	mass fraction
Z	mixture fraction

Greek Symbols

α	acoustic attenuation coefficient or thermal diffusivity
β	power law constant
γ	specific heat capacity ratio
ϵ	rate of dissipation of turbulent kinetic energy k
ζ	vortical wave amplitude
η	power law exponent
Θ	linearised heat conduction factor
κ	thermal conductivity or confocal volume geometric factor
λ	wavelength
μ	chemical potential, dynamic viscosity or arithmetic mean

ν	kinematic viscosity
$\tilde{\nu}$	linear spectroscopic wavenumber
ξ	compositional wave amplitude
π	acoustic wave amplitude
ρ	density
σ	entropic wave amplitude or standard deviation
τ	acoustic round-trip time delay
$\boldsymbol{\tau}$	viscous stress tensor
τ_c	convective time delay
τ_w	heating grid wire's time constant
Φ_e	energy flux perturbation
Φ_M	momentum flux perturbation
Φ_m	mass flux perturbation
Φ_Z	mass fraction perturbation
φ_e	normalised energy flux perturbation
φ_M	normalised momentum flux perturbation
φ_m	normalised mass flux perturbation
φ_Z	normalised mass fraction perturbation
Ψ	chemical potential function
Ω	vorticity
ω	angular frequency or turbulent dissipation rate

Superscripts

$(\bar{\cdot})$	mean component
$(\cdot)'$	fluctuating component

- $(\cdot)^-$ backward-propagating
 $(\cdot)^+$ forward-propagating
 $\overline{(\cdot)}$ Reynolds-averaged
 $\tilde{(\cdot)}$ Favre-averaged
 $\hat{(\cdot)}$ frequency domain (FFT)

Subscripts

- $(\cdot)_\infty$ ambient
 $(\cdot)_0$ upstream of compact wave source
 $(\cdot)_1$ upstream of nozzle
 $(\cdot)_2$ downstream of nozzle
 $(\cdot)_a$ anechoic
 $(\cdot)_B$ background Raman (Stokes) signal
 $(\cdot)_{cl}$ centreline
 $(\cdot)_i$ indirect, inlet, injected, or incident
 $(\cdot)_j$ jet
 $(\cdot)_k$ kinetic
 $(\cdot)_l$ laminar or laser
 $(\cdot)_{mol}$ molecular vibration
 $(\cdot)_o$ outlet
 $(\cdot)_p$ pulse(s), photon, or probe volume
 $(\cdot)_r$ radial
 $(\cdot)_s$ shots
 $(\cdot)_S$ full Raman (Stokes) signal
 $(\cdot)_{S'}$ background-free Raman (Stokes) signal

- $(\cdot)_{sc}$ scattered light
 $(\cdot)_t$ total (stagnation) property, turbulent or throat
 $(\cdot)_W$ wall
 $(\cdot)_w$ wire

Other Symbols

- \aleph heat capacity factor
 $\frac{d\sigma}{d\Omega}$ differential Raman scattering cross-section

Acronyms / Abbreviations

- 0D Zero-Dimensional
1D One-Dimensional
2D Two-Dimensional
ACARE Advisory Council for Aeronautics Research and Innovation in Europe
APU Auxiliary Power Unit
BOS Background-Oriented Schlieren
CARS Coherent Anti-Stokes Raman Spectroscopy
CFD Computational Fluid Dynamics
CIPCF Cambridge Intermediate Pressure Combustion Facility
CNC Computer Numerical Control
CPU Central Processing Unit
CW Continuous Wave
CWG Cambridge Wave Generator
CWR Canonical Wave Rig
DOF Depth Of Focus

DPSSL	Diode-Pumped Solid-State Laser
EMCCD	Electron Multiplying Charge-Coupled Device
EM	Electron Multiplication Factor
EWG	Entropy Wave Generator
HAT	Hot Acoustic Test
ID	Inner Diameter
OD	Outer Diameter
JICF	Jet In Cross-Flow
LabVIEW	Laboratory Virtual Instrument Engineering Workbench
LDA	Laser Doppler Anemometry
LES	Large Eddy Simulations
LIF	Laser-Induced Fluorescence
LITGS	Laser-Induced Thermal Grating Spectroscopy
LNSE	Linearised Navier–Stokes Equations
LPP	Lean Premixed Prevaporised
MCP	Microchannel Plates
NA	Numerical Aperture
NASA	National Aeronautics and Space Administration
NGV	Nozzle Guide Vane
NI	National Instruments
OTRF	Oxford Turbine Research Facility
PDA	Photodetector Array
PIV	Particle Image Velocimetry
PLIF	Planar Laser-Induced Fluorescence

PML	Perfectly Matched Layer
PVC	Polyvinyl Chloride
PWM	Pulse Width Modulation
RANS	Reynolds-Averaged Navier–Stokes
RECORD	Research On Core Noise Reduction
ROI	Region Of Interest
RQL	Rich-Quench-Lean
RWE	Reflected Wavefront Error
SAF	Sustainable Aviation Fuel
SLPM	Standard Litre Per Meter
SBR	Signal-to-Background Ratio
SSME	Space Shuttle Main Engine
SST	Shear Stress Transport
TAFG	Temperature and Acoustic Fluctuations Generator
TDLAS	Tunable Diode Laser Absorption Spectroscopy
TEENI	Turboshaft Engine Exhaust Noise Identification
VDC	Voltage Direct Current
VWG	Vorticity Wave Generator
WMS	Wavelength Modulation Spectroscopy

Chapter 1

Introduction

FROM ancient times and into the Middle Ages, man had dreamed of taking to the sky, of soaring into the blue like the birds. One savant in Spain in the year 875 is known to have covered himself with feathers in the attempt. Others devised wings of their own design and jumped from rooftops and towers – some to their deaths – in Constantinople, Nuremberg, Perugia. Learned monks conceived schemes on paper. And starting about 1490, Leonardo da Vinci made the most serious studies. He felt predestined to study flight, he said, and related a childhood memory of a kite flying down onto his cradle.

(...)

What had transpired that day in 1903, in the stiff winds and cold of the Outer Banks in less than two hours time, was one of the turning points in history, the beginning of change for the world far greater than any of those present could possibly have imagined. With their homemade machine [here illustrated in Fig. 1.1], Wilbur and Orville Wright had shown without a doubt that man could fly.

– *The Wright Brothers* by McCullough²¹⁹

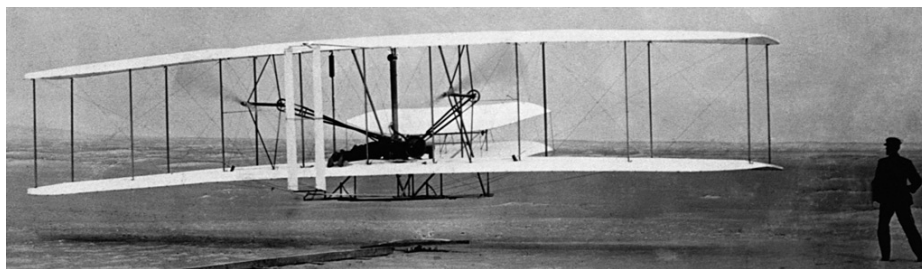


Fig. 1.1 The Wright Flyer takes off for the first time (Dec. 17th, 1903).

1.1 Motivation

More than a century after the flight of the first Wright Flyer prototype, the globe is evermore dependent on propulsive technologies to drive the economy, connect us with our loved ones, and power our dreams of exploring the unknown. The development of the primitive aircraft that took flight in 1903, soon led to rocket systems that propelled us into the stars: in fewer than 70 years, we went from a 37 m flight at Kitty Hawk to travelling almost 400,000 km to put humans on the Moon. The technologies that have, and continue to, enable us to achieve such historic feats are not without their trials and tribulations, however. A phenomenon termed the *thermoacoustic effect*, in particular, has created some challenges in our endeavour to explore the cosmos.

1.1.1 Thermoacoustic instabilities

The thermoacoustic effect was known anecdotally to European glassblowers in the eighteenth century as they heard a monotone sound when blowing a hot glass bulb at the end of a cold tube. Shortly after, the first scientific works on ‘singing flames’ were published, named specifically after the phenomenon of flames producing sound when placed inside a tube with a specific length^{119,122,179,268,328}. The physical mechanism behind this effect was qualitatively described by Lord Rayleigh¹⁹⁷ who proposed that thermoacoustic oscillations occur when the heat released by a flame is in phase with the acoustic pressure^{199,200}. It has since been shown that entropic, velocity, and mixture fraction fluctuations are also important coupling parameters¹⁵⁴.

Practically, thermoacoustically-driven instabilities have been an issue for rockets since the 1930s^{49,52,267}. When the aforementioned phase relationships are appropriate, discrete tones can be measured at resonant frequencies which are a function of the acoustic properties of the combustor²⁴⁹. These oscillations can then grow, causing fluctuations in thrust and enhancing heat transfer, the latter of which leads to increased chamber wall erosion⁵³. Further consequences include violent structural vibrations – which can accelerate component fatigue and reduce an engine’s lifetime by a factor of two or more – and, *in extremis*, component and engine failure^{67,190}, as shown in Fig. 1.2. Combustion chambers are inherently prone to these large-scale coherent pressure disturbances as they have substantial energy densities and low acoustic damping, the latter of which is caused by their highly acoustically reflective boundaries^{49,309}. The Saturn V rocket (Apollo’s astronaut-bearing vehicle which was powered by the Rocketdyne F-1 engine, 22 GW m⁻³) is an example of a large energy density system which encountered instability problems during development stages⁵³. As a result, the F-1 engine was one of the most expensive

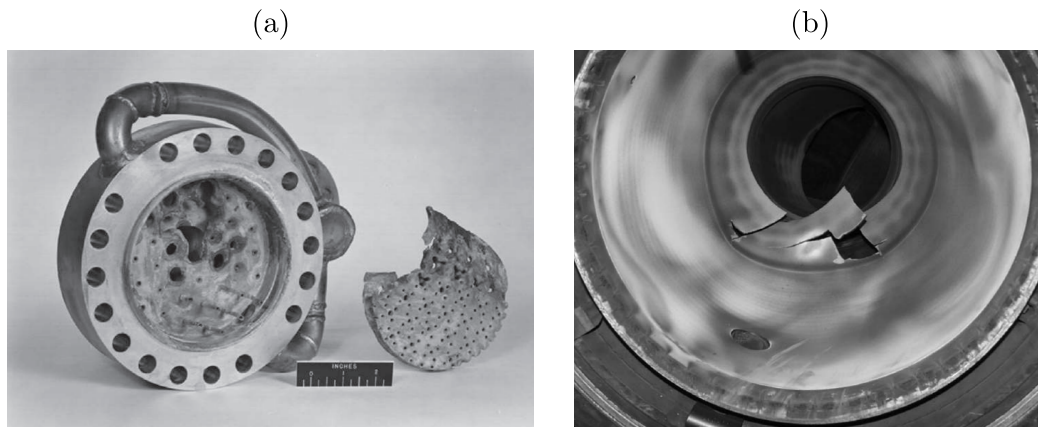


Fig. 1.2 Combustion instability damage: (a) rocket engine injector (Rocket Engine Testing Facility, NASA, 1957)²⁶⁰ and (b) combustion chamber liner¹⁹⁰.

engine development programs in history²⁴⁷. The explosion of an F-1 engine half a second after ignition in June of 1962 placed the entire Apollo Program in jeopardy⁵⁹. Passive control methods – such as the addition of baffle plates⁴⁸ and acoustic liners^{115,285} – can be used to stabilise engines. Active control methods are also gaining traction³⁵⁴. However, the instability’s high sensitivity to a myriad of design parameter – such as operating point, fuel composition, and injector geometry^{164,188} – make it a highly complex issue to fully solve. A recent case of the ever-present thermoacoustic-related problems is Virgin Galactic’s SpaceShipOne motor, which struggled with both low and high frequency combustion instabilities during initial testing phases⁴³.

The development of engine systems via trial and error is an expensive and impractical experimental endeavour. Ideally, one would identify and fix combustion instability problems during early design phases. Using computational fluid dynamics (CFD) is also expensive as the problem involves a wide spectrum of characteristic length scales. For reacting flows, these can range from molecular mixing and combustion (10^{-8} – 10^{-9} m) to acoustic oscillations at 100–1000 Hz (10^{-2} – 10^0 m); that’s a $O(7-9)$ range of scale. The problem is further compounded by the fact that these scales interact in a time-resolved manner!¹⁹⁰ A promising and economic avenue of research employs adjoint methods to predict instabilities and propose geometry changes to stabilise unstable modes³.

Nonetheless, despite almost a century of work, instability-generated oscillations still plague the rocket and gas turbine industries today³¹¹. It has been demonstrated that noise produced inside the combustion chamber (i.e. combustion noise) can be one of the sources triggering these instabilities^{107,262}. It is, therefore, of paramount importance to understand the mechanisms that lead to its generation and propagation.

1.1.2 The pollution problem

In parallel to thermoacoustic instability considerations, there are climate change and environmental noise concerns, especially for aircraft engines²⁸¹. The airline industry's contributions to air and noise pollution have long been a topic of public discussion. Of particular concern to policy makers has been the emission of carbon dioxide (CO_2) and nitrous oxides (NO_x), two of various harmful exhaust gases caused by the combustion of hydrocarbon fuels⁸¹, as presented in Fig. 1.3. The Advisory Council for Aeronautics Research and Innovation in Europe (ACARE) has set ambitious environmental and technological objectives for 2050 (relative to 2000). In particular, the *Flightpath 2050* vision outlines the goal of reducing CO_2 emissions by 75%, NO_x emissions by 90%, and aircraft noise by 65%⁸⁶.

Unsurprisingly, global aviation CO_2 emissions have been steadfastly increasing since 1940¹⁸⁰. As shown in Fig. 1.4a, they have quadrupled since 1966 and doubled since 1987, showing an average 4–5% growth per year since 2010^{93,275}. In 2018, global aviation (passenger and freight) is estimated to have emitted over 1 billion tonnes of CO_2 ; this constituted about 2.5% of total CO_2 emissions that year^{93,275}, approximately 1/6th of which was emitted in Europe⁸⁷; NO_x emissions show a similar trend (Fig. 1.4a). More recently, the widespread cancellation of flights during the 2020 pandemic led to an estimated 44% drop in aviation carbon emissions during the first half year, 70% of which were caused by international flights¹⁹⁶. In fact, according to the Global Carbon Project, the pandemic led to the largest relative annual fall in global carbon emissions since World

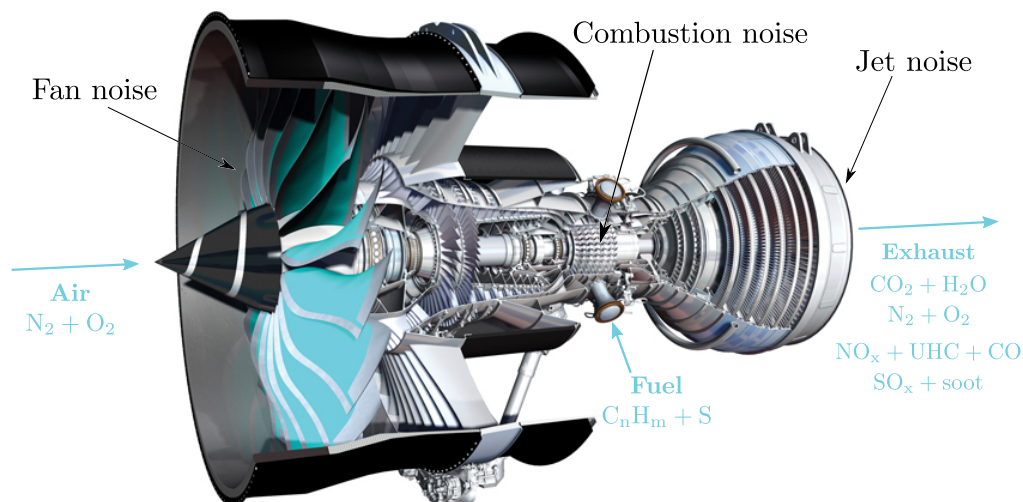


Fig. 1.3 Summary of primary engine noise sources⁶⁸ and greenhouse gas emissions⁸¹. Inspired by Dowling and Mahmoudi⁶⁸.

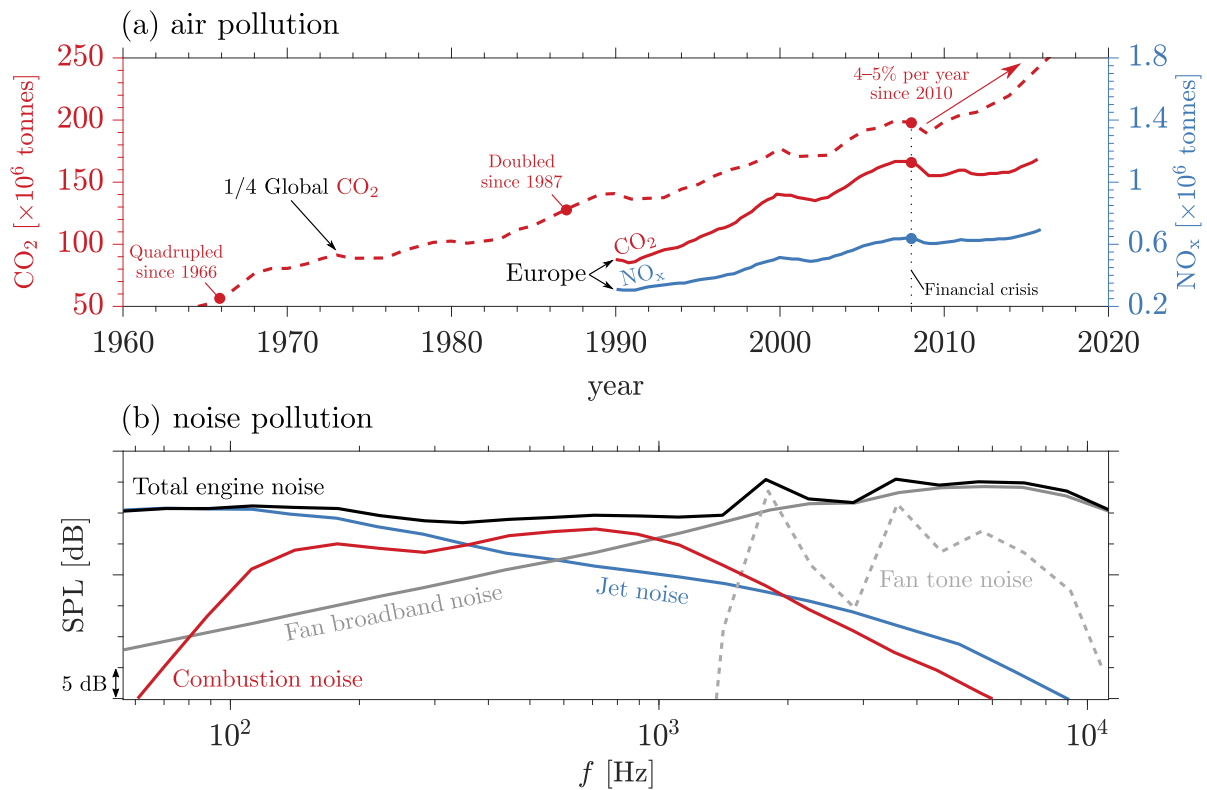


Fig. 1.4 Environmental pollution from commercial aviation: (a) air pollution – CO₂ and NO_x emissions. Global data (1964–2018) from Lee et al.¹⁸⁰, adapted from Ritchie²⁷⁵. European data (1990–2018) from European Union Aviation Safety Agency⁸⁷; (b) noise pollution – turbojet engine noise sources during approach conditions. Data from Safran Aircraft Engines (previously Snecma), adapted from Dowling and Mahmoudi⁶⁸.

War II^{94,221}. Notwithstanding this, if emissions are not halved by 2030, the average temperature on Earth is expected to increase above the 1.5 degrees Celsius threshold set out in the Paris Climate Agreement¹¹⁴.

Modern turbojet aircraft are approximately 80% more fuel efficient per seat kilometre than their 1960s analogues, and are expected to keep improving in efficiency at a rate of 1% per year⁴. This is partly due to engine design development, improved air traffic control efficiency, and increased passenger capacity⁶. Other factors contributing to overall increases in fuel efficiency include reduction of flight loads (e.g. through use of lighter aircraft components, paints, and external coatings), optimisation of aircraft operations, and improved engine cleanliness programs⁴.

More recently, there has been a push for a *net-zero future*. In the UK, this led to the establishment of a Jet Zero Council whose main objective is to fund new technologies to reduce aviation greenhouse gas emissions¹²⁷. Sustainable aviation fuels (SAFs) have been highlighted as important pillars to these goals as they have been shown to reduce

aviation's CO₂ emissions by up to 80% over their life cycle⁵. In parallel to funding SAF research, the Jet Zero council also created the FlyZero initiative which targets the development of zero-emission aircraft¹²⁷. In fact, novel propulsive ideas which target reduced emissions already exist. These ideas range from theoretical aircraft concepts – such as MIT's recent *turbo-electric* design proposal²⁶⁶ – to development programs that are deep into testing stages – such as Rolls-Royce's UltraFan engine, which is planned to be in service after 2025 and is predicted to improve fuel efficiency by 25% relative to the first-generation Trent engine¹³⁰. Ultimately, it is important to acknowledge that the reliable gas turbine is a part of our short to medium-term future, while other potential propulsive ideas are proposed, researched and developed. Indeed, approximately 80% of aviation CO₂ emissions are caused by flights of over 1500 kilometres for which there is no practical alternative mode of transport at the present time⁶. Greener engines are needed in order to meet a net-zero future, and low-NO_x advanced combustion strategies, such as lean premixed prevaporised (LPP) devices, have recently surfaced as viable solutions²⁸. The key change in these novel low-NO_x propulsion technologies is the burning of flames at extremely lean conditions and unusually low temperatures^{72,85}. Running these modern engines near their flammability limit leads to oscillations in equivalence ratio which makes the combustion process more unsteady⁶⁹. This, in turn, makes them considerably noisier and more prone to combustion instabilities^{44,166}.

In addition to its vicious effects in the combustion chamber (described in §1.1.1), combustion noise is transmitted downstream of the nozzle. This noise emanates out of the engine and contributes to overall aircraft noise, which has important societal and physiological implications. In fact, aircraft noise has been shown to be the source of transportation noise that most annoys people, ahead of road traffic and railway^{225,303}. More concerning, however, is its link to increased risk in the development of serious health complications, namely cardiovascular diseases^{156,302} (such as arterial hypertension⁸⁴, stroke¹⁷, and heart failure²⁴¹) as well as depression and anxiety²¹. Negative extraaural effects are particularly evident for people living near major airports, such as London Heathrow airport¹¹³, Munich International airport¹⁵¹ and New York City airports¹¹⁰. Global airline traffic is predicted to double by 2035 (and almost triple by 2045) relative to 2020¹⁵³. Although the COVID-19 pandemic is expected to affect air traffic demand predictions¹⁵², the negative impacts of aircraft noise pollution will escalate unless technological improvements are made. This has been the driving motivator behind ACARE's noise reduction objectives and NASA's technology goals^{149,154,322}.

An aircraft's noise sources can be traced to two general origins: the airframe and the engine^{281,299}. The former includes noise generated by the fuselage, landing gear

and any lifting surface (e.g. wings, flaps, etc). These tend to be more significant noise sources on approach conditions¹⁵⁴. The latter includes fan, combustion and jet noise, as shown in Fig. 1.3. Total aircraft noise per aircraft has generally been decreasing over the past decades owing mainly to the development of the turbofan engine¹²³. With higher by-pass ratios, the exhaust velocity is decreased, leading to a significant reduction in jet noise^{154,243}. The use of chevrons (the saw-tooth pattern on the trailing edge of nozzles) has also aided in minimising the exhaust jet noise³⁵³. Similarly, fan noise has been successfully reduced through intricate intake, fan blade, and combustion liner designs^{68,210}. For instance, negatively-scarfed intakes minimise perceived fan noise by reflecting it away from the ground²⁴⁴.

The reductions in jet and fan noise have made combustion noise a leading contributor to total engine noise (Fig. 1.4b). Indeed, its importance in auxiliary power units (APUs)³¹⁶ and aircraft (at low-power and idle conditions during landing approach) has already been identified¹⁵⁴, making combustion noise a subject of heightened interest among academics and industry researchers alike.

1.1.3 Combustion noise

The sound produced by the combustion process in combustors can generally be divided into two categories: direct and indirect, as illustrated in Fig. 1.5. In the reactive region, turbulent combustion leads to an unsteady heat release rate. The resulting volumetric contraction and expansion of the flame generates acoustic waves²⁹. This sound is termed *direct noise*⁶⁸. It acts as a monopole source⁴⁶ and scales with the rate of consumption of the fuel and oxidiser mixture in the flame^{150,321}. Unlike thermoacoustic instabilities, direct noise is incoherent and broadband in nature, and generally low in acoustic intensity¹⁵⁴. The direct noise mechanism in open, turbulent flames has been a topic of various studies since the 1960s^{38,116,306,307,312}. However, when a turbulent flame is no longer unconfined – as seen in practical aero-engine combustor, land-based gas turbine, and rocket engine applications – the flame dynamics are modified^{34,178} and another sound generation mechanism is present.

Synchronously to the generation of direct noise, a myriad of processes lead to the generation of further disturbances inside a combustor. Turbulent mixing, swirling flow, and incomplete combustion can lead to inhomogeneities in temperature (i.e. hot and cold spots, or *entropic waves*)³⁵, velocity (i.e. *vortical waves*)¹³⁸, and local mixture fraction (i.e. *compositional waves*)¹⁵⁴. The degree of heterogeneity in the flow can be further compounded downstream of the reactive region. For gas turbine combustors, in particular, there is cooling flow injected along the wall^{205,293}, as well as dilution jets in the quenching

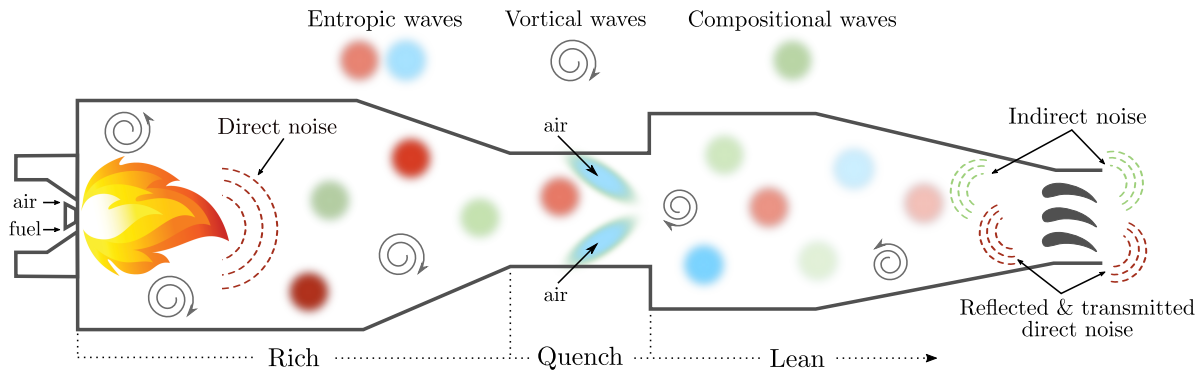


Fig. 1.5 Schematic of the GE Rich-Quench-Lean (RQL-2) gas turbine combustor⁹⁰. Inspired by Magri et al.²⁰⁵.

region of Rich-Quench-Lean (RQL) systems which contribute to additional compositional and temperature stratification. These inhomogeneities convect with the bulk flow and are usually accelerated at the outlet of the combustor by nozzle guide vanes (NGVs)¹, turbine blade rows, or a nozzle. The acceleration of these inhomogeneities produces a second acoustic source called *indirect noise*^{54,213}. It acts as an acoustic dipole²³⁵ and can be particularly problematic at low frequencies⁶⁸. Direct and indirect combustion noise can (1) reflect back into the combustion chamber to trigger thermoacoustic instabilities (as detailed in §1.1.1) and (2) propagate downstream of the acceleration region, contributing to the perceived far-field aircraft noise (as detailed in §1.1.2).

The relative contributions of direct and indirect noise are dependent on engine type, operating conditions, boundary conditions, and interaction with other noise sources¹⁵⁴. Recently, it was demonstrated that compositional indirect noise can be as large as direct and entropic noise, particularly when the outlet is choked and the mixture is lean²⁰⁶. Compositional noise has gained importance with the advent of low-emission combustors¹⁰⁴ and is, therefore, a compelling topic for research.

¹Entropic waves also negatively affect the performance of engine cooling systems leading to significantly reduced component life, such as in high pressure nozzle guide vanes²⁶⁴.

1.2 Thesis outline

The goal of this thesis is to further the understanding of the mechanisms that govern the generation, mixing, and convection of entropic and compositional inhomogeneities in the context of direct and indirect noise generation.

In chapter 2, the relevant research on direct and indirect noise is dissected and summarised. A theoretical framework for the thesis is established and a one-dimensional direct noise model is derived for the low-frequency, co-flow injection of gases.

In chapter 3, the generation, mixing, and convection of entropic and compositional waves is investigated using the URANS formulation. Issues pertaining to the modelling and experimental studies are underscored. This work informs the design of a new experimental setup which is presented in chapter 4.

In chapter 4, the experimental methods are described. The Canonical Wave Rig (CWR) is introduced as a new model thermoacoustic system which is used to study direct and indirect noise under simplified, well-controlled conditions. The acoustic and spontaneous Raman spectroscopy measurement techniques are described and characterised.

In chapter 5, the CWR is used for the simultaneous measurement of acoustics and species due to the single pulse, co-flow injection of air or methane into a low Mach number mean flow of air at low frequency (infra-sound range). Experimental data is obtained for subsonic and sonic (i.e. choked) nozzle conditions. Indirect noise is quantified and nozzle transfer functions are computed.

In chapter 6, the CWR is used for the simultaneous measurement of acoustics and species due to the pulse burst, co-flow injection of methane into a low-Mach number mean flow of air at frequencies of up to 250 Hz. Experimental data is obtained for subsonic and sonic nozzle conditions. A frequency-domain method of extracting indirect noise is used for the preliminary analysis of the acoustic measurements.

In chapter 7, the final remarks are outlined. In particular, the conclusions of this thesis are presented along with future work recommendations.

Chapter 2

State of the art

THIS chapter is used to dissect and summarise current and relevant literature on direct and indirect combustion noise. Firstly, the conservation equations are introduced and the mechanisms governing direct and indirect noise generation in combustion systems are briefly discussed. Secondly, analytical models are considered and a theoretical framework for the thesis is established. Lastly, past experimental studies are reviewed and current research challenges are discussed.

2.1 Theory of combustion noise

2.1.1 Governing equations

The spatio-temporal evolution of turbulent combustion processes can be described by the conservation equations for a multi-component, chemically reacting, ideal gas mixture without external forces.

Starting with mass and momentum conservation, respectively:

$$\frac{D\rho}{Dt} = -\rho \nabla \cdot \mathbf{u}, \quad (2.1)$$

$$\rho \frac{D\mathbf{u}}{Dt} = -\nabla p + \nabla \cdot \boldsymbol{\tau}, \quad (2.2)$$

where ρ is the density, \mathbf{u} is the velocity, p is the pressure, and $\boldsymbol{\tau}$ is the viscous stress tensor³⁸. We have made use of the density-weighted material derivative $\rho D(\cdot)/Dt$ where $D(\cdot)/Dt = \partial(\cdot)/\partial t + \mathbf{u} \cdot \nabla(\cdot)$ ¹⁷⁸.

Additionally, species are conserved and governed by:

$$\rho \frac{DY_i}{Dt} = -\nabla \cdot \mathbf{j}_i^M + \dot{w}_i, \quad (2.3)$$

where Y_i is the mass fraction, $\mathbf{j}_i^M = \rho Y_i \mathbf{u}_{D,i}$ is the mass diffusion flux, $\mathbf{u}_{D,i}$ is the diffusive velocity, and \dot{w}_i is the chemical production/consumption rate of species i ^{34,38}.

Finally, we consider the conservation of energy in terms of the specific enthalpy:

$$\rho \frac{Dh}{Dt} = \frac{Dp}{Dt} + q - \nabla \cdot \mathbf{j}_i^H + \boldsymbol{\tau} : (\nabla \mathbf{u}), \quad (2.4)$$

where h is the specific enthalpy, q is the heat source term (per unit volume), and \mathbf{j}_i^H is the heat flux due to conduction, mass diffusion, and radiation^{189,261}.

The system is closed using Gibbs' equation for a calorically perfect multi-component gas:

$$T ds = dh - \frac{1}{\rho} dp - \sum_{i=1}^N \left(\frac{\mu_i}{W_i} \right) dY_i, \quad (2.5)$$

where T is the temperature, s is the specific entropy, $\mu_i = W_i \left(\frac{\partial h}{\partial Y_i} \right)$ is the chemical potential, and W_i is the molecular weight of species i ³⁴⁴.

These are used in conjunction with the equation of state, which relates the pressure, density, and temperature of an ideal gas:

$$p = \rho RT \quad (2.6)$$

where R is the specific gas constant, which is a function of molecular weight and mixture composition⁴².

Combining Eqs. (2.4) and (2.5) leads to the equation governing entropy transport:

$$\underbrace{\rho T \frac{Ds}{Dt}}_{\text{Entropy advection}} = \underbrace{q}_{\text{Heat addition}} - \underbrace{\nabla \cdot \mathbf{j}_i^H}_{\text{Heat transfer}} + \underbrace{\tau : (\nabla \mathbf{u})}_{\text{Viscous effects}} - \underbrace{\rho \sum_{i=1}^N \left(\frac{\mu_i}{W_i} \right) \frac{DY_i}{Dt}}_{\text{Chemical reactions}}. \quad (2.7)$$

This evidently presents heat addition, heat transfer, viscous effects, and chemical reactions as entropic sources and sinks^{38,69,236}.

Analogously, the equation governing the behaviour of vorticity $\boldsymbol{\Omega} = \nabla \times \mathbf{u}$ can be derived by taking the curl of Eq. (2.2) and using the result in Eq. (2.1):

$$\underbrace{\frac{D}{Dt} \left(\frac{\boldsymbol{\Omega}}{\rho} \right)}_{\text{Vorticity advection}} = \underbrace{\left(\frac{\boldsymbol{\Omega}}{\rho} \cdot \nabla \right) \mathbf{u}}_{\text{Stretching of vortex lines } \propto \text{ local vorticity}} + \underbrace{\frac{1}{\rho^3} \nabla \rho \times \nabla p}_{\text{Misalignment of pressure and density gradients}} + \underbrace{\frac{1}{\rho} \nabla \times \left(\frac{1}{\rho} \nabla \cdot \boldsymbol{\tau} \right)}_{\text{Viscous effects}}. \quad (2.8)$$

Dowling and Stow⁶⁹ present the case of a circumferential wave in the reactive region as an example of a vorticity-generating mechanism, otherwise termed the *baroclinic mechanism* (i.e. $\nabla \rho \times \nabla p$)^{68,187}. This is a case where a pressure gradient and density gradient (i.e. the flame front) are not aligned.

2.1.2 Decomposition and evolution of disturbances

The governing equations derived so far can be used to fully describe the flow regime of interest. When it comes to analysing the acoustic behaviour of a system, a decomposition approach is commonly employed¹⁸⁹. In other words, we decompose the flow variables into their mean $\bar{\phi}(\mathbf{x})$ and first-order fluctuating $\phi'(\mathbf{x}, t)$ components, such that:

$$\phi(\mathbf{x}, t) = \bar{\phi}(\mathbf{x}) + \phi'(\mathbf{x}, t). \quad (2.9)$$

By assuming the fluctuations are linear, we are considering that their amplitude is small relative to the mean quantity (i.e. $\phi' \ll \bar{\phi}$). Higher-order fluctuating terms are neglected¹⁸⁹.

We can further simplify our analysis by assuming the flow is non-reacting ($\dot{w}_i = 0$), irrotational ($\mathbf{\Omega} = 0$), inviscid ($\boldsymbol{\tau} = 0$), calorically perfect ($p = \rho RT$, where c_p and c_v are constant) and without heat losses ($\nabla \cdot \mathbf{j}_i^H = 0$). This yields the linearised version of the governing equations:

$$\frac{\bar{D}\rho'}{Dt} = -\bar{\rho}\nabla \cdot \mathbf{u}', \quad (2.10)$$

$$\frac{\bar{D}\mathbf{u}'}{Dt} = -\frac{1}{\bar{\rho}}\nabla p', \quad (2.11)$$

$$\frac{\bar{D}s'}{Dt} = 0, \quad (2.12)$$

$$\frac{\bar{D}\mathbf{\Omega}'}{Dt} = 0, \quad (2.13)$$

$$\frac{\bar{D}\mathbf{Y}}{Dt} = 0. \quad (2.14)$$

Molecular transport effects on acoustic fluctuations are assumed to be negligible. These are only significant in boundary layers and when the acoustic wavelength is of the same order of magnitude of the molecular mean path (i.e. very high frequencies)¹⁸⁹.

Under the small perturbation conditions considered, the pressure fluctuations propagate at a speed represented by the local isentropic sound speed \bar{c} where $\bar{c}^2 = (\partial p / \partial \rho)_s$. In other words, if the flow is isentropic, the pressure solely depends on density, such that $p' = \bar{c}^2 \rho'$ ⁴⁶. Using Eqs. (2.10) and (2.11), we can obtain the acoustic wave equation:

$$\frac{\bar{D}^2 p'}{Dt^2} - \bar{c}^2 \nabla^2 p' = 0. \quad (2.15)$$

The wave equation has harmonic solutions representing superpositioned acoustic waves which propagate upstream and downstream.

For a one-dimensional flow, we can define pressure p' and velocity u' perturbations which travel at the speed of sound \bar{c} relative to the mean flow \bar{u} as:

$$\frac{p'}{\bar{\gamma}\bar{p}} = \pi^+ e^{i\omega(t - \frac{x}{\bar{c} + \bar{u}})} + \pi^- e^{i\omega(t - \frac{x}{\bar{c} - \bar{u}})}, \quad (2.16)$$

$$\frac{u'}{\bar{c}} = \pi^+ e^{i\omega(t - \frac{x}{\bar{c} + \bar{u}})} - \pi^- e^{i\omega(t - \frac{x}{\bar{c} - \bar{u}})}, \quad (2.17)$$

where π^\pm is the amplitude of the downstream and upstream-travelling acoustic waves²¹³.

Entropic s' , compositional Y' , and vortical Ω' perturbations are incompressible and stationary relative to the fluid, with a solution of frequency ω that is convected at the bulk flow velocity \bar{u} :

$$\frac{s'}{C_p} = \sigma e^{i\omega\left(t - \frac{x}{\bar{u}}\right)}, \quad (2.18)$$

$$Y' = \xi e^{i\omega\left(t - \frac{x}{\bar{u}}\right)}, \quad (2.19)$$

$$\frac{\Omega'}{\omega} = \zeta e^{i\omega\left(t - \frac{x}{\bar{u}}\right)}, \quad (2.20)$$

where σ , ξ , and ζ are the entropic, compositional, and vortical perturbation amplitudes, respectively^{35,68,74}.

As a result, we identify that the flow has both propagating (p' , u') and convecting (s' , Y' , Ω') disturbances.

2.1.3 Canonical mode coupling

In the linear analysis described, and assuming a homogeneous and uniform flow, the acoustic, entropic, compositional, and vortical canonical waves (or modes) are decoupled and propagate independently^{40,204}. However, modes can interact with each other (i.e. transfer energy to one another) at boundaries²⁵⁹, regions of flow inhomogeneity^{192,245}, and non-linearities¹⁸⁹. These coupling processes are sometimes also called *mode conversion mechanisms*.

Of particular interest to this thesis are the interactions due to flow inhomogeneities. The concept dates back to 1878 when Lord Rayleigh¹⁹⁷ demonstrated that regions of fluctuating density act as ‘scatterers’ for incident acoustic waves. Later, Chu and Kovásznay⁴⁰ extended the analogy to viscous heat-conducting gases. It wasn’t until 1973 that Morfey²³⁴ described the mechanism analytically using Lighthill’s analogy. Williams and Howe³⁴⁵ later coined the term *acoustic bremsstrahlung* owing to the fact that the convecting source requires a mean flow gradient to produce pressure waves.

We will now focus our attention on the entropy-sound²¹² and composition-sound²⁰⁷ coupling mechanisms produced by mean flow gradients (i.e. $d\bar{u}/dx \neq 0$).

Entropy-sound mechanism

Following on from the work of Tsien^{326,327} and Crocco⁴⁷ on rocket nozzles, Candel³⁵ reasoned that entropy spots could represent a significant source of noise when considering their acceleration through a nozzle. Not long after, Marble and Candel²¹³ presented a

reasoning for the entropy-sound mechanism. Assuming a one-dimensional adiabatic flow, the following normalised form of the momentum equation was derived:

$$\underbrace{\frac{\bar{D}}{Dt} \left(\frac{u'}{\bar{u}} \right) + \frac{\bar{c}^2}{\bar{u}} \frac{\partial}{\partial x} \left(\frac{p'}{\bar{\gamma}\bar{p}} \right) + \left(2\frac{u'}{\bar{u}} - (\bar{\gamma} - 1) \frac{p'}{\bar{\gamma}\bar{p}} \right) \frac{d\bar{u}}{dx}}_{\text{Refraction and reflection due to geometry and mean flow gradients}} = \underbrace{\frac{s'}{\bar{c}_p} \frac{d\bar{u}}{dx}}_{\text{Dipole source term}}. \quad (2.21)$$

Important physical insights can be obtained from Eq. (2.21). Firstly, we identify terms on the left-hand side which physically represent refraction and reflection effects due to the geometry and mean flow gradients. Secondly, on the right-hand side, the unsteady entropic fluctuation s'/\bar{c}_p interacts with the mean flow velocity gradient $d\bar{u}/dx$, appearing as a dipole source term. This describes the indirect (entropic) noise generation mechanism.

Tam and Parrish^{315,318} proposed a more physical interpretation of the entropy-sound mechanism assuming the processes associated with the convection through the nozzle are isentropic. They suggested that, during the acceleration and deceleration processes of the entropic wave, mass conservation and pressure conservation between the front and back ends of the entropy spot lead to the emission of pressure waves.

Composition-sound mechanism

Up until very recently, the work on indirect noise considered the flow to be compositionally homogeneous. In reality, and as mentioned in §1.1.3, the flow will likely be imperfectly mixed or, in the case of RQL systems, dilution jets upstream of the outlet will generate compositional waves.

Sinai²⁹⁶ first proposed that compositional perturbations generate sound when advected through low-Mach number flame fronts using the theory presented by Chiu and Summerfield³⁸. Magri²⁰⁴ and Ihme¹⁵⁴ then extended the theory of Marble and Candel²¹³ by accounting for mixture inhomogeneities, leading to the following normalised momentum equation:

$$\underbrace{\frac{\bar{D}}{Dt} \left(\frac{u'}{\bar{u}} \right) + \frac{\bar{c}^2}{\bar{u}} \frac{\partial}{\partial x} \left(\frac{p'}{\bar{\gamma}\bar{p}} \right) + \left(2\frac{u'}{\bar{u}} - (\bar{\gamma} - 1) \frac{p'}{\bar{\gamma}\bar{p}} \right) \frac{d\bar{u}}{dx}}_{\text{Refraction and reflection due to geometry and mean flow gradients}} = \underbrace{\left(\frac{s'}{\bar{c}_p} + (\bar{\Psi} + \bar{\aleph})Z' \right) \frac{d\bar{u}}{dx}}_{\text{Dipole source term}}, \quad (2.22)$$

where Ψ is the chemical potential function, \aleph is the heat capacity factor, and Z is the mixture fraction.

Analogously to the entropy-sound mechanism, the compositional inhomogeneity components appear as a dipole source term on the right-hand side of Eq. (2.22). Indirect noise is generated due to the unsteady interaction between the entropic s'/\bar{c}_p and compositional Z' perturbations (which are caused by density and species variation and are represented by the chemical potential Ψ and heat-capacity variation \aleph functions), and the mean flow gradient $d\bar{u}/dx$. Magri²⁰⁴ suggests that this indirect noise mechanism is physically caused by the compositional inhomogeneity's propensity to deform at a different rate than the encompassing mean flow when subjected to a velocity gradient.

2.2 Analytical modelling of direct and indirect noise

2.2.1 Review

The progress on the theoretical modelling of direct and indirect combustion noise has been reviewed many times over the past decades^{34,68,74,154,235,265,307,317}. In this subsection, we summarise the literature relevant to the work in this thesis. For both direct and indirect noise, we begin by discussing models which assume linear perturbations and acoustic compactness. The former assumption has been considered in §2.1.2. The latter assumption physically means that the acoustic perturbation wavelength is significantly larger than a system's characteristic axial length L_c (e.g. nozzle length). This is generally considered using the Helmholtz number $He = fL_c/\bar{c}$ where f is the perturbation frequency, and c is the speed of sound. Note, that there can be a 2π difference amongst literature – i.e. a system's reduced frequency can sometimes be defined as $He = \omega L_c/\bar{c}$ instead. When $He \ll 1$, then the compactness assumption is generally assumed to be valid²⁷⁴.

Direct noise

The direct noise generated by turbulent flames has been a topic of various theoretical studies since the 1960s^{34,313}. Particularly relevant to this thesis, however, are analytical models developed for non-reacting experiments (see §2.3.3). For instance, in the case of heat addition via Joule heating of wires, the entropy generated has been modelled using an unsteady heat source q' where it is assumed that there is no mean heat release. When the length of the unsteady source is negligible relative to the perturbation wavelength, a *compact wave source* can be assumed for linear perturbations. Jump conditions can be formulated for mass, momentum, total temperature, and entropy^{54,55,64,75,181,185}. The same was done in the work of Rolland et al.²⁷⁷ who extended the model to account for the cross-flow injection of gases of different composition. In their work, normalised jump

conditions for mass, momentum, energy, and composition were used instead, validating their predictions with experimental data. Rolland²⁷⁸ showed that their model agreed with previous literature when the appropriate flux additions were considered. This analytical model is derived in §2.2.3 and extended to model the waves generated by the co-flow injection of gases.

Indirect noise

The early work on nozzles' acoustic response was initially motivated by the desire to understand their effect on the stability of rocket systems. The response of a 'discharge' nozzle to acoustic fluctuations was first investigated analytically in 1952 by Tsien³²⁷. Other similar studies soon followed^{47–50}. In the late 1960s, the study of the acoustic response due to non-acoustic perturbations started to develop, firstly by Cuadra⁵¹. Candel³⁵, Marble²¹², and Bohn²⁵ followed suit shortly after, analytically studying the response of nozzles to entropic and acoustic perturbations.

The seminal work of Marble and Candel²¹³ was published in 1977. Acoustic and entropic transfer functions for a compact convergent divergent nozzle were derived assuming the nozzle is isentropic and the flow is accelerated quasi-steadily for both subsonic and supersonic flow conditions. In this case, the acoustic compactness assumption physically translates to cases where the perturbations are low frequency, and where the nozzle is treated as an infinitesimally small discontinuity. The interaction with a normal shock downstream of the nozzle was also investigated²¹³. Much later, Moase et al.²³² considered the presence of a normal shock downstream of the throat for arbitrarily shaped choked nozzles and supersonic diffuser geometries.

Pickett²⁵⁸ developed a low-frequency actuator disk theory to model the acoustic response of a blade row due to entropic wave impingement. Their theory showed positive agreement with experimental far-field pressure measurements. Shortly after, Cumpsty and Marble⁵⁶ presented analytical predictions using actuator disk theory for the interaction of entropic, vortical, and pressure waves with acoustically compact blade rows. In particular, the acoustic response of three limit cases (isolated blade rows, a single turbine stage, and multiple turbine stages) were investigated⁵⁵. Mishra and Bodony²³¹ tested the validity of the aforementioned actuator disk theory models using two-dimensional Euler calculations. It was concluded that it performs well for the cut-on acoustic modes, but less so for the cut-off modes. More recently, Bach et al.¹¹ extended the model of Cumpsty and Marble⁵⁶ to account for film cooling effects on the indirect noise generated by a stator blade row.

De Domenico et al.⁶³ extended the compact nozzle theory to account for nozzle losses, therefore relaxing the isentropic assumption for acoustic and entropic wave impingement.

It was made evident that the isentropic assumption should only be interpreted as a limit case since most acceleration regions will have isentropic losses and this significantly affects their acoustic response. Recently, Yang et al.³⁴⁹ proposed a model for sudden flow expansions which accounts for three-dimensional and non-isentropic effects.

Magri et al.²⁰⁷ and Ihme¹⁵⁴ extended the compact theory of Marble and Candel²¹³ to account for impinging compositional fluctuations applied to subsonic and sonic nozzle flows. The additional jump condition assumes that the compositional perturbation is conserved across the nozzle (i.e. non-porous wall assumption). This work demonstrated that compositional noise could exceed direct and entropic noise for supercritical nozzle flows and lean mixtures, highlighting the importance of its consideration. O'Brien and Ihme²⁴⁶ then investigated the dependency of compositional indirect noise generation on the species being accelerated. Soon after, Rolland²⁷⁸ and De Domenico et al.⁶⁴ extended the non-isentropic nozzle theory of De Domenico et al.⁶³ to account for compositional fluctuations. Recently, Guzmán-Iñigo et al.¹¹¹ studied the interaction of compositional inhomogeneities with a cascade of aerofoils.

Realistic gas engine nozzle geometries deviate from quasi-steady theory: acceleration regions have a spatial extent that should be considered and perturbations are generally not restricted to low frequencies. In an effort to more accurately predict the acoustic response of nozzles, the compact theory assumption has been relaxed using a variety of methods for acoustic, entropic, vortical, and compositional perturbations¹⁵⁴.

The linear nozzle profile method was used by Zinn et al.³⁵⁷ for acoustic wave impingement, and by Bohn²⁵, Marble and Candel²¹³ and Leyko et al.¹⁸⁵ for acoustic and entropic wave impingement. This approach limited the analysis to a specific nozzle profile. Moase et al.²³² and Giauque et al.¹⁰², and Giauque et al.¹⁰³ adapted the method through using piece-wise mean velocity distributions in order to discretise and model any finite length nozzle geometry. Giauque et al.¹⁰³, in particular, used this in tandem with an optimisation algorithm in order to minimise/maximise the downstream travelling indirect noise.

An *effective nozzle length* technique was proposed by Stow et al.³⁰⁵ and Goh and Morgans¹⁰⁶ for the case of a choked outlet nozzle. In both studies, the phase of the transfer functions was corrected for by using the asymptotic expansion of the linearised Euler equations. The first-order correction term was found to be dependent on the velocity profile through the region of acceleration (i.e. nozzle geometry) and type of disturbance impinging upon the nozzle.

Bohn²⁵ and Mani²¹¹ took a different approach using expansion methods. In the same vein, Durán and Moreau⁷³ employed the Magnus expansion²⁰³ to solve the linearised Euler equations in the frequency domain. The frequency dependence was shown to be

in good agreement with experiments by Zinn et al.³⁵⁷ for acoustic wave impingement. Durán and Morgans⁷⁶ extended this to circumferential modes in annular combustors (acoustic, entropic and vortical waves). More recently, Younes and Hickey³⁵¹ used the same method to model a one-dimensional, multi-stream compressible nozzle flow. Lastly, non-compact effects due to compositional wave impingement were investigated by Magri et al.²⁰⁶ and Magri²⁰⁴ using asymptotic expansions. The finite length of nozzles was shown to significantly change the transfer functions, with the authors equating said behaviour to a low-pass filter since higher frequencies are dampened out.

It is also important to highlight models which consider non-linear perturbations. non-linearities can be found in combustors due to combustion instabilities (whereby pressure fluctuations are coherent³⁵⁸), substantial unsteady heat release rates which generate large temperature inhomogeneities⁷⁴, or air injection in RQL systems which produce significant compositional perturbations¹⁰⁴. Moase et al.²³² studied the non-linear acoustic response of compact choked nozzles and supersonic diffusers. Huet and Giauque¹⁴⁵ studied the response of subsonic and supersonic compact nozzles (without shocks) subjected to non-linear entropic and acoustic perturbations. Analytically, the model of Marble and Candel²¹³ was re-derived and extended to the non-linear domain, using numerical simulations to validate the results. This was then further extended by Huet¹⁴¹ to account for shocks in the divergent section.

All the works previously referenced have assumed the perturbations are one-dimensional and unchanged during the acceleration process. Bohn²⁵ computed the response of a nozzle to a two-dimensional entropic wave. Zheng et al.³⁵⁵ extended the one-dimensional models of Giauque et al.¹⁰² and Durán and Moreau⁷³ by considering radial deformation of entropic waves in a two-dimensional axisymmetric model. Emmanuelli et al.⁸² underlined the importance of two-dimensional effects on entropic noise predictions using a 2D analytical model. The authors attribute this to a decorrelation of acoustic sources caused by the deformation of the entropic wave. The inviscid assumption was relaxed by Huet et al.¹⁴⁴ who studied the effect of viscosity on entropic noise generation. Lastly, Hosseinalipour et al.¹³⁵, Fattahi et al.⁸⁸, and Yeddula and Morgans³⁵⁰ studied the effects of heat transfer inside of a nozzle. It was shown that non-adiabatic conditions play a role in the acoustic response of a nozzle to entropic wave impingement.

2.2.2 Theoretical framework

We consider a multi-component ideal gas mixture where its species are expressed in terms of mixture fraction Z (i.e. $Y_i = Y_i(Z)$) and the specific heat capacity is only a function of the mixture composition (i.e. *frozen internal energy modes* assumption)¹⁵⁴. This is analogous to a combustor condition where the reaction process is completed and the gas mixture is chemically frozen. In an engine, this may hold true upstream of the acceleration region, where compositional fluctuations are still being generated (e.g. by quenching jets in RQL systems) and are then convected downstream⁶⁴.

The disturbance waves are expressed as fluctuations in the flow variables, which are decomposed into their mean and fluctuating components, as outlined in §2.1.2. In specific, these are described by the upstream π^- and downstream π^+ propagating acoustic waves⁶⁴:

$$\pi^- \equiv \frac{1}{2} \left(\frac{p'}{\gamma \bar{p}} - \frac{u'}{\bar{c}} \right), \quad \pi^+ \equiv \frac{1}{2} \left(\frac{p'}{\gamma \bar{p}} + \frac{u'}{\bar{c}} \right), \quad (2.23a-b)$$

the convecting entropic wave:

$$\sigma \equiv \frac{s'}{c_p}, \quad (2.24)$$

and the convecting compositional wave:

$$\xi \equiv Z'. \quad (2.25)$$

The entropic wave σ can be re-written in a more physically meaningful form. Firstly, we linearise the ideal gas law (Eq. (2.6)):

$$\frac{p'}{\bar{p}} = \frac{\rho'}{\bar{\rho}} + \frac{R'}{\bar{R}} + \frac{T'}{\bar{T}}. \quad (2.26)$$

Combining Gibbs' equation (2.5) with the linearised state equation (2.26) gives:

$$\sigma \equiv \frac{s'}{c_p} = \frac{p'}{\gamma \bar{p}} - \frac{\rho'}{\bar{\rho}} + \frac{c'_p}{\bar{c}_p} - \frac{R'}{\bar{R}} - \frac{1}{\bar{c}_p \bar{T}} \sum_{n=1}^N \frac{\mu_n}{W_n} dY_n. \quad (2.27)$$

Following Magri²⁰⁴, we define two non-dimensional terms:

$$\bar{\Psi} = \frac{1}{\bar{c}_p \bar{T}} \sum_{n=1}^N \left(\frac{\mu_n}{W_n} \right) \frac{dY_n}{dZ}, \quad (2.28)$$

$$\bar{\aleph} = \frac{R'}{\bar{R}} - \frac{c'_p}{\bar{c}_p} = \sum_{i=1}^N \left(\frac{1}{\bar{R}} \frac{d\bar{R}}{dY_i} - \frac{1}{\bar{c}_p} \frac{d\bar{c}_p}{dY_i} \right) \frac{dY_i}{dZ}, \quad (2.29)$$

which considers the variations in chemical potential Ψ , and in the specific heat capacity ratio and molecular weight \aleph .

Using Eqs. (2.28) and (2.29), Eq. (2.27) can be recast as:

$$\sigma = \frac{p'}{\bar{\gamma}\bar{p}} - \frac{\rho'}{\bar{\rho}} - (\bar{\aleph} + \bar{\Psi})\xi. \quad (2.30)$$

This demonstrates that entropic and compositional waves are inherently coupled²⁷⁸.

2.2.3 Compact wave source

In this section, we briefly present the theoretical basis behind a compact wave source model which can be used to describe the generation of acoustic, entropic, and compositional waves due to the unsteady addition of heat or mass into a one-dimensional flow duct as shown in Fig. 2.1. The compact hypothesis holds true as long as the length of the wave source is small with respect to the perturbation wavelengths of interest.

The mean flow is described by its velocity u , pressure p , density ρ , and mixture fraction Z . The disturbance waves are generated by applying mass ϕ_m , momentum ϕ_M , energy ϕ_e , and mixture fraction ϕ_Z fluxes to the flow. These are implemented as jump conditions across the compact discontinuity:

$$\left. \begin{aligned} \left[\dot{m}' \right]_0^1 &= \phi'_m, \\ \left[(p + \rho u^2)' \right]_0^1 &= \phi'_M, \\ \left[(\rho u h_t)' \right]_0^1 &= \phi'_e, \\ \left[Z' \right]_0^1 &= \phi'_Z. \end{aligned} \right\} \quad (2.31)$$

We assume these fluxes are small, such that mean flow properties remain unchanged across the wave generator. The notation $[\cdot]_0^1$ denotes the difference in flow properties between the downstream [1] and upstream [0] sections of the wave source discontinuity (i.e. $[\cdot]_0^1 = [\cdot]_1 - [\cdot]_0$).

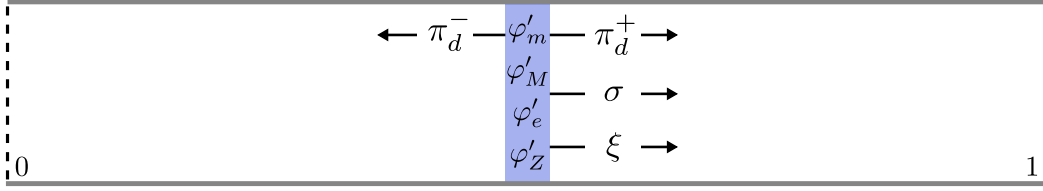


Fig. 2.1 Compact wave source: added fluxes (mass φ'_m , momentum φ'_M , energy φ'_e , and mixture fraction φ'_Z) and generated waves (acoustic π_d^\pm , entropic σ , and compositional ξ).

Normalising Eq. (2.31) yields:

$$\left. \begin{aligned} \left[\left(\frac{\rho'}{\bar{\rho}} \right) + \frac{1}{\bar{M}} \left(\frac{u'}{\bar{c}} \right) \right]_0^1 &= \varphi'_m, \\ \left[\frac{1}{\bar{M}^2} \left(\frac{p'}{\bar{\gamma} \bar{p}} \right) + \left(\frac{\rho'}{\bar{\rho}} \right) + \frac{2}{\bar{M}} \left(\frac{u'}{\bar{c}} \right) \right]_0^1 &= \varphi'_M, \\ \left[\frac{\rho'}{\bar{\rho}} + \frac{1}{\bar{M}} \frac{u'}{\bar{c}} + \frac{1}{1 + \frac{\bar{\gamma}-1}{2} \bar{M}^2} \left(\bar{\gamma} \frac{p'}{\bar{\gamma} \bar{p}} - \frac{\rho'}{\bar{\rho}} + (\bar{\gamma}-1) \bar{M} \frac{u'}{\bar{c}} - \bar{\aleph} \xi \right) \right]_0^1 &= \varphi'_e, \\ [Z']_0^1 &= \varphi'_Z, \end{aligned} \right\} \quad (2.32)$$

where \bar{M} is the Mach number, and φ'_m , φ'_M , φ'_e , and φ'_Z are the normalised fluxes for mass, momentum, energy, and mixture fraction, respectively:

$$\varphi'_m = \frac{\phi'_m}{\bar{\rho} \bar{u}}, \quad \varphi'_M = \frac{\phi'_M}{\bar{\rho} \bar{u}^2}, \quad \varphi'_e = \frac{\phi'_e}{\bar{\rho} \bar{u} \bar{c}_p \bar{T}_t}, \quad \varphi'_Z = \phi'_Z, \quad (2.33a-d)$$

and T_t is the total temperature.

Considering a low Mach number flow ($\bar{M} \ll 1$), the waves generated are given by¹:

$$\left. \begin{aligned} \frac{1}{2} \left(\frac{\bar{M}}{1 + \bar{M}} \right) (\varphi'_e + \bar{\aleph} \varphi'_Z) + \frac{1}{2} \left(\frac{\bar{M}^2}{1 + \bar{M}} \right) (\varphi'_M - \varphi'_m) &= \pi_d^+, \\ \frac{1}{2} \left(\frac{\bar{M}}{1 - \bar{M}} \right) (\varphi'_e + \bar{\aleph} \varphi'_Z) - \frac{1}{2} \left(\frac{\bar{M}^2}{1 - \bar{M}} \right) (\varphi'_M - \varphi'_m) &= \pi_d^-, \\ (\varphi'_e - \varphi'_m) + \frac{(\bar{\gamma}-1)}{2} \bar{M}^2 (\varphi'_m - 2\varphi'_M + \varphi'_e) - \bar{\Psi} \varphi'_Z &= \sigma, \\ \varphi'_Z &= \xi. \end{aligned} \right\} \quad (2.34)$$

General theories for compact wave sources have been derived previously with particular application to unsteady heat addition^{54,75,185,278,280} and transverse injection of gases (i.e. cross-flow jet)^{64,277,278}. In the latter studies, the added momentum flux was considered

¹A full derivation is provided in Appendix A.2.

to be zero. For the experiments presented in §5 and §6, injection is in the direction of the flow (i.e. co-flow jet), so a momentum flux contribution needs to be included (i.e. $\phi'_M \neq 0$). Co-flow injection is directly pertinent to engine systems, such as fuel injection in LPP combustor concepts^{8,284}.

In this section, the subscript $(\cdot)_i$ refers to the properties of the injected gas. Assuming a small injection area, the added momentum flux across the co-flow injection plane can be cast as:

$$\phi'_M = \dot{m}_i \bar{u}_i. \quad (2.35)$$

Unsteady co-flow air injection

In the case of the unsteady co-flow injection of air, the compositional flux is nil and the normalised fluxes are expressed as:

$$\phi'_m = \frac{\dot{m}_i}{\bar{m}}, \quad \phi'_M = \frac{\dot{m}_i \bar{u}_i}{\bar{m} \bar{u}}, \quad \phi'_e = \frac{\dot{m}_i}{\bar{m}}, \quad \phi'_Z = 0, \quad (2.36a-d)$$

where $\bar{u} = \bar{m}/\bar{\rho}A$ is the bulk velocity of the mean air flow and $\bar{u}_i = \dot{m}_i/\rho_i A_i$ is the bulk velocity of the injected gas. Assuming the temperature, pressure, and composition of the injected gas and mean air flow are the same at the injection plane ($T_i = \bar{T}$, $p_i = \bar{p}$, $R_i = \bar{R}$), then:

$$\frac{\bar{u}_i}{\bar{u}} = \frac{\dot{m}_i A}{\bar{m} A_i}, \quad (2.37)$$

which means the momentum flux is $\phi'_M = \dot{m}_i^2 A / \bar{m}^2 A_i$.

Substituting these into Eq. (2.34), we see that the unsteady co-flow injection of air generates direct noise waves²:

$$\left. \begin{aligned} \frac{1}{2} \left(\frac{\bar{M}}{1 + \bar{M}} \right) \frac{\dot{m}_i}{\bar{m}} + \frac{1}{2} \left(\frac{\bar{M}^2}{1 + \bar{M}} \right) \frac{\dot{m}_i}{\bar{m}} \left(\frac{\dot{m}_i A}{\bar{m} A_i} - 1 \right) &= \pi_d^+, \\ \frac{1}{2} \left(\frac{\bar{M}}{1 - \bar{M}} \right) \frac{\dot{m}_i}{\bar{m}} - \frac{1}{2} \left(\frac{\bar{M}^2}{1 - \bar{M}} \right) \frac{\dot{m}_i}{\bar{m}} \left(\frac{\dot{m}_i A}{\bar{m} A_i} - 1 \right) &= \pi_d^-, \\ 0 &= \sigma, \\ 0 &= \xi. \end{aligned} \right\} \quad (2.38)$$

²In truth, an entropic wave is also generated – however, it is at least four orders of magnitude smaller than the entropic wave generated by a gas of different composition (as per Eq. (2.41)) and can therefore be neglected (i.e. hence $\sigma = 0$).

Unsteady co-flow methane injection

For the injection of a gas of different species, we change the energy and compositional fluxes⁶⁴, such that:

$$\varphi'_m = \frac{\dot{m}_i}{\dot{m}}, \quad \varphi'_M = \frac{\dot{m}_i \bar{u}_i}{\dot{m} \bar{u}}, \quad \varphi'_e = \frac{\dot{m}_i h_{t,i}}{\dot{m} \bar{h}_t}, \quad \varphi'_Z = \frac{\dot{m}_i}{\dot{m}}, \quad (2.39a-d)$$

where $h_t = h + u^2/2$. For the test cases presented in this thesis, the enthalpy associated with the fluid temperature ($h = c_p T$) is at least two orders of magnitude larger than the enthalpy associated with the kinetic energy ($u^2/2$). As a result, and for simplicity, the latter term can be neglected. We further assume the temperature of the injected gas is the same as the mean flow temperature ($T_i = \bar{T}$), such that the normalised energy flux simplifies to $\varphi'_e = \frac{\dot{m}_i c_{p,i}}{\dot{m} \bar{c}_p}$. Lastly, we assume the pressure of the injected gas and mean flow are the same at the injection plane ($p_i = \bar{p}$), such that:

$$\frac{\bar{u}_i}{\bar{u}} = \frac{\dot{m}_i R_i A}{\dot{m} \bar{R} A_i}, \quad (2.40)$$

which means the momentum flux is $\varphi'_M = \dot{m}_i^2 R_i A / \dot{m}^2 \bar{R} A_i$.

Substituting these fluxes into Eq. (2.34), shows us that the unsteady co-flow injection of methane generates direct noise waves, in addition to entropic and compositional waves:

$$\left. \begin{aligned} \frac{1}{2} \left(\frac{\bar{M}}{1 + \bar{M}} \right) \frac{\dot{m}_i}{\dot{m}} \left(\frac{c_{p,i}}{\bar{c}_p} + \bar{\aleph} \right) + \frac{1}{2} \left(\frac{\bar{M}^2}{1 + \bar{M}} \right) \frac{\dot{m}_i}{\dot{m}} \left(\frac{\dot{m}_i R_i A}{\dot{m} \bar{R} A_i} - 1 \right) &= \pi_d^+, \\ \frac{1}{2} \left(\frac{\bar{M}}{1 - \bar{M}} \right) \frac{\dot{m}_i}{\dot{m}} \left(\frac{c_{p,i}}{\bar{c}_p} + \bar{\aleph} \right) - \frac{1}{2} \left(\frac{\bar{M}^2}{1 - \bar{M}} \right) \frac{\dot{m}_i}{\dot{m}} \left(\frac{\dot{m}_i R_i A}{\dot{m} \bar{R} A_i} - 1 \right) &= \pi_d^-, \\ \frac{\dot{m}_i}{\dot{m}} \left(\frac{c_{p,i} - \bar{c}_p}{\bar{c}_p} - \bar{\Psi} \right) &= \sigma, \\ \frac{\dot{m}_i}{\dot{m}} &= \xi. \end{aligned} \right\} \quad (2.41)$$

A secondary term is neglected for the entropic wave as it is four orders of magnitude smaller than the entropic wave term shown above.

Assuming small perturbation theory where the temperature of the perturbation is the same as the mean flow temperature ($T_i = \bar{T}$), Eqs. (2.28) and (2.29) can be written as:

$$\bar{\Psi} = \frac{c_{p,i} - \bar{c}_p}{\bar{c}_p} - \frac{s_i - \bar{s}}{\bar{c}_p}, \quad (2.42)$$

$$\bar{\kappa} = \frac{\bar{W} - W_i}{W_i} - \frac{c_{p,i} - \bar{c}_p}{\bar{c}_p}, \quad (2.43)$$

such that Eq. (2.30) can be simplified to³:

$$\sigma = \frac{p'}{\bar{\gamma}\bar{p}} - \frac{\rho'}{\bar{\rho}} - \left(\frac{W_i - \bar{W}}{W_i} - \frac{s_i - \bar{s}}{\bar{c}_p} \right) \xi. \quad (2.44)$$

Using Eqs. (2.42) and (2.43), Eq. (2.41) may be further simplified to:

$$\left. \begin{aligned} \frac{1}{2} \left(\frac{\bar{M}}{1 + \bar{M}} \right) \frac{\dot{m}_i}{\bar{m}} \left(\frac{\bar{W}}{W_i} \right) + \frac{1}{2} \left(\frac{\bar{M}^2}{1 + \bar{M}} \right) \frac{\dot{m}_i}{\bar{m}} \left(\frac{\dot{m}_i R_i A}{\bar{m} \bar{R} A_i} - 1 \right) &= \pi_d^+, \\ \frac{1}{2} \left(\frac{\bar{M}}{1 - \bar{M}} \right) \frac{\dot{m}_i}{\bar{m}} \left(\frac{\bar{W}}{W_i} \right) - \frac{1}{2} \left(\frac{\bar{M}^2}{1 - \bar{M}} \right) \frac{\dot{m}_i}{\bar{m}} \left(\frac{\dot{m}_i R_i A}{\bar{m} \bar{R} A_i} - 1 \right) &= \pi_d^-, \\ \frac{\dot{m}_i}{\bar{m}} \left(\frac{s_i - \bar{s}}{\bar{c}_p} \right) &= \sigma, \\ \frac{\dot{m}_i}{\bar{m}} &= \xi, \end{aligned} \right\} \quad (2.45)$$

where, as shown previously in Eq. (2.30), the entropic and compositional sources are linked.

As such, an *entropic-compositional coupling term* $\Delta s/\bar{c}_p$ can be defined:

$$\frac{\Delta s}{\bar{c}_p} = \frac{s_i - \bar{s}}{\bar{c}_p}. \quad (2.46)$$

Using this, the entropic wave can be re-cast more simply as:

$$\sigma = \frac{\Delta s}{\bar{c}_p} \xi. \quad (2.47)$$

Summary

The normalised fluxes and resultant wave amplitudes for different compact source types are summarised in Table 2.1. Included are also the cases of cross-flow (transverse) gas injection (where the injected gas is at the same temperature as the mean flow) and unsteady heat addition^{75,278}.

³The full derivation of Eq. (2.44) is presented in Appendix A.1.

Table 2.1 Summary of compact wave sources. For gas injection, it is assumed the injected gas and mean flow air are at the same temperature ($T_i = \bar{T}$) and that the pressure is equilibrated at the injection plane ($p_i = \bar{p}$).

Source type	Co-flow injection		Cross-flow injection		Heat addition	
	Air	Other gases	Air	Other gases		
Normalised fluxes	φ'_m	$\frac{\dot{m}_i}{\dot{m}}$	$\frac{\dot{m}_i}{\dot{m}}$	$\frac{\dot{m}_i}{\dot{m}}$	0	
	φ'_M	$\frac{\dot{m}_i^2 A}{\dot{m}^2 A_i}$	$\frac{\dot{m}_i^2 R_i A}{\dot{m}^2 R A_i}$	0	0	
	φ'_e	$\frac{\dot{m}_i}{\dot{m}}$	$\frac{\dot{m}_i h_{t,i}}{\dot{m} h_t}$	$\frac{\dot{m}_i}{\dot{m}}$	$\frac{\dot{m}_i h_{t,i}}{\dot{m} h_t}$	q'
	φ'_Z	0	$\frac{\dot{m}_i}{\dot{m}}$	0	$\frac{\dot{m}_i}{\dot{m}}$	0
Canonical waves	π^+_p	$\frac{1}{2} \left(\frac{\bar{M}}{1+\bar{M}} \right) \frac{\dot{m}_i}{\dot{m}} + \frac{1}{2} \left(\frac{\bar{M}^2}{1+\bar{M}^2} \right) \frac{\dot{m}_i}{\dot{m}} \left(\frac{\bar{h}_i A}{\bar{h} A_i} - 1 \right)$	$\frac{1}{2} \left(\frac{\bar{M}}{1+\bar{M}} \right) \frac{\dot{m}_i}{\dot{m}} \left(\frac{\bar{W}}{\bar{W}_i} \right) + \frac{1}{2} \left(\frac{\bar{M}^2}{1+\bar{M}^2} \right) \frac{\dot{m}_i}{\dot{m}} \left(\frac{\bar{h}_i R_i A}{\bar{h} R A_i} - 1 \right)$	$\frac{1}{2} \left(\frac{\bar{M}}{1+\bar{M}} \right) \frac{\dot{m}_i}{\dot{m}}$	$\frac{1}{2} \left(\frac{\bar{M}}{1+\bar{M}} \right) \frac{\dot{m}_i h_{t,i}}{\dot{m} h_t}$	$\frac{1}{2} \frac{1}{1+\bar{M}} q'$
	π^-_p	$\frac{1}{2} \left(\frac{\bar{M}}{1-\bar{M}} \right) \frac{\dot{m}_i}{\dot{m}} - \frac{1}{2} \left(\frac{\bar{M}^2}{1-\bar{M}^2} \right) \frac{\dot{m}_i}{\dot{m}} \left(\frac{\bar{h}_i A}{\bar{h} A_i} - 1 \right)$	$\frac{1}{2} \left(\frac{\bar{M}}{1-\bar{M}} \right) \frac{\dot{m}_i}{\dot{m}} \left(\frac{\bar{W}}{\bar{W}_i} \right) - \frac{1}{2} \left(\frac{\bar{M}^2}{1-\bar{M}^2} \right) \frac{\dot{m}_i}{\dot{m}} \left(\frac{\bar{h}_i R_i A}{\bar{h} R A_i} - 1 \right)$	$\frac{1}{2} \left(\frac{\bar{M}}{1-\bar{M}} \right) \frac{\dot{m}_i}{\dot{m}}$	$\frac{1}{2} \left(\frac{\bar{M}}{1-\bar{M}} \right) \frac{\dot{m}_i h_{t,i}}{\dot{m} h_t}$	$\frac{1}{2} \frac{1}{1-\bar{M}} q'$
	σ	0	$\left(\frac{s_i - \bar{s}}{c_p} \right) \frac{\dot{m}_i}{\dot{m}}$	0	$\left(\frac{s_i - \bar{s}}{c_p} \right) \frac{\dot{m}_i}{\dot{m}}$	$\frac{T'}{\bar{T}}$
	ξ	0	$\frac{\dot{m}_i}{\dot{m}}$	0	$\frac{\dot{m}_i}{\dot{m}}$	0

2.2.4 Reverberation

When investigating the acoustics of combustion systems, the effect due to reflections at boundaries cannot be neglected²⁸⁰. Indeed, boundaries play a key role in the stability of engine systems^{252,309}. Accurate consideration of reflection coefficients has been shown to be a major factor in getting agreement between experiments, numerical, and theoretical results for model thermoacoustic experiments (see §2.3.3)¹⁸².

When acoustic waves are generated in a confined chamber by an unsteady source, they propagate upstream and downstream of the source location (Figure 2.2 shows upstream and downstream-travelling direct noise waves π_d^\pm). These waves are reflected at the inlet and outlet boundaries, losing energy depending on the respective reflection coefficients (R_i and R_o). Their amplitude is further reduced during propagation between the boundaries due to attenuation mechanisms¹⁷⁰ often characterised by an attenuation coefficient α . As a result of the reflections, and assuming the energy added to the system is greater than the energy lost to the aforementioned effects, the pressure in the chamber builds up. This effect is called *acoustic reverberation*.

Rolland et al.²⁸⁰ presented a time-domain theoretical model on acoustic reverberation, highlighting its significance to thermoacoustic systems. They later extended this to the frequency domain, for arbitrary pulse shapes²⁷⁸. This theory characterises a thermoacoustic system using transfer functions that incorporate reflection, transmission, and attenuation coefficients, while also accounting for time delays between boundaries, transducers, and wave sources. The derivation is not presented here, but relevant equations are employed in §5 and §6. For details on the full derivation, the author kindly forwards the reader to the referenced work²⁷⁸.

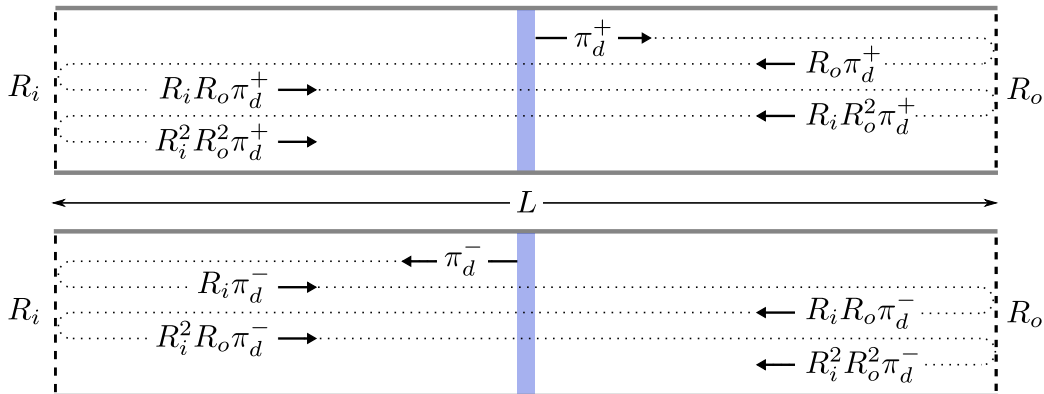


Fig. 2.2 Effect of reverberation on upstream-travelling π_d^- and downstream-travelling π_d^+ direct noise waves where L is the system length, and R_i and R_o are the inlet and outlet reflection coefficients, respectively.

2.3 Experimental investigations on indirect noise

2.3.1 Commercial engines

Experimental campaigns aiming to identify combustion noise in engine systems started in the 1970s³¹. Measurements demonstrated that more sound power was being emitted from the exhaust jet of engines than estimated by Lighthill's eighth-power law (i.e. acoustic power $\propto u_{\text{jet}}^8$)^{191,193}. Hoch and Hawkins¹²⁸ presented sound pressure levels for two Rolls-Royce/Snecma Olympus 593 Concorde engines that were built with different combustion chambers (cannular and annular). The cannular engine spectra had the higher values of the two. As a result of this, and other concurrent experimental results^{101,109}, it was hypothesised that the measured *excess noise* was sourced upstream of the jet. More specifically, that it was attributed to processes relating to unsteady combustion and convecting temperature perturbations²⁵.

Pickett²⁵⁸ analysed temperature data at the first row of nozzle guide vanes on a Pratt & Whitney JT3D engine. Using the temperature fluctuations as inputs to a compact actuator disk theory model, they showed that their radiated power estimates were in agreement with far-field pressure results. Shortly after, Cumpsty and Marble^{55,56} proposed an indirect noise model and applied it to three different commercial engines; in particular, two low-bypass turbofan engines (Rolls-Royce Spey 512, Pratt & Whitney JT8D-9) and one turbojet engine with afterburners (Rolls-Royce/Snecma Olympus 593-3B). Their results showed good agreement, leading them to claim there was circumstantial evidence linking the measured excess noise to the temperature disturbances. Confirmation, however, only arrived the following year through the work of Muthukrishnan et al.²⁴² who analysed data from a Boeing 502-7D combustor. They used a multitude of frequency-based analysis techniques (spectral, cross-spectral, correlation, and ordinary and partial coherence) to extract information from pressure and temperature measurements made inside and outside of the combustor. Cross-correlation had been used a few years prior by Mathews and Peracchio²¹⁵ to compare pressure measurements inside and outside of an engine, helping them deduce the peak frequency of core noise. However, in investigating the behaviour of the combustor with and without a choked nozzle termination, Muthukrishnan et al.²⁴² managed to – for the first time – confirm that, in the case of the choked nozzle termination, entropy noise was identifiable and significant. Specifically, the peak of the coherence function between interior pressure and temperature measurements was observed around 100 Hz. The authors also speculated that the results indicated there were other noise components present. This could be attributed to vortical (as suggested by the authors) or compositional disturbances (as hypothesised by Rolland²⁷⁸).

Coherence methods have since been used at the NASA Glenn Research Center to investigate combustion noise generated by a Honeywell TECH977 dual-spool turbofan engine^{148,227–230}. In one particular study, Miles²²⁶ used a cross-spectrum phase-angle method to separate direct and indirect noise contributions. Using interior and far-field pressure measurements, a time delay of 3 ms was identified between direct and indirect noise (attributed to the respective convective time delay). The former was found to dominate the 200–400 Hz band, whereas the latter dominated in the 0–200 Hz band.

Motheau et al.²³⁷ investigated a combustion instability identified experimentally in a SAFRAN Group aero-engine combustor. An LES/Helmholtz solver hybrid numerical methodology was employed, showing good agreement in terms of the instability frequency. The model led the authors to postulate that the 350 Hz instability was caused by temperature inhomogeneities convecting through the choked nozzle.

More recently, Tam et al.³¹⁶ analysed experimental data obtained from a Honeywell RE220 Auxiliary Power Unit (APU). Using pressure measurements at various locations inside and outside of the APU, an unusual technique was proposed to identify the spectral region of indirect noise generation: a direct noise model by Tam³¹³ was fitted to the data, and spectral peaks above the fit were identified as indirect noise. In particular, it was speculatively concluded that indirect combustion noise is present between 2000–5000 Hz – albeit the authors admit that further supporting evidence is needed.

Durán et al.⁷⁴ presented the Turbohaft Engine Exhaust Noise Identification (TEENI) project with the goal of identifying noise sources in turbohaft engines. A Safran Helicopter Engines (previously known as Turbomeca) engine was modified for the purpose of the investigation. Using 36 internal pressure measurements and 9 thermocouples, direct noise was identified via frequency content analysis. The spectral contents did not, however, confidently demonstrate that indirect combustion noise was present.

Lastly, Tam and Parrish³¹⁴ analysed the measured noise data from Pratt & Whitney F119 (F-22A Raptor) engine tests. A low-frequency, low-level unidentifiable noise component was highlighted at frequencies above 200 Hz, at direction angles ranging between 110–130°. Numerical simulations were employed to support the hypothesis that indirect noise was the unknown noise source. However, since temperature measurement were not made, this could not be confirmed.

2.3.2 Lab-scale combustors

Experimental campaigns using realistic engines are expensive to run, and separating direct and indirect noise contributions has proven to be a complex endeavour as the two sources are extremely correlated. Additionally, there is little to no optical access

for laser diagnostics tools and the harsh environment can prove to be too much for the time-resolved, clean measurement of mean flow and fluctuating properties. As a result, other experimental studies have focused on employing lab-scale combustors to investigate indirect noise and its influence in systems' thermoacoustics.

Schemel et al.²⁹⁰ and Bake et al.^{14,15} designed a 40 kW axisymmetrical combustor terminated by a convergent-divergent nozzle. Pressure measurements were made upstream and downstream of the nozzle, and thermocouple measurements were made upstream of the nozzle and in the throat. Separation of direct and indirect noise sources was not presented. Still, the phase between the microphones and thermocouple signals provided evidence for generation of indirect noise. Particular emphasis was given to indirect noise generated at higher frequencies (1–3.5 kHz). However, this goes against the conclusions of Giusti et al.¹⁰⁵, Wassmer et al.^{333–335}, and Hajjaligol and Mazaheri¹¹² who showed that dissipation of entropic perturbations is more significant at higher frequencies.

Rausch et al.²⁷² also confirmed the presence of indirect noise in their setup. They used Rayleigh scattering to demonstrate that density fluctuations at 170 Hz generated by a small-scale combustor flame were present at the nozzle entry. In fact, the Rayleigh and pressure measurements were shown to be correlated, evidencing the generation of entropic noise. Similarly, Wassmer et al.³³⁵ measured temperature fluctuations generated by periodically-forced fuel injection in a lean, premixed, atmospheric combustion rig at the Technical University of Berlin (TU Berlin). Entropic waves up to 50 Hz survived the convection process through the system, particularly at lower forcing frequencies and larger bulk flow rates. This is in agreement with the conclusions of Xia et al.³⁴⁷.

Other works seem to validate the idea that indirect noise is a key player in lab-scale combustor dynamics. For instance, Hield and Brear¹²¹ demonstrated that flame-generated entropic disturbances interacting with a choked nozzle affected the acoustics of their system. In particular, the presence of entropic noise changed the operating condition from stable to unstable. A few years later, Hochgreb et al.¹²⁹ reached the same conclusion after analysing experimental results obtained in the Cambridge Intermediate Pressure Combustion Facility (CIPCF). They hypothesised that a self-excitation present in their system was caused by entropic waves. This conclusion was supported by numerical simulations that indicated the results were consistent with the convective time of an entropic wave that is accelerated through a choked nozzle outlet. Bonciolini and Noiray^{26,27} presented a sequential burner configuration developed at ETH Zürich which reaffirmed that entropic waves had a strong influence in the combustion dynamics. Also in a sequential burner, Weilenmann et al.³⁴⁰ demonstrated the link between equivalence ratio fluctuations and the triggering of thermoacoustic instabilities. Wang et al.³³¹ investigated

the generation of entropic waves in a premixed flame setup with acoustic forcing using a combination of PIV, infrared imaging, and Tunable Diode Laser Absorption Spectroscopy (TDLAS). It was shown that the acoustic field has a strong influence on the generation of entropic waves. In particular, their amplitude increased with larger acoustic forcing levels and lower forcing frequencies. More recently, Weilenmann et al.³³⁸ presented OH-LIF measurements of entropic waves in a premixed turbulent combustor with acoustic forcing. Equivalence ratio fluctuations due to acoustic velocity forcing were identified to be the primary source of entropic waves. The entropic wave amplitude was found to heavily depend on the burner used, and the matrix-type burner was shown to be more prone to low-frequency instabilities than the swirl flame burner.

Eckstein et al.⁷⁸ reached a different verdict using a model RQL combustor fitted with either a nozzle or a resonance tube. Measurements obtained using OH* chemiluminescence and PIV demonstrated that the entropic waves were significantly dissipated and were, therefore, too weak to contribute to the self-excited instabilities. This was not a lone result. As part of the European project ‘Research on Core Noise Reduction’ (RECORD), a high pressure combustion test bench (CESAM-HP) was developed at the EM2C laboratory^{143,217}. The combustion chamber was terminated by a convergent-divergent nozzle optimised to maximise indirect noise generation¹⁰³. Pressure, thermocouple, and optical diagnostic techniques were used in tandem with high-fidelity numerical simulations¹⁶⁹. Although a quantity representing the ratio of direct and indirect noise was defined and presented, no definitive quantitative measurements were made for each noise source. Moreover, an instability was identified in the pressure measurements. However, it was shown to be related to the feeding lines, combustion chamber, and pre-mixer geometries, and, therefore, was likely not associated to indirect noise²¹⁶. Tao et al.³¹⁹ attempted to shed a light on the indirect noise generated by the CESAM-HP by using numerical simulations as inputs to an analytical indirect noise model.

Lastly, Bluemner et al.²³ measured compositional inhomogeneities in an acoustically forced swirl burner using PIV and Wavelength Modulation Spectroscopy (WMS). They demonstrated that 1D mixing models wrongly predict streamwise compositional wave transport as a result of neglecting velocity field perturbations, which has important implications to the development of accurate thermoacoustic models. Using a similar setup, Kather et al.¹⁶⁵ identified the need for models to consider 2D, non-local mixing.

Based on the literature survey presented, it is clear that the survivability of entropic and compositional perturbations is highly dependent on geometry, heat transfer, mixing properties, and test conditions. Separation of direct and indirect noise contributions in combustion systems is still an unresolved issue in the field⁶⁸.

2.3.3 Model setups

In order to validate analytical models for entropic and compositional noise, model experiments have been designed to synthetically generate and quantify direct and indirect noise. These are non-reacting experiments which are used to emulate the fundamental physics of combustion acoustics processes, providing a more clearly discernible scientific output and facilitating the understanding of this complex problem.

All of the model experiments found in literature are described in this section. In particular, their experimental setups, methodologies, and results are detailed. The respective entropic amplitudes generated are compared (inspired by Rolland²⁷⁸) and summarised in Table 2.2. These were computed using the definitions found in Table 2.1:

$$\text{Gas injection:} \quad \xi = \frac{\dot{m}_i}{\dot{m}}, \quad \sigma = \left(\frac{s_i - \bar{s}}{\bar{c}_p} \right) \xi. \quad (48a-b)$$

$$\text{Heat addition:} \quad \xi = 0, \quad \sigma \simeq \frac{T'}{\bar{T}}. \quad (49a-b)$$

Caltech

Zukoski and Auerbach³⁵⁹ first attempted to develop a synthetic indirect noise experiment at the California Institute of Technology (Caltech). In 1976, they developed a wind-tunnel experiment using a mean flow of nitrogen which was perturbed by a nichrome wire heater and accelerated through a supersonic nozzle. The heater's duty cycle and frequency varied from 20% to 100% and from 200 Hz to 1200 Hz, respectively. Pressure measurements were made upstream and downstream of the nozzle, as well as inside the nozzle. Temperature perturbations on the order of 0.01–1% of the mean temperature ($\sigma_{\max} \approx 1.0 \times 10^{-2}$) were generated. Concurrently, Bohn²⁵ (also at Caltech) developed a setup to test the response of a nozzle to one-dimensional and two-dimensional temperature perturbations. A mean flow of nitrogen was perturbed with temperature perturbations of about 0.3 K ($\sigma_{\max} \approx 0.1 \times 10^{-2}$) at 250 Hz and 400 Hz. Subsonic and supersonic nozzle flows were investigated with pressure measurements made upstream and downstream of the nozzle.

Although ingeniously designed, the experimental campaigns of both Zukoski and Auerbach³⁵⁹ and Bohn²⁵ were circumscribed by the technology at the time: only very weak entropic spots were produced due to the wires' thermal inertia, and data acquisition and processing limitations meant that results could not be interpreted at a high enough time resolution to allow for the extraction of conclusive information.

DLR

Three decades later, Bake et al.¹⁶ developed the Entropy Wave Generator (EWG) at the German Aerospace Center (DLR). The EWG consisted of a pressurised flow duct with an electric heater which produced 100 ms long entropic wave pulses at 1 Hz. Temperature fluctuations on the order of 10 K ($\sigma_{\max} \approx 3.4 \times 10^{-2}$) were accelerated through a subsonic or supersonic nozzle. The resulting acoustic pressure signal was measured downstream of the nozzle by microphones; no upstream pressure measurements were made^{13,16}. The EWG experiments generated significant interest within the thermoacoustics community, leading to a series of analytical and numerical projects aiming to clear up some of the unanswered questions brought about by their results^{18,75,102,137,182,184,201,233,238,239,330}.

Modelling efforts were hampered by uncertainties in the acoustic boundary conditions. In all simulations of the EWG cases, an adjustment of the inlet and outlet reflection coefficients was required to improve the agreement with experimental data. In particular, the outlet was not as anechoic as initially thought. Further complications may have been caused by the microphones which have a transfer function that does not seem to have been accounted for⁶². As of today, it's still unclear how much direct and indirect noise was generated in these experiments.

A year later, the Vorticity Wave Generator (VWG) was developed at DLR to study the vorticity-sound mechanism¹⁶⁷. Swirling flow was produced by injecting air at an angle, and accelerated through a convergent-divergent nozzle. The level of vorticity was monitored using Particle Image Velocimetry (PIV). A quadratic relationship was found between the downstream sound pressure and the injected mass flow rate – this was attributed to vorticity noise^{168,329}. However, more recent work contradicts this conclusion¹²⁶.

Following the EWG and VWG, DLR developed the Hot Acoustic Test (HAT) rig as part of the European RECORD project¹⁷¹. Cold air was injected into a mean flow of heated air at a frequency of 2 Hz and accelerated through a convergent-divergent nozzle. The HAT rig produced a maximum temperature difference of -20 K for a mean flow at 773 K ($\sigma_{\max} \approx -2.6 \times 10^{-2}$)¹⁷⁴. The results showed a linear dependence of peak entropic noise with temperature difference for the choked nozzle condition. Additionally, it was demonstrated that larger injection flow rates would produce more indirect noise for the same temperature difference, although no conclusive reasoning was provided for this result¹⁷⁵. Pressure measurements for subsonic nozzle flows were not presented as the authors claim that the indirect noise produced was not significant at those conditions. The HAT rig was later investigated analytically and numerically by Huet¹⁴².

The DLR experiments sparked a newfound interest in this research topic. As a result, other model experiments sprouted worldwide aiming to quantify direct and indirect noise.

Paris

Tao et al.³²⁰ developed the Temperature and Acoustic Fluctuations Generator (TAFG) at the Université Paris-Saclay. The TAFG was a modular setup consisting of a duct terminated by a converging nozzle. It was designed to generate temperature fluctuations up to 10 K ($\sigma_{\max} \approx 3.4 \times 10^{-2}$) at frequencies from 10 Hz to 100 Hz. Pressure and temperature measurements were made upstream of the nozzle by use of microphones and a two-thermocouple sensor. In their setup, the injection was driven by a loudspeaker such that forced acoustic and entropic waves were generated at the same time and frequency. Two different nozzle throat diameters were studied, and the authors demonstrate that the smaller diameter throat produced the largest entropic noise. Acoustic-acoustic and entropic-acoustic reflection coefficients were computed using an analytical method. The former was in good agreement with the theory of Marble and Candel²¹³. The latter, on the other hand, was significantly limited by the low signal-to-noise ratio and entropic noise produced.

Oxford

Ron²⁸² investigated the mixing of cold streams injected into a hot mixture in the Oxford Turbine Research Facility (OTRF). Oxford University's OTRF is a short-duration wind tunnel with a high-pressure research turbine terminated by annular NGVs. The authors presented the Fourier transforms of time-resolved pressure measurements and spatially resolved temperature measurements made upstream of the throat. Simulation results (using 3D URANS and LES) of pressure spectra upstream of the throat were compared with experimental values. A spatially resolved temperature profile was presented showing a temperature difference of 250 K for a maximum mean flow temperature of 560 K ($\sigma_{\max} \approx 45.5 \times 10^{-2}$). Ron and Chana²⁸³ suggest that entropic noise had a 10 dB contribution in the 10–2000 Hz frequency range. However, time-series comparisons between experiments and numerical results were not presented.

Iran

At the Iran University of Science and Technology, Hosseinalipour et al.¹³³ performed an experimental investigation on the evolution of convected entropic waves in their own Entropy Wave Generator (EWG). Their EWG consists of a circular duct with varying mean flow Reynolds numbers and perturbation frequencies terminated by an open end. The maximum perturbation measured at the outlet of the duct was 7% of the mean flow temperature ($\sigma_{\max} \approx 7.0 \times 10^{-2}$). Entropic wave decay was found to be dependent on the

convective wavelength. In particular, the larger the wavelength, the higher the likelihood of survival before reaching the outlet. Furthermore, the one-dimensionality assumption was shown to be acceptable for adiabatic channel flows. There was no measurement of acoustic fluctuations.

In a following study, Hosseinalipour et al.¹³⁴ presented pressure measurements for the EWG terminated with two different nozzles. In particular, pressure perturbations were measured upstream of and inside the nozzles for a maximum temperature difference of approximately 39% of the mean flow temperature ($\sigma_{\max} \approx 39.0 \times 10^{-2}$). Results similar to De Domenico et al.⁶² were presented, but they were not compared to analytical or numerical models.

Milan

As part of the European RECORD project – funded by the 7th Framework Programme (FP7) of the European Commission – a single-stage high pressure turbine stage was developed at the Politecnico di Milano. The test rig could operate at subsonic and transonic conditions, with mean pressures ranging from 1.4–1.9 bar. Of particular interest was the interaction of acoustic, vortical, and entropic waves with the turbine. The rig could operate in an Entropy Wave Generator (EWG) or Vorticity Generator (VWG) mode. The resulting pressure fluctuations were measured by 100 microphones upstream and downstream of the accelerating region. The temperature field was measured by thermocouples at the inlet and exit of the turbine. Entropic waves were generated via the injection of hot and cold air at frequencies between 10–100 Hz using a combination of a two-way rotary valve and an electric heater.

Initial characterisation tests by Gaetani et al.⁹⁹ demonstrated that, in the *immersed* configuration, the injection system could produce entropic perturbations of 5.5% ($\sigma_{\max} \approx 5.5 \times 10^{-2}$) and 3.5% ($\sigma_{\max} \approx 3.5 \times 10^{-2}$) of the mean temperature for 10 Hz and 100 Hz injection frequencies, respectively. No pressure measurements were detailed for indirect noise.

Soon after, Bake et al.¹² and Knobloch et al.^{172,173} measured the reflection and transmission properties of the high pressure turbine stage due to acoustic, entropic, and vortical perturbations generated at 30 Hz and 90 Hz. The turbine stage was operated at subsonic (1.4 bar) and transonic (1.9 bar) conditions, with a maximum temperature fluctuation of 34 K ($\sigma_{\max} \approx 10.0 \times 10^{-2}$). Direct noise was found to be heavily attenuated by the turbine blades and the downstream entropic noise was found to linearly scale with the square of the temperature fluctuations.

There was also interest in characterising the evolution and attenuation of the entropic waves as they convect through the turbine, generating a number of both experimental^{95,96,255} and numerical^{22,97,98} studies.

Zürich

Weilenmann et al.^{341,342} presented a non-reacting experimental setup, consisting of a rectangular cross-section wind tunnel developed at ETH Zürich. A siren was used to generate pulsed hot jets which were cross-flow injected into a colder mean flow at 315 K³⁴². The setup was run at a steady flow rate of 150 g s⁻¹, resulting in a mean pressure of 1.3 bar. The siren forcing frequencies were varied from 240 Hz to 900 Hz. Using Background-Oriented Schlieren (BOS) and PIV measurements, the maximum jet temperature was estimated to be 519 K ($\sigma_{\max} \approx 64.6 \times 10^{-2}$). With the support of LES simulations, the authors demonstrate that shear dispersion models based solely on mean velocity profiles underestimate the decay for their setup. Pressure measurements were not made.

More recently, Weilenmann and Noiray³³⁹ adapted the previous setup by adding a convergent-divergent nozzle and an exhaust designed to be anechoic for frequencies above 500 Hz. Using the same siren injection system, they produced entropic perturbations at frequencies ranging from 60 Hz to 180 Hz. Experiments were run at high mass flow rates (up to 200 g s⁻¹) leading to a 3 bar mean pressure upstream of the nozzle. Using the BOS thermometry/PIV system presented in Weilenmann et al.³⁴², a maximum temperature difference of 45 K was measured relative to the colder mean flow at 315 K ($\sigma_{\max} \approx 14.2 \times 10^{-2}$). Upstream pressure measurements were made for choked nozzle conditions. Using the methodology of Tao et al.³²⁰, they extracted reflection coefficients for a convergent-divergent nozzle and compared their results to a one-dimensional model.

Cambridge

A model setup similar to the DLR EWG was developed at Cambridge University, termed Cambridge Wave Generator (CWG)^{60,278}. The CWG was employed to experimentally study entropic and compositional noise in the infrasound range (i.e. frequencies on the order of <1 Hz). It consisted of a duct fitted with different nozzle and orifice terminations. Studies used pulsed heat and compositional perturbations.

Using the CWG, De Domenico et al.⁶² was able to, for the first time, separate direct and indirect noise contributions generated upstream of an orifice plate due to temperature (entropic) perturbations at subsonic and sonic flow conditions. This was accomplished via time-separation as allowed by the convective time of the entropic wave

in the long CWG configuration. A short CWG configuration was also presented, however, individual contributions for this geometry were not able to be time-separated due to the reduced convective time. A maximum temperature fluctuation of approximately 20 K ($\sigma_{\max} \approx 6.8 \times 10^{-2}$) was measured at the outlet of the short configuration. Following this, Rolland et al.²⁸⁰ considered the effect of acoustic reverberation on direct and indirect entropic noise for the experiments of De Domenico et al.⁶². This work highlighted the importance of appropriate characterisation of acoustic boundaries, while also emphasising the need for the derivation of transfer functions for non-isentropic boundaries. Shortly after, De Domenico et al.⁶³ presented the transfer functions for outlets with different levels of isentropicity. By measuring the pressure upstream and downstream of different converging and diverging geometries, they demonstrated that non-isentropic effects significantly affect the acoustic response of accelerating regions of flow. For this study, the maximum measured temperature at the outlet was 8 K ($\sigma_{\max} \approx 2.7 \times 10^{-2}$). Rolland²⁷⁸ extended this model to compositional wave impingement.

Rolland et al.²⁷⁷ demonstrated, for the first time, the generation of direct and indirect noise due to the acceleration of compositional inhomogeneities through a choked nozzle. A maximum injection mass fraction $\xi = 0.023$ of helium was injected into a mean flow of air ($\sigma_{\max} \approx 55.9 \times 10^{-2}$). Pressure measurements were made upstream of the nozzle and the extracted indirect noise was compared to compact one-dimensional isentropic nozzle theory showing good agreement. Soon after, De Domenico et al.⁶⁴ extended the work to subsonic flows. By *dereverberating* (i.e. removing effects of reverberation) the upstream and downstream pressure traces, the indirect noise wave amplitudes were extracted for the injection of argon, helium, methane, and carbon dioxide. Assuming a non-dispersed compositional wave, indirect noise transfer functions were estimated and compared to the one-dimensional nozzle transfer functions. The maximum entropic wave was generated by the injection of carbon dioxide where $\xi = 0.20$ ($\sigma_{\max} \approx -132.0 \times 10^{-2}$).

At the same time, time-resolved temperature and compositional measurements were made in the CWG terminated by an open end using Laser-Induced Thermal Grating Spectroscopy (LITGS)⁶⁵. In particular, the convection of argon, carbon dioxide, helium, and temperature disturbances was studied for the validation of the diagnostics technique. Pressure measurements were not made. A maximum mass fraction $\xi = 0.69$ of carbon dioxide was measured in the mean flow of air producing the largest entropic perturbation out of three gases studied ($\sigma_{\max} \approx -458.7 \times 10^{-2}$). Numerical simulations by Rodrigues et al.²⁷⁶ provided data for comparison with experimental temperature and compositional measurements made by De Domenico et al.^{62,65} (see §3).

Summary

The model experiments are summarised in Table 2.2. Worth highlighting are the magnitudes of the entropic waves generated, the method used to quantify the indirect noise source, the nozzle flows conditions, and whether pressure fluctuations were measured.

Table 2.2 Summary of model experiments in literature presented in chronological order. From left to right: first author, year of publication, unsteady synthetic source type (temperature T' , vorticity Ω' , composition Y'), approximate maximum absolute entropic wave amplitude σ_{\max} , source identification method used (TC: thermocouple sensor; PIV: Particle Image Velocimetry; LITGS: Laser-Induced Thermal Grating Spectroscopy; BOS: Background-Oriented Schlieren; APs: aerodynamic probes, including pneumatic probes, five-hole probes, aerodynamic pressure probes, and total pressure probes; Sp. Raman: spontaneous Raman spectroscopy), nozzle flow condition \bar{M} (subsonic/choked/supersonic), and measurement of pressure fluctuations p' (upstream/downstream of acceleration region).

First author	Year	Synthetic source			Nozzle flow			Pressure	
		Type	σ_{\max} [$\times 10^{-2}$]	Method	\bar{M}	\bar{M}	\bar{M}	p'	p'
					< 1	= 1	> 1	US	DS
Zukoski ³⁵⁹	1976	T'	1.0	TC	–	•	•	•	•
Bohn ²⁵	1976	T'	0.1	TC	•	•	•	•	•
Bake ¹⁴	2009	T'	3.3	TC	•	•	•	–	•
Kings ¹⁶⁸	2010	Ω'	–	PIV	–	•	–	–	•
Gaetani ⁹⁹	2015	T'	5.5	TC	•	–	–	–	–
Knobloch ¹⁷⁵	2015	T'	–2.6	TC	–	•	–	–	•
De Domenico ⁶²	2017	T'	6.8	TC	•	•	–	•	–
Tao ³²⁰	2017	T'	3.4	TC	•	–	–	•	–
Knobloch ¹⁷³	2017	T'/Ω'	10.0	TC/APs	•	•	–	•	•
Ron ²⁸³	2017	T'	46.0	TC	•	•	•	•	–
Rolland ²⁷⁷	2018	Y'	56.0	–	–	•	–	•	–
De Domenico ⁶³	2019	T'	2.7	TC	•	•	–	•	•
De Domenico ⁶⁵	2019	T'/Y'	–460.0	TC/LITGS	•	–	–	–	–
Hosseinalipour ¹³³	2020	T'	7.0	TC	•	–	–	–	–
Weilenmann ³⁴²	2020	T'	65.0	BOS/PIV	•	–	–	–	–
Hosseinalipour ¹³⁴	2020	T'	39.0	TC	•	–	–	•	–
De Domenico ⁶⁴	2021	Y'	–130.0	–	•	•	–	•	•
Weilenmann ³³⁹	2021	T'	14.0	BOS/PIV	–	•	–	•	–
Present work (§5)	2021	Y'	120.0	Sp. Raman	•	•	–	•	•
Present work (§6)	2021	Y'	130.0	Sp. Raman	•	•	–	•	•

2.4 Summary

Combustion noise is a complex problem underlined by the intricate coupling of many different physical phenomena including, but not limited to, flame dynamics, linear and non-linear acoustics, heat transfer, turbulent mixing, and multi-species diffusion. There is little agreement on the general importance of indirect noise relative to direct noise⁶⁸. Measurements suggest that relative contributions may depend on geometry, operating conditions, frequency, and boundary conditions³¹⁶. Indeed, it is crucial that these variables are well characterised when running experimental campaigns designed to study indirect noise⁶⁸. Additionally, the processes governing the decay of perturbations in combustion chambers remain unclear⁶⁸. There is little quantitative data describing entropic and compositional wave transport, diffusion, and decay. This affects the accuracy of analytical and numerical tools. As a result, Dowling and Mahmoudi⁶⁸ suggested that these should be further explored.

Ideally this would all be done in a reacting system. However, there is an inherent difficulty in separating contributions under the extreme operating conditions of a real combustor. As a result, model experiments have been designed to simplify the problem of combustion noise to its fundamental principles.

Chapter 3

Numerical simulations: generation, mixing & convection of flow inhomogeneities

NUMERICAL simulations are undertaken using the URANS formulation to model the generation, mixing, and convection of unsteady, synthetic entropic and compositional waves in an open-ended flow duct in the transitional and turbulent regimes ($2500 < Re < 8100$). The flow is perturbed by either heat addition or cross-flow (i.e. transverse) injection of an inert gas that is heavier (argon) or lighter (helium) than air. The computed temperature and mass fraction fields are compared to experimental results obtained using both intrusive and non-intrusive techniques at multiple axial locations along the centreline of the duct¹.

¹A version of the work presented in this chapter has been published in: Rodrigues, J., Busseti, A., Hochgreb, S. (2020) ‘Numerical investigation on the generation, mixing and convection of entropic and compositional waves in a flow duct’, *Journal of Sound and Vibration*, **472**, 115155²⁷⁶.

3.1 Motivation and objectives

Experimental studies using the CWG (as described in §2.3) concluded that there is a measurable acoustic response of nozzles to entropic and compositional perturbations, producing indirect noise of the same order of magnitude as the associated direct noise. One dimensional simulations^{277,280} showed that at the low frequencies used in these studies, the response is well captured by the models provided that the time history of the sources is well captured (typically via experiments), and the acoustic boundary conditions are well determined. The next step in producing full-scale simulations of systems is to confirm that models for calculating the history of axial disturbances through gas turbines or representative ducts are capable of capturing the behaviour of these convective waves.

The convection and acceleration of entropic and compositional spots has been the topic of several simulation studies. Ron and Chana²⁸³ investigated the mixing of hot and cold streams in the Oxford Turbine Research Facility (OTRF), including time-resolved pressure measurements and spatially resolved temperature measurements. Numerical simulation results were obtained using 3D URANS and LES. The pressure spectra upstream of the throat was compared with experimental values. Measured and predicted noise results were of the same order of magnitude, but failed to predict the expected additional peaks due to entropic fluctuations. No time domain comparison was presented. Giusti et al.¹⁰⁴ studied the evolution of compositional and entropic fluctuations in a realistic RQL geometry using high-fidelity LES. For the geometry and conditions studied, entropic noise was found to exceed compositional noise. No comparison with experimental data was presented. Shao et al.²⁹⁵ investigated the relative contributions of direct and indirect noise using a hybrid LES/linearised Euler method for a realistic gas turbine geometry operating near lean blow-out during cruise conditions. Both compositional and entropic noise were greater than direct noise. Moreover, compositional inhomogeneities were found to be greater contributors than the entropic. However, owing to a phase shift between them, they interfered destructively. Other numerical work has investigated the contributions of entropic and compositional inhomogeneities to flows in nozzles^{80,207,290,293} as well as in nozzle guide vane, turbine blade row, and stator geometries^{22,36,80,83,140,181,251,264,332}.

The DLR EWG model experiments generated significant interest in the field leading to numerous numerical investigations. These generally employed either compressible Unsteady Reynolds-Averaged Navier–Stokes (URANS) with a rotationally symmetric geometry^{201,238,239} or Large Eddy Simulation (LES) using 2D axisymmetric and/or fully 3D geometries^{18,75,182,184,233}. Models for heat addition varied from a simple volumetric energy source term (i.e. block heat deposition into a single volume), to more complex approaches, such as time-delayed activation (capturing the heat addition from each wire).

When employing the single deposition model, a lack of consistency is found in terms of the length of the heating volume used in the numerical models; to model the same DLR EWG experiment, the different length values implemented were 30 mm^{182,183}, 32 mm²³⁸, 40 mm^{18,233}, 48 mm²³⁹ and 60 mm⁷⁵. It is unknown whether this had any effect on the results. The amount of energy added was adjusted to match experimental measurements of temperature and pressure fluctuations. No experimental validation of the dispersion of the convecting entropic wave was presented since the temperature signal for the entropic spot was measured at only one location downstream of the heating grid.

Other work has specifically focused on the effects of convection (without acoustics) on the entropic waves using high-fidelity simulations. Original work by Sattelmayer²⁸⁹ hypothesised that temperature fluctuations would decay by shear dispersion and turbulent mixing. Indeed, the validity of the non-diffusive flow assumption for entropic wave convection is still up in the air²³⁵. Entropic wave convection was studied using LES by Morgans et al.²³⁶, Xia et al.³⁴⁷, Fattahi et al.⁸⁹, and Giusti et al.¹⁰⁵, and DNS by Christodoulou et al.³⁹. Morgans et al.²³⁶ suggested that the dispersion in a combustor may not be significant and that entropic waves would, therefore, be a contributor to acoustics in a combustor. In the same vein, Xia et al.³⁴⁷ concluded that entropic transport is governed by advection, claiming thermal diffusion is negligible, and that the wave would reach the nozzle and generate indirect noise. Fattahi et al.⁸⁹, on the other hand, concluded that turbulent intensity and heat loss contribute significantly to the decay of entropic waves. Giusti et al.¹⁰⁵ highlighted that entropic spots advect as a function of the non-dimensional Strouhal number (termed ‘local Helmholtz number’ in their study), demonstrating that the dispersion could simply be accounted for by the velocity profile obtained from URANS simulations. Lastly, Christodoulou et al.³⁹ suggest that linear perturbation theory is only accurate for (and should be limited to) entropic waves where the perturbation temperature is less than 2% of the mean flow temperature.

In this chapter, gaseous species are transversely injected as an unsteady Jet in Cross Flow (JICF); hence, prior work in this field is of interest. The fluid mechanics phenomena due to JICFs has been exhaustively studied, both experimentally and numerically. Experiments by Fric and Roshko⁹² showed that four principal coherent vortical structures are present in cross-flow injection: jet shear-layer vortices, counter-rotating vortex pair, wake vortices, and a system of horseshoe vortices. The first attempt at studying the unsteadiness of JICFs using three dimensional URANS was made by Hsu et al.¹³⁹, where the standard k - ε model with appropriate wall functions was used¹⁷⁷. It was shown that three of the features described by Fric and Roshko⁹², with the exception of the horseshoe vortices, could be captured by URANS when a JICF is modelled under fully unsteady

3D conditions. Innumerable studies have used numerical tools to understand mixing jets, comparing results to experimental data^{100,158,323}. Although the collective interaction of small vortices make a very important contribution to the overall mixing process in JICFs, URANS models are able to produce sensible results as long as an adequate turbulence model is chosen and a sufficiently fine mesh is employed.

To the author's best knowledge, there has not yet been a direct comparison of numerical and experimental results for temperature perturbation measurements at multiple locations in model setups. In this chapter, the URANS formulation is used to model the unsteady scalar generation and transport in a transitional-to-turbulent flow duct ($2500 < Re < 8100$) terminated by an open end. The flow is perturbed by either heat addition or cross-flow (transverse) injection of an inert gas that is heavier (argon) or lighter (helium) than air. Specific to the context of the CWG experiments are questions relating to the importance of heat loss in the convection of the entropic waves in the case of heat addition. In the case of compositional injection, the goal is to provide more clarity on the mixedness of the compositional wave before reaching the outlet as well as how the mixedness is affected by different injected momenta and densities. Comparisons of the numerical results for mass fractions and temperature fluctuations due to compositional and thermal perturbations are made with the experimental results presented by De Domenico et al.^{62,65}. Unlike in the DLR model experiments, measurements were made at various axial locations. Finally, the two perturbation types are contrasted and the underlying assumptions made in their respective numerical methodologies are assessed. No evaluation of sound generation is presented.

This chapter is organised as follows. The geometric and measurement details relating of the experiments are presented in §3.2. The numerical setup, grids, boundary conditions and solvers used for the URANS studies are outlined in §3.3. The corresponding results are shown in §3.4, where the numerical calculations are compared to experimental measurements. Finally, the results for entropic and compositional perturbations are contrasted in §3.4.3.

3.2 Experimental details

The CWG consists of a modular duct with a mean flow of air which can be perturbed by two sources of inhomogeneities: temperature or composition. The methods for temperature non-uniformity generation and the resulting measurements using fast probes and diagnostics techniques are described in detail in the works of De Domenico et al.^{62,65}. Pulsed injection of different gases generate compositional non-uniformities,

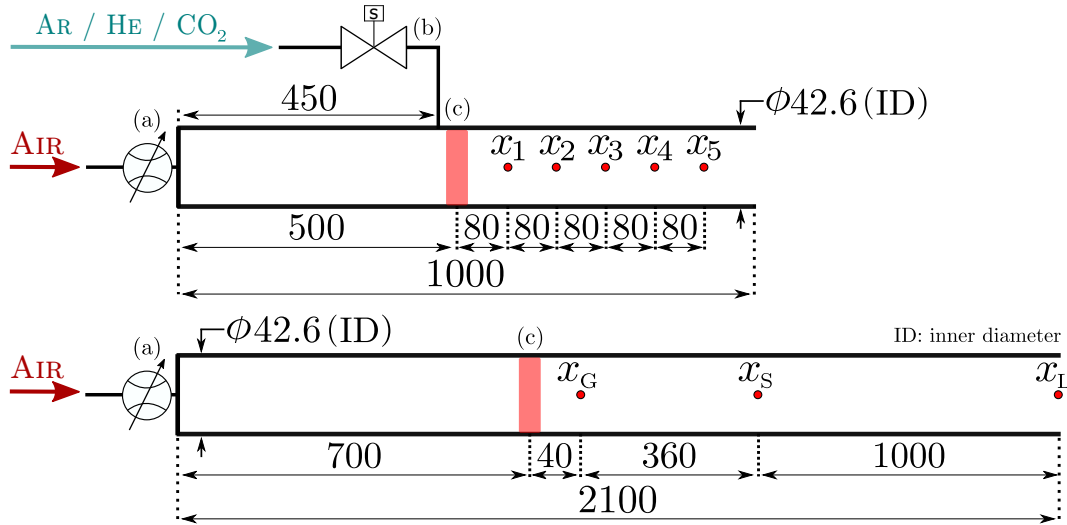


Fig. 3.1 Experimental setup for the LITGS (top)⁶⁵ and thermocouple (bottom)⁶² measurements with (a) mass flow controller, (b) fast response solenoid valve and (c) heating grid. The probe locations are identified for each experimental campaign (\bullet). All dimensions in mm.

and the corresponding methods and results are described in the work of De Domenico et al.⁶⁵. Briefly, in all cases, the mean flow of air was delivered by a mass flow controller connected to a 160 mm long hose (8 mm ID) into a duct (42.6 mm ID) of variable length. The description below outlines the experimental setup, while measurement details and uncertainties are available in the original work. A schematic of both setups is shown in Fig. 3.1.

De Domenico et al.⁶² generated temperature spots in a duct of 2.1 m length using a pulsed electrical heating grid source placed 0.7 m and 1.4 m from the inlet and outlet, respectively. For this study, the mass flow rate of air was varied from 1.54 to 4.93 g s⁻¹, providing eight different test cases. Temperature fluctuations were measured at three different locations along the centreline using K-type thermocouples. A hot-film anemometer was used to correct for the long response time of the thermocouples. The probe locations are shown in Fig. 3.1 (bottom).

More recently, De Domenico et al.⁶⁵ generated both temperature and compositional spots using a shorter version of the CWG setup, as shown in Fig. 3.1 (top). The mean flow of air was fixed at 1.57 g s⁻¹. Temperature spots were generated using the same heating grid setup developed by De Domenico et al.⁶². Compositional waves were generated via the cross-flow (transverse) injection of a secondary gas (argon, carbon dioxide or helium) using an actuated solenoid valve. The tube connecting the injection valve to the main duct was 30 mm long (4.8 mm ID). Measurements of density, mass fraction, and

temperature fluctuations due to the passage of the different perturbations were made at five axial locations along the duct centreline using LITGS as shown in Fig. 3.1 (top).

In both experimental studies, and for both types of perturbation, the pulse frequency was set to 1 Hz, with a pulse duration of $t_p = 200$ ms. Once generated, the perturbations convected and exited the duct, which was terminated by an open end.

Probe volume

Measurements of the local concentration and temperature were obtained by using LITGS⁶⁵. The technique involves using a gas phase tracer (in this case, biacetyl) which absorbs the incident light wavelength (355 nm). Two coherent pulsed beams from the same source are crossed at an angle θ to generate a grating of wavelength Λ over a rhombic region of length δ_z , width δ_x , and thickness δ_y as shown in Fig. 3.2. The laser light is absorbed by the tracer, generating a small perturbation in density, along with corresponding counter-propagating pressure pulses. The density can be determined by a continuous wave (CW) laser with a different wavelength λ_l incident at an angle θ_l corresponding to the Bragg condition³⁰. The effective probed region corresponds to the intersection of the probe volume $V_p \approx 0.5\delta_x\delta_y\delta_z$ with the probe beam at the Bragg angle.

The outgoing signal from the CW laser beam is captured by a photomultiplier whose frequency is proportional to the local speed of sound. The latter is a function of the mass fraction of the perturbing species and can, therefore, be related to the measured speed of sound. Probe volume dimensions can be estimated via:

$$\delta_z = \frac{2d \sin\left(\frac{\pi}{2} - \frac{\theta}{2}\right)}{\sin(\theta)}, \quad \delta_x = \frac{2d \cos\left(\frac{\pi}{2} - \frac{\theta}{2}\right)}{\sin(\theta)}, \quad (3.1a-b)$$

where $d \approx 1$ mm is the beam diameter and the same as the probe volume thickness, δ_y . From experiments, $\theta = 2.338^\circ$ ⁶⁵. Since $d = \delta_y \approx 1$ mm, we obtain $\delta_z \approx 50$ mm (perpendicular to the flow direction as shown in Fig. 3.2) and $\delta_x \approx 1$ mm, for an estimated probe volume region of approximately 25 mm^3 .

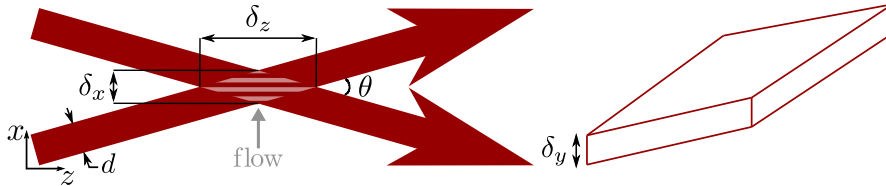


Fig. 3.2 Probe volume schematic.

3.3 Numerical methodology

3.3.1 Governing equations

In the modelling of the generation of compositional and entropic waves, besides the mass and momentum equations, two other governing equations are of particular interest. For the compositional case, we solve the species equation formulated as follows:

$$\bar{\rho} \frac{D\tilde{Y}}{Dt} = \nabla \cdot \left(\left(\frac{\mu_l}{Sc_l} + \frac{\mu_t}{Sc_t} \right) \nabla \tilde{Y} \right), \quad (3.2)$$

where μ is the dynamic viscosity, and Sc is the Schmidt number. The source term is neglected in the present study since there are no chemical reactions taking place. The subscripts $(\cdot)_l$ and $(\cdot)_t$ refer to the laminar and turbulent components, respectively. The Favre- and Reynolds-averaged terms are denoted by a tilde ($\tilde{\cdot}$) and an overbar ($\overline{\cdot}$), respectively.

For the heat addition test case, a volumetric source term \dot{S}_q is incorporated into the total energy equation to represent the power input by Joule heating:

$$\bar{\rho} \frac{D\tilde{e}_t}{Dt} = -\nabla \cdot (p^* \tilde{\mathbf{u}}) + \nabla \cdot \left(\gamma (\alpha_l + \alpha_t) \nabla \tilde{e} \right) + \dot{S}_q, \quad (3.3)$$

where α is the thermal diffusivity and $\tilde{e}_t = \tilde{e} + \tilde{e}_k$ is the total specific energy, where \tilde{e} is the specific internal energy and $\tilde{e}_k = \frac{1}{2} |\tilde{\mathbf{u}}|^2$ is the specific kinetic energy, with $|\tilde{\mathbf{u}}|^2 = \tilde{\mathbf{u}} \cdot \tilde{\mathbf{u}}$. Lastly, $p^* = \bar{p} + \frac{2}{3} \bar{\rho} \tilde{e}_k$ is the modified mean pressure²⁶³.

3.3.2 General solver details

The open-source CFD software package OpenFOAM 4.1 is used to perform compressible RANS simulations of the steady flow and the unsteady cross-flow (transverse) gas injection or heat addition in the duct. The solver *rhoSimpleFoam* is used in both studies to obtain a steady-state solution for the velocity field inside the duct. In all simulations the maximum Courant number is limited to 0.35.

The cases for gas injection pulse and temperature pulse are described separately, since the transient solvers, meshes and operating conditions are different. The transient solvers are both 1st order accurate in time and 2nd order accurate in space, employing the PIMPLE algorithm for the pressure-velocity coupling. More details on the solvers used to obtain the unsteady solutions for the gas injection and heat addition cases are described in §3.3.3 and §3.3.4, respectively.

3.3.3 Gas injection

Numerical setup

A modified version of the OpenFOAM solver *reactingFoam* is employed to solve this problem. The standard *reactingFoam* solver is commonly used in single-phase, multi-species problems; its species transport equation assumes that the ratio between mass diffusivity and momentum diffusivity is unity for both laminar and turbulent terms (i.e. assumes the Schmidt numbers are equal to one, $Sc_l = Sc_t = 1$). The modified version employed here removes this assumption by using Eq. (3.2) which allows for the implementation of different laminar and turbulent Schmidt numbers, and, therefore, diffusion coefficients depending on the gas simulated, as shown in Table 3.1². Although Busseti³² demonstrated that this change has a minimal effect on the results, it has been employed here for completeness. The laminar values are based on the assumption of binary diffusion coefficients and computed with respect to air according to the Chapman-Enskog theory³⁷. Turbulent numbers are assumed to be 0.7 as is done in commercial software and to ensure the turbulent Lewis number is equal to one³²⁵. Buoyancy effects are also accounted for via the incorporation of the respective gravitational terms in the momentum and energy equations.

The present work deals with steady and unsteady simulations involving a variety of Mach and Reynolds numbers. The main flow of air has a fixed flow rate of $\bar{m} = 1.57 \text{ g s}^{-1}$ ($\bar{u} = 0.92 \text{ m s}^{-1}$, $\bar{M} = 0.003$) falling under the transitional regime ($Re = 2580$), while the secondary gases produce cross-flow jets with Reynolds numbers ranging from 790 to 8350 and Mach numbers ranging from 0.02 to 0.07 (for helium and argon, respectively) as shown in Table 3.1. The $k-\omega$ SST model²²⁴ with wall functions is used to model the turbulent fluctuations in the flow. Tkatchenko et al.³²³ showed that the SST turbulence model was the most accurate model for simulating this type of problem using URANS, based on comparisons with LIF and LDA measurements. Since the temperature in the domain is constant throughout the simulation, the dynamic viscosity μ and the Prandtl number Pr are also constant and specified for each gas as inputs; these are outlined in Table 3.1. The dynamic viscosity and Prandtl number for air are set to $\mu = 18.3 \text{ }\mu\text{Pa s}$ and $Pr = 0.7$, respectively.

²The author kindly acknowledges the work of Andrea Busseti (visiting MSc student). Andrea worked on the gas injection case. In particular, he was responsible for the meshing of the two grids (Fig. 3.3) and the implementation of the first modification to the solver (i.e. accounting for laminar and turbulent Schmidt numbers – Eq. (3.2)). Andrea ran the mean flow case as well as injection simulations (without buoyancy effects) for a different experimental dataset. For more details, please refer to his Master’s thesis³².

Table 3.1 Estimated injected mass flow rate (\dot{m}_i), Reynolds number (Re_i), Mach number (M_i), jet-to-crossflow momentum flux ratio (J), molecular weight (W), density ratio ($\rho_i/\bar{\rho}$), entropic-compositional coupling term defined by Eq. (2.46) ($\Delta s/\bar{c}_p$), dynamic viscosity (μ), and laminar and turbulent Schmidt numbers (Sc_l, Sc_t) for each gas at $T = 293$ K¹⁰⁸. The mean flow rate of air is $\bar{m} = 1.57$ g s⁻¹ ($\bar{u} = 0.92$ m s⁻¹, $Re = 2580$) for all cases. For air, $\mu = 18.3$ μ Pa s and $Pr = 0.7$.

Gas	\dot{m}_i [g s ⁻¹]	Re_i [-]	M_i [-]	J [-]	W [g mol ⁻¹]	$\rho_i/\bar{\rho}$ [-]	$\Delta s/\bar{c}_p$ [-]	μ [μ Pa s]	Sc_l [-]	Sc_t [-]
Ar	0.692	8350	0.07	864	39.948	1.69	-2.98	22.3	0.812	0.7
He	0.058	790	0.02	60	4.003	0.17	24.33	19.6	0.220	0.7

Each simulation was run using 96 cores and required a maximum of 4.5 hours of wall clock time to obtain statistics for 1 s of physical time.

Modelling of injection

The solenoid valve delivers a fast pulse $t_p = 200$ ms with a response time of around 10 ms. Given that direct measurements of the instantaneous mass flow rate are not available, another method is required to estimate the perturbation amplitude. In this study, the phase-averaged mass fraction measurements obtained via LITGS due to the passage of 30 injections is used to drive the numerical simulations. Specifically, the injected mass flow rates are evaluated assuming full radial mixing at the most upstream location x_1 . In that case, species conservation for injected species i yields:

$$\dot{m}_i = \frac{Y_{i_{\max}}(x_1)}{1 - Y_{i_{\max}}(x_1)} \bar{m}, \quad (3.4)$$

where $Y_{i_{\max}}$ is the maximum mass fraction measured in time at x_1 . The estimated injected flow rates for each gas are shown in Table 3.1.

Grid and geometry

For the gas injection cases, the full domain is discretised using a structured multi-block mesh, employing 1.6 million cells, as shown in Fig. 3.3. Symmetry boundary conditions are applied at the jet centre plane allowing for reduced computational costs. The structures generated by a jet in crossflow are three-dimensional⁹², therefore the planar symmetry condition employed is an approximation. Since the focus of this work is the convection

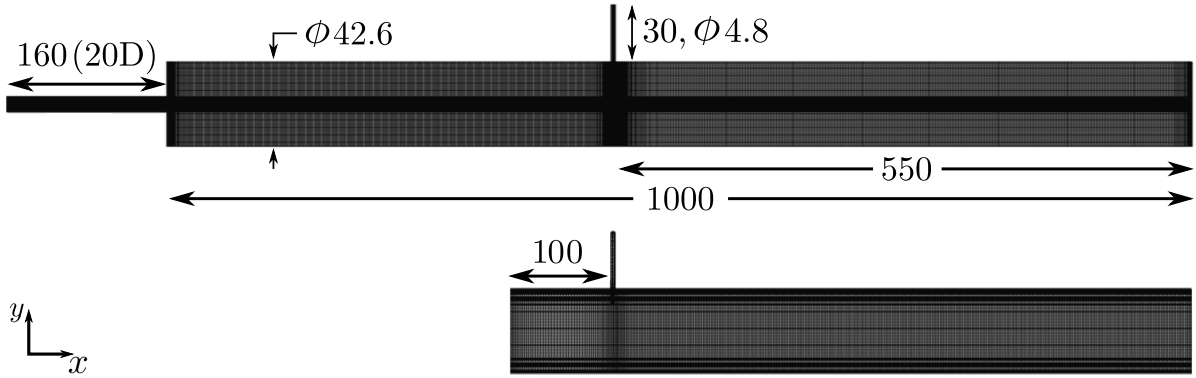


Fig. 3.3 Meshes for the full (top) and reduced (bottom) configurations used in the gas injection cases (x - y midplane). Planar symmetry is assumed. Figures scaled axially by a factor of 0.33. Dimensions in mm.

and dispersion of the compositional wave once it has been injected, the reduced accuracy of the injection process is accepted.

Before applying the unsteady injection, a test case is run with the full geometry for the steady undisturbed flow with a fixed inlet mass flow rate for all injection cases ($\bar{m} = 1.57 \text{ g s}^{-1}$). The velocity profile 0.1 m upstream of the injection location is observed to be fully developed, therefore, a reduced geometry is used starting at the stated location, where the inlet condition imposed for velocity corresponds to the velocity profile measured in the original steady-state calculation. Figure 3.3 shows the final grid used for the unsteady injection. This mesh has a total of 712,000 cells and is designed using an O-grid with 423 cells in the axial direction, 56 cells in the radial direction, and 148 cells in the azimuthal direction, ensuring a circumferential resolution smaller than 2.5° . A mesh sensitivity study was undertaken to ensure that the wave characteristic times and amplitudes were independent of the mesh.

Boundary conditions

Zero pressure gradient and no-slip velocity boundary conditions are imposed at the wall. A zero gradient pressure condition is imposed at the inlet and a mean atmospheric pressure condition is specified at the outlet. The wall is assumed to be isothermal since the injected gases were at the same temperature as the mean flow ($T_W = 293 \text{ K}$).

3.3.4 Heat addition

Numerical setup

The *sonicFoam* solver is a transient pressure-based solver used to model laminar or turbulent flows of a compressible gas. It is used for this problem because no other gas species needs to be modelled and to prepare grounds for measuring pressure fluctuations at transonic flow rates. The standard solver is modified to allow for the addition of a volumetric heat source term with adaptable profile and power input as shown in Eq. (3.3). Since the temperature in the domain changes throughout the simulation, the dynamic viscosity μ is computed using Sutherland's law. The k - ε turbulence model with wall functions is employed for all test cases presented¹⁷⁷ with a turbulent Prandtl number of $Pr_t = 0.7$ for air^{209,220}.

Each simulation was run using 4 cores and required a maximum of 2.5 hours of wall clock time to obtain statistics for 2 s of physical time.

Modelling of source term \dot{S}_q

The source term \dot{S}_q in Eq. (3.3) represents the heat transfer per unit volume arising from the heating grid. This is determined by estimating the total effective power delivered during the unsteady heating interval based on temperature measurements. This is analogous to the block deposition model referenced in §3.1, in which all the energy is assumed to be transferred into a single region^{18,75,182,233,238}. The heat power convected into the air \dot{Q}_c and volumetric source term \dot{S}_q can be described by a semi-empirical formulation derived from fitting to the average of an ensemble of experimental measurements:

$$\dot{Q}_c = \begin{cases} a^2 b \dot{Q}_0 \left(1 - e^{-\frac{t}{\tau_w}}\right), & \text{for } t \leq t_t \\ b \dot{Q}_0 \left(1 - e^{-\frac{t}{\tau_w}}\right), & \text{for } t_t < t \leq t_p \\ h A_w \left((T_{w_{\max}} - \bar{T}) e^{-\frac{(t-t_p)}{\tau_w}} \right), & \text{for } t > t_p \end{cases} \quad (3.5)$$

$$\dot{S}_q = \frac{\dot{Q}_c}{V}, \quad (3.6)$$

where \dot{Q}_0 is the steady-state power input, T_w is the wire temperature (assumed to be uniform), \bar{T} is the mean flow temperature (assumed to be 293 K), h is the convective heat transfer coefficient for flow over a cylinder²⁰ (calculated from the Nusselt number and gas properties using Hilpert correlations¹²⁴), A_w is the cross sectional area of each wire (computed from the wire thickness, assumed to be 56 μm), $\tau_w = \rho_w d_w c_{p,w} / 4h$ is

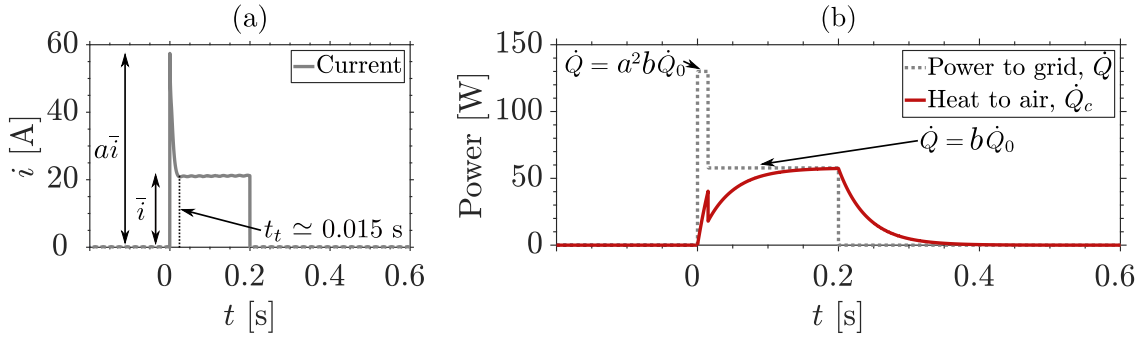


Fig. 3.4 (a) Current delivered to grid driving system (—); (b) modelled power input (---) and convected power (—) for case 8 ($\bar{u} = 2.56 \text{ m s}^{-1}$). Heat addition from $t = 0$ to 0.2 s.

the time constant (assuming the properties are independent of temperature), t_p is the unsteady heating duration (set to 200 ms) and t_t is the transient current surge duration (measured experimentally to be approximately 15 ms). This is shown in Fig. 3.4a. The additional power supplied to the air during the transient period t_t , can be modelled by a transient multiplier factor a applied to the steady state current \bar{i} . This factor appears in Fig. 3.4b as a^2 since $\dot{Q} \propto i^2$ and was optimised to match the direct noise produced in the experiments (not shown here). For all computations, a was set to 1.50. A bulk multiplier factor for the total power b was then included to account for the loss of overall power to the copper metal holder during the pulse duration. Experimental temperature measurements at probe location x_G (0.04 m downstream of the heating grid) are used to validate the modelling coefficients for each bulk flow velocity. Mühlbauer et al.²³⁹ also studied the effect of the energy supplied on the measured temperature and pressure fluctuations. Eight test cases are selected to study the effect of the mean flow rate on the convection of the entropic waves. Table 3.2 summarises the values for each test case.

The volume of the modelled computational heating grid V is approximated as the product of the duct area and the heating module length (assumed to be 10 mm).

Grid and geometry

The geometry modelled in the simulations is shown in Fig. 3.5. The full grid consists of a rotationally symmetric grid represented by a segment of 2.5° and radius 21.3 mm which models a duct of 42.6 mm ID and 2.1 m length. This simplification was also employed by Mühlbauer et al.²³⁸ and Leyko et al.¹⁸², albeit using a 10° slice as it did not show a decrease in the accuracy of the results obtained from the simulations. The mesh shown in Fig. 3.5 has 26,350 cells and is divided into three blocks (pre-heating grid, heating grid, and post-heating grid), each with varying numbers of cells in the axial direction

Table 3.2 Summary of test cases: bulk flow velocity \bar{u} , Reynolds number Re , bulk power factor b , maximum heat transferred to air $\dot{Q}_{c_{\max}}$, and time constant τ_w . Transient factor $a = 1.50$ for all cases.

Case	\bar{u} [m s ⁻¹]	Re [-]	b [-]	$\dot{Q}_{c_{\max}}$ [W]	τ_w [ms]
1	0.88	2510	0.1250	52.9	61.9
2	1.12	3220	0.1259	53.8	57.2
3	1.24	3580	0.1263	54.2	55.9
4	1.49	4350	0.1272	54.9	50.9
5	1.75	5160	0.1281	55.7	47.7
6	1.98	5960	0.1290	56.2	52.0
7	2.27	6930	0.1300	56.8	42.6
8	2.56	8060	0.1310	57.4	40.3

(120, 7 and 400 cells, respectively). There are 50 cells in the radial direction (with a 50% expansion ratio) and one cell in the azimuthal plane (due to the axisymmetry assumption). The mesh was refined near the heating grid to capture the steep temperature gradients. A mesh sensitivity study was undertaken to ensure that the wave characteristic times and amplitudes were independent of the mesh.

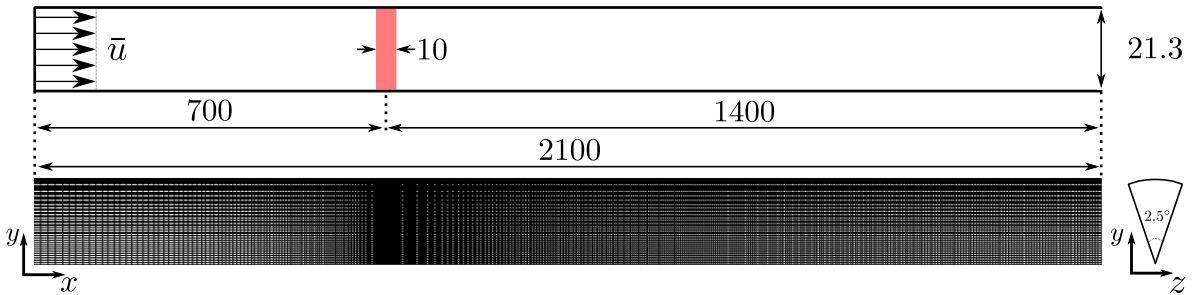


Fig. 3.5 Numerical schematic (top) and mesh (bottom) used in the heat addition cases (x - y midplane). Rotational symmetry is assumed – shown is the modelled 2.5° segment (z - y plane). Heating grid modelled as volume with length of 10 mm. Dimensions in mm.

Boundary conditions

A uniform velocity profile is used for the inlet flow and zero pressure gradient and no-slip velocity boundary conditions are imposed at the wall. A zero gradient pressure condition

is imposed at the inlet and a mean atmospheric pressure is enforced at the outlet. The wall is assumed to be isothermal ($T_W = 293$ K).

To assess the influence of heat loss on the convection of an entropic wave, a one-dimensional linearised conduction and convection boundary condition is derived. The temperature boundary condition is determined by assuming radial conduction across the thin duct thickness, whilst axial conduction is neglected²⁰:

$$q'_r = \Theta(T_W(x) - T_\infty), \quad \Theta = \left(\frac{\ln(r_2/r_1)}{2\pi\kappa_W} + \frac{1}{h_\infty 2\pi r_2} \right)^{-1}, \quad (3.7a-b)$$

where q'_r is the radial heat transfer rate per unit length, $T_W(x)$ is the inner wall temperature, T_∞ is the ambient temperature, κ_W is the metal wall conductivity, h_∞ is the free convection heat transfer coefficient, and r_1 and r_2 are the inner and outer radii, respectively.

Although the CWG rig is made of both PVC and steel modules, the thermal conductivity of the wall is assumed to be $\kappa_W = 50.2$ W m⁻¹ K⁻¹ (steel). The ducts are not perfectly round, but a mean thickness of 3.2 mm is assumed.

It is also important to consider the possible range of values for the free convection heat transfer coefficient h_∞ . The convection heat transfer coefficient for the free convection of gases typically ranges from 2 to 25 W m⁻² K⁻¹ according to Bergman et al.²⁰; values within this range are investigated and presented in §3.4.2. The change in thermal conductivity is found to be negligible due to the small range of temperatures investigated (293–320 K).

3.4 Results

3.4.1 Gas injection

From the three cases studied by De Domenico et al.⁶², the injections of argon and helium have been selected for this numerical work as they are both inert gases with one being heavier and the other lighter than air.

Compositional and entropic source field evolution

The injection and convection of the compositional waves is shown at different time steps in Fig. 3.6. Two orthogonal midplanes are presented with the corresponding flow-field distributions coloured by the entropic and compositional wave amplitude expressions given in Table 2.1 for the case of cross-flow injection of other gases. The injection occurs from $t = 0$ to 200 ms.

Figure 3.6 shows that the mass fraction of argon added during the injection process reaches a maximum of 50% ($\xi = 0.5$). Comparatively, helium produces a much weaker compositional disturbance ($\xi = 0.1$) due to the low molecular mass of helium (one order of magnitude lower than air) and the reduced injected mass flow rate, which is only 4% of the mean air flow. However, it still generates a significant entropic perturbation ($\sigma = 2.4$) owing to the considerable specific entropy difference between air and helium estimated using Eq. (2.46) ($\Delta s/\bar{c}_p = 24.33$)³. In contrast, argon has a lower specific entropy difference to air ($\Delta s/\bar{c}_p = -2.98$) and, therefore, needs a larger injected mass flow rate to produce the same absolute entropic disturbance as helium. For the test cases presented, and despite the larger injected flow rate, argon produces a weaker absolute entropic disturbance ($\sigma = -1.5$) than helium.

As the jets cross the duct, they are both diverted by the axial momentum of the mean flow according to their respective jet-to-crossflow momentum flux ratios, J . The argon jet has the largest momentum flux ratio ($J_{\text{Ar}} = 864$), impinging on the opposing side of the duct and producing a toroidal vortex upstream of the injection location (see $t = 25$ – 100 ms on the x - y and x - z midplanes). In the case of helium, however, the momentum flux ratio is one order of magnitude smaller ($J_{\text{He}} = 60$) and the jet is instead promptly advected by the surrounding air flow. The jet barely touches the opposing side of the duct, producing a minimal vortex upstream of the injection location (see $t = 100$ ms on the x - y midplane). By $t = 250$ ms, radial mixing at probe location x_1 is

³The original paper²⁷⁶ has an incorrectly defined sign for the entropic-compositional coupling term $\Delta s/\bar{c}_p$. This term should be positive for helium and negative for argon. This has been corrected here. The conclusions are unaffected by this as the absolute magnitude of the perturbations are unchanged.

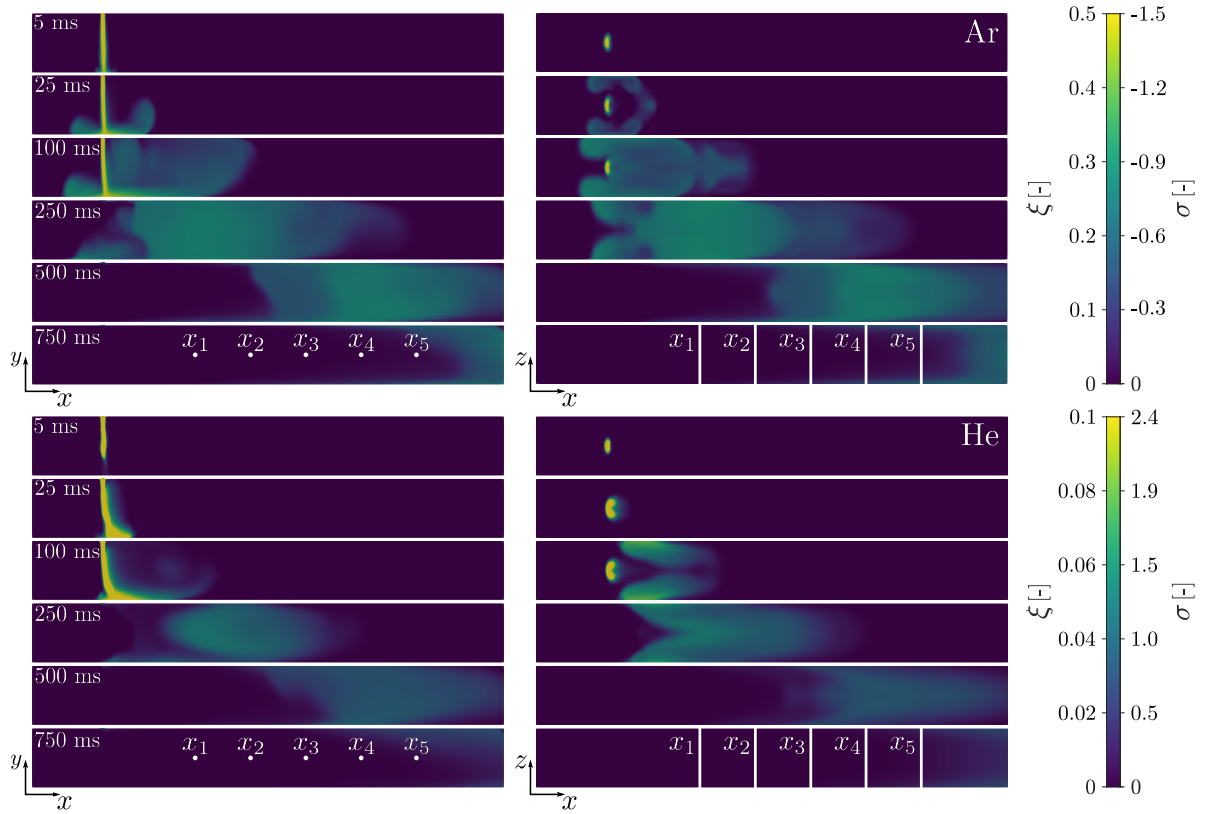


Fig. 3.6 Evolution of the compositional and entropic wave amplitude distribution for argon (top) and helium (bottom) on the x - y midplane (left) and x - z midplane (right). Probe volume schematics are shown to scale (based on Figs. 3.1 and 3.2): $x_1 = 0.13$ m, $x_2 = 0.21$ m, $x_3 = 0.29$ m, $x_4 = 0.37$ m and $x_5 = 0.45$ m downstream of the injection location. Figures scaled axially by a factor of 0.5. Injection from $t = 0$ to 200 ms.

completed in the core of the argon plume, but not in the core of the helium plume; this is more clearly seen on the x - z midplane.

The evolution in time of the centreline entropic and compositional perturbations downstream of the injection location is shown in Fig. 3.7 for both gases. The transport of the inhomogeneities is controlled by advection, given by the mean slope of the t - x plot along an iso-concentration line which coincides with the velocity of the centreline flow ($u_{cl} \approx 1.1$ m s⁻¹). In fact, buoyancy and molecular diffusion are both negligible since accounting for these effects showed minimal differences in the resulting mass fraction signatures (not shown here). All plumes are, therefore, convected downstream at similar rates. However, there are evident dissimilarities between the two cases. In particular, the results for the injection of helium show a highly localised region of maximum amplitude (0.10–0.15 m downstream of the injection location). In the case of argon, on the other hand, the region of maximum amplitude is convected at the centreline from the injection

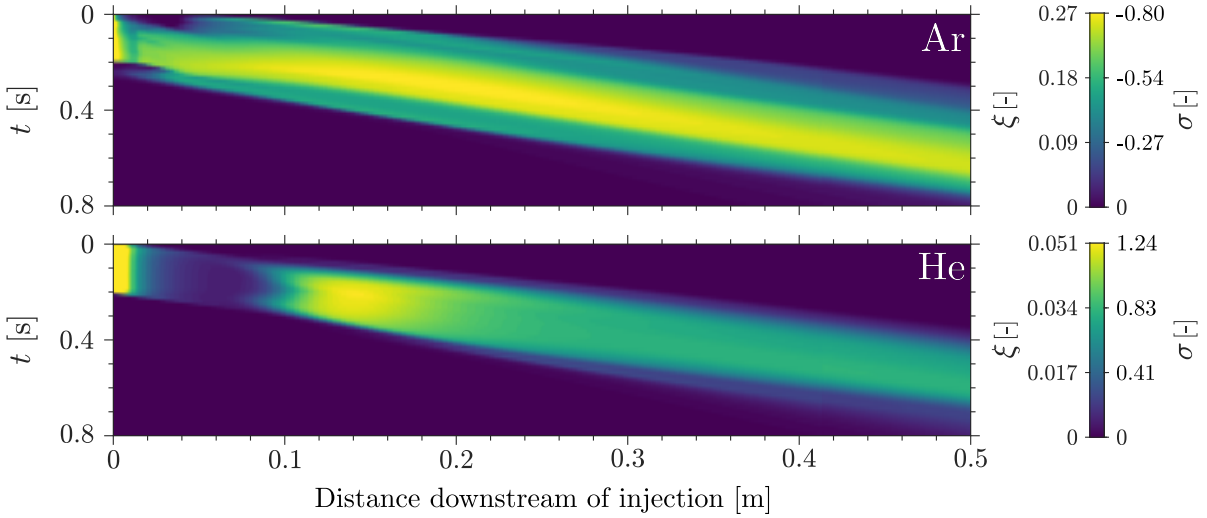


Fig. 3.7 Evolution of the centreline compositional and entropic perturbations downstream of the injection location for argon (top) and helium (bottom). Injection from $t = 0$ to 0.2 s.

point to the outlet (see $t = 100$ – 250 ms on the x – z midplane). This difference is associated with the contrasting jet momenta and the resulting radial mixing dissimilitude discussed previously. Finally, and as an additional consequence of the larger injection flow rate, the injection of argon produces a longer disturbance plume than the injection of helium. Most notably at $t = 0.3$ s, the maximum disturbance length is 0.30 m for the helium case and 0.45 m for the argon case (30% and 45% of the duct’s total length, respectively).

Comparison with experimental measurements

The numerical results for the mass fractions of the injected gases were sampled at a frequency of 1 kHz at selected axial positions downstream of the injection point shown in Fig. 3.1. The LITGS results are averaged across a probe volume⁶⁵. In the comparison of the simulation and experimental measurements shown in Fig. 3.8, three sampling methodologies are studied: centreline point, probe volume-averaged (described in §3.2) and cross-sectional area-averaged.

In all cases, the advection of the plume is well captured by the numerical models. The width of the axially dispersing wave is similar, but the numerical results become less symmetric downstream of the injection region, whereas the experimental results show a fairly invariable profile. Differences in characteristic convection times appear for both gases further downstream, but more so for helium. Specifically, the numerical results lag the experimental measurements by 0.05 – 0.10 s. The mismatch in the arrival time of the wave at the probe and in the time at which the peak is measured would suggest a lower

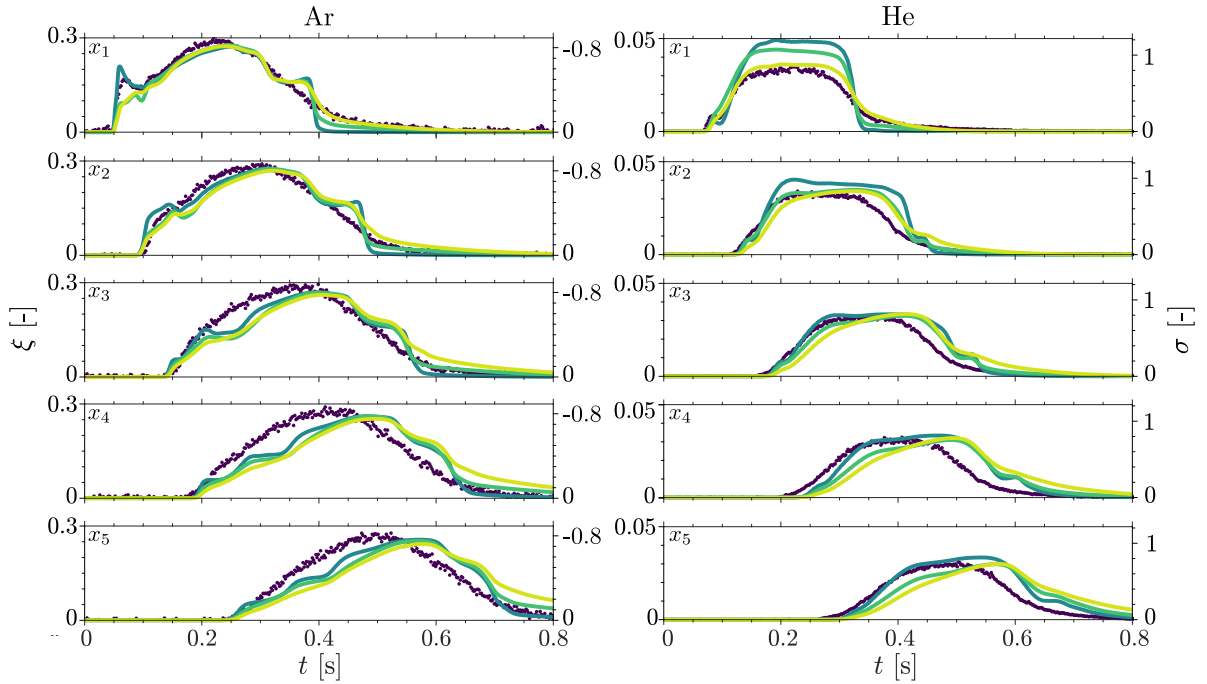


Fig. 3.8 Time series of the centreline compositional and entropic perturbations for argon and helium at $x_1 = 0.13$ m, $x_2 = 0.21$ m, $x_3 = 0.29$ m, $x_4 = 0.37$ m and $x_5 = 0.45$ m downstream of the injection location. Comparison between experimental data using LITGS phase-averaged from 30 shots (\bullet)⁶⁵ and the numerical results using URANS: centreline point (—), probe volume average (—) and cross-sectional area average (—).

predicted velocity at the centreline relative to the experiments. However, no velocity measurements are currently available for comparison.

Numerical results for argon show good agreement with experiments at x_1 for all three sampling methodologies, specifically in capturing the leading and trailing edge signatures, as well as the wave's convective time and peak perturbation amplitude. The leading edge peak associated with the initial vortex at injection is well predicted by the point measurement but seems to be smeared out by the probe volume and cross-sectional area averages. Numerical results capture a trailing edge structure which is not present in the experimental data; this is more clearly visible in probes x_1 and x_2 . At x_2 , the probe volume-averaged result follows the experimental data more closely, with the point measurement slightly overpredicting the leading edge profile. At the three remaining downstream probe locations, however, all sampling methodologies incur a slight discrepancy in the time at which the peak value is measured. Despite this, the numerical results at x_3 , x_4 and x_5 agree with experiments in terms of the wave's arrival time and peak perturbation amplitudes.

For helium, the width of the plume and peak perturbation amplitude are well captured. The maximum perturbation amplitude at x_1 agrees with the cross-sectional area-averaged simulation results, whereas it is overpredicted by both the point and probe volume-averaged results. The mass fraction profiles for helium in Fig. 3.6 show that the wave is not fully mixed across the duct's diameter at x_1 ($t = 100\text{--}250$ ms); it only becomes radially homogeneous further downstream ($t = 500$ ms), as previously discussed in §3.4.1. This is in contrast to the experimental data which shows the same amplitude being convected through all probe locations (see Figs. 3.8 and 3.12). Since the peak amplitudes agree at the probes further downstream for helium (x_2 to x_5), as well as at all probe locations for argon (x_1 to x_5), the error at x_1 for helium is not due to the mass flow rate estimation. Instead, it is due to the planar symmetry assumption which, for this particular case, affects the mixing and leads to the flow requiring a longer convective length to fully homogenise. This is not an issue with argon since the high jet momenta generates significant mixing such that the mass fraction rapidly becomes homogeneous before reaching x_1 . Therefore, the simulated compositional amplitude for argon does not vary when convected by the mean flow (see Figs. 3.7, 3.8 and 3.12).

3.4.2 Heat addition

Entropic source field evolution

The generation and convection of the entropic waves is shown at different time steps for case 1 ($\bar{u} = 0.88$ m s⁻¹) and case 8 ($\bar{u} = 2.56$ m s⁻¹) in Fig. 3.9. The flow-field distribution on the x - y midplane is coloured by the entropic wave amplitude expression given in Table 2.1 for the case of heat addition (note that $\xi = 0$). The heat addition occurs from $t = 0$ to 200 ms.

The inlet velocity to the heater consists of a fully developed velocity profile. As a result, velocities and mass fluxes are lower in the boundary layer; therefore, a uniform heat flux results in the maximum temperature fluctuation occurring near the wall. Downstream of the heating grid, the temperature in the boundary layer proceeds to dissipate faster than at the centre of the pipe due to heat transfer to the wall. The wave disperses axially in time, owing to the axial velocity profile, thermal diffusion and heat loss to the wall: starting from the initial 10 mm heating module length, the perturbations become significantly longer during the period of heat addition. Looking specifically at $t = 450$ ms (at which point no more heat is being transferred to the mean flow of air), the maximum disturbance length is 310 mm for case 1 and 730 mm for case 8 (15% and 35% of the

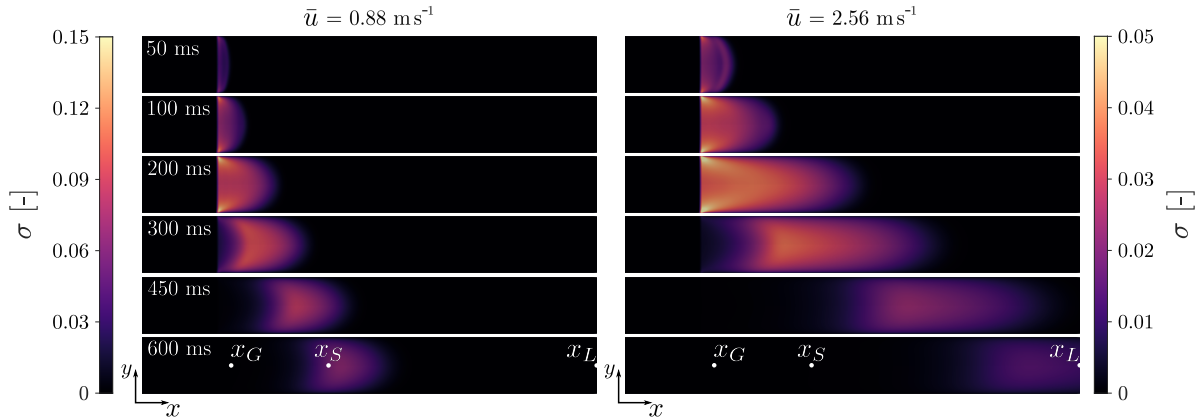


Fig. 3.9 Evolution of the entropic wave amplitude distribution on the x - y midplane for case 1 (left) and case 8 (right) ($\xi = 0$). Part of the upstream section has been omitted; 1.68 m of the duct is shown. Probe locations shown to scale: $x_G = 0.04$ m, $x_S = 0.36$ m, and $x_L = 1.4$ m downstream of the heating grid. Figures scaled axially by a factor of 0.4. Heat addition from $t = 0$ to 200 ms.

duct's total length, respectively). For these operating conditions and this convective length (1.4 m), the remaining perturbation at the outlet is very small ($\sigma \approx 0.01$).

The evolution of the centreline entropic perturbations downstream of the grid is shown in Fig. 3.10. The behaviour is similar to that of the compositional plume. The entropy spot moves along the duct according to the centreline velocity and, therefore, higher bulk velocities lead to higher slopes on the t - x plane. The width of the entropic spot at the centreline increases as discussed above owing to axial dispersion. Furthermore, higher bulk velocities lower the peak temperature for the given power delivered, as outlined in Table 3.2; this trend is also evident in Fig. 3.11. Finally, and as discussed for Fig. 3.9, the energy is dissipated towards the end of the duct owing to heat transfer to the wall.

Comparison with experimental measurements

The comparison between URANS and thermocouple results for four test cases is shown in Fig. 3.11a. The peak entropic perturbation at x_S is matched for all cases; this is expected since the power profile was scaled to agree with near-grid measurements. The comparison further downstream shows differences in the decay of the peak temperature with time: at x_S , the simulations slightly over-predict the peak measurements, while at x_L they under-predict. Despite the mismatch in peak amplitudes, the overall signature of the wave at the centreline is best captured at x_S and x_L , whereas at x_G the trailing edge of the heat pulse decays much faster than the thermocouple measurement.

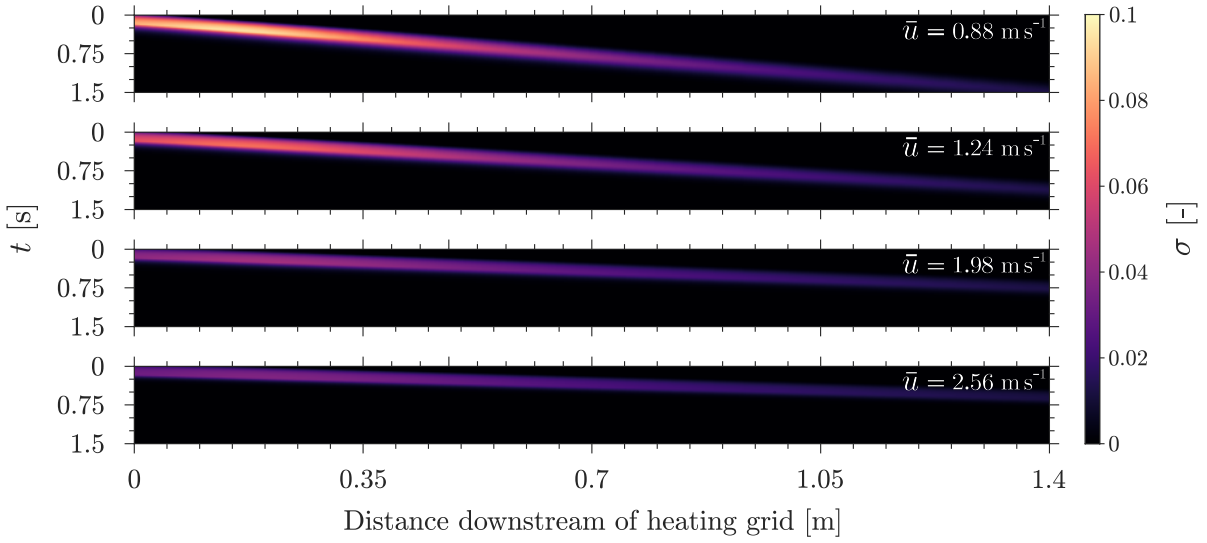


Fig. 3.10 Evolution of the centreline entropic perturbations downstream of the heating grid for cases 1, 3, 6 and 8 ($\xi = 0$). Heat addition from $t = 0$ to 0.2 s.

Figure 3.11b compares the URANS results to both thermocouple and LITGS measurements at two positions⁶⁵. Since $x_5 - x_S$ are at the same distance downstream from the heating grid and $x_1 - x_G$ are separated only by 0.04 m, this figure provides a fair comparison in terms of perturbation amplitude and signature. At the first position, the peak entropic perturbation using LITGS is slightly lower than the URANS and thermocouple results. At the second position, however, the three results are in accordance. Although the agreement is good overall, it is clear to see that the experimental techniques can yield slightly different temperature profiles for the same heat input.

The shapes and arrival times of the temperature perturbations shown in Fig. 3.11a are in better agreement at higher bulk flow velocities. Similar to what is seen in the gas injection cases, the discrepancy in timings would suggest a lower predicted velocity at the centreline relative to the experiments. Likewise, no velocity measurements are currently available for comparison. Additionally, the Reynolds numbers in the duct range from 2500 to 8100, a relatively transitional region within which the URANS two-equation turbulence model may not fully capture the dispersion effects. In fact, the temperature results at x_S were found to be quite sensitive to turbulence models (not shown here). Furthermore, there could also be differences due to the wall temperature boundary condition. Specifically, a constant temperature (isothermal condition) may not fully represent the behaviour at the wall.

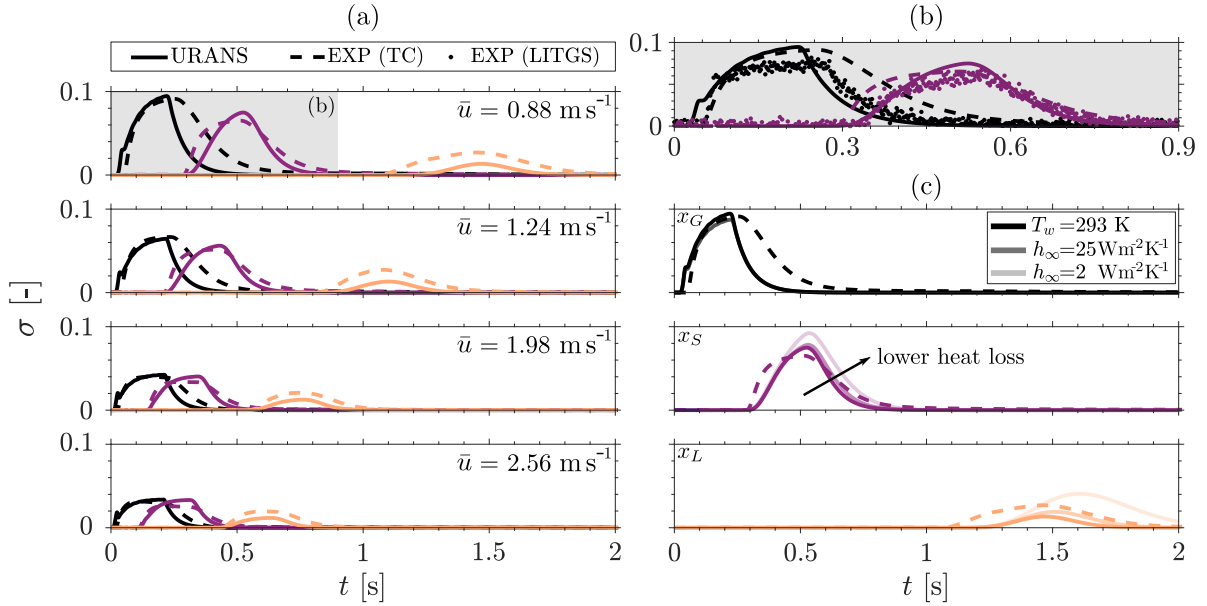


Fig. 3.11 Time series of the centreline entropic perturbations ($\xi = 0$): (a) comparison between experiments using thermocouples (TC) (---) and numerical results using URANS for test cases 1, 3, 6 and 8 at $x_G = 0.04 \text{ m}$ (—), $x_S = 0.4 \text{ m}$ (—) and $x_L = 1.4 \text{ m}$ (—) downstream of the heating grid; (b) comparison between TC and URANS results for case 1 with LITGS (\bullet) results phase-averaged from 30 shots⁶⁵; (c) comparison between TC and URANS results for case 1 using the heat transfer boundary condition (— $h_\infty = 25 \text{ W m}^{-2} \text{ K}^{-1}$ and — $h_\infty = 2 \text{ W m}^{-2} \text{ K}^{-1}$).

Heat loss study

To investigate the effect of the temperature condition at the wall on the results, a sensitivity study to the boundary condition derived in §3.3.4 is presented. Figure 3.11c shows the effect of altering the boundary conditions from a fixed wall temperature of 293 K (isothermal) to the heat transfer formulation using different convection coefficients (2 and 25 $\text{W m}^{-2} \text{ K}^{-1}$). Results presented are for case 1 ($\bar{u} = 0.88 \text{ m s}^{-1}$).

The time at which the entropy wave arrives at the probe location is independent of the temperature boundary condition. However, when the one-dimensional heat transfer boundary condition is used, the peak entropic perturbation increases significantly, both at x_S and x_L . When the thermal flux at the wall is low (such as with the one-dimensional heat transfer boundary condition, in comparison to the isothermal wall condition), temperature fluctuations remain large in the boundary layer. Since convection of thermal fluctuations is lower in the boundary layer due to lower mean velocity, the radial temperature gradient between the walls and the centreline remains low in the back end of the temperature

spot, leading to reduced thermal diffusion to the walls. This explains the larger centreline temperature fluctuations at the trailing edge of the entropic wave shown in Fig. 3.11c.

From this, we can conclude that, although the entropic fluctuations are relatively small ($\sigma \approx 0.1$), the results downstream of the heating grid are highly sensitive to the temperature boundary condition at the wall. This is in agreement with the conclusions of Fattahi et al.⁸⁹.

3.4.3 Comparison of scalar perturbations

The transport of the inhomogeneities can be explained by appropriately normalising the results with equal centreline velocities. In this study, the results are shifted in time relative to the x_2 probe location for the gas injection cases and the x_S probe location for the heat addition case. This allows us to compare the changes in wave signature as they propagate downstream of the duct by overlapping them. The variables are normalised by the bulk convective time, $\tau_c = L_c/\bar{u}$:

$$\tau_i = \left(t - \frac{z_j - x_2}{u_{cl}} \right) \tau_c^{-1}, \quad \tau_q = \left(t - \frac{z_j - x_S}{u_{cl}} \right) \tau_c^{-1}, \quad (3.8a-b)$$

where $u_{cl} \approx 1.1 \text{ m s}^{-1}$ is the centreline velocity extracted from the URANS simulations upstream of the injection, L_c is the convective length (distance from the perturbation location to the outlet as shown in Fig. 3.1), and j is a counter for the different probe locations. The bulk convective time is $\tau_c = 0.6 \text{ s}$ for the compositional cases and $\tau_c = 1.6 \text{ s}$ for the entropic case.

Figure 3.12 shows the results of this analysis using the probe volume-averaged results for the compositional cases. In the case of argon, the profiles can be entirely accounted for by the normalisation procedure. There are minor diffusive dispersion effects visible, which seem to flatten and spread the trailing edge spike seen in the first three probe locations. However, since advection is the main transport mechanism and species are conserved, the maximum perturbation amplitude remains constant. This also holds true for helium's experimental data, and is in contrast with the heat addition case, where significant thermal diffusion and heat loss to the wall means that the original perturbation decays quickly.

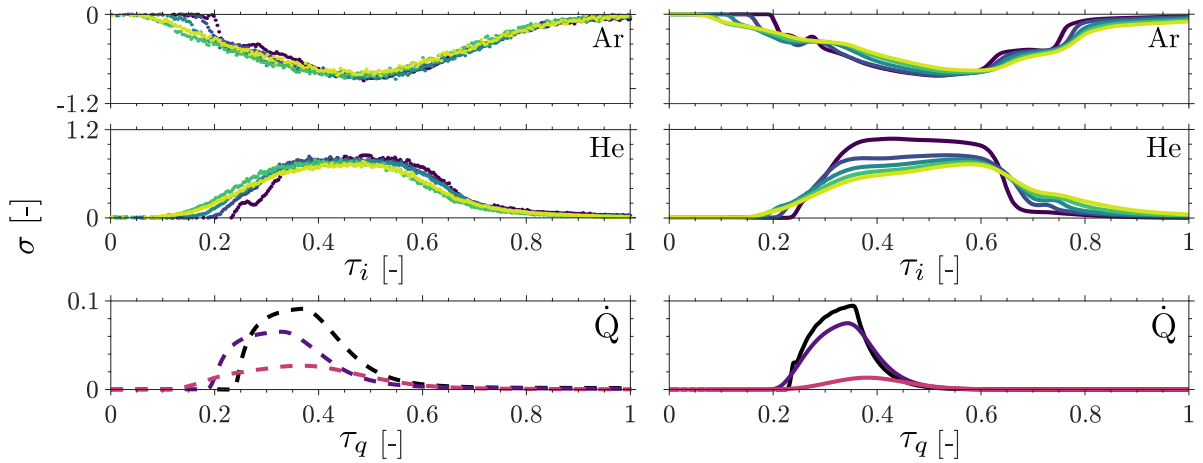


Fig. 3.12 Centreline entropic perturbations as a function of time (shifted for each probe location and normalised by the respective bulk convective time). Comparison between experiments using LITGS (\bullet) for the gas injection cases and thermocouples (---) for the heat addition (left) and numerical results using URANS (—) (right). For heat addition, case 1 ($\bar{u} = 0.88 \text{ m s}^{-1}$) is shown.

3.5 Summary

In this chapter, URANS calculations were undertaken to model the generation, mixing, and convection of unsteady entropic and compositional waves in an open-ended flow duct. The computations were compared to experimental results obtained using both intrusive and non-intrusive techniques at multiple axial locations along the centreline of the duct.

For the gas injection cases, argon produced a peak compositional perturbation on the x - y midplane five times larger than that of helium. This is due to the low molecular mass of helium and the lower injection mass flow rate. Despite the lower injection mass flow rate, helium produced a larger absolute entropic disturbance owing to the considerable specific entropy difference between air and helium. For the heat addition cases, the absolute entropic disturbance generated was an order of magnitude smaller than that of argon and helium.

Despite the fact that the flows investigated were in the transitional and turbulent regimes, all scalars convected in similar ways and were reproduced well. For the comparison of the gas injection results, three sampling methodologies were studied in the analysis of the numerical data: point, probe volume-averaged and cross-sectional area-averaged. For the injection of argon, agreement was found at all probe locations using all three sampling methodologies. The peak disturbance amplitude at the first probe for helium was well captured by the cross-section average value, but was overpredicted by the point and probe-volume averaged results. This is due to the planar symmetry assumption em-

ployed for the geometry. Despite this, good agreement was found for helium at the probes further downstream. For the heat addition cases, although the centreline temperature perturbations were small, it was found that, in the context of these model experiments, heat transfer to the wall needs to be accounted for. The results at downstream locations lag behind the experiments in terms of arrival time for both perturbations, suggesting that the centreline velocity was underpredicted in the numerical simulations. However, no velocity measurements were available for comparison.

Chapter 4

Experimental methods: phase-locked measurement of acoustic & compositional waves

THE methods employed in the experimental campaigns are outlined. In particular, the Canonical Wave Rig (CWR) is introduced and characterised. The CWR is used in tandem with a spontaneous Raman setup which allows for the point-wise, time-resolved measurement of compositional perturbations at 1.5 kHz. The Raman technique is detailed and a calibration method is presented.

4.1 Motivation and objectives

From the literature review presented in §2.3, we ascertained that model experiments can be used to separate direct and indirect noise contributions under simplified, well-controlled conditions. This concept is employed here, making use of the lessons learnt from the numerical simulations presented in §3 which inform the design of the model system introduced in this chapter.

In §3, we established that convecting temperature perturbations are significantly affected by heat transfer to the walls. Compositional inhomogeneities, on the other hand, are simpler to account for as they cannot permeate non-porous walls²⁰⁴ and are, therefore, the preferred method of perturbation. In particular, gases with a larger entropic-compositional coupling term $\Delta s/\bar{c}_p$ generate a larger entropic disturbance for the same injection mass fraction Y_i . In addition to this, we learnt that transversely injected jets may hit the opposing wall of the chamber before being convected downstream by the bulk flow. This is highlighted for the following reason: Magri et al.^{204,206} recently demonstrated the effects of non-compactness on the acoustic response of a nozzle. The theory predicts that at high enough perturbation frequencies, the indirect noise generated by a nozzle is reduced (i.e. the nozzle behaves as a low-pass filter). Yet, so far there is no experimental validation of this phenomenon. If a transverse injection system were employed for high frequency perturbations, it is possible that the compositional spots would hit the opposing side of the chamber. Consequently, they may mix and lose their frequency content before arriving at the nozzle. This is highly undesirable as we want the nozzle to be perturbed at controllable frequencies. Another potential issue with transverse injection is that it is likely to generate axially non-uniform perturbations, which complicates the 1D analysis. As a result, the design of the injection system used for the CWG needs to be re-assessed, preferably one that provides symmetric injection.

In addition, the non-reverberated measurement of indirect noise waves due to compositional inhomogeneities has not yet been done. De Domenico et al.⁶⁴ measured reverberated acoustic signals and dereverberated them using system transfer functions to extract the wave amplitudes. The comparison of direct (i.e. without acoustic reflections) and dereverberated measurements would also be an interesting output. For the direct measurement, an anechoic boundary of sorts is required to negate the effect due to reflections.

Time-resolved phase-locked measurements of the acoustic and compositional waves would provide both the input (compositional perturbation) and the output (pressure perturbation) of indirect noise. There are a few methods that can be used for the high frequency measurement of compositional spots in confined systems. One viable method

is hot-wire anemometry⁴⁵. Using two probes, the velocity and concentration of a binary gas mixture can be obtained using King's law³³⁶. Anemometry is a well-known technique with a proven track record in turbulent flow applications, providing a fairly high frequency response and good resolution. Although cheap to implement, hot-wire anemometry has its disadvantages. Besides from being intrusive and affecting the flow (specially when using two hot wires, as per the method proposed by Corrsin⁴⁵), signals tend to be noisy, and the probes are prone to breakage.

Optical diagnostics have also been used extensively. Table 2.2 summarises diagnostics techniques used to characterise the perturbations in past model experiments. Four wave mixing techniques, such as LITGS and CARS, are quite popular amongst combustion academics, but are overly complex for our applications. In this work, we employ Raman scattering. Although it generates low signal, spontaneous Raman offers the possibility of measuring two species simultaneously (which is desirable for our applications).

With all of the aforementioned considerations:

1. A new model thermoacoustic system is designed and presented in §4.2 which:
 - (a) can operate at subsonic and sonic (choked) nozzle conditions,
 - (b) can force the nozzle using the symmetric injection of compositional inhomogeneities at a range of controllable frequencies,
 - (c) can delay the onset of acoustic reflections from the boundaries to allow for the direct measurement of acoustic wave amplitudes,
 - (d) measures acoustic pressure fluctuations upstream and downstream of the nozzle in phase-locked mode with the measurement of species concentration.
2. A spontaneous Raman spectroscopy technique is developed and presented in §4.3 that allows for the point-wise measurement of local species concentration at 1.5 kHz. For this,
 - (a) the diagnostic technique is characterised and potential factors affecting the Raman signal are investigated,
 - (a) calibration curves are obtained and a method is proposed to translate a time-resolved Raman signal into a compositional wave amplitude ξ .

4.2 The Canonical Wave Rig: a model thermoacoustic system

The Canonical Wave Rig (CWR) is a model thermoacoustic system designed to study direct and indirect noise generation under simplified, well-controlled conditions. It is composed of four principal modules which are shown in Fig. 4.1: (1) inlet (perforated plate), (2) upstream chamber, (3) outlet (convergent-divergent nozzle), and (4) downstream chamber. Depending on the goals of each campaign, pseudo-anechoic tubes are added/removed from in between each of the four modules (or at/from the end of the downstream chamber as shown in Fig. 4.1). The termination of the pseudo-anechoic tube is an open end. All modules are bolted together with either O-rings or gaskets in between them to prevent leakages.

The primary air mass flow rate \bar{m} was filtered and supplied from the laboratory's compressed air supply at 5 bar. It was controlled using an Alicat MCR2000 mass flow controller (max. flow rate: 2000 SLPM, accuracy: $\pm 1\%$) and delivered by a flexible polyurethane tube (SMC TU1208, 8 mm ID) to a 2.1 m piston (36 mm ID for 2.06 m and 31 mm ID for the last 0.04 m). The piston is a modified version of an ISO 15552 pneumatic cylinder¹⁵⁷, adapted to attach to the CWR. The piston can extend the length of the upstream section by up to 1.6 m, allowing for the tuning of the rig's natural modes as well as the changing of the acoustic round-trip time (this feature, however, was not used in the experiments presented in this thesis). The piston is terminated by a thick perforated plate which is the inlet to the CWR as shown in Fig. 4.2 (see §4.2.1 for more details).

The upstream chamber consists of a 520 mm long duct with a constant area (40 mm ID) connected to a circular quartz section with 45 mm length of optically accessible length. Multiple quartz pieces were designed and manufactured specifically for the experiments

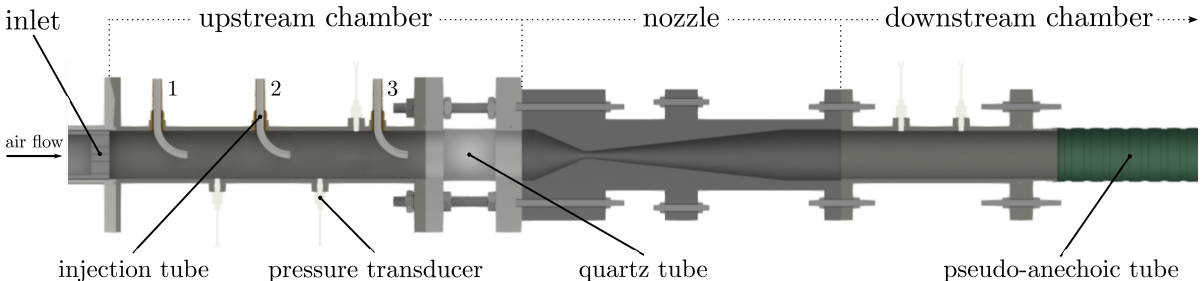


Fig. 4.1 General setup of the modular Canonical Wave Rig (CWR). Note: in the experimental campaigns presented, only one injection tube is inserted at a time – all three are shown here solely for visual purposes. Lengths are not to scale.

in this thesis (H. Baumbach & Co. Ltd). The quartz section has the same area as the duct (40 mm ID) to avoid reflections due to area changes and is 4 mm thick in order to withstand the pressurised test conditions. The quartz ends are square to axis and chip free; they were lightly flame polished to minimise the likelihood of failure under pressure. The upstream chamber is terminated by a convergent divergent nozzle which can run at subsonic and sonic (choked) conditions (see §4.2.2 and §4.2.6 for more details).

The injection of gases is performed in the upstream chamber and three different locations are provided for the studies (details of the gas injection system are described in §4.2.4). Acoustic pressure measurements are made upstream and downstream of the nozzle (as shown in Fig. 4.1) in order to characterise system properties, acoustic wave amplitudes, and transfer functions for reflected and transmitted noise (details of the pressure measurements are described in §4.2.5).

4.2.1 Inlet: perforated plate

The perforated plate is shown in Fig. 4.2. It is 15.5 mm thick ($t/d \approx 8$) and has 13 square-edged orifices. The average orifice diameter is $d_{pp} = 1.95$ mm, yielding a porosity of 3%²⁸⁸. The total wetted area is approximately 12% larger than the nozzle's throat area. This was done to ensure the nozzle chokes before the perforated plate, while keeping the

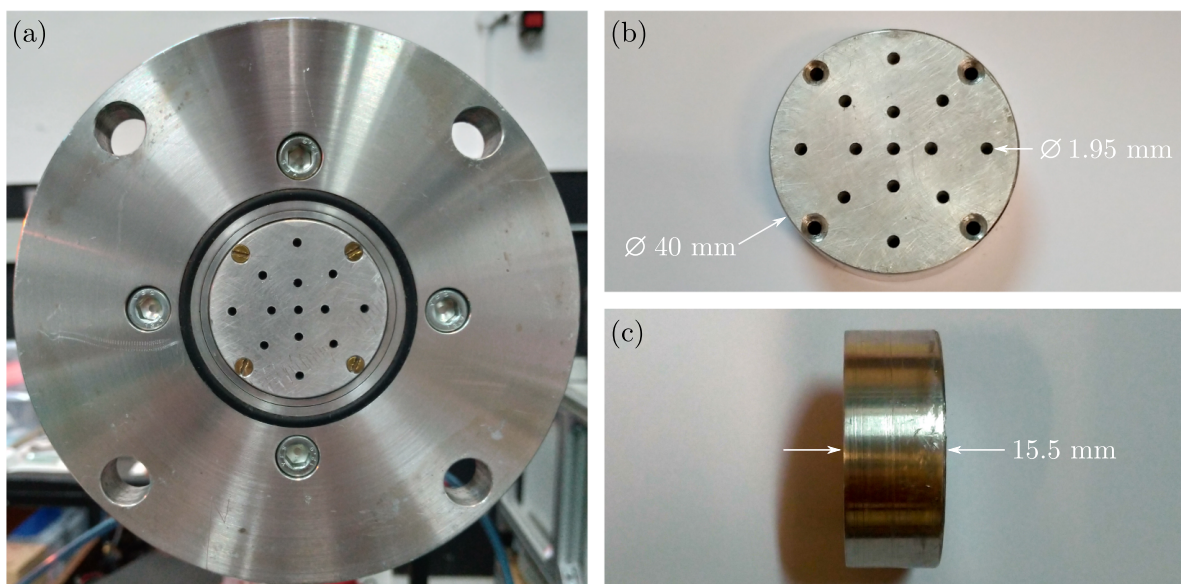


Fig. 4.2 Perforated plate inlet: (a) upstream view of plate in the CWR, (b) upstream view of plate and (c) side view of plate.

flow through the orifices at mid-to-high Mach numbers (as shown in Fig. 4.3a) in order to maximise the plate's downstream acoustic reflection coefficient (see §5.3.3 and §6.3.3).

The jets are assumed to be fully mixed before the first injection location (65 mm downstream from the plate). This can be checked by assuming each orifice produces a round/axisymmetric free turbulent jet. For a high-speed fluid issuing into a large quiescent reservoir, the jet spreading diameter can be estimated based on the half-angle of the jet's turbulent cone ($\theta_{tc} \simeq 12^\circ$)³²⁴:

$$D_{jet} = 2(x + x_0)\tan(\theta_{tc}) \quad (4.1)$$

where x is the distance from the exit plane of the perforated plate and $x_0 = 5d_{pp}/2$ is the distance from the virtual source^{70,263}. The bulk jet velocity \bar{u}_j and centreline (or maximum) jet velocity u_{cl} are proportional to x^{-1} :

$$\bar{u}_j = \frac{u_{cl}}{2} = \frac{5}{2} \frac{d_{pp}}{(x + x_0)} \bar{u}_0 \quad (4.2)$$

where \bar{u}_0 is the bulk jet exit velocity^{132,263,343}.

Figure 4.3 shows a CAD rendering of the jets under the free turbulent jet assumptions (i.e. jet interaction is not considered). The bulk jet exit velocity \bar{u}_0 and Mach number \bar{M}_0 are estimated at the exit plane using the mean pressure in the main duct (i.e. instantaneous

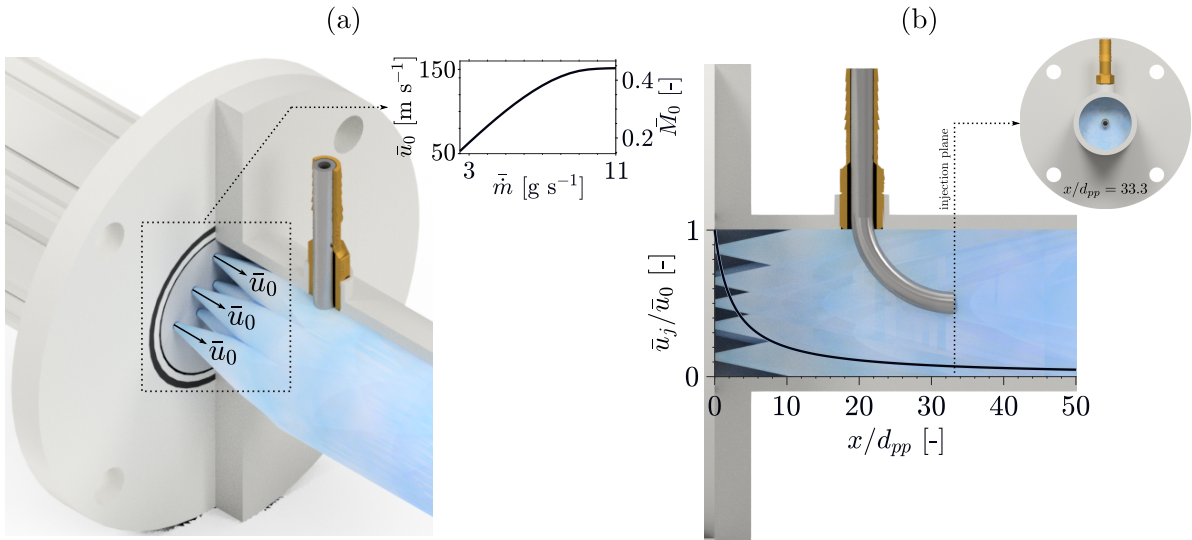


Fig. 4.3 CAD rendering of air flow through the perforated plate assuming a turbulent cone half-angle of 12° : (a) isometric view with bulk jet exit velocity \bar{u}_0 and Mach number \bar{M}_0 of jet as a function of mean flow rate \bar{m} ; (b) decay of normalised bulk axial jet velocity \bar{u}_j/\bar{u}_0 as a function of perforated plate hole diameter d_{pp} ²⁶³.

jet pressure equalisation) as shown in Fig. 4.3a. As a result of this assumption, the bulk jet exit velocity \bar{u}_0 is expected to follow the same trend with flow rate (i.e. it saturates due to the nozzle reaching choked conditions). At the injection plane ($x/d_{pp} = 33.3$), the bulk velocity of a free turbulent jet is approximately 7% of its bulk jet exit velocity \bar{u}_0 as shown in Fig. 4.3b. Physically, some degree of jet interaction is expected, leading to higher mixing, and ensuring the air flow behaves as one bulk flow as opposed to 13 separate jets. Computational fluid dynamics simulations would be helpful to confirm this is accurate.

4.2.2 Outlet: convergent-divergent nozzle

The convergent-divergent nozzle used was designed by De Domenico⁶⁰ and is shown in Fig. 4.4. It was manufactured from rigid polyvinyl chloride (PVC) in three parts via CNC machining and bolted together with O-rings between each part to avoid leakages. The nozzle has a total length of 299 mm. The convergent section is 60 mm long with a 16.9° linear profile while the divergent section is 230 mm long with a 4.5° linear profile as shown in Fig. 4.4. The throat is 9 mm long and has a geometric diameter of 6.6 mm.

The areas of the upstream and downstream sections of the nozzle are the same (ID = 42.6 mm). The area difference between the nozzle ends and the upstream and downstream chambers (ID = 40 mm) is assumed to be negligible in the analysis. The nozzle can be operated either at subsonic or sonic conditions ($\bar{M}_t \leq 1$).

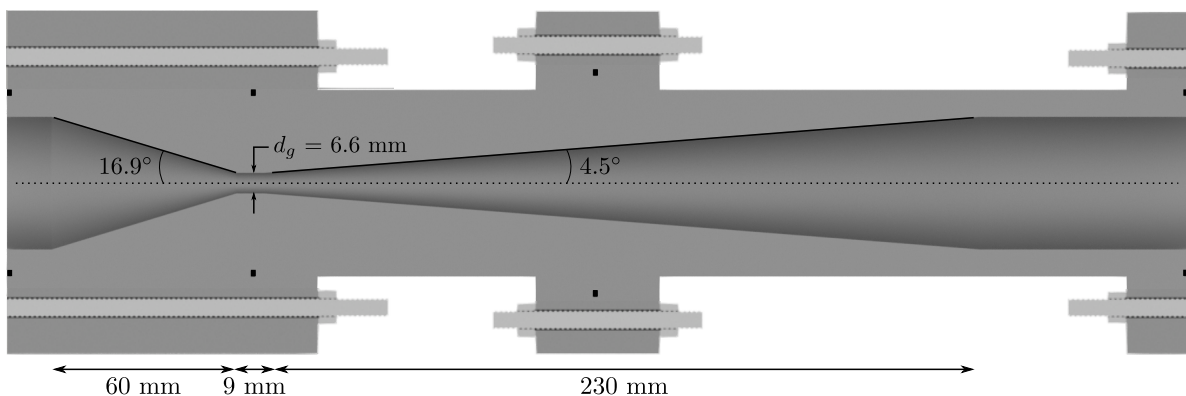


Fig. 4.4 Convergent-divergent nozzle used in the Canonical Wave Rig (CWR).

4.2.3 Pseudo-anechoic tube

In acoustics, anechoic boundary conditions can be used to avoid dealing with problems associated with reflected pressure waves. This is difficult to achieve experimentally, especially at low frequencies. One viable workaround is to delay the measurement of a reflected wave by using long tubes^{61,63,64}. A lightweight and flexible PVC hose was adapted for this purpose, termed here as *pseudo-anechoic tube*. It has a rigid internal structure with a smooth bore and a diameter close to that of the CWR (45 mm ID). It is assumed that reflections are not generated at the connection boundaries since the area change is gradual and we assume planar wave propagation. Each hose is $L_h = 30$ m long and different numbers of hoses n_h were used depending on the experimental campaign. The time duration τ_a over which the measurement of a wave is delayed (rendering that boundary effectively anechoic) is the acoustic round-trip time defined as the *anechoic time* τ_a . It can be calculated via:

$$\tau_a = \frac{n_h(L_h + \Delta x_p)}{\bar{c} + \bar{u}} + \frac{n_h(L_h + \Delta x_p)}{\bar{c} - \bar{u}} \quad (4.3)$$

where Δx_p is the distance from the transducer to the start of the hose.

A reasonable estimate can be found by neglecting convective effects and the distance from the transducers:

$$\tau_a \simeq \frac{2L_a}{\bar{c}} \quad (4.4)$$

where the anechoic length can be defined as $L_a = n_h L_h$.

Figure 4.5 shows the pressure time series of a sample test case for the injection of air (test case Air-A-6 from §5.3.2) measured upstream of the nozzle. This shows the effectiveness of the tube in delaying the measurement of the reflected pressure wave to

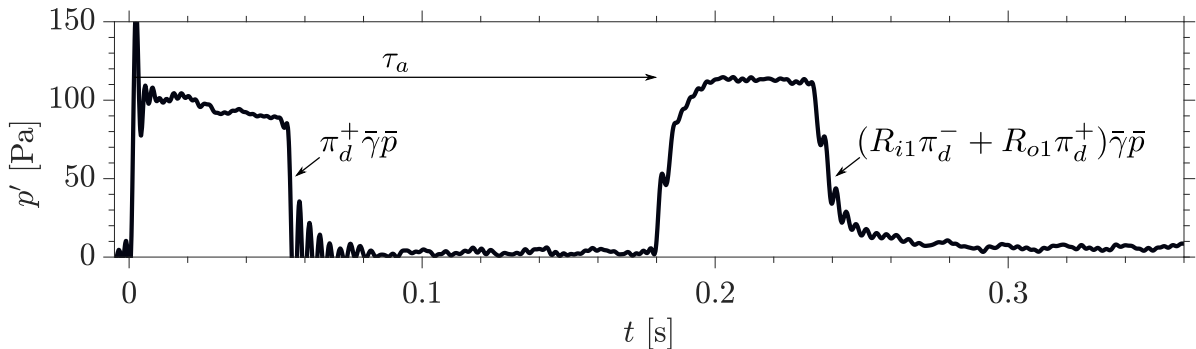


Fig. 4.5 Measured direct noise pressure fluctuations due to air injection $\pi_d^+ \bar{\gamma} \bar{p}$ and reflected waves $(R_{o1} \pi_d^+ + R_{i1} \pi_d^-) \bar{\gamma} \bar{p}$ demonstrating the effectiveness of the pseudo-anechoic tube ($L_a = 30$ m) in creating time separation.

allow for clear time separation⁶⁰. The first downstream-travelling wave π_d^+ is measured by the transducer at $t = 0$ s. The ringing at the end of the pulse is hypothesised to be caused by valve dynamics. The upstream-travelling wave π_d^- is not measured as it is generated upstream of the transducer. It is, however, reflected at the inlet, while the downstream travelling wave π_d^+ is reflected at the nozzle. The reflections change the overall shape of both pressure pulses. They then return to the transducer at the same time and constructively interfere after $\tau_a = 0.18$ s, as expected.

4.2.4 Gas injection system

Perturbations are generated via the single pulse or pulse burst injection of air or methane (at room temperature) at the centreline of the duct (i.e. co-flow injection). The injection of each gas generates direct noise (i.e. acoustic waves π_d^\pm). Since methane has a different specific entropy and chemical potential relative to air, its injection additionally produces entropic σ and compositional ξ waves (as per Eq. (2.41))²⁷⁸. The waves generated by the injection of each respective gas (as derived in §2.2.3) are summarised in Table 4.1.

Table 4.1 Canonical waves generated due to the injection of air or methane²⁷⁸.

Injected gas	Acoustic (direct noise) waves π_d^\pm	Entropic wave σ	Compositional wave ξ
Air	●	-	-
Methane	●	●	●

The injection is carried out using one of three high-speed solenoid valves (SMC SX10 series¹) depending on the test case. The valves have an on/off response time ranging between 0.40 ms and 0.75 ms. The flow out of the mass flow meter and out of the valve is delivered by a flexible polyurethane tube (SMC TU0805, 5 mm ID). The injected gas enters the duct at the centreline via a 90° L-bend pipe with inner and outer diameters of $d_i = 3.4$ mm and $d_{i,OD} = 6$ mm, respectively, as shown in Fig. 4.6. The injection pipe cross-section has a negligible area since it is $A_{i,OD}/A \approx 2\%$ of the main duct's cross-sectional area.

The valve is actuated by a trigger signal – either from the laser system (when running optical diagnostics in phase-locked mode) or from a button in the energy-saving circuit (more details on page 77). The mass flow rate of injected gas \dot{m}_i is chosen to achieve

¹SX11F-AH (50 L/min, 80 W); SX11F-EH (100 L/min, 80 W); SX11F-JH (150 L/min, 80 W).

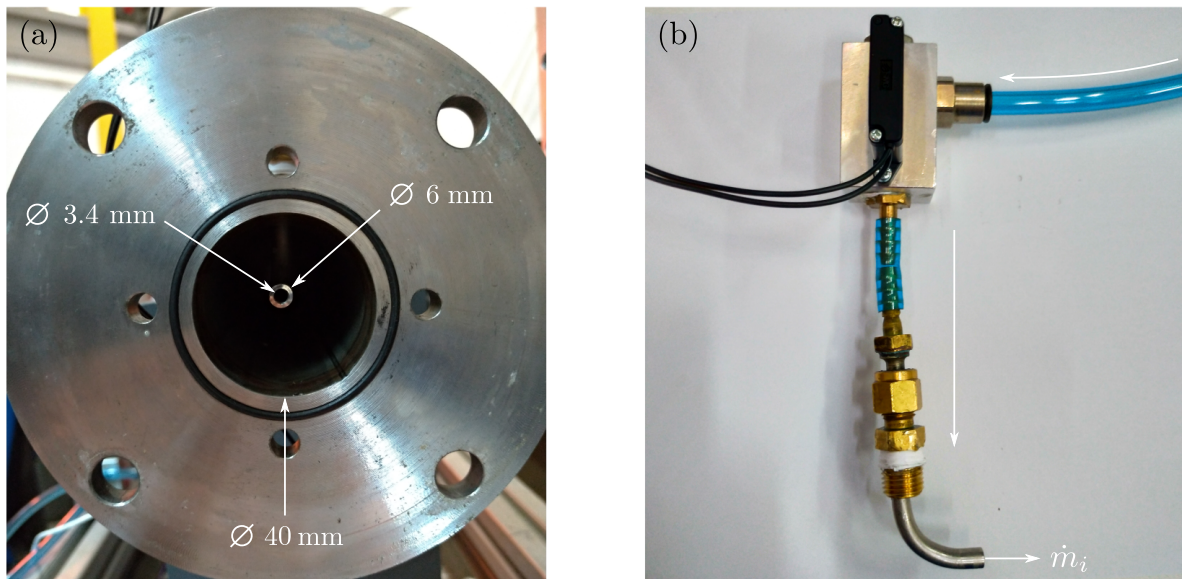


Fig. 4.6 Injection system: (a) upstream view inside the CWR and (b) side view showing the high-speed valve and the direction of the injected flow.

a specific injection mass fraction $Y_i = \dot{m}_i / \bar{m}$. It can be adjusted by using a pressure regulator downstream of the respective gas tanks², as shown in Fig. 4.7. The mass flow rate of injected gas \dot{m}_i is monitored in real-time using the NI Laboratory Virtual Instrument Engineering Workbench (LabVIEW) software which plots and acquires the output from an Alicat M100 mass flow meter (max. flow rate: 100 SLPM, accuracy: $\pm 1\%$). The mass flow meter is connected to a lab computer via an Alicat BB9 breakout box. The meter hosts on-board calibrations for multiple gases which can be manually selected depending on the injected gas. The mass flow rate is logged at a sampling frequency of approximately 35 Hz. In light of the short pulse durations ($t_p = 2 - 50$ ms), this is admittedly a low sampling rate. The sampling rate was initially thought to be a limitation of the mass flow meter as per conversations with the manufacturer. However, in more recent communications, it is thought that this sampling rate can be increased (this was only communicated to the author after the experimental campaigns had been concluded). To reduce the error in this measurement, experiments were repeated for a fixed regulator pressure and the peak mass flow measurement was taken to be the true injected value. Ideally, future work would use a higher sampling rate for the mass flow measurements.

²Methane tank has the following impurities: $O_2 = 25$ ppmv; $N_2 = 1000$ ppmv; $H_2O = 10$ ppmv; C_2H_4 and other HC's = 3000 ppmv. Air tank has the following impurities: $CO_2 < 500$ ppmv; $CO < 10$ ppmv; moisture < 250 ppmv; oil < 1 mg m^{-3} .

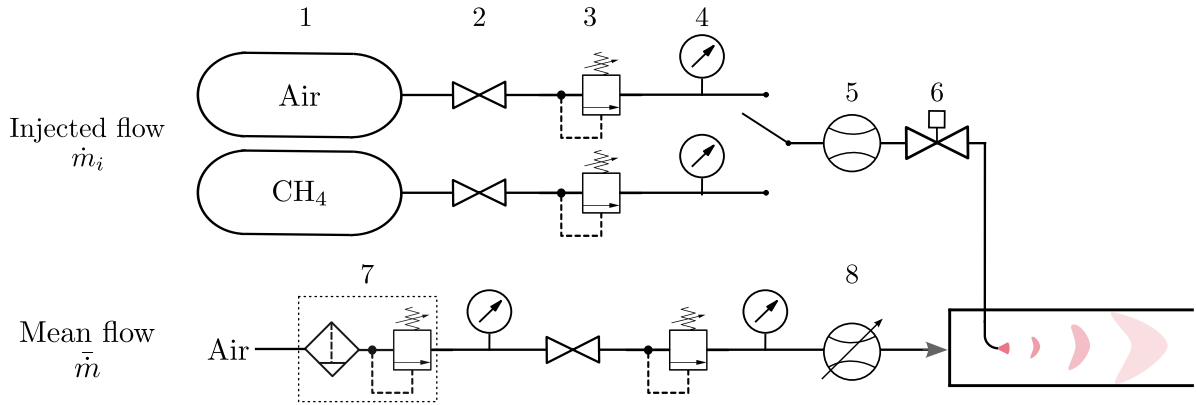


Fig. 4.7 Circuit diagram with flow lines for mean and injected flows: (1) gas cylinders (air or methane), (2) manual valve, (3) pressure regulator, (4) pressure gauge, (5) mass flow meter, (6) solenoid valve, (7) air filter regulator with pressure gauge, and (8) mass flow controller.

Effect of injection tube on injected flow

By calculating the cross-flow Reynolds number Re_{cf} for the injected pipe, we can understand if the interaction between the mean flow of air and the injection tube has any influence on the injected gas jet⁵⁸ (which is downstream of the injection tube):

$$Re_{cf} = \frac{\bar{\rho}\bar{u}d_{i,OD}}{\mu} = \frac{\bar{p}\bar{u}d_{i,OD}}{\bar{R}\bar{T}\mu} \quad (4.5)$$

Assuming $\mu = 18.12 \times 10^{-6}$ Pa s (for $\bar{T} = 293.15$ K³¹⁰), $d_{i,OD} = 6$ mm, $\bar{R} = 287$ J kg⁻¹ K⁻¹, the tube's crossflow Reynolds range is $660 < Re_{cf} < 2900$ depending on the air mass flow rate. As a result of these low (laminar) to moderate (transitional) Reynolds numbers, the injection pipe is expected to have some influence on the flow of the injected compositional perturbation.

Energy-saving circuit

To achieve a high-speed response, the injection valve employs a high power coil. The coil quickly overheats (and can be permanently damaged) if 80 W is continuously and directly supplied to the valve for pulses longer than 0.62 ms. Holding the valve open requires much less power than actuating it, so the 80 W can be applied to open the valve, then quickly reduced to hold it open. This can be achieved using one of two methods: (1) using two power supplies (starting and holding voltage supplies) and switching from high to low voltage, or (2) using a high-speed switching control of high voltage by pulse width modulation (PWM) control.

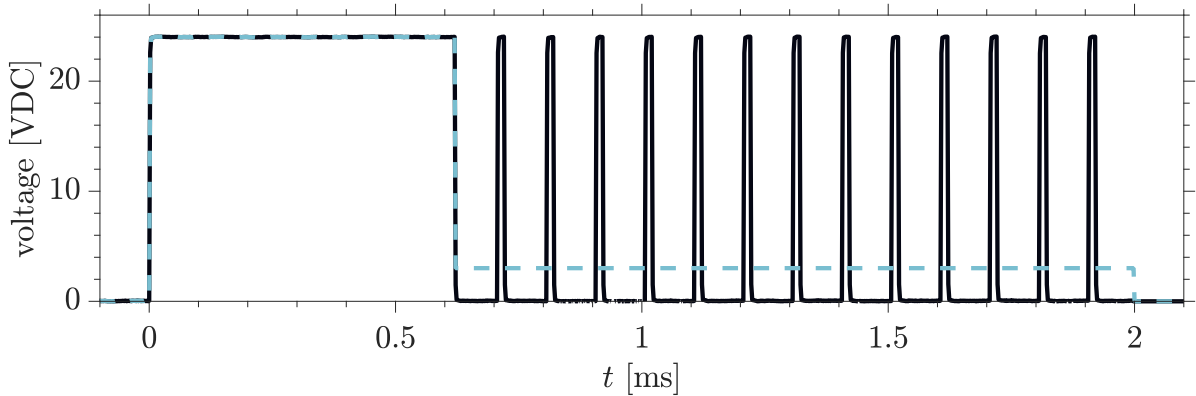


Fig. 4.8 Pulse width modulation (PWM) used in the energy saving circuit for a high frequency injection test case (2 ms pulse, 12.5% holding voltage): output voltage (—) and average voltage (---).

An in-house energy saving circuit was designed to ensure the valve could be used successfully over a wide range of injection frequencies and pulse durations³. Specifically, the circuit allows for the high-speed switching control of high voltage via PWM. It was used along with a 72-2690 Tenma power supply to drive the valve safely (i.e. without overheating). The PWM system controls the output voltage of the power supply using an Mbed NXP LPC1768 Microcontroller operating at a CPU frequency (or processor clock speed) of 96 MHz. The board is run using a C++ code which is specific for each test case and compiled using the online Mbed platform. The valve requires a PWM frequency of at least 10 kHz. For the experiments in this thesis, it is set to 100 kHz (i.e. period of 0.01 ms). On average, the valve is driven by 24 VDC (100% duty cycle) for 0.62 ms and then kept open with a holding voltage of 3 VDC (12.5% duty cycle) for the rest of the pulse duration. The voltage supplied to the valve for a case presented in §6 was recorded using a Tektronix DPO 3014 Digital Phosphor Oscilloscope and is shown in Fig. 4.8. In theory, this PWM circuit allows for the valve to be used in continuous operation mode (i.e. in which the valve is constantly open) although this was not attempted.

For the experiments presented in this thesis, the energy-saving circuit allowed for injections at frequencies ranging from 0.01 Hz to 250 Hz with pulse durations ranging from 2 ms to 50 ms.

³The author kindly acknowledges the work of Mark Garner (Chief Technician, Hopkinson Lab) who designed the energy-saving circuit.

4.2.5 Acoustic pressure measurements

Acoustic pressure measurements are carried out using piezoresistive pressure transducers (Kulite XTE-190M) flush-mounted at several $M5 \times 0.8$ mm transducer ports along the duct as shown in Fig. 4.1.

The transducers are terminated by male RJ50 (10-pin) connectors which individually plug into SHB12X-6RJ50 shielded InfiniBand 12x cable inputs. The pressure transducer signals are acquired using a National Instruments (NI) PXIe-4480 Sound and Vibration Module. It is housed in a PXI Express Peripheral slot of an NI PXIe-1073 chassis. Direct PXI remote control using a computer is possible through the use of a PCIe-8361 MXI-Express device. This device consists of a PCI Express board slotted to the back of the lab's desktop computer which connects to a PXI module in slot 1 of the PXI chassis via a high-bandwidth MXI-Express cable.

The signal is sampled at 10 kHz, recorded using NI LabVIEW and post-processed in MATLAB. Preliminary post-processing includes (1) the phase-averaging of multiple pulses to remove random noise effects and mean flow oscillations, and (2) the filtering out of frequencies between 49.5 and 50.5 Hz to remove contributions due to the UK power grid. Additional filtering may be used to remove unwanted contributions due to high frequency flow noise (e.g. $f > 400$ Hz), as shown in Fig. 4.9.

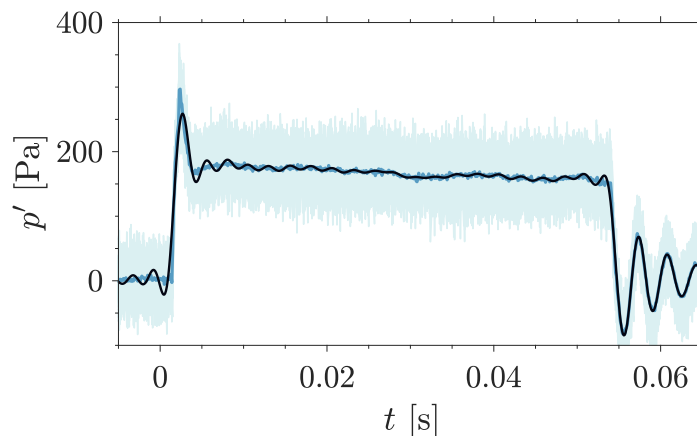


Fig. 4.9 Example of acoustic pressure signal post-processing: raw signals from 100 pulses (—), phase-averaged signal over 100 pulses (—), and phased-averaged and filtered signal (—).

4.2.6 Mean flow properties

The experimental campaigns investigate the effect of mean air flow rate on the generation of direct and indirect noise. Tested conditions range from $2.5 \leq \bar{m} \leq 11.0 \text{ g s}^{-1}$. Figure 4.10 shows the mean flow properties investigated based off experimental pressure measurements. The standard deviation ($\pm 1\sigma$) of the measured (\bar{p}) and calculated (\bar{u} , \bar{M} , Re) variables is also included to show the variability of the mean flow properties.

The bulk velocity inside the upstream chamber varies between $1.6 \leq \bar{u}_1 \leq 4.9 \text{ m s}^{-1}$ ($0.005 \leq \bar{M}_1 \leq 0.014$), meaning that the low Mach number assumption (i.e. $\bar{M} \ll 1$) is valid and all test cases investigated are in the turbulent regime ($4300 \leq Re \leq 19,000$)²⁷³. Finally, the pressure increase in the upstream chamber starts to show a linear dependency with flow rate around 10 g s^{-1} . This is assumed to be the choking point \bar{m}_c of the convergent-divergent nozzle.

The values listed above can be used to calculate the non-dimensional acoustic $He = fL_n/\bar{c}$ and convective $St = fL_c/\bar{u}$ frequencies for the experiments in this thesis, where L_n is the nozzle length and L_c the convective length. These are shown in Fig. 4.11 and compared to estimated values for aero-engines and gas turbines. For the

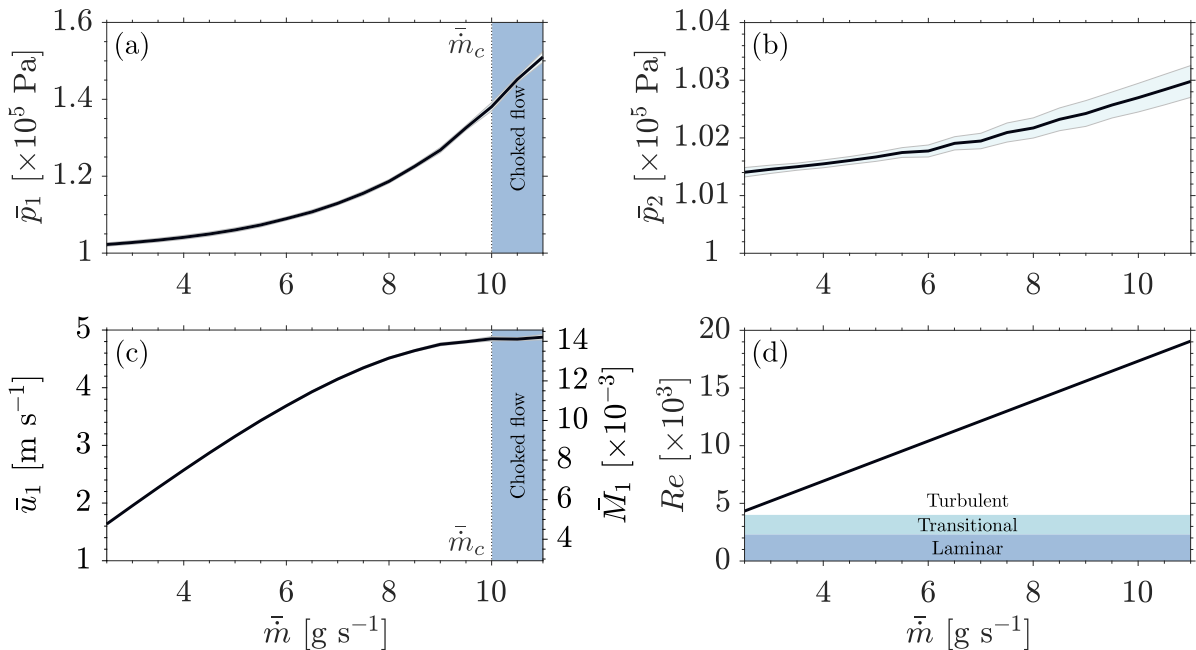


Fig. 4.10 Evaluation of mean flow properties as a function of flow rate: (a) upstream pressure \bar{p}_1 (with choking flow rate \bar{m}_c and choked flow region highlighted), (b) downstream pressure \bar{p}_2 , (c) upstream bulk velocity \bar{u}_1 and Mach number \bar{M}_1 (with choked flow region highlighted), and (d) upstream Reynolds number Re (with laminar, transitional and turbulent flow regimes highlighted²⁷³).

single pulse experiments presented in §5, the perturbation frequency is below 1 Hz and convective lengths range from 0.1 to 1 m, as there are two injection locations (more details on this later). For the pulse burst experiments presented in §6, higher frequencies are used (up to 250 Hz) but with a single, short convective length (approximately 0.1 m). The compact regime does not have a clear He boundary. However, nozzle non-compactness has been shown to be a key factor in a system's indirect noise generation^{204,206}. Indeed, Leyko et al.¹⁸¹ showed that the compactness assumption is no longer valid for $He > 0.1$. In a different study, Leyko et al.¹⁸⁵ suggests the limit is instead 0.03. The former limit has been included in Fig. 4.11 for reference.

For the gas turbines estimates, it is been assumed that convective lengths range from 0.3 to 1.5 m, with frequencies ranging between 50 Hz (rumble/axial modes) and 1000 Hz (screeching/annular and radial modes) and nozzle lengths from 0.1 to 0.25 m. Furthermore, the combustion chamber sound speeds are assumed to vary from 750 to 900 m s⁻¹ with bulk flow velocities between 15 and 200 m s⁻¹ (i.e. $\bar{M}_1 < 0.3$).

As Fig. 4.11 shows, from the point of view of acoustic compactness, the CWR can be considered a gas turbine model thermoacoustic experimental setup. It is important to note that the Reynolds numbers Re shown in Fig. 4.10 are still at least an order of magnitude lower than those in gas turbines, which can lead to very different dissipation and mixing characteristics³⁴. Similarly, the mean pressures are much lower, but found to be sufficient for the purposes of the model experiment.

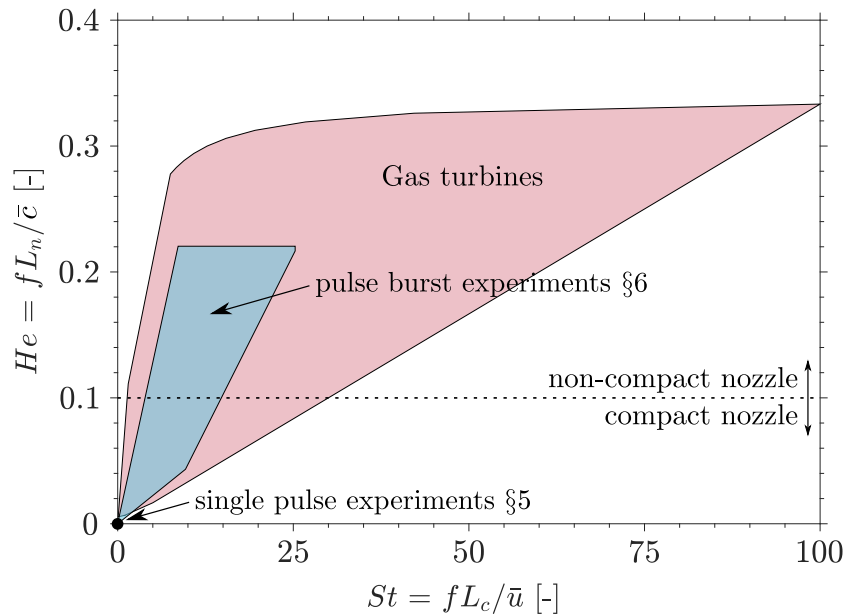


Fig. 4.11 General comparison of estimated acoustic He and convective St non-dimensional frequencies for gas turbines and experiments presented in this thesis.

4.3 Spontaneous Raman spectroscopy: time-resolved concentration measurements

A spontaneous Raman system is employed for the purpose of measuring the local concentration. High speed time resolution is needed to accurately capture the compositional inhomogeneities at the range of the injection frequencies ($f_i \leq 250$ Hz) and pulse widths ($t_p \leq 50$ ms) investigated. A general background is presented, followed by a description of the setup, methods, and calibration results.

4.3.1 Background

The inelastic scattering of light was first postulated to exist theoretically by Smekal²⁹⁷ in 1923. Shortly thereafter, Raman and Krishnan^{269,270} made the first experimental observations of the effect. Since the advent of laser systems, the application of this eponymous effect has garnered widespread interest from the scientific community.

When light interacts with matter, it can be absorbed, scattered or pass through unaffected. In scattering, photons distort and polarise a molecule's electron cloud. As a result of this, a short-lived and unstable 'virtual' state is formed, and a photon is promptly re-radiated afterwards²⁹⁸. The light scattering process can be elastic or inelastic. In the case of the former, there is no energy transfer between the molecule and the incident photon – this is *Rayleigh* scattering. It is the dominant process, producing the largest signal at the excitation wavelength of the laser. In the case of the latter, energy is transferred from the molecule to the photon (or vice-versa) – this is *Raman* scattering. Energy, and thus angular frequency, is conserved so that the shift of the scattered light can be described by:

$$\omega_{sc} = \omega_{mol} \pm \omega_p, \quad (4.6)$$

where subscripts $(\cdot)_{sc}$, $(\cdot)_{mol}$, and $(\cdot)_p$ refer to the scattered light, molecular vibration, and incident photon frequencies, respectively. Depending on whether energy is transferred to or from the molecule, Eq. (4.6) can describe a red-shift or blue-shift mechanism¹⁶³. A shift of the scattered light towards a lower energy (i.e. lower frequency, longer wavelength) is called *Stokes* scattering, whereas a shift to a higher energy (i.e. higher frequency, shorter wavelength) is called *anti-Stokes* scattering. These processes are shown in Fig. 4.12.

Spontaneous Raman spectroscopy is a linear and instantaneous process which employs the Raman scattering effect to identify molecules since the photon's frequency shift is related to the rovibrational modes of the probed species. For room temperature conditions (as per the work of this thesis), the number of molecules in a vibrationally excited state

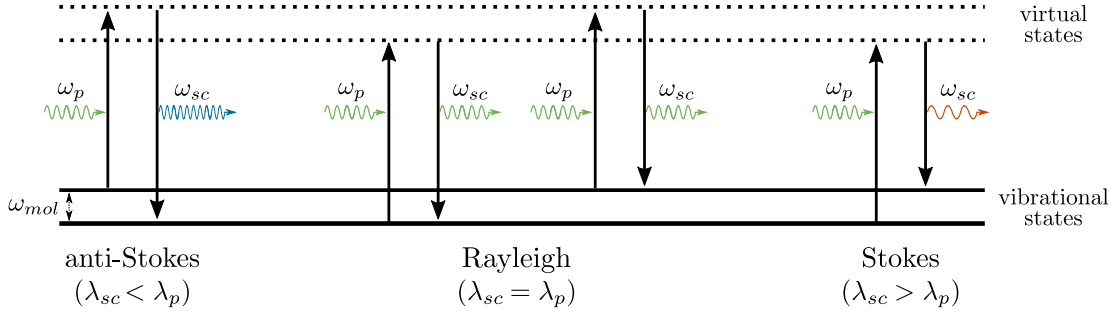


Fig. 4.12 Diagram of the Rayleigh and Raman (Stokes and anti-Stokes) scattering processes. Conservation of angular frequency is depicted where subscripts $(\cdot)_{sc}$, $(\cdot)_{mol}$, $(\cdot)_p$ refer to the scattered light, the molecule vibration, and the incident photon, respectively. Inspired by Jones et al.¹⁶³ and Smith and Dent²⁹⁸.

are extremely low relative to the ground state. In this case, the Stokes signal is larger than the anti-Stokes and is the signal collected and presented in this thesis.

The Raman Stokes signal intensity I_s has the following proportional relationships:

$$I_s \propto c \frac{d\sigma}{d\Omega} P_l \quad (4.7)$$

where c is the concentration, $d\sigma/d\Omega$ is the differential Raman scattering cross-section, and P_l is the power of the excitation laser^{118,218,298}.

The differential Raman scattering cross sections $d\sigma/d\Omega$ are generally very small (on the order of $\times 10^{-35} \text{ m}^2 \text{ sr}^{-1}$), so high laser powers P_l are required to produce signals that are observable relative to ambient noise. The source of excitation radiation is a monochromatic laser which can be operated continually or pulsed. Pulsed lasers are used to supply high powered, short-duration pulses to help maximise the Stokes signal and minimise the broadband fluorescent signal^{117,250}.

In this work, spontaneous Raman spectroscopy is used for local compositional wave source characterisation. By monitoring single-shot Raman signals, this experiment quantifies, on a cycle-averaged basis²⁹², the time-resolved methane–air mixture fraction fluctuations as a source of compositional noise through a nozzle. Specifically, we probe a non-reacting binary gas mixture and track the modal peaks of two selected species (N_2 and CH_4). In the next section, the setup is described, followed by methods and calibration results.

4.3.2 Setup

The measurement of compositional waves in the model thermoacoustic system was done using the spontaneous Raman spectroscopy system⁴ shown in Fig. 4.13.

A Litron LDY303 PIV laser system was used in dual-pulsed mode to generate the excitation radiation at 527 nm. It is an Nd:YLF diode-pumped solid-state laser (DPSSL) with a dual cavity configuration and Q-switching capability. The laser system produces pulse widths of approximately 350 ns (in dual-pulsed mode), as shown in Figs. 4.13a and 4.20. The two laser cavities can be operated at a wide range of repetition rates (0.2 to 20 kHz) with individual pulse energies that start at 28 mJ and exponentially decrease to 0.4 mJ with increasing frequency for a 65% laser power setting¹⁹⁵, as shown in Fig. 4.13b. Using the LaVision Davis 8.4 software, the repetition rate was set to 1.5 kHz with 0 μ s time separation between the two pulses. The Litron Lasers control software was used to turn the system, pump, and laser on/off, as well as to open/close the shutter, and vary the laser power. The system and pump were turned on for at least 15 minutes before each experiment was run.

The pulses were guided by various high reflectivity 532 nm mirrors onto a long-pass 532 nm dichroic beamsplitter (LPD02-532RU-25), which is designed to minimise reflected wavefront error (RWE) and was positioned at 45° relative to the incident light. Most of the 527 nm light was reflected by the beamsplitter towards an achromatic doublet lens ($\varnothing = 50.8$ mm, $f = 100$ mm) (AC254-100-A-ML) which focused the light into the quartz test section. A traverse was used to control the alignment of the test section in the x , y and z directions, ensuring that the focal point of the lens was at the centre of the duct. The alignment was done with the laser power set to its minimum value (20%). The collection confocal volume is estimated to be between $0.5\text{--}12.0 \times 10^{-4}$ mm³ with a length of approximately 1–5 mm along the z -axis (details of which are described in Appendix B.1). A photodiode array detector (PDA10A2) – positioned on the opposing side of the quartz section – captured the shape and relative amplitude of the laser pulses for use in the data analysis, as described in §4.3.3.

The Raman system used for this work employed a backward-scattering (180°) configuration, as opposed to a forward-scattering (0°) or right-angled (90°) configuration. In preliminary tests, this configuration was shown to produce higher signal than the latter. It also had the added advantage of simplifying the alignment procedure. Backward collection was made possible by the use of a dichroic beamsplitter which reflected the excitation light, while efficiently passing the longer back-scattered Raman-shifted (Stokes)

⁴The author kindly acknowledges the work of Dr. Lee Weller who set up the Raman system and collected the Raman data.

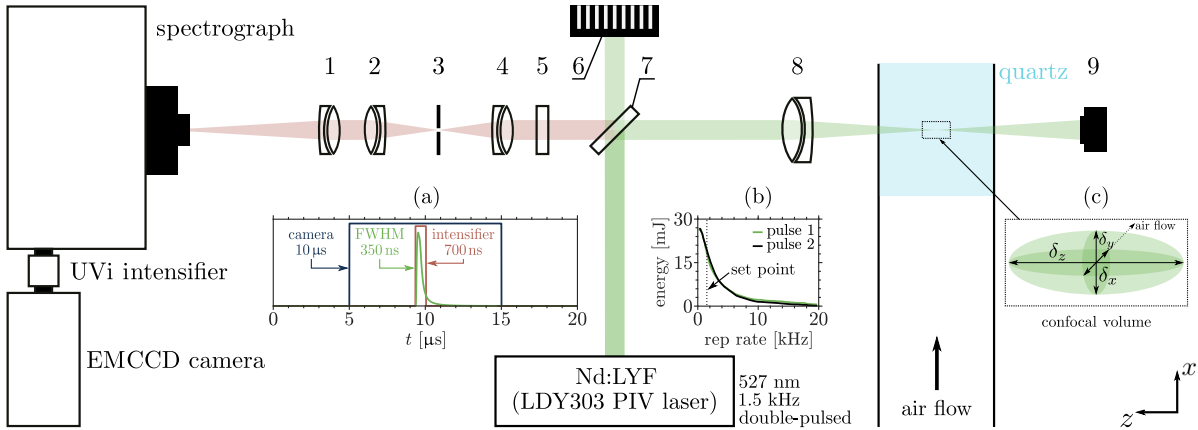


Fig. 4.13 Schematic of the spontaneous Raman spectroscopy system. The main components of the system are: (1) achromatic doublet lens ($\text{Ø} = 25.4 \text{ mm}$, $f = 100 \text{ mm}$), (2) achromatic doublet lens ($\text{Ø} = 25.4 \text{ mm}$, $f = 50 \text{ mm}$), (3) mounted pin-hole ($\text{Ø} = 25.4 \text{ mm}$, $25 \text{ }\mu\text{m}$), (4) achromatic doublet lens ($\text{Ø} = 25.4 \text{ mm}$, $f = 50 \text{ mm}$), (5) 532 nm single-notch filter ($\text{Ø} = 25.4 \text{ mm}$), (6) beam trap, (7) long-pass 532 nm dichroic beamsplitter ($\text{Ø} = 25.4 \text{ mm}$), (8) achromatic doublet lens ($\text{Ø} = 50.8 \text{ mm}$, $f = 100 \text{ mm}$), (9) photodiode array (PDA) detector. Also included: (a) timings of the camera-intensifier-laser system, (b) measured laser pulse energies as a function of repetition rate¹⁹⁵ and (c) confocal volume schematic (oblate ellipsoid) assuming a spherically Gaussian beam. Dimensions not to scale.

wavelengths. The dichroic filter reflected most of the green Rayleigh photons and shorter Raman-shifted wavelengths (anti-Stokes).

A 532 nm single-notch filter (NF01-532U-25) was used to isolate the lower energy Raman-scattered light from the remaining, more intense Rayleigh signal (at the excitation wavelength) that passed through the dichroic beamsplitter and any back-scattered laser photons from optical elements along the path. The collimated light was then focused by an achromatic doublet lens ($\text{Ø} = 25.4 \text{ mm}$, $f = 50 \text{ mm}$) (AC254-050-A-ML) through a $25 \text{ }\mu\text{m}$ pinhole (P25C) and was then re-collimated using another achromatic doublet lens ($\text{Ø} = 25.4 \text{ mm}$, $f = 50 \text{ mm}$) (AC254-050-A-ML). The Raman-scattered photons were then focused by an achromatic doublet lens ($\text{Ø} = 25.4 \text{ mm}$, $f = 100 \text{ mm}$) (AC508-100-A-ML) onto the aperture of an Andor Shamrock SR-303i spectrograph⁹ which was used to collect and disperse the Raman-scattered light. The spectrograph was set such that any stray green light that entered the spectrograph did not exit from the back. It had a side input slit size of $200 \text{ }\mu\text{m}$. The diffraction grating inside the spectrograph had 1200 lines/mm and was blazed at 500 nm, allowing for the collection of wavelengths ranging from 596 to 627 nm (Raman shifts of $2197 \leq \Delta\tilde{\nu} \leq 3008 \text{ cm}^{-1}$) with an average wavenumber resolution of approximately $\delta\tilde{\nu} = 13 \text{ cm}^{-1}$.

To amplify the measured Stokes signal, whilst minimising the capturing of any unwanted light sources, an intensifier with a narrow timed shutter was employed. In particular, an Invisible Vision UVi camera intensifier (1850-10-S20) was connected to the output of the spectrograph with an exposure of 700 ns and a delay of 4.4 μ s to capture the Raman photons, as shown in Fig. 4.13a. It is a customised second generation intensifier employing a chevron pair (extended dynamic range) MCP plates, where 1% and 100% gain G correlate to 970 V and 1705 V across both plates (approximately evenly split), respectively, with a linear increase in voltage between those two values. The trigger mode was continuous with positive edge triggering. The intensifier has a high sensitivity in the UV to visible regions (200 – 550 nm). The wavelengths investigated here were in the lowest sensitivity range of the intensifier, where the quantum efficiency is lower than 5%.

The intensifier was coupled to an Andor iXon Ultra-888 back-illuminated EMCCD camera¹⁰. It was Peltier-cooled to -60°C before experiments were run. The Andor Solis software was used to control the camera and spectrograph. The quantum efficiency of the camera is >90% for the wavelengths investigated. The exposure interval on the camera is inversely proportional to the frame rate of detection and can be set to a wide range of values (1 μ s to 1 s). For the experiments presented in this thesis, it was set to 10 μ s, as shown in Fig. 4.13a. Nevertheless, the camera was only exposed to light during the opening interval of the intensifier gate (700 ns). The camera was run in kinetic acquisition mode with an external trigger given from the laser. The number of accumulations was set to 1. The kinetic series length (which determines the number of shots collected) was varied depending on the experiment. However, for series lengths above 2250 (1.5 s of data for 1.5 kHz acquisition) the camera began to suffer from broadband saturation and signal drift (see §4.3.6). The output amplifier of the camera was set to electron multiplying, however the EM gain was not used during these experiments. The chip was set to frame transfer (optically centered ROI), with crop mode (1024(W) \times 32(H)) and a binning of 16 \times 16, which allowed for a frequency of detection of 1.5 kHz. A background and reference image was taken before collecting signal. The single-shot Raman counts data was saved in ASCII format.

A 4-channel Teledyne LeCroy 6104A High Definition oscilloscope was used to record the trigger signals to the intensifier, the camera, and the energy-saving circuit (see §4.2.4), as well as the output signal from the photodiode array (PDA) detector. These were saved as LeCroy trace files and post-processed using the ReadLeCroyBinaryWaveform MATLAB function. The oscilloscope was controlled using the TeleDyne LeCroy Wave Studio where the sampling was set to sequential mode. Each shot (or segment) recorded 2.5 kS (kilo samples) at a rate of 8 ns per sample, capturing 20 μ s of data per shot.

4.3.3 Data processing

The single-shot signal is represented by the raw Raman counts C_{raw} . The laser beam energy fluctuates from shot to shot, so it is necessary to normalise the raw counts by the corresponding total energy E of the two overlapping laser pulses. This yields the energy-normalised counts C with units of counts per joule ($\# \text{ J}^{-1}$). The averaged counts \bar{C} for the total number of shots N_s can then be calculated:

$$\bar{C}(\Delta\tilde{\nu}) = \frac{1}{N_s} \sum_{i=1}^{N_s} C_i(t, \Delta\tilde{\nu}), \quad (4.8)$$

where

$$C_i(t, \Delta\tilde{\nu}) = \frac{C_{\text{raw},i}(t, \Delta\tilde{\nu})}{E_i(t)} \quad \text{for} \quad 1 \leq i \leq N_s, \quad (4.9)$$

where t is time and $\Delta\tilde{\nu}$ is the Raman shift, which is reported in wavenumbers and has units of cm^{-1} . It is calculated using:

$$\Delta\tilde{\nu} = \left(\frac{1}{\lambda_p} - \frac{1}{\lambda} \right) \times 10^7, \quad (4.10)$$

where $\lambda_p = 527 \text{ nm}$ is the excitation wavelength and λ is the Raman spectral wavelength in nm.

A PDA detector was used to monitor the time-history and magnitude of the two pulses for every shot. The average pulse shape is shown in Figs. 4.13a and 4.20. A quantitative measurement of the energy per shot is needed. As such, the mean integral $\bar{\mathcal{V}}$ of the PDA signal V is firstly computed:

$$\bar{\mathcal{V}} = \frac{1}{N_s} \sum_{i=1}^{N_s} \mathcal{V}_i = \frac{1}{N_s} \sum_{i=1}^{N_s} \int_{t_0}^{t_f} V_i(t) dt, \quad (4.11)$$

where t_0 and t_f are the start and finish times for each shot, respectively. The mean PDA integral $\bar{\mathcal{V}}$ is then equated to the total output energy of the laser at 1.5 kHz, $\hat{E} = 38 \text{ mJ}^5$ to calibrate each shot:

$$E_i(t) = \hat{E} \frac{\mathcal{V}_i}{\bar{\mathcal{V}}}, \quad \text{for} \quad 1 \leq i \leq N_s, \quad (4.12)$$

where the standard deviation of E_i is measured to be approximately 2.5–5% of the mean energy \hat{E} (i.e. $\pm 1\text{--}2 \text{ mJ}$).

⁵This was the recorded value for a test at the 65% laser power setting¹⁹⁵. The laser was used at 70% for all experiments presented in this thesis; the difference in energies is assumed to be negligible.

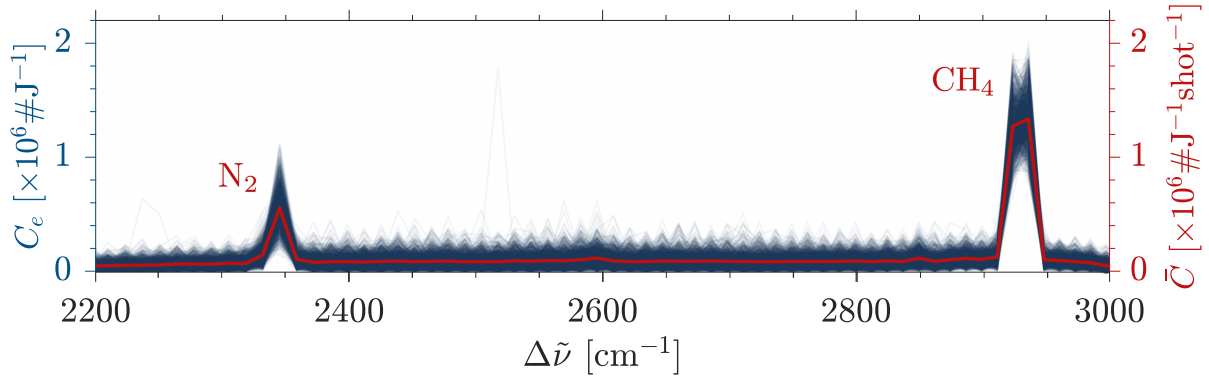


Fig. 4.14 Energy-normalised counts C (—) and averaged counts \bar{C} (—). Case presented is for a methane–air mixture ($Y_{\text{CH}_4} = 20\%$) where $N_s = 1450$ shots, $G = 55\%$, and $\bar{p} = 101,325$ Pa.

Figure 4.14 shows the energy-normalised counts C and averaged counts \bar{C} for a calibration case. In this thesis, the spontaneous Raman scattering results are presented only as the Stokes spectrum (i.e. positive Raman shifts).

The background signal $\bar{C}_B(\Delta\tilde{\nu})$ is then estimated. This broadband background signal, shown in Fig. 4.15, is caused by CCD camera noise sources (e.g. dark current, photon shot noise and readout noise²⁴⁰) and intensified luminescence (fluorescence and phosphorescence) from the cylindrical quartz tube (SiO_2)^{117,250,298} (a comparison is made of Raman results with and without quartz in §4.3.4). The background subtraction is done by fitting a linear polynomial function to the $\bar{C}(\Delta\tilde{\nu})$ signal³³. A background-subtracted signal $\bar{C}_{S'}(\Delta\tilde{\nu})$ can be obtained by subtracting $\bar{C}_B(\Delta\tilde{\nu})$ from the total signal $\bar{C}_S(\Delta\tilde{\nu})$, such that $\bar{C}_{S'}(\Delta\tilde{\nu}) = \bar{C}_S(\Delta\tilde{\nu}) - \bar{C}_B(\Delta\tilde{\nu})$. This procedure is demonstrated visually in Fig. 4.15.

We then integrate these variables to obtain the integrated counts $\bar{\bar{C}}$. For the background-subtracted signal and for the background signal, respectively:

$$\bar{\bar{C}}_{S'} = \int_{\Delta\tilde{\nu}_1}^{\Delta\tilde{\nu}_2} \bar{C}_{S'}(\Delta\tilde{\nu}) d\Delta\tilde{\nu}, \quad \bar{\bar{C}}_B = \int_{\Delta\tilde{\nu}_1}^{\Delta\tilde{\nu}_2} \bar{C}_B(\Delta\tilde{\nu}) d\Delta\tilde{\nu}, \quad (4.13a-b)$$

where $\Delta\tilde{\nu}_1$ and $\Delta\tilde{\nu}_2$ are the bounding wavenumbers for the respective molecules' peaks. These values are dependent on the spectrograph's diffraction grating. For the experiments presented here, $\Delta\tilde{\nu}_1(\text{N}_2) = 2319 \text{ cm}^{-1}$, $\Delta\tilde{\nu}_2(\text{N}_2) = 2372 \text{ cm}^{-1}$ (mode width of 53 cm^{-1}), $\Delta\tilde{\nu}_1(\text{CH}_4) = 2898 \text{ cm}^{-1}$ and $\Delta\tilde{\nu}_2(\text{CH}_4) = 2947 \text{ cm}^{-1}$ (mode width of 49 cm^{-1}). This is in agreement with published data (within the limitations of the setup's wavenumber resolution)^{57,91,125}. Variability of the Stokes mode half-widths $\delta\tilde{\nu}_S$ and Raman shifts $\Delta\tilde{\nu}_S$

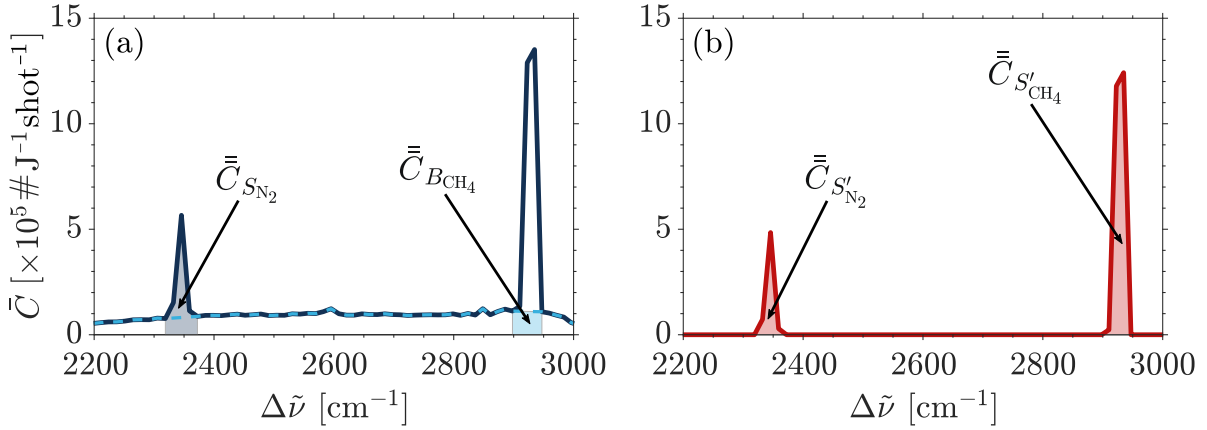


Fig. 4.15 (a) Averaged counts for the full signal (\bar{C}_S —) and for the fitted background signal (\bar{C}_B ---); (b) background-subtracted averaged counts ($\bar{C}_{S'}$ —) and integrated counts ($\bar{C}_{S'_{\text{N}_2}}$ and $\bar{C}_{S'_{\text{CH}_4}}$) for the two molecules of interest. Case presented is for a methane-air mixture ($Y_{\text{CH}_4} = 20\%$) where $N_s = 1450$ shots, $G = 55\%$, and $\bar{p} = 101,325$ Pa.

of both molecules due to changes in mean pressure^{71,159,337} or concentrations^{256,257} are assumed to be negligible.

4.3.4 Potential factors affecting the Raman signal

We characterise the signal-to-background ratio (SBR) as the ratio of the averaged background-subtracted signal to the background signal, such that:

$$\text{SBR} = \frac{\bar{C}_{S'}}{\bar{C}_B} \quad (4.14)$$

A number of factors were studied to see how they would affect the measured Raman signal and/or SBR for each molecule. These studies are presented here.

Mass flow rate

The mass flow rate of air \bar{m} through the test section was varied between 0 and 10 g s^{-1} for three different intensifier gain values ($G = 40\%$, 50%, 60%). The tests were all conducted at atmospheric pressure.

The results are shown in Fig. 4.16. Some variation is seen in the data. This may be attributed to temperature changes which are unaccounted for. Indeed, the coefficient of variation σ/μ is approximately 2% for the intensifier gains investigated in this study. As a result, it is concluded that the signal is independent of mass flow rate \bar{m} .

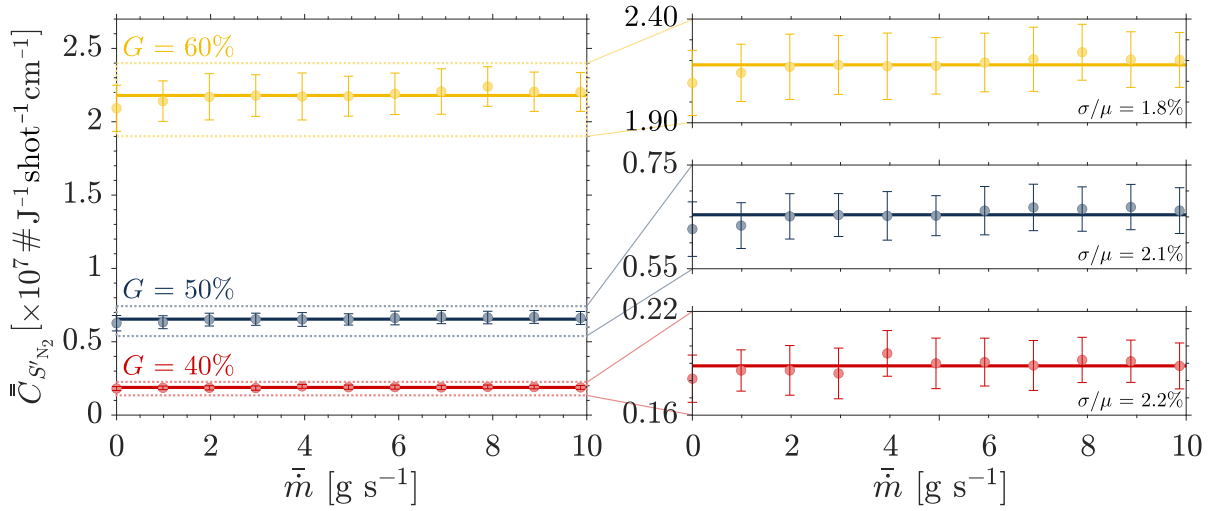


Fig. 4.16 Integrated counts for N_2 ($\bar{C}_{S'N_2}$) as a function of mean flow rate \bar{m} of air for different intensifier gains G (\bullet 40%, \bullet 50%, \bullet 60%) at $\bar{p} = 101,325$ Pa.

Mean pressure

The mass flow rate of air \bar{m} through the test section was varied between 0 and 10 g s^{-1} for three different intensifier gain values – but this time, with the nozzle connected to the end of the rig. As a result, the mean pressure was varied.

The results are shown in Fig. 4.17. For each gain, the integrated counts for the respective atmospheric pressure case are subtracted from the rest of the dataset yielding the atmospheric subtracted integrated counts $\bar{C}_{S'N_2}^{\text{atm}}$. This helps see the effect of pressure on the integrated counts. Since temperature and molar fraction are kept constant, an increase in pressure produces an increase in concentration. As per Eq. (4.7), this should lead to a linear increase in Raman intensity. As the experimental results in Fig. 4.17 show, this relationship is corroborated for nitrogen. No pressurised tests were run with methane.

Intensifier gain

The intensifier gain G was varied between 35% and 70%. As a result, its effect on the nitrogen and methane integrated counts can be studied directly. Figure 4.18 shows the results plotted for different methane mass fractions. Figure 4.18b shows that the methane signal saturates at approximately $\bar{C}_{S'CH_4} \simeq 4 \times 10^7 \# J^{-1} \text{shot}^{-1} \text{cm}^{-1}$. Since methane has a larger differential Raman scattering cross section $d\sigma/d\Omega$, its signal is found to always saturate before the nitrogen signal^{57,91}. Saturated data can be identified in Fig. 4.18 as points that deviate from the respective exponential fit. For particular

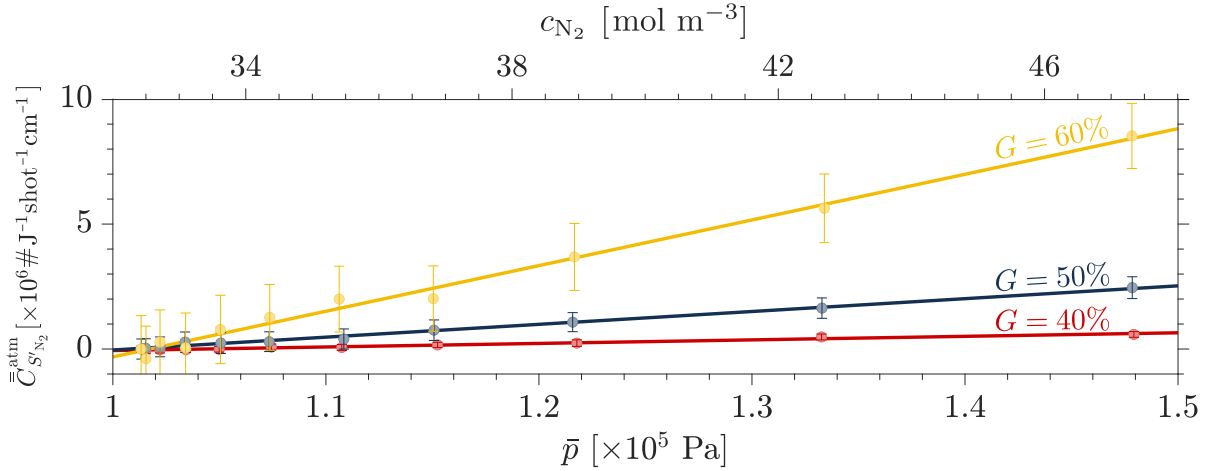


Fig. 4.17 Integrated counts with atmospheric value subtracted for N_2 ($\bar{C}_{S'_{N_2}}^{\text{atm}}$) as a function of mean pressure \bar{p} (bottom axis) and concentration (top axis) with linear fits for different intensifier gains G (● 40%, ● 50%, ● 60%) where the standard deviation is shown ($\pm 1\sigma$).

gains, the nitrogen and methane signals saturate at the same gain value. However, for the majority of gains, the nitrogen signal only shows saturation in the subsequent gain value (e.g. for $Y_i = 100\%$ methane, the methane signal saturates at $G = 50\%$, whereas the nitrogen signal saturates at $G = 55\%$). Since signals are expected to be low for the injection experiments, it is important to maximise gain, while at the same time ensuring saturation is avoided so that the results obtained are accurate. From this study, and since the expected mass fractions for the injection experiments are lower than 50% methane, we learn that the intensifier gain should be kept at 55 or lower to avoid camera saturation.

We now focus our attention on the cases where the camera does not saturate. An exponential relationship is found between gain and integrated counts. Owing to the nature of the intensifier's microchannel plates (MCPs) – of which the intensifier has two – this is the expected relationship. Each intensifier gain value has a corresponding voltage that is applied to each MCP. This voltage increases linearly with intensifier gain from 300 V to 1600 V for gains 1% to 100%²¹⁴. As a general rule, the mean pixel value doubles every time the applied voltage increases by 50 V (i.e. the electron output doubles), which explains the exponential nature of the results shown in Fig. 4.18.

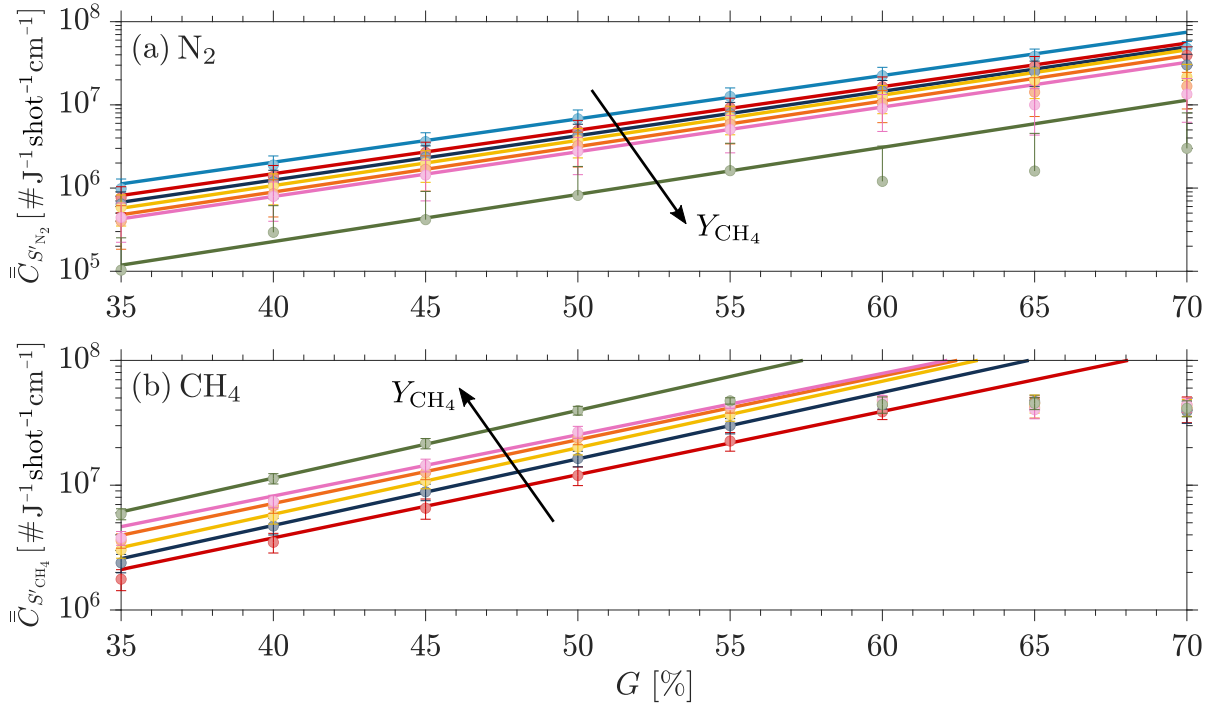


Fig. 4.18 Integrated counts for the two molecules of interest as a function of intensifier gain G : (a) N_2 ($\bar{C}_{S'_{\text{N}_2}}$) and (b) CH_4 ($\bar{C}_{S'_{\text{CH}_4}}$) with exponential fits for different methane mass fractions Y_{CH_4} (\bullet 0%, \bullet 10%, \bullet 20%, \bullet 30%, \bullet 40%, \bullet 50%, \bullet 100%). Data points which fall outside the exponential fits are caused by camera saturation.

Quartz tube luminescence

Measurements with and without the quartz tube were made in order to understand the effect that the presence of the quartz tube (positioned between the imaging lens and the probe volume) has on the signal. The averaged counts \bar{C} for both cases are shown in Figure 4.19. Without quartz, the nitrogen's $\text{SBR} = 14$. When the quartz is added, the background-subtracted integrated counts reduce by 9% and the SBR is reduced to 5. This is a significant reduction in signal-to-background ratio. Quartz luminescence (comprised of fast decay fluorescence and slow-decay phosphorescence) makes up the majority of the background signal (62%, for this particular case – although this is expected to vary depending on wavenumber, setup alignment, quartz curvature, quartz thickness, among other factors). Since the Stokes signal is spontaneous (i.e. does not need a resonant transition, interaction time $< 1 \text{ ps}^{250}$), whereas the luminescent signal is usually resonant and longer lived (emission times of at least $> 100 \text{ ps}^{250}$), the intensifier's exposure was selected as a compromise between maximising the Stokes signal and minimising the quartz luminescence. The remaining background noise signal (38%, for this particular

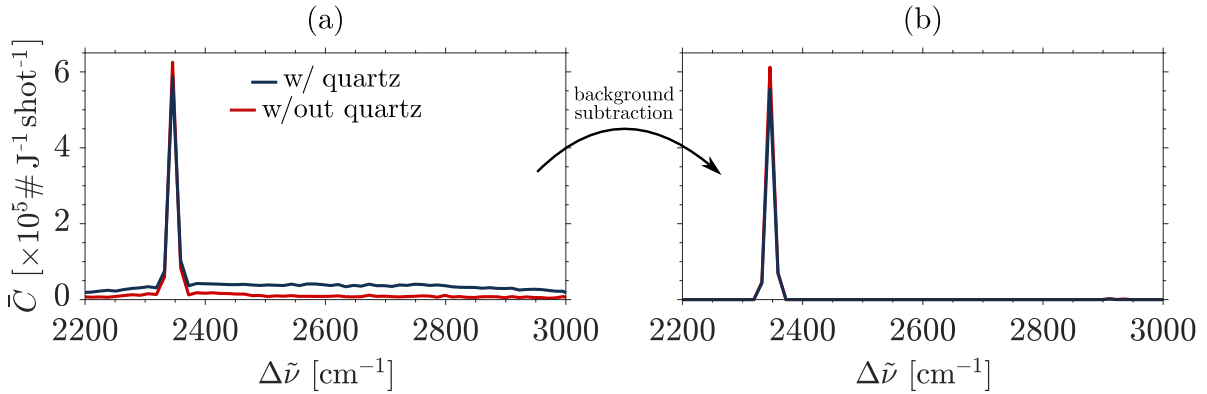


Fig. 4.19 Averaged counts for air flow with (—) and without (—) quartz where $N_s = 1450$ shots and $G = 55\%$: (a) full signals and (b) background-subtracted signals.

case) can be attributed to CCD camera noise sources (e.g. dark current, photon shot noise and readout noise²⁴⁰) as well as noise from other elements along the optical path.

Laser excitation: single-pulsed vs. dual-pulsed mode

The theoretical benefits of running a laser in dual-pulsed mode are clear: two pulses should provide double the excitation energy without the added cost of increased noise since the intensifier exposure is fixed at 700 ns (i.e. increased SBR).

The difference in pulse shapes is shown in Fig. 4.20. Although set to 0 μs , the time separation between the two pulses in dual-pulse mode is not nil as there are two peaks evident. From inspection, the time separation seems to be approximately 0.1 μs . The pulse duration and shape are expected to fluctuate due to temperature non-linearities across the crystal in the laser, as well as other effects such as room temperature and humidity.

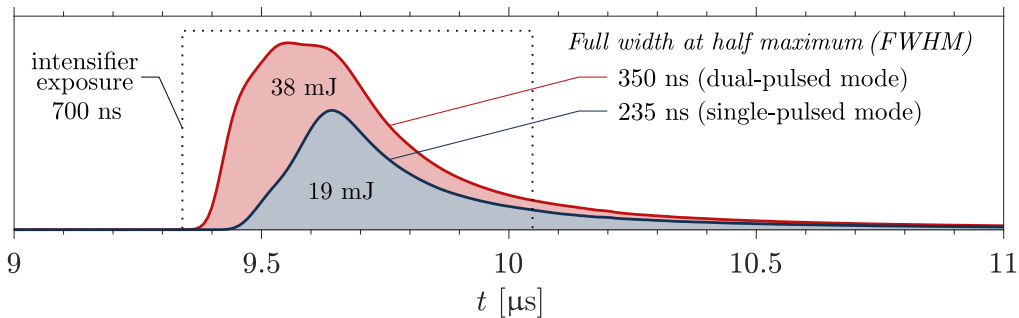


Fig. 4.20 Cycle-averaged laser pulses for single-pulsed and dual-pulsed mode excitation.

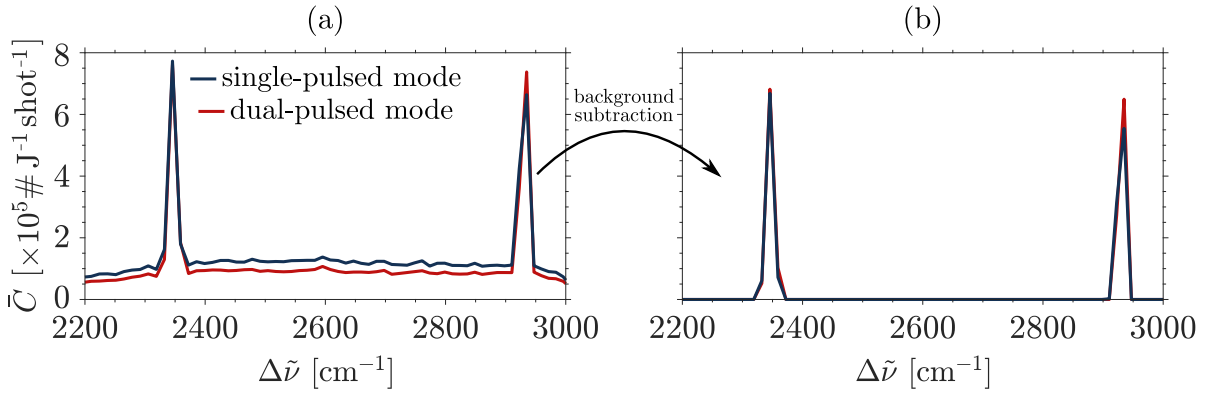


Fig. 4.21 Averaged counts for mean flow ($Y_{\text{CH}_4} = 10\%$) with laser in single-pulsed (—) and dual-pulsed mode (—) where $N_s = 1450$ shots and $G = 55\%$: (a) full signals and (b) background-subtracted signals.

Figure 4.21 shows the results for a 10% methane–air mixture with single-pulsed and double-pulsed excitation modes. The background-subtracted nitrogen $\bar{C}_{S'_{\text{N}_2}}$ and methane $\bar{C}_{S'_{\text{CH}_4}}$ signals remain about the same (an increase of 4% and 6%, respectively is seen). This is expected since the counts are normalised by energy. However, since the background noise is reduced using the dual-pulsed mode excitation, this translates to an increase in SBR of 31% for methane and 37% for nitrogen.

4.3.5 Calibration

For the injection test cases, and as outlined in §4.3.4, a fixed gain of $G = 55\%$ was used. As such, we take a close look at the behaviour of both molecules at this particular value⁶. The background-subtracted integrated counts $\bar{C}_{S'}$ are plotted as a function of concentration in Fig. 4.22 for constant, atmospheric pressure conditions.

The nitrogen signal follows a linear fit as per Eq. (4.7):

$$\bar{C}_{S'_{\text{N}_2}} = \beta c_{\text{N}_2} + \epsilon \quad (4.15)$$

where $\beta = 3.174 \times 10^5$ and $\epsilon = 1.292 \times 10^6$ are the gradient and y -intercept, respectively.

The methane signal follows a two-term exponential:

$$\bar{C}_{S'_{\text{CH}_2}} = \zeta_1 e^{\zeta_2 c_{\text{CH}_4}} + \zeta_3 e^{\zeta_4 c_{\text{CH}_4}} \quad (4.16)$$

⁶For a presentation of the full calibration dataset, see Appendix B.2.

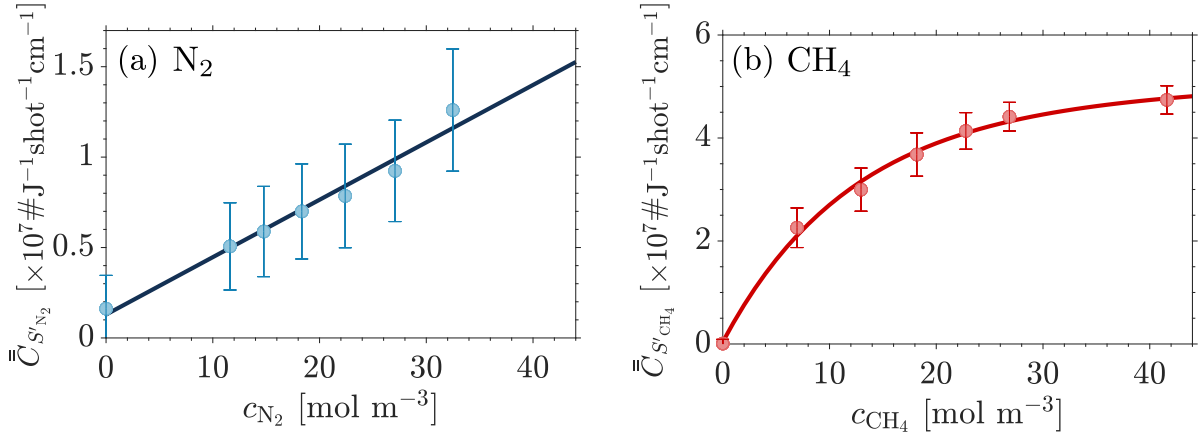


Fig. 4.22 Calibration curves for (a) N_2 and (b) CH_4 at $\bar{p} = 101,325$ Pa for $G = 55\%$.

where $\zeta_1 = -4.61 \times 10^7$, $\zeta_2 = -8.29 \times 10^{-2}$, $\zeta_3 = 4.65 \times 10^7$, and $\zeta_4 = 1.33 \times 10^{-3}$ are the model constants.

This is admittedly unexpected – as shown by Eq. (4.7), the signal should theoretically be linearly proportional to concentration. The reason for the deviation from the expected result may be caused by the poor wavenumber resolution. However, no cause has been confirmed. Nevertheless, it is possible to invert the equations describing the relationship between counts and concentration (i.e. Eqs. (4.15) and (4.16)), and on that basis, we can use the calibration curves to determine the corresponding concentrations.

4.3.6 Temporal resolution

As previously mentioned in §4.2, for the infrasound range frequency studies in §5, we use single pulse injection, whereas for the higher frequency studies in §6, we use pulse bursts. In order to obtain time-resolved measurements on a cycle-averaged basis, the single-shot results from multiple single pulse injections N_p or pulse bursts N_b are cycle-averaged:

$$\begin{aligned} \bar{C}_S^p(t, \Delta\tilde{\nu}) &= \frac{1}{N_p} \sum_{i=1}^{N_p} C_i(t, \Delta\tilde{\nu}) & \text{for } 1 \leq i \leq N_p, \\ \bar{C}_S^b(t, \Delta\tilde{\nu}) &= \frac{1}{N_b} \sum_{i=1}^{N_b} C_i(t, \Delta\tilde{\nu}) & \text{for } 1 \leq i \leq N_b, \end{aligned} \quad (4.17)$$

After this step, the background is removed using the procedure described in §4.3.5. The background-subtracted signal \hat{C}_S is then integrated (over the range of wavelengths relevant to the mode, $\Delta\nu_1$ to $\Delta\nu_2$) at every shot to obtain time-resolved, cycle-averaged

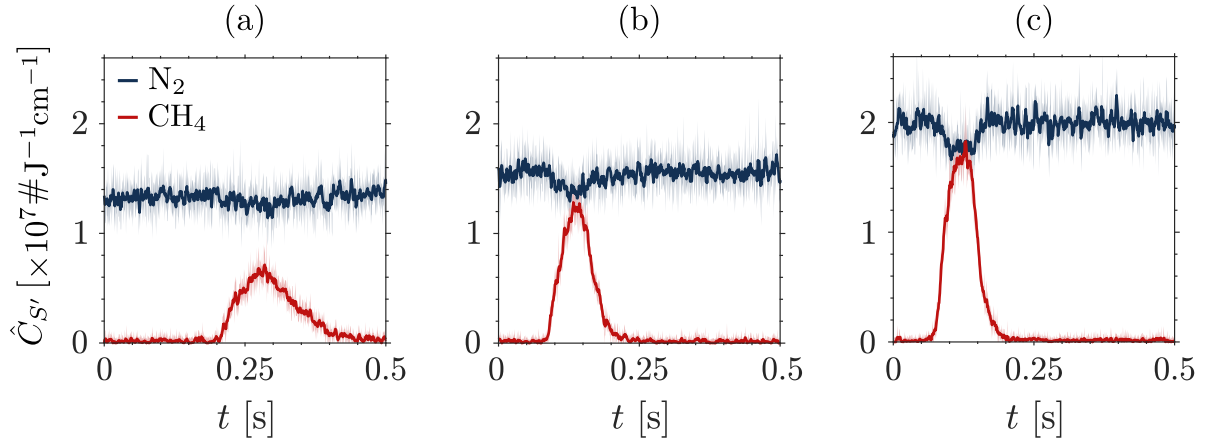


Fig. 4.23 Time-resolved, cycle-averaged integrated counts for N_2 (—) and CH_4 (—) due to a single pulse, co-flow injection of methane with air mass flow rate \bar{m} of (a) 2.5 g s^{-1} , (b) 6.5 g s^{-1} , and (c) 10.5 g s^{-1} (with nozzle termination). A five point moving average has been used and the standard error is shown ($\pm 1\sigma_{\bar{x}}$). Ten pulses ($N_p = 10$) have been averaged. Intensifier gain $G = 55\%$.

integrated counts:

$$\begin{aligned}\hat{C}_{S'}(t) &= \int_{\Delta\tilde{\nu}_1}^{\Delta\tilde{\nu}_2} \bar{C}_{S'}^p(t, \Delta\tilde{\nu}) d\Delta\tilde{\nu}, \\ \hat{C}_{S'}(t) &= \int_{\Delta\tilde{\nu}_1}^{\Delta\tilde{\nu}_2} \bar{C}_{S'}^b(t, \Delta\tilde{\nu}) d\Delta\tilde{\nu}.\end{aligned}\quad (4.18)$$

When N_p and N_b are large enough, the time-resolved, cycle-averaged integrated counts will approach the integrated counts obtained in §4.3.5 (i.e. $\hat{C}_{S'} \rightarrow \bar{C}_{S'}$).

Figure 4.23 shows the time-resolved signal due to the single pulse, co-flow injection of methane. The increase in signal amplitude with increasing mass flow rate is caused by the increase in mean upstream pressure (and, therefore, concentration – see §4.3.4) resulting from the losses across the nozzle discharge⁶³.

Limitation: broadband camera saturation

During preliminary experiments, it was found there was a drift in the camera background signal which limited the time that could be used. In order to assess how long experiments could be run for before the results were no longer valid, a study was run for a 9% methane–air mixture. Figure 4.24a shows the energy-normalised counts C as a function of Raman shift and time. After some time, the background starts to increase unevenly across the wavenumber spectrum such that as $t \rightarrow \infty$, we see that $SBR \rightarrow 0$. This is a broadband effect that starts in the lower and higher wavenumbers.

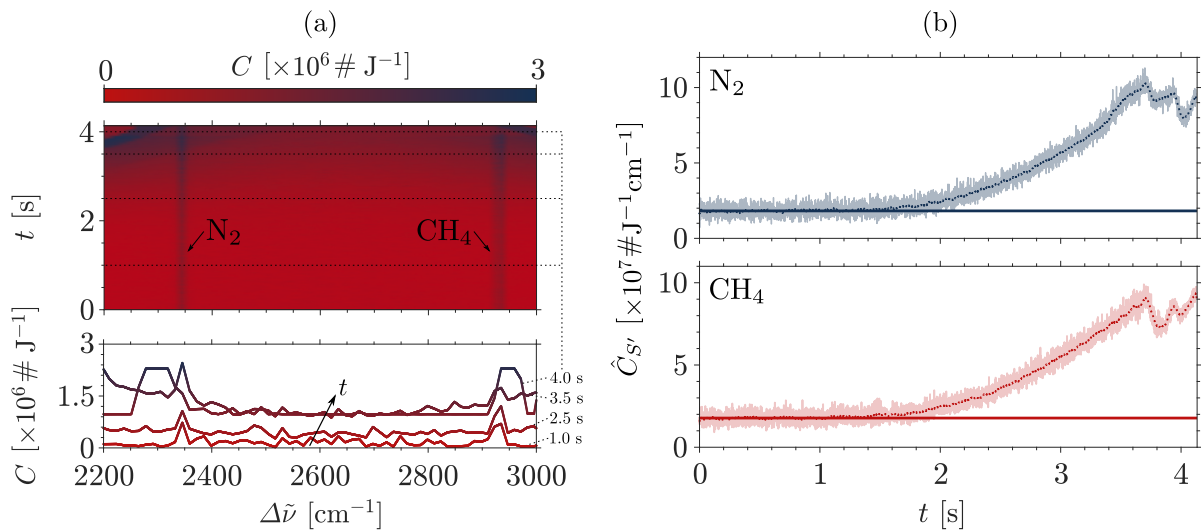


Fig. 4.24 For a 9% methane-air mixture: (a) energy-normalised counts C as a function of time and wavenumber; (b) time-resolved integrated counts for N_2 ($\hat{C}_{S'_{\text{N}_2}}$) and CH_4 ($\hat{C}_{S'_{\text{CH}_4}}$) as a function of time.

During preliminary experiments, it was found there was a drift in the camera background signal which limited the time that could be used. In order to assess how long experiments could be run for before the results were no longer valid, a study was run for a 9% methane-air mixture. Figure 4.24a shows the energy-normalised counts C as a function of Raman shift and time. After some time, the background starts to increase unevenly across the wavenumber spectrum such that as $t \rightarrow \infty$, we see that $\text{SBR} \rightarrow 0$. This is a broadband effect, but is more pronounced in the lower and higher wavenumbers.

The time-resolved integrated counts $\hat{C}_{S'}$ presented in Fig. 4.24b show the effect this has on the accuracy of the measurement of both the nitrogen and methane signals. The difference between the mean expected signal and the 50 point moving average for both molecules deviates past $1/2\sigma_{\hat{C}_{S'}}$ around 1.1 seconds. Within 4 seconds, the signal increases by an order of magnitude.

The reason for this drift is not fully understood. Potential causes include the camera sensor heating up and causing some glow. However, this is usually only expected for signal durations on the order of minutes. Another hypothesis is that scattered light falling above the cropped region eventually clocked down and became background for the acquisitions¹⁸⁶.

From this exercise, we learn that the maximum time interval that can be used for data collection is 1 second.

4.3.7 Translation to compositional wave amplitude

In order to apply the spontaneous Raman measurements to the acoustic objectives of the project, the measured time-resolved integrated counts $\hat{C}_{S'}(t)$ need to be converted to a compositional wave amplitude ξ (i.e. methane mass fraction Y_{CH_4} , as defined by Eq. (2.41)).

From a physical standpoint, we know that the sum of the mole fractions should be unity (i.e. $X_{\text{air}} + X_{\text{CH}_4} = 1$) at all times. This, however, was not the case. Since the calibration experiments were performed a month prior to the injection experiments, the straying of the result from the expected total is hypothesised to have been caused by a couple of reasons. Firstly, due to deviation of the optics and quartz tube from the original alignment used during the calibration process. Secondly, due to the deterioration of the quartz glass due to the repetitive, high energy pulse beams (i.e. etching effects). For simplicity, we assume that the two species are affected in the same way. The injection results are scaled appropriately while staying true to the proportionalities described by Eqs. (4.15) and (4.16).

At certain times in the signal, we know the concentration of nitrogen in the system based on the molar fraction and measured pressure. For example, after 0.6 seconds in Fig. 4.23, we know that the compositional spot has convected through the probe volume. As such, the following procedure is used to evaluate the new nitrogen and methane concentrations curves for each injection case:

1. Calculate concentration of nitrogen when methane is not present in the mean flow: $c_{\text{N}_2} = X_{\text{N}_2} \bar{p} / \mathcal{R}_u \bar{T}$ (since there is only air, $X_{\text{N}_2} = 0.78$).
2. Use Eq. (4.15) to compute what the expected counts from the original calibration \hat{C}_{cal} would be for that concentration of nitrogen.
3. Compute the correction factor $r = \hat{C}_{\text{new}} / \hat{C}_{\text{cal}}$, which is the ratio between the new counts measured in the injection experiments \hat{C}_{new} and the expected calibration counts \hat{C}_{cal} , as shown in Fig. 4.25a.
4. Generate a corrected linear fit for nitrogen for each injection case (we explicitly assume nitrogen will always have a linear relationship between concentration and counts for a fixed gain).
5. The correction factor r is assumed to be the same for methane and is applied to the methane calibration curve, as shown in Fig. 4.25b.

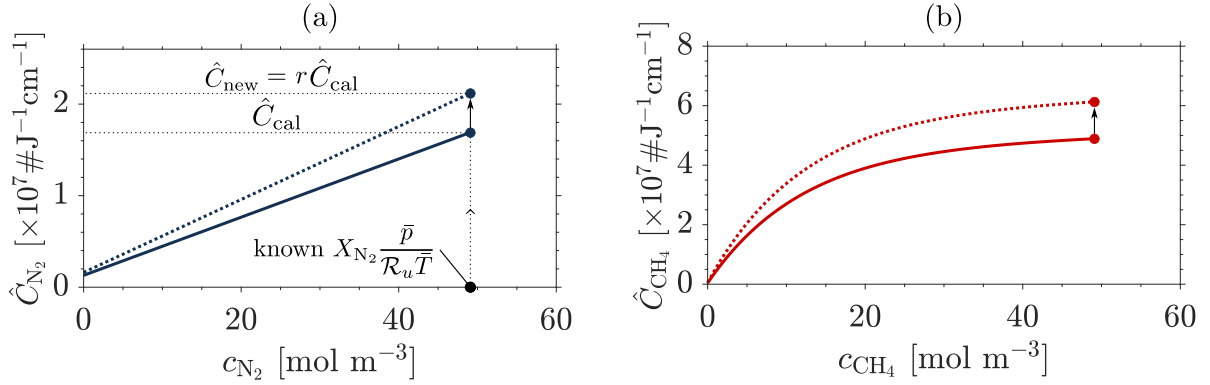


Fig. 4.25 Original calibration curve (—) and corrected calibration curve scaled by r (.....) for N_2 (—) and CH_4 (—).

After obtaining the corrected calibration curves, the time-resolved concentrations can be extracted from the time-resolved integrated counts. From each independent curve, we obtain the molar fractions for nitrogen and methane:

$$X_i = c_i \frac{\mathcal{R}_u \bar{T}}{\bar{p}}, \quad (4.19)$$

From this, we can calculate the oxygen and air mole fractions, respectively:

$$\begin{aligned} X_{O_2} &= \frac{0.22}{0.78} X_{N_2}, \\ X_{\text{air}} &= X_{N_2} + X_{O_2}, \end{aligned} \quad (4.20)$$

where the contributions of minor components in dry air (i.e. argon, carbon dioxide, etc.) are included in the O_2 estimate for simplicity. Two results for different injection locations are presented in Fig. 4.26a-b. The total mole fraction does not always add up to unity. This is likely due to associated measurement errors as well as the assumption made in step 5 of the method used to find the new calibration curve (i.e. methane may be affected differently to nitrogen).

Finally, to compute the respective mass fractions:

$$\begin{aligned} \xi = Y_{CH_4} &= \frac{X_{CH_4} W_{CH_4}}{X_{CH_4} W_{CH_4} + X_{\text{air}} W_{\text{air}}}, \\ Y_{\text{air}} &= \frac{X_{\text{air}} W_{\text{air}}}{X_{CH_4} W_{CH_4} + X_{\text{air}} W_{\text{air}}}, \end{aligned} \quad (4.21)$$

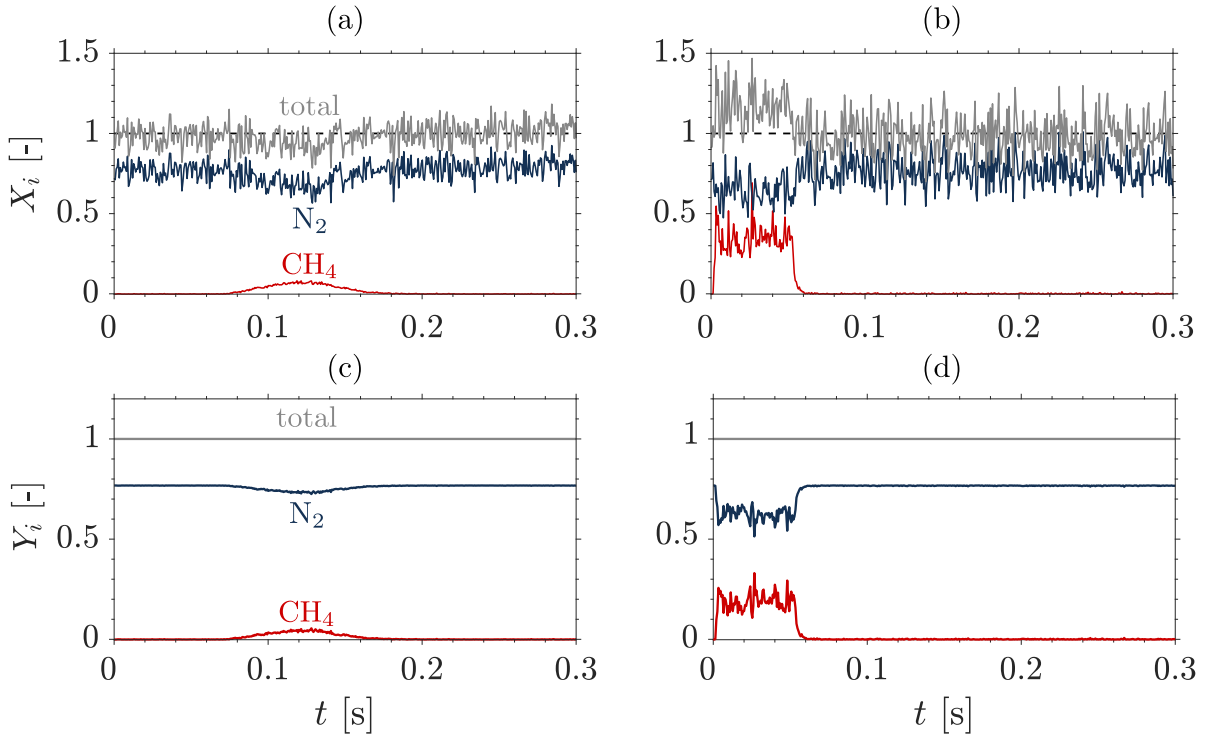


Fig. 4.26 Mole X and mass Y fractions for measured (— N_2 , — CH_4) and inferred total (—) due to a single pulse, co-flow injection of methane with air mean flow rate \bar{m} of 11 g s^{-1} for (a) far and (b) close injection locations. Expected total (---) is also included. Ten pulses ($N_p = 10$) have been averaged. Intensifier gain $G = 55\%$.

and

$$\begin{aligned} Y_{O_2} &= 0.23Y_{\text{air}}, \\ Y_{N_2} &= 0.77Y_{\text{air}}. \end{aligned} \quad (4.22)$$

The resulting mass fractions for the co-flow injection of methane at three different mean air mass flow rates are shown in Fig. 4.26c-d.

4.4 Summary

This chapter presented a new model thermoacoustic setup called the Canonical Wave Rig (CWR). The various modules of the system were described and the mean flow properties across the investigated flow regime (subsonic to sonic nozzle flow conditions) were calculated. The canonical waves generated by the CWR can be controlled by choosing the gas that is injected into a low Mach number mean flow of air. Air injection generates acoustic perturbations, while methane injection generates acoustic, entropic, and compositional perturbations. A symmetric injection profile is ensured through the

use of a centreline co-flow injection system. Injection frequencies for the high-speed valve can be controlled by using an energy-saving circuit. As a result, the convergent-divergent nozzle can be forced at a range of controllable frequencies.

Methane was selected as the perturbation gas for three reasons. Firstly, it has a large entropic-compositional coupling term $\Delta s/\bar{c}_p$ which lends itself to the generation of indirect noise. Secondly, the CWR is used in tandem with a spontaneous Raman spectroscopy system in phase-locked mode (i.e. pressure and Raman measurements are acquired simultaneously). Methane has a large differential Raman scattering cross-section $d\sigma/d\Omega$ which is favourable for the maximisation of the Stokes Raman signal. Thirdly and lastly, the Raman shift of methane is near that of nitrogen which means we can track both molecules concurrently.

Potential factors affecting the Raman measurement were investigated, namely mass flow rate, mean pressure, intensifier gain, quartz tube luminescence, and laser excitation mode. Lastly, calibration curves were obtained: a linear dependence between concentration and counts was identified for nitrogen, whereas a non-linear dependence was identified for methane. The calibration curves can be inverted and a method of extracting time-resolved measurements of local species concentration at 1.5 kHz was presented.

Chapter 5

Direct & indirect noise experiments I: single pulse injection

THE low-frequency (infrasound), single pulse, co-flow injection of air or methane into a low Mach number mean flow of air is presented. Experiments are carried out using the CWR – subsonic and sonic (choked) conditions are investigated for a convergent-divergent nozzle. Two convective lengths are considered in order to study the effect of compositional wave dispersion on indirect noise. Acoustic measurements are made for systems with reverberating and non-reverberating upstream chambers. Spontaneous Raman spectroscopy measurements of the local concentration upstream of the nozzle are made for the case of the reverberating upstream chamber. Acoustic and compositional measurements are used to compute upstream and downstream indirect noise nozzle transfer functions. This chapter serves as validation of the phase-locked measurement of acoustic and compositional waves.

5.1 Motivation and objectives

Since Marble and Candel²¹³ derived the entropic indirect noise transfer functions π_i^\pm/σ for compact isentropic nozzles, their validation has been a major source of interest for experimentalists^{16,62}. Recently, Magri et al.²⁰⁷ derived transfer functions π_i^\pm/ξ to incorporate the effects of compositional noise. Their theory was then extended to non-isentropic nozzles by Rolland²⁷⁸. Soon after, De Domenico et al.⁶⁴ used a model setup to provide the first experimental dataset for validation of the analytical model. Of particular relevance to the experimental estimate of indirect noise transfer functions π_i^\pm/ξ and π_i^\pm/σ are two variables: the indirect noise wave amplitudes (π_i^\pm) and the source term amplitude (ξ or σ). Dowling and Mahmoudi⁶⁸ outlined three guiding principles for experiments aimed at comprehensively studying the indirect noise problem. Adapted, they read:

1. the acoustic boundary conditions of the system must be known,
2. separation of different effects must be done by controlling and independently introducing acoustic π , entropic σ , compositional ξ , or vortical Ω waves,
3. the entropic σ , compositional ξ , or vortical Ω disturbances must be measured.

In the study by De Domenico et al.⁶⁴, it was assumed that ξ was equal to the injection mass fraction $Y_i = \dot{m}_i/\bar{m}$, defined as the ratio of the injected flow rate \dot{m}_i (measured by a mass flow meter) and the mass flow rate of air \bar{m} . In other words, a measurement of the local concentration upstream of the nozzle was not made. Moreover, π_i^\pm were computed by removing the effects of reverberation from the pressure signal²⁸⁰. Using this methodology, De Domenico et al.⁶⁴ obtained fair agreement with the non-isentropic model. However, some discrepancies were noted and attributed to non-compact, non-linear, and dissipation and dispersion effects.

In this chapter, we provide a new experimental dataset for validation purposes using a different methodology to the one employed by De Domenico et al.⁶⁴. In particular, the three points outlined by Dowling and Mahmoudi⁶⁸ are considered and the quantities of interest (π_i^\pm and ξ) are directly measured. Firstly, the acoustic boundary conditions of the system are characterised. Secondly, by injecting air or methane, the types of disturbances generated are controlled. Moreover, using the pseudo-anechoic tube presented in §4.2.3 allows for the direct measurement of π_i^\pm . These are contrasted with dereverberated signals. Thirdly, and lastly, the local concentration (i.e. ξ) is measured using spontaneous Raman spectroscopy. This work serves as validation of the phase-locked acoustic and compositional wave measurement technique introduced in §4. Since the injection is done in the infrasound frequency range (i.e. < 1 Hz), these experiments are considered to be in the compact limit (i.e. $He \approx 0$).

5.2 Test cases

In order to investigate the effect of varying mean flow properties on the direct and indirect noise generated by the co-flow injection of air or methane, 18 air mass flow rate \bar{m} conditions were run: from 2.5 to 11 g s⁻¹ in 0.5 g s⁻¹ increments. In particular, this allows us to study how the upstream mean pressure \bar{p}_1 (102–153 kPa), throat Mach number \bar{M}_t (0.2–1.0), upstream bulk velocity \bar{u}_1 (1.6–4.8 m s⁻¹), and Reynolds number Re (4300–19,100) influence the acoustic generation and compositional wave convection processes in the CWR. The pulse has a duration of $t_p = 50$ ms, with an injection mass fraction $Y_i = \dot{m}_i/\bar{m} = 10\%$. As per previous studies^{64,277,278}, and as described in §4.2.4, this is estimated based on the dynamic mass flow meter measurement \dot{m}_i upstream of the injection valve (see Fig. 4.7). Table 5.1 summarises the test conditions.

Table 5.1 Experimental test conditions: primary mass flow rate \bar{m} , approximate bulk throat Mach number \bar{M}_t , injected mass flow rate of methane \dot{m}_i , estimated methane bulk injection velocity \bar{u}_{i,CH_4} , upstream mean pressure \bar{p}_1 , upstream Mach number \bar{M}_1 , downstream mean pressure \bar{p}_2 , downstream Mach number \bar{M}_2 , upstream bulk flow velocity \bar{u}_1 , and upstream Reynolds number Re .

Case	\bar{m} [g s ⁻¹]	\bar{M}_t [-]	\dot{m}_i [g s ⁻¹]	\bar{u}_{i,CH_4} [m s ⁻¹]	\bar{p}_1 [kPa]	\bar{M}_1 [$\times 10^{-3}$]	\bar{p}_2 [kPa]	\bar{M}_2 [$\times 10^{-3}$]	\bar{u}_1 [m s ⁻¹]	Re [$\times 10^3$]
1	2.5	0.20	0.25	39	102.39	4.8	101.35	4.8	1.63	4.3
2	3.0	0.24	0.30	47	102.85	5.7	101.40	5.8	1.95	5.2
3	3.5	0.29	0.35	54	103.42	6.6	101.44	6.7	2.27	6.1
4	4.0	0.33	0.40	61	104.09	7.5	101.46	7.7	2.57	6.9
5	4.5	0.38	0.45	69	104.93	8.4	101.51	8.6	2.87	7.8
6	5.0	0.42	0.50	75	105.96	9.2	101.55	9.6	3.16	8.7
7	5.5	0.47	0.55	82	107.23	10.0	101.61	10.6	3.43	9.5
8	6.0	0.52	0.60	88	108.88	10.8	101.65	11.5	3.69	10.4
9	6.5	0.58	0.65	94	110.68	11.5	101.72	12.5	3.93	11.3
10	7.0	0.63	0.70	99	112.92	12.1	101.79	13.4	4.15	12.1
11	7.5	0.69	0.75	104	115.50	12.7	101.85	14.4	4.35	13.0
12	8.0	0.75	0.80	108	118.81	13.1	101.93	15.3	4.51	13.9
13	8.5	0.82	0.85	111	122.63	13.5	102.03	16.3	4.64	14.7
14	9.0	0.88	0.90	113	127.45	13.8	102.11	17.2	4.73	15.6
15	9.5	0.96	0.95	114	133.11	13.9	102.24	18.1	4.78	16.5
16	10.0	1.00	1.00	115	139.48	14.0	102.34	19.1	4.80	17.3
17	10.5	1.00	1.05	115	146.10	14.0	102.45	20.0	4.81	18.2
18	11.0	1.00	1.10	115	152.96	14.0	102.58	20.9	4.81	19.1

5.3 Non-reverberating system

5.3.1 Setup and methodology

Three variations of the CWR setup are employed as shown in Fig. 5.1, each using different permutations of pseudo-anechoic tubes. Their usage impedes the system from reverberating. The modular nature of the CWR allows for the direct measurement of the acoustic sources (direct noise π_d^\pm and indirect noise π_i^\pm waves) and the system's acoustic properties (attenuation α , as well as the inlet R_{i1} and outlet R_{o1} reflection coefficients).

Table 5.2 summarises the experimental setups and the respective acoustic measurements that are made with each one. Tests Air-A and CH₄-A are designed to directly measure the direct acoustic waves travelling upstream and downstream of the injection region for each gas (using injection location 2 – see Fig. 4.1). Tests Air-B employ the results from Air-A to compute the acoustic transmission T_{o1} and reflection R_{o1} coefficients of the nozzle. Tests CH₄-B then use the results from CH₄-A and Air-B to extract the upstream and downstream-travelling indirect noise waves π_i^\pm for two different injection

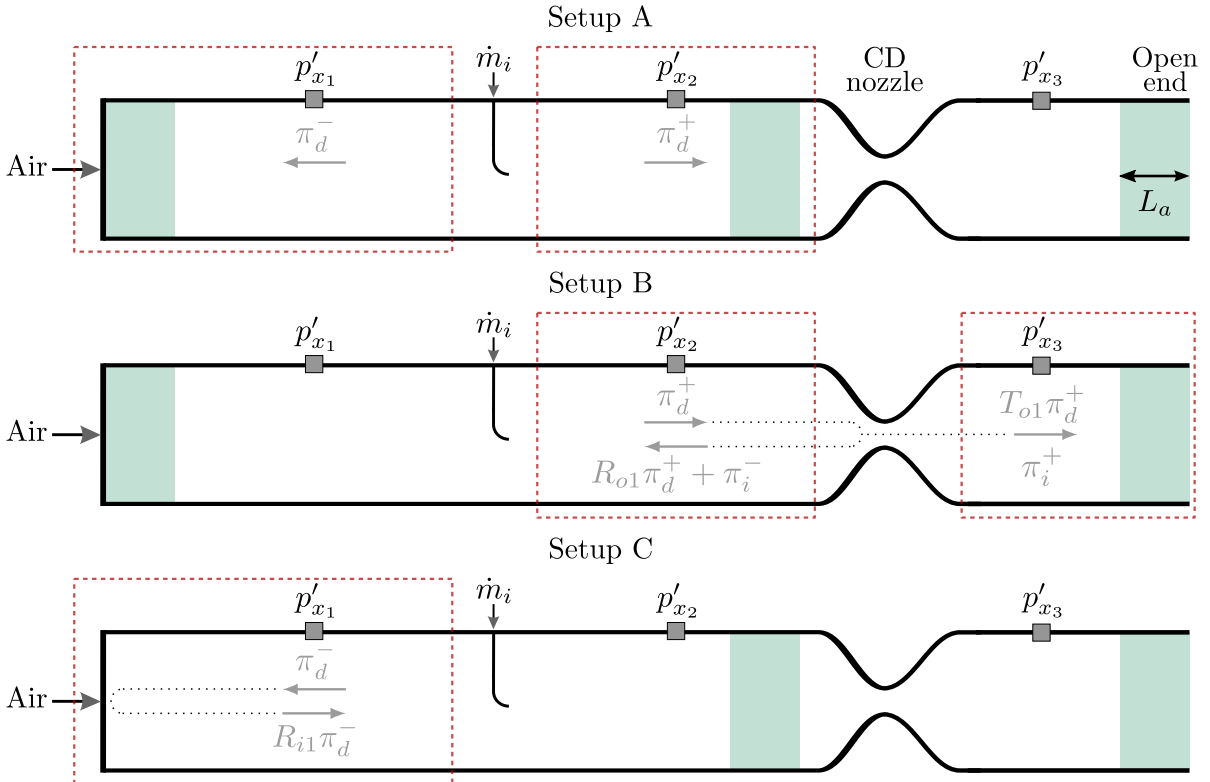


Fig. 5.1 Schematics of setups used for characterisation experiments. For the injection of air, $L_a = L_h$ (30 m) and for the injection of methane, $L_a = 2L_h$ (60 m).

Table 5.2 System and source characterisation test cases and measured variables. Each setup was used at every flow rate (18 cases, from 2.5 to 11 g s⁻¹ in 0.5 g s⁻¹ increments) for the co-flow injection of the two gases (air or methane). Methane experiments using setup B were run for two convective lengths (close and far injections – see Fig. 5.16).

Setup	Air		Methane	
A	π_d^+	$= \frac{p'_{x_2}}{\bar{\gamma}\bar{p}_1}$ (5.1)	π_d^+	$= \frac{p'_{x_2}}{\bar{\gamma}\bar{p}_1}$ (5.2)
	π_d^-	$= \frac{p'_{x_1}}{\bar{\gamma}\bar{p}_1}$ (5.3)	π_d^-	$= \frac{p'_{x_1}}{\bar{\gamma}\bar{p}_1}$ (5.4)
B	R_{o1}	$= \frac{p'_{x_2}}{\bar{\gamma}\bar{p}_1} \frac{1}{\pi_d^+} - 1$ (5.5)	π_i^+	$= \frac{p'_{x_3}}{\bar{\gamma}\bar{p}_2} - T_{o1}\pi_d^+$ (5.6)
	T_{o1}	$= \frac{p'_{x_3}}{\bar{\gamma}\bar{p}_2} \frac{1}{\pi_d^+}$ (5.7)	π_i^-	$= \frac{p'_{x_2}}{\bar{\gamma}\bar{p}_1} - \pi_d^+(1 + R_{o1})$ (5.8)
C	R_{i1}	$= \frac{p'_{x_1}}{\bar{\gamma}\bar{p}_1} \frac{1}{\pi_d^-} - 1$ (5.9)		
	α	$= -\frac{1}{\Delta x} \ln \left(\frac{\pi_{x+\Delta x}}{\pi_x} \right)$ (5.10)		

locations (close and far from the nozzle to study the effects of dispersion). Specifically, we identify injection location 1 as the *far* injection location ($L_c = 0.55$ m) and injection location 3 as the *close* injection location ($L_c = 0.11$ m) – see Fig. 5.16. Finally, tests Air-C employ the results from Air-A to extract the inlet reflection coefficient R_{i1} and the system's acoustic attenuation coefficient α . From hereon out, test cases are referred to as GAS-SETUP-TEST. For example, for the first test case of air injection using setup A, it would be referenced as Air-A-1, whereas for the last test case it would be Air-A-18 (tests go from 2.5 to 11 g s⁻¹ in 0.5 g s⁻¹ increments – see Table 5.1). The x -axis for the presented figures are normalised by the nozzle choking flow rate $\bar{m}_c = 10$ g s⁻¹.

The anechoic acquisition windows are 175 ms ($L_a = 30$ m) and 350 ms ($L_a = 60$ m) for the air and methane experiments, respectively. Over these long distances, the compositional waves are entirely dissipated before the end of the pseudo-anechoic tube, eliminating unwanted indirect noise contributions. The wave amplitudes are measured using three transducers. For the purposes of the experiments, the attenuation between the injection plane and the transducers is neglected. The signals presented are the result of an averaging of 100 pulses, followed by the filtering of the mains frequency (50 Hz) as well as frequencies above 400 Hz.

5.3.2 Direct noise waves

Figures 5.2 and 5.3 show the direct noise waves π_d^\pm for the co-flow injection of air and methane, respectively (i.e. tests Air-A-1 to Air-A-18 and CH₄-A-1 to CH₄-A-18) calculated using Eqs. (5.1)–(5.4). For both figures, (a) and (b) show the acquired time series for the upstream and downstream travelling direct noise waves, respectively. The ringing visible at the end of the pulse may be attributed to valve dynamics. The mean amplitude is computed across the π_d^+ and π_d^- pulses. These are plotted as a function of the normalised air mass flow rate \bar{m}/\bar{m}_c in (c), and their ratio is shown in (d). Both are plotted alongside the co-flow injection and cross-flow injection theory predictions presented in §2.2.3 assuming an injection mass fraction $Y_i = 0.10$ and injection diameter $d_i = 3.4$ mm (i.e. equal to the geometric diameter). The velocity ratio \bar{u}_i/\bar{u} (expressed by Eqs. (2.37) and (2.40)) is independent of flow rate and equal to 14 and 25 for air and

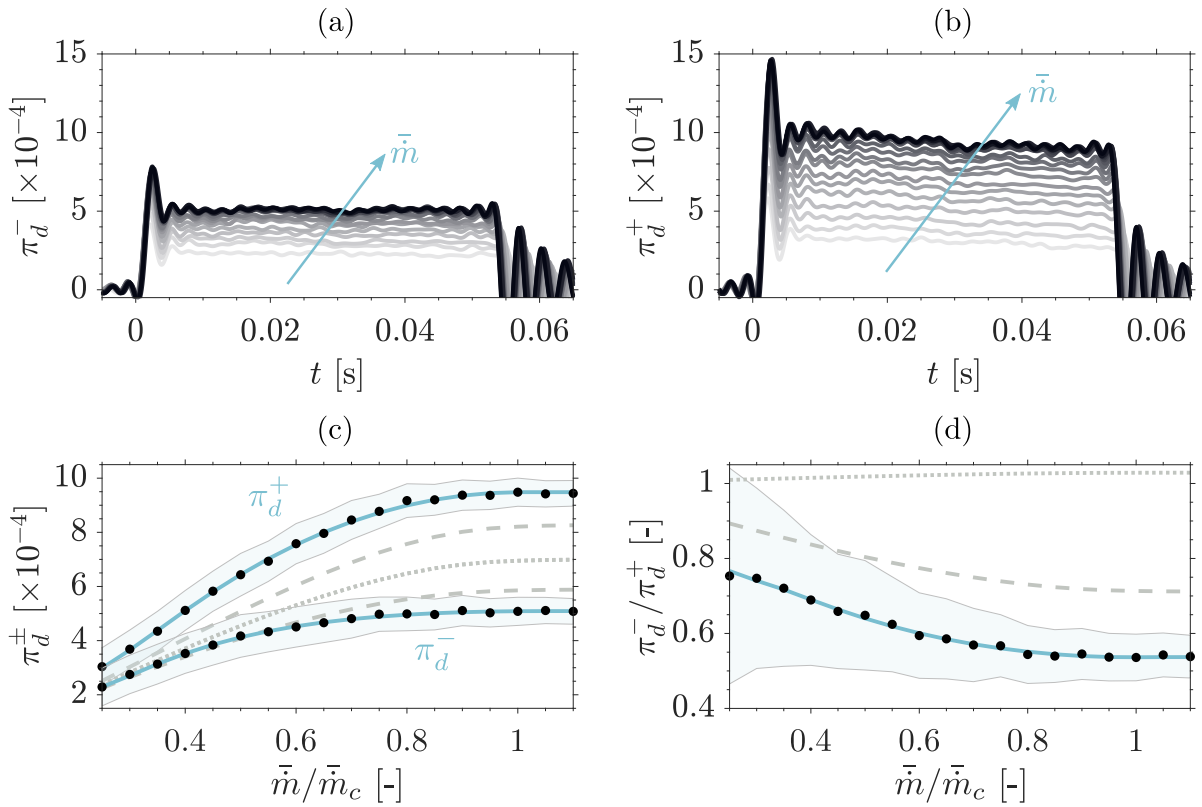


Fig. 5.2 Acoustic waves generated by the co-flow injection of air: (a) upstream-travelling direct noise waves π_d^- ; (b) downstream-travelling direct noise waves π_d^+ ; (c) mean perturbation amplitude from experiments (\bullet) with polynomial fit (—) and theoretical model predictions for co-flow injection (---) and cross-flow injection (.....) for both waves; (d) ratio of direct noise waves π_d^-/π_d^+ .

methane, respectively. The fit through the direct noise wave amplitudes was done using a polynomial function with a plateau for the last three cases.

The co-flow theory predictions for both gases show good qualitative agreement with the experimental data. The difference between co-flow injection and cross-flow injection is evident, particularly in the ratio π_d^-/π_d^+ . For most of the flow rates, however, the co-flow injection estimates fall outside of the standard deviation boundaries ($\pm 1\sigma$). This is not completely unexpected as there are some effects that may be important here which are not considered. Phenomena such as non-1D effects (e.g. vortex shedding) and turbulent jet noise are not accounted for. Additionally, as noted by Rolland et al.²⁷⁷, the injection process (deceleration and depressurisation of the methane gas) may drive indirect noise generation at the injection plane, such that the measured pressure could be an aggregate of direct and indirect noise contributions.

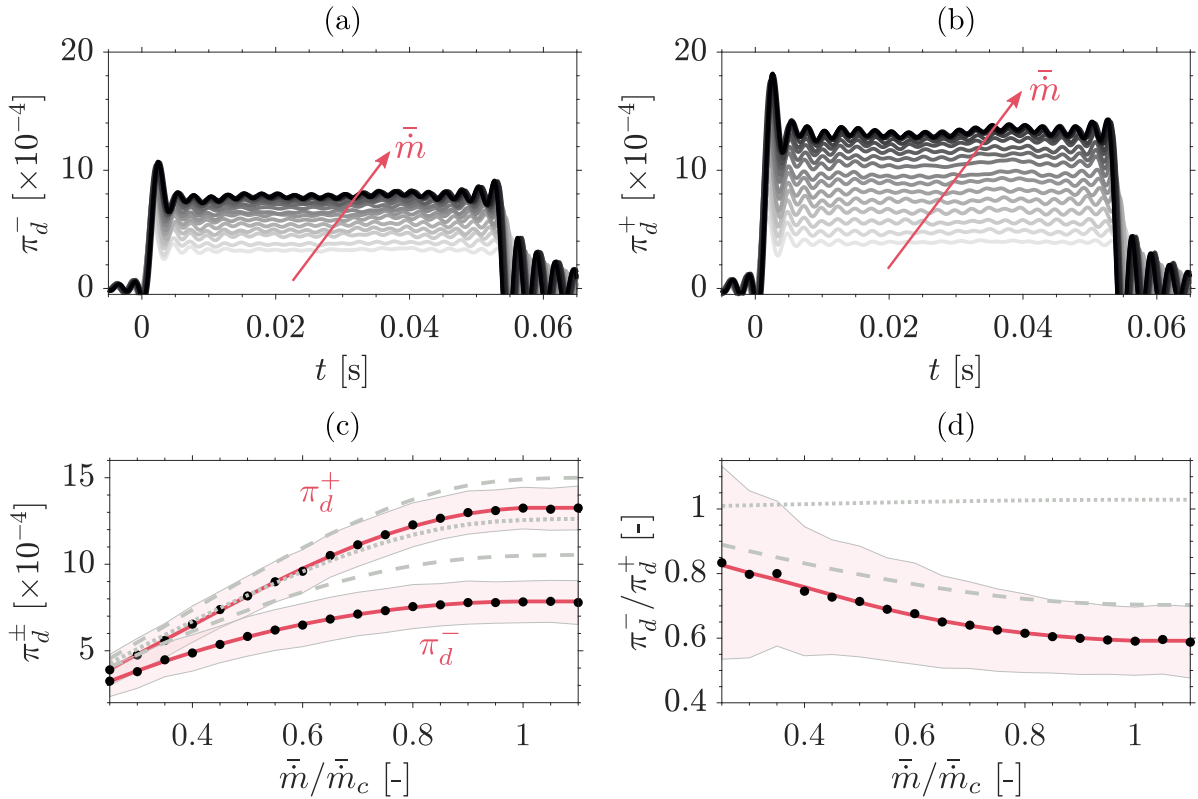


Fig. 5.3 Acoustic waves generated by the co-flow injection of methane: (a) upstream-travelling direct noise waves π_d^- ; (b) downstream-travelling direct noise waves π_d^+ ; (c) mean perturbation amplitude from experiments (\bullet) with polynomial fit (—) and theoretical model predictions for co-flow injection (---) and cross-flow injection (.....) for both waves; (d) ratio of direct noise waves π_d^-/π_d^+ .

Sensitivity study

We now explore the reason for the discrepancies between the model and experiments. This is done by considering the sensitivities of the model results to the uncertainties in the input values of the injected mass fraction Y_i and the effective diameter of the injection d_i . Firstly, as described in §4.2.4, the low sampling rate of the mass flow meter is a likely source of error and may lead to an injected mass fraction different to what is expected. Secondly, the effective injection diameter d_i : owing to the high injection flow velocities and short elbow geometry, the flow inside the injection tube could have a separation point, generating a recirculation zone and leading to an effective injection diameter that is smaller than the geometric diameter^{77,248}.

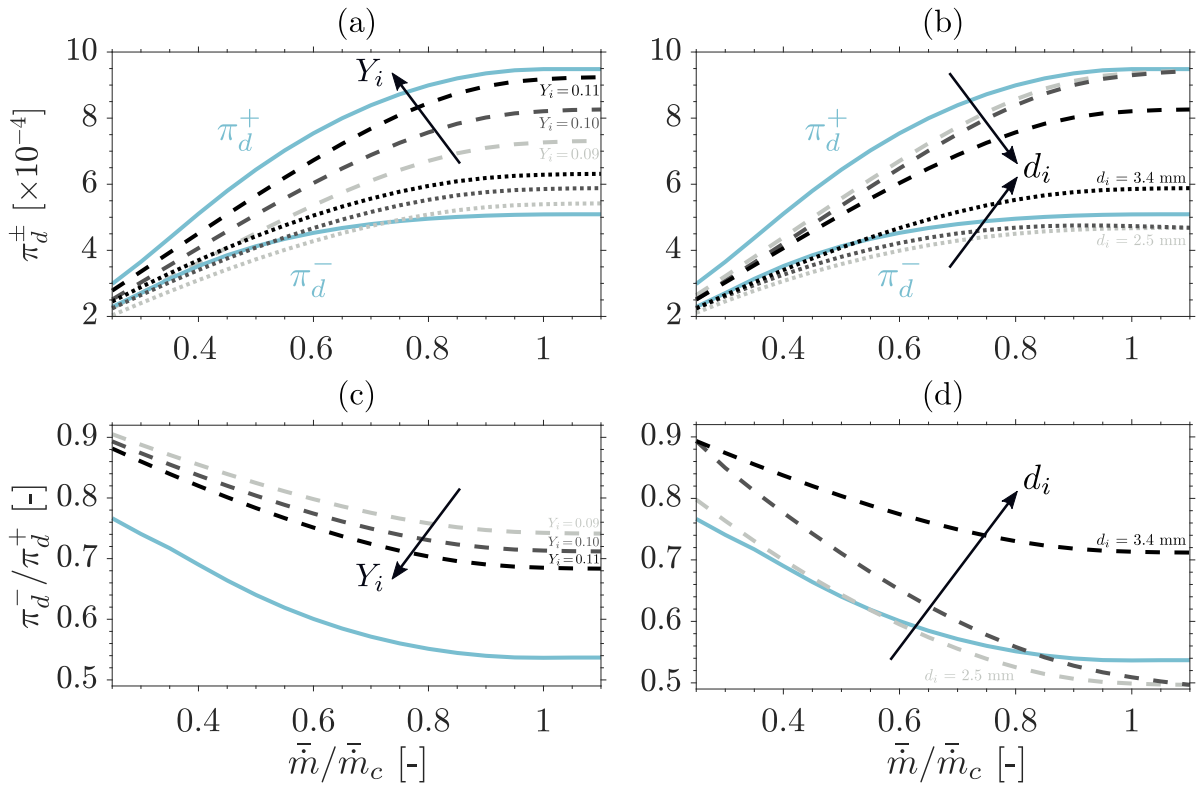


Fig. 5.4 Co-flow injection of air: (a) polynomial fits for experimental data (—) compared to co-flow theory for π_d^+ (---) and π_d^- (.....) using $d_i = 3.4$ mm for $Y_i = 0.09, 0.10$ and 0.11 ; (b) polynomial fits for experimental data (—) compared to co-flow theory for π_d^+ (---) and π_d^- (.....) using $Y_i = 0.10$ for $d_i = 3.4$ mm, $d_i = 2.5$ mm and decreasing $d_i = 3.4 \rightarrow 2.5$ mm; (c) ratio of experimental fits for direct noise wave amplitudes π_d^-/π_d^+ (—) compared to co-flow theory using $d_i = 3.4$ mm for $Y_i = 0.09, 0.10$ and 0.11 ; (d) ratio of experimental fits (—) for direct noise wave amplitudes π_d^-/π_d^+ compared to co-flow theory using $Y_i = 0.10$ for $d_i = 3.4$ mm, $d_i = 2.5$ mm and decreasing $d_i = 3.4 \rightarrow 2.5$ mm.

A sensitivity study is undertaken to understand the individual effect of both variables on the predicted acoustic wave amplitudes π_d^\pm . Figures 5.4 and 5.5 show the results of this study for the co-flow injection of air and methane, respectively. With increased injection mass fraction Y_i , the amplitude of both waves π_d^\pm increase. By reducing the injection diameter, however, we see an increase in π_d^+ but a decrease in π_d^- . In reality, both variables may play a role simultaneously. In light of this, we can calculate what combination of injection mass fraction and injection diameter is required for each case to agree with the measured direct noise.

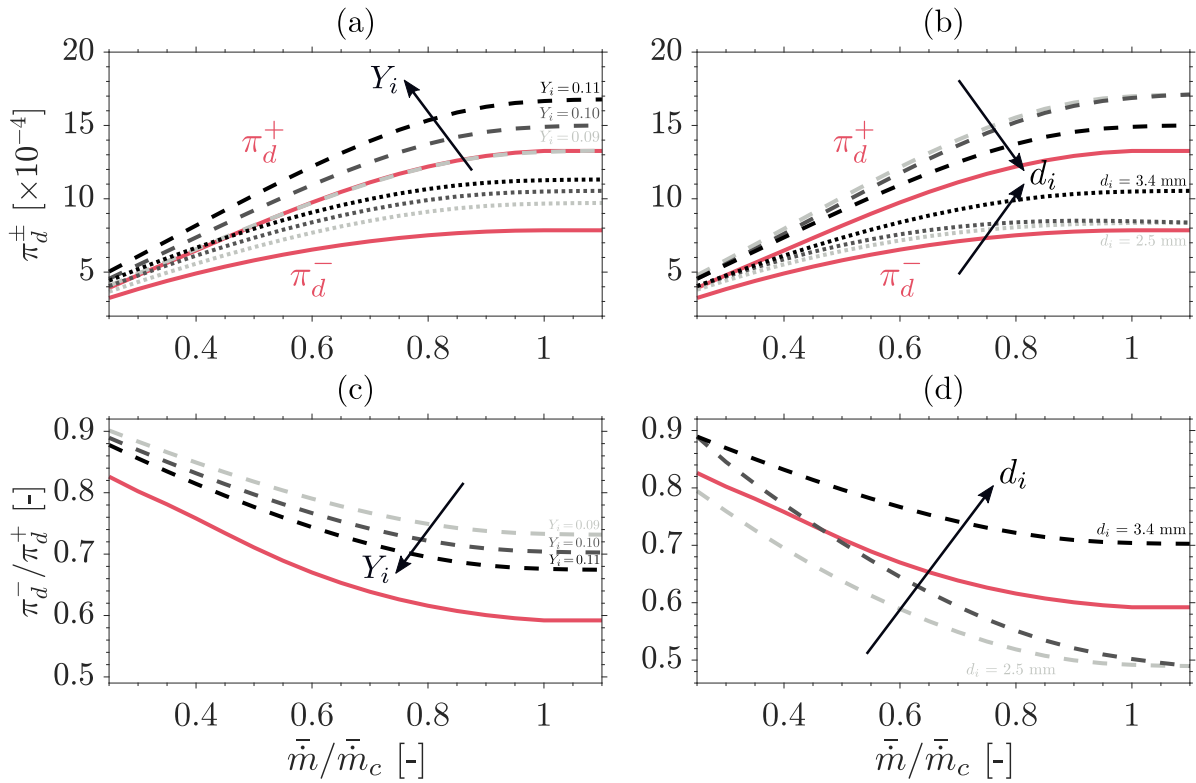


Fig. 5.5 Co-flow injection of methane: (a) polynomial fits for experimental data (—) compared to co-flow theory for π_d^+ (---) and π_d^- (.....) using $d_i = 3.4$ mm for $Y_i = 0.09, 0.10$ and 0.11 ; (b) polynomial fits for experimental data (—) compared to co-flow theory for π_d^+ (---) and π_d^- (.....) using $Y_i = 0.10$ for $d_i = 3.4$ mm, $d_i = 2.5$ mm and decreasing $d_i = 3.4 \rightarrow 2.5$ mm; (c) ratio of experimental fits for direct noise wave amplitudes π_d^-/π_d^+ (—) compared to co-flow theory using $d_i = 3.4$ mm for $Y_i = 0.09, 0.10$ and 0.11 ; (d) ratio of experimental fits (—) for direct noise wave amplitudes π_d^-/π_d^+ compared to co-flow theory using $Y_i = 0.10$ for $d_i = 3.4$ mm, $d_i = 2.5$ mm and decreasing $d_i = 3.4 \rightarrow 2.5$ mm.

As such, we solve the theoretical equations for π_d^+ and π_d^- (as derived in §2.2.3) by equating them to the experimentally measured values:

$$\begin{aligned} a^+ Y_i + b^+ \frac{Y_i^2}{A_i} - c^+ Y_i - \pi_d^+ &= 0, \\ a^- Y_i - b^- \frac{Y_i^2}{A_i} + c^- Y_i - \pi_d^- &= 0, \end{aligned} \quad (5.11)$$

where

$$a^\pm = \frac{1}{2} \frac{\bar{M}_1}{1 \pm \bar{M}_1} \frac{\bar{W}}{W_i}, \quad b^\pm = \frac{1}{2} \frac{\bar{M}_1^2}{1 \pm \bar{M}_1} \frac{R_i}{R} A, \quad c^\pm = \frac{1}{2} \frac{\bar{M}_1^2}{1 \pm \bar{M}_1}. \quad (5.12a-c)$$

For the injection diameter, the solution is constrained with an upper boundary equal to the geometric diameter $d_i = 3.4$ mm (no lower boundary is set). For the injection mass fraction Y_i , a constrained and unconstrained solution is computed. For the former,

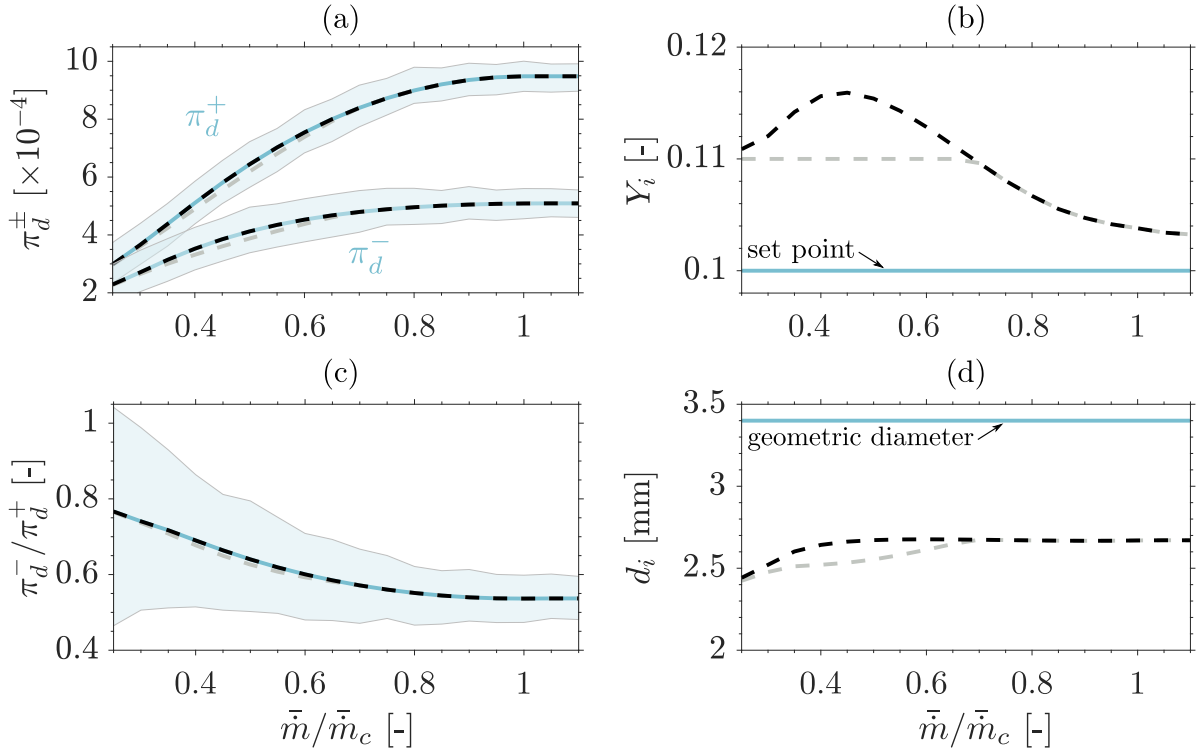


Fig. 5.6 Co-flow injection of air with constrained $Y_i \pm 0.01$ (---) and unconstrained (---) solutions for co-flow theory predictions: (a) π_d^\pm waves with fit (—); (b) injection mass fraction with assumed experimental set point (—); (c) ratio of waves with fit (—); (d) optimised injection diameter with geometric diameter (—)

Y_i is allowed to fluctuate by 10% (i.e. $Y_i = 0.10 \pm 0.01$) and a local minimum is found via the least squares formulation. For the latter, the solutions can be computed directly.

The results of this study are shown in Figs. 5.6 and 5.7 for air and methane injection, respectively. The optimisation results for each gas are in good agreement with each other when it comes to the injection diameter. As \bar{m}/\bar{m}_c (and \bar{u}_i) increases, we would expect the recirculation zone to grow and, therefore, the effective injection diameter to decrease. However, the results shows that the injection diameter is approximately constant (2.5–2.7 mm), which, along with an injection mass fraction of $Y_i = 0.10 \pm 0.01$, is found to yield agreement with experimental data. Presumably, the different properties of air and methane are responsible for the slight difference in the diameters obtained from the respective optimisation procedures.

With respect to the injection mass fraction Y_i , the results indicate that air was underestimated and methane was overestimated compared to the expected injection mass fraction. This could be a symptom of an additional source of error that had not yet been identified (for instance, the mass flow meter may need re-calibration).

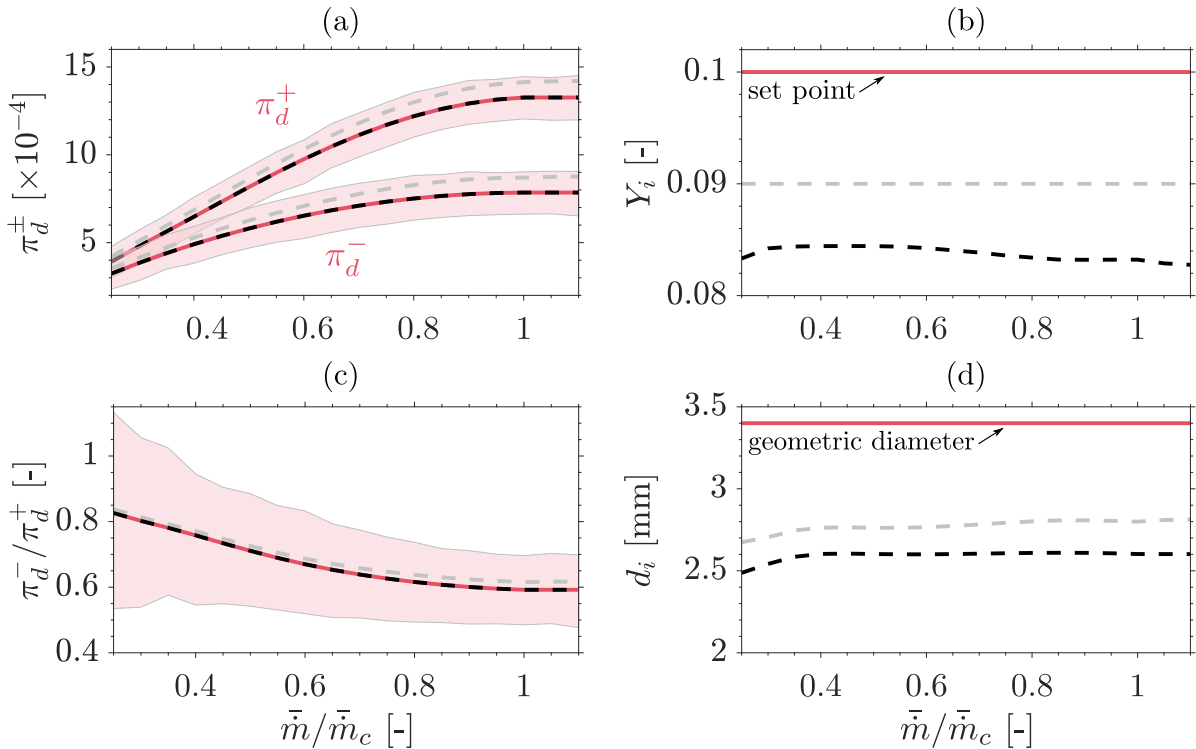


Fig. 5.7 Co-flow injection of methane with constrained $Y_i \pm 0.01$ (---) and unconstrained (---) solutions for co-flow theory predictions: (a) π_d^\pm waves with fit (—); (b) injection mass fraction with assumed experimental set point (—); (c) ratio of waves with fit (—); (d) optimised injection diameter with geometric diameter (—)

5.3.3 System characterisation

Once the direct noise sources for air are characterised, the results can be used to extract the acoustic properties of the system. In particular, the inlet reflection coefficient R_{i1} , the upstream reflection R_{o1} and transmission T_{o1} coefficients of the nozzle, and the acoustic attenuation α of the system. It is important to obtain these as they are needed to dereverberate pressure signals²⁷⁸. Under the compact assumption, the phase shift at the boundaries is zero.

Inlet reflection coefficient R_{i1}

As outlined in Table 5.2, experiments Air-A and Air-C are used to obtain the reflection coefficient of the inlet using Eq. (5.9).

Figure 5.8 shows the normalised pressure perturbations due to the co-flow injection of air using setup A to measure π_d^- and setup C to measure $(1 + R_{i1})\pi_d^-$ plotted for the minimum and maximum air mass flow rates normalised by the nozzle's choking flow rate ($\bar{m}/\bar{m}_c = 0.25$ and $\bar{m}/\bar{m}_c = 1.1$ in Figs. 5.8a and 5.8b, respectively). Figure 5.9 shows the reflection coefficient for each mean flow rate \bar{m} with standard deviation ($\pm 1\sigma$) highlighted. There is a negligible dependency of the reflection coefficient on air mass flow rate. This may be attributed to the low porosity of the perforated plate (see §4.2.1). A mean value of $R_{i1} = 0.91$ is computed and used henceforth for all the experiments presented in this chapter.

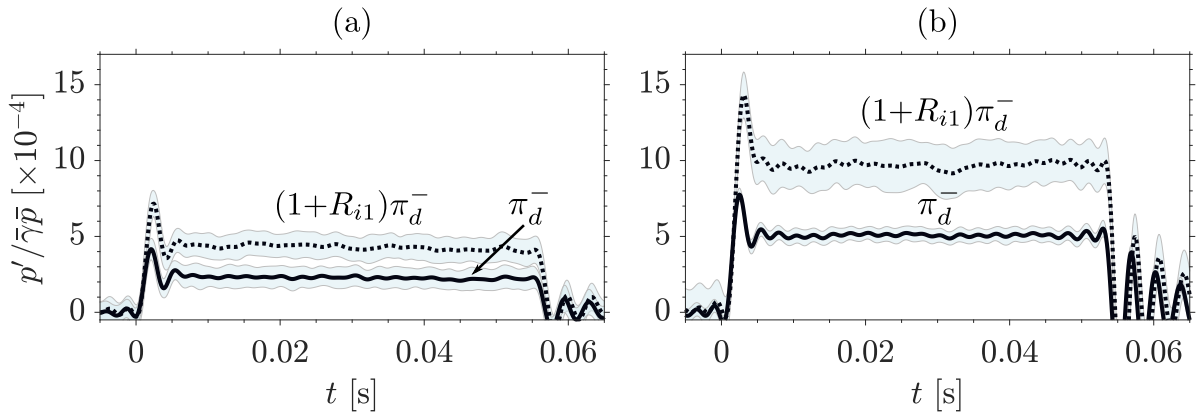


Fig. 5.8 Pressure perturbations due to co-flow injection of air using setup A (—) and setup C (····) for (a) $\bar{m}/\bar{m}_c = 0.25$ and (b) $\bar{m}/\bar{m}_c = 1.1$ with standard deviation ($\pm 1\sigma$) used to compute the inlet's reflection coefficient R_{i1} .

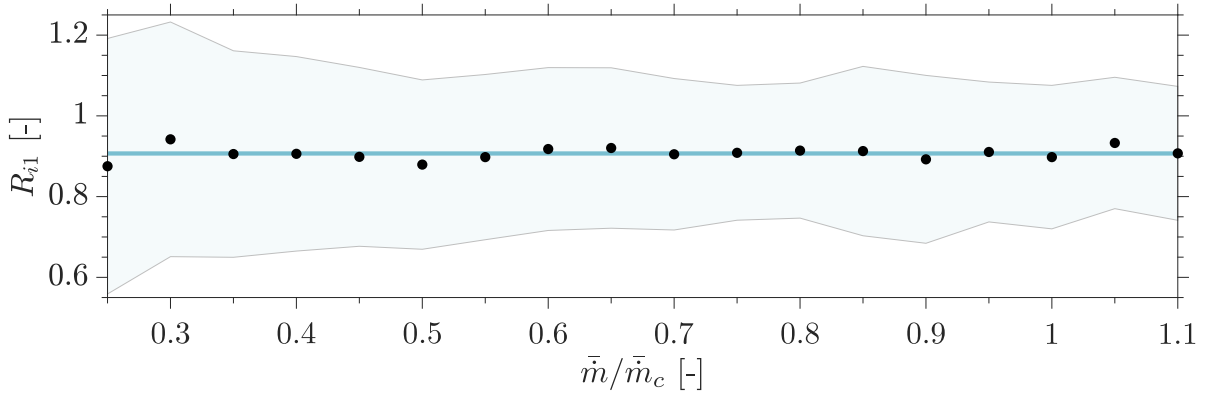


Fig. 5.9 Inlet reflection coefficient R_{i1} : experiments (\bullet) with standard deviation ($\pm 1\sigma$) and mean (—).

Nozzle reflection R_{o1} and transmission T_{o1} coefficients

As outlined in Table 5.2 experiments Air-A and Air-B are used to obtain the reflection and transmission coefficients of the nozzle using Eqs. (5.5) and (5.7), respectively.

Figure 5.10 shows the pressure perturbations due to the co-flow injection of air using setup A to measure π_d^+ and setup B to measure both $(1 + R_{o1})\pi_d^+$ and $T_{o1}\pi_d^+$ for the minimum and maximum normalised air mass flow rates ($\bar{m}/\bar{m}_c = 0.25$ and $\bar{m}/\bar{m}_c = 1.1$). The transmitted wave $T_{o1}\pi_d^+$ is measured approximately 1.5 m downstream of the nozzle. In the figure, it has been time-shifted by 4 ms (the respective acoustic delay), for the purpose of clarity (i.e. to start at $t=0$).

Figure 5.11 shows the reflection and transmission coefficients as a function of normalised air mass flow rate \bar{m}/\bar{m}_c . There is a strong dependence on flow rate, showing the same trend as results obtained by De Domenico et al.⁶⁴ using non-isentropic theory. The experimental data yields a reflection coefficient above unity for the last 7 flow rates, and around 1.05 for the choked cases (the last three). Indeed, we know the theoretical limits for a choked compact nozzle ($R_{o1} \simeq 1$)^{63,64,213}.

In order for this dataset to agree with the physical limits established by published theory, the pressure perturbations obtained using setup B are scaled down by 2.5%. This result is also presented in Fig. 5.11. The scaled result falls within the error bars computed, showing good agreement with experimental data from a similar nozzle¹ used in the work of De Domenico et al.⁶⁴ and with the numerical results presented in §6.3.3 using the linearised Navier–Stokes equations method. The transmission coefficient T_{o1} is virtually unaffected by the scaling since the error propagates differently. The scaled

¹The nozzle employed by De Domenico et al.⁶⁴ had the same divergent section, but a different convergent section (24 mm long with a linear geometric profile and 40° angle).

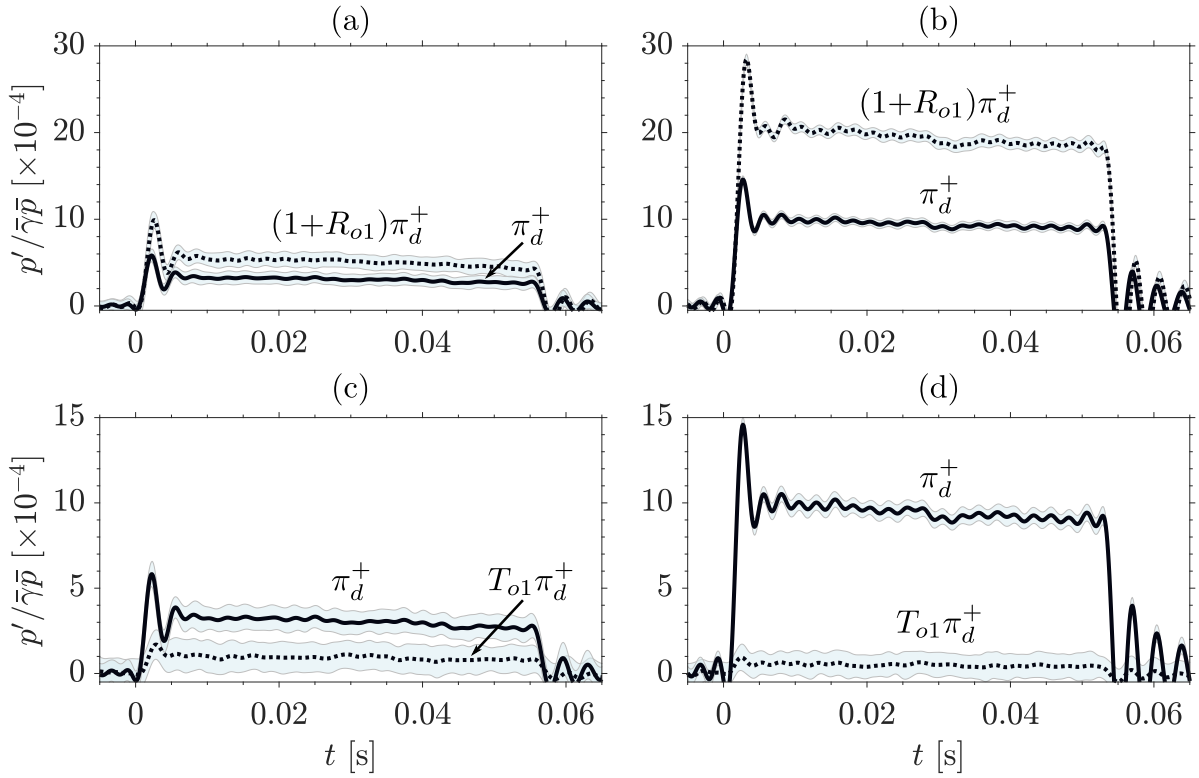


Fig. 5.10 Pressure perturbations due to co-flow injection of air using setup A (—) and setup B (.....) for (a, c) $\bar{m}/\bar{m}_c = 0.25$ and (b, d) $\bar{m}/\bar{m}_c = 1.1$ with standard deviation ($\pm 1\sigma$) used to compute the nozzle's upstream reflection R_{o1} and transmission T_{o1} coefficients.

results are, henceforth, used to describe the nozzle's compact acoustic properties in this thesis.

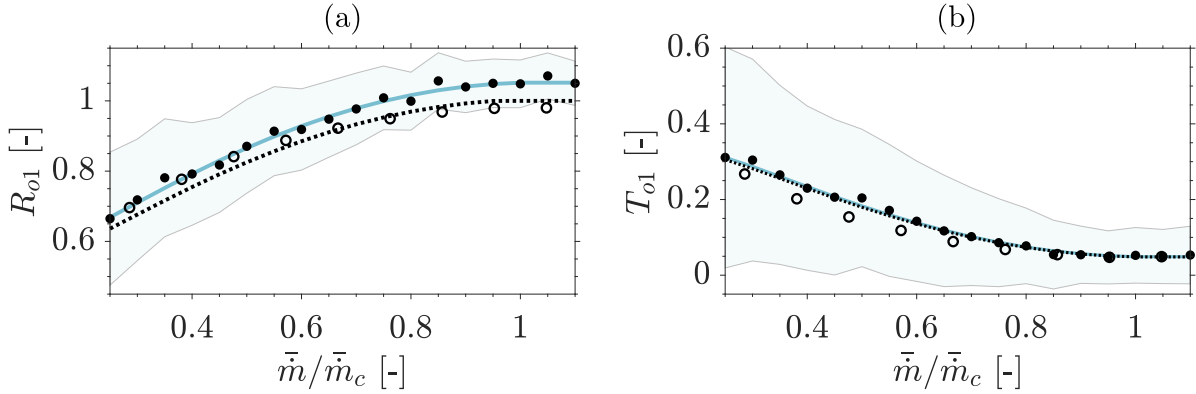


Fig. 5.11 Nozzle's acoustic (a) reflection coefficient R_{o1} and (b) transmission coefficient T_{o1} : experiments (\bullet) with standard deviation ($\pm 1\sigma$), polynomial fit (—), scaled polynomial fit (.....), and experimental data from similar nozzle⁶⁴ (\circ).

Attenuation coefficient α

Attenuation of propagating acoustic waves occurs due to turbulence, mixing, heat viscous effects, as well as losses at the walls (such as heat conduction)²⁷⁴. The amplitude change of an acoustic wave over a distance Δx due to attenuation is expressed by Eq. (5.10).

Experimentally, this is measured using two of the characterisation setups (Air-A and Air-C). For experiments Air-A, we inspect the first reflected wave measured by the two upstream transducers:

$$\frac{p'_{x_1}}{\gamma p_1} = \frac{p'_{x_2}}{\gamma p_1} = R_{i1}\pi_d^- e^{-2\alpha l_\alpha^-} + R_{o1}\pi_d^+ e^{-2\alpha l_\alpha^+}, \quad (5.13)$$

where l_α^\pm is the distance travelled by the respective waves π_d^\pm .

If there were no attenuation, the measured reflected acoustic perturbation at both transducers would be:

$$\frac{p'}{\gamma \bar{p}} = R_{i1}\pi_d^- + R_{o1}\pi_d^+. \quad (5.14)$$

Using the results from §5.3.2, we estimate what the amplitude of the reflected wave would be without attenuation (Fig. 5.12). Since there is no analytical solution to Eq. (5.13), α can be found iteratively.

For experiments Air-C, the transducers upstream and downstream of the injection source will measure different perturbation amplitudes (as a result of the removal of the

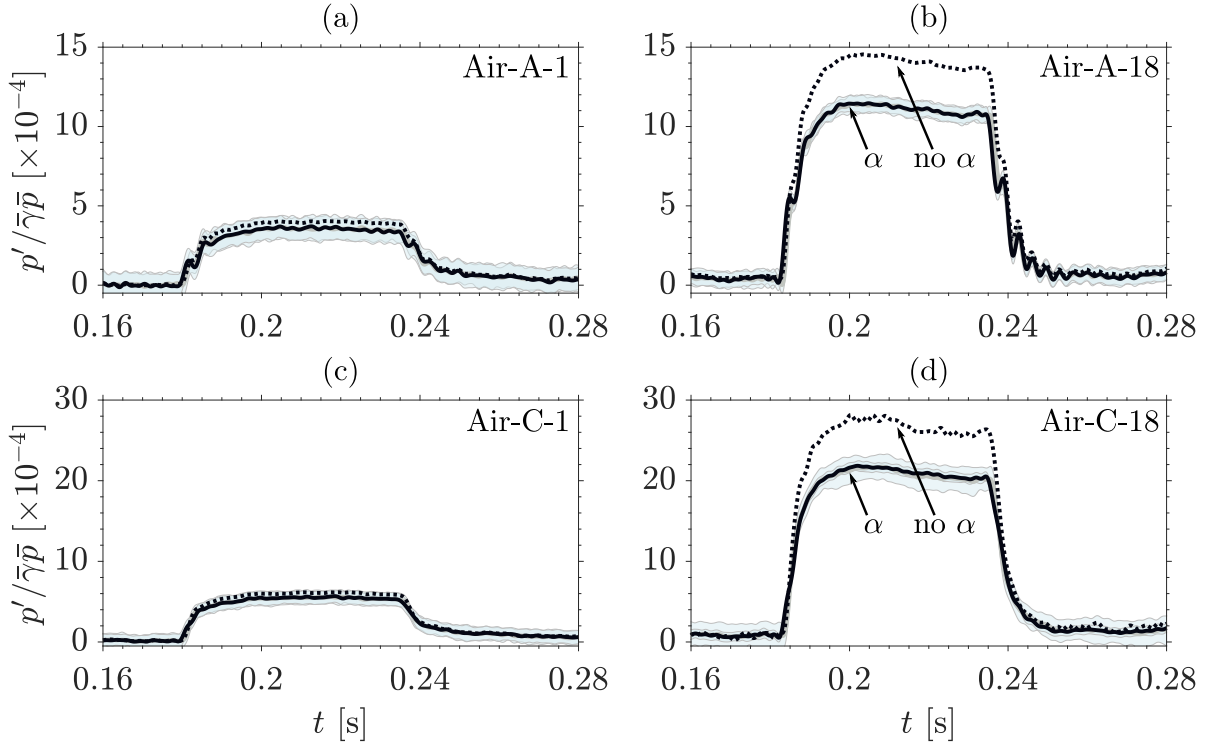


Fig. 5.12 Acoustic waves for (a) test case Air-A-1 ($\bar{m}/\bar{m}_c = 0.25$), (b) test case Air-A-18 ($\bar{m}/\bar{m}_c = 1.1$), (c) test case Air-C-1 ($\bar{m}/\bar{m}_c = 0.25$) and (d) test case Air-C-18 ($\bar{m}/\bar{m}_c = 1.1$), with standard deviation ($\pm 1\sigma$) used to compute the system's acoustic attenuation α . Pressure perturbations at x_1 (—) and x_2 (—) are shown along with predicted p' if there were no attenuation of the waves ($\alpha = 0 \text{ m}^{-1}$).

upstream pseudo-anechoic tube):

$$\begin{aligned} \frac{p'_{x_1}}{\bar{\gamma}\bar{p}_1} &= (1 + R_{i1}) \pi_d^-, \\ \frac{p'_{x_2}}{\bar{\gamma}\bar{p}_1} &= \pi_d^+ + R_{i1}\pi_d^-. \end{aligned} \quad (5.15)$$

The reflected wave at both transducers is now:

$$\frac{p'_{x_1}}{\bar{\gamma}\bar{p}_1} = \frac{p'_{x_2}}{\bar{\gamma}\bar{p}_1} = R_{o1} (1 + R_{i1}) (\pi_d^+ + R_{i1}\pi_d^-) e^{-2\alpha l} \quad (5.16)$$

Similarly to what was done using experiments Air-A, we can use the results from §5.3.2 to compute the unattenuated reflected wave, and solve Eq. (5.16) for α .

The resulting α values calculated for each transducer using setups A and c are averaged and shown in Fig 5.13. The attenuation α ranges from $2.0\text{--}4.2 \times 10^{-3} \text{ m}^{-1}$. The

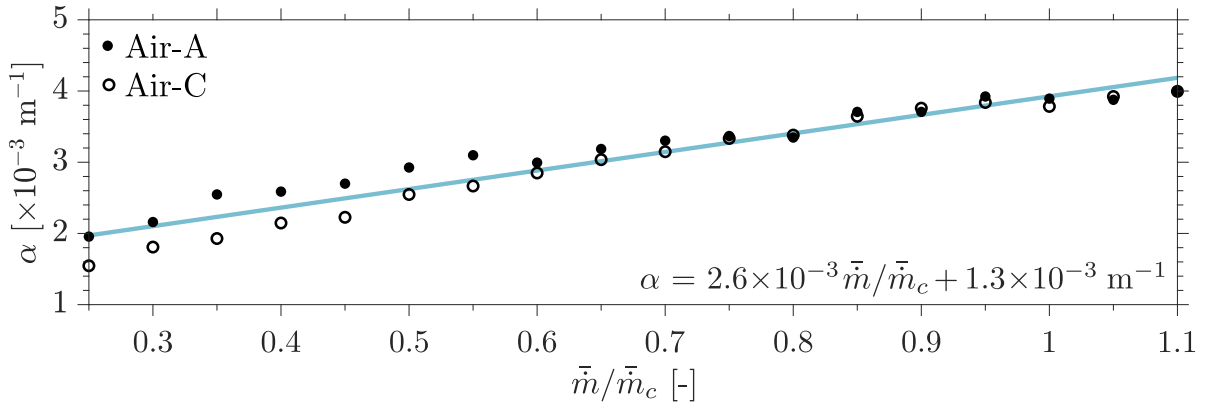


Fig. 5.13 Acoustic attenuation α as a function of normalised mean flow rate \bar{m}/\bar{m}_c : experimental data using test cases Air-A (\bullet) and Air-C (\circ) and a linear fit (—).

results show a linear trend with normalised mass flow rate and are in good agreement with results from Rolland²⁷⁸ for the CWG model setup.

5.3.4 Indirect noise waves

In this subsection, non-reverberated indirect noise waves π_i^\pm are measured for the first time by using the variables obtained in the previous sections. As outlined in Table 5.2, experiments CH₄-B are used for this purpose. The equations presented assume linearity (i.e. the total noise is a sum of direct and indirect noise).

Figure 5.14 visually demonstrates the *anechoic subtraction* method employed for the far and close injection locations in the case of the highest mass flow rate ($\bar{m}/\bar{m}_c = 1.1$, test CH₄-B-18). To obtain the downstream-travelling indirect noise π_i^+ , the direct noise signal π_d^+ is simply multiplied by T_{o1} before being subtracted from the result of CH₄-B, as per Eq. (5.6). In order to extract the upstream-travelling indirect noise waves π_i^- , the direct noise waves π_d^\pm (obtained in §5.3.2) need to be scaled according to the positioning of the transducers relative to the source. For the far injection case (Fig. 5.14a), the transducer is downstream of the injection, so π_d^+ is multiplied by $(1+R_{o1})$ before being subtracted from the result of CH₄-B, as per Eq. (5.8). For the close injection location (Fig. 5.14b), the transducer is upstream of the injection so π_d^+ is multiplied by R_{o1} and summed with π_d^- , before being subtracted from the result of CH₄-B. After the scaling of the direct noise contributions, but before the subtraction, the signals are aligned in time by inspection of the respective pulses' leading edges.

In the far injection case, there is time separation between the direct and indirect noise waves for all mean flow rates (Figs. 5.14a and 5.14c). It is for the case of the injection close to the nozzle that the subtraction method is most useful as there is a

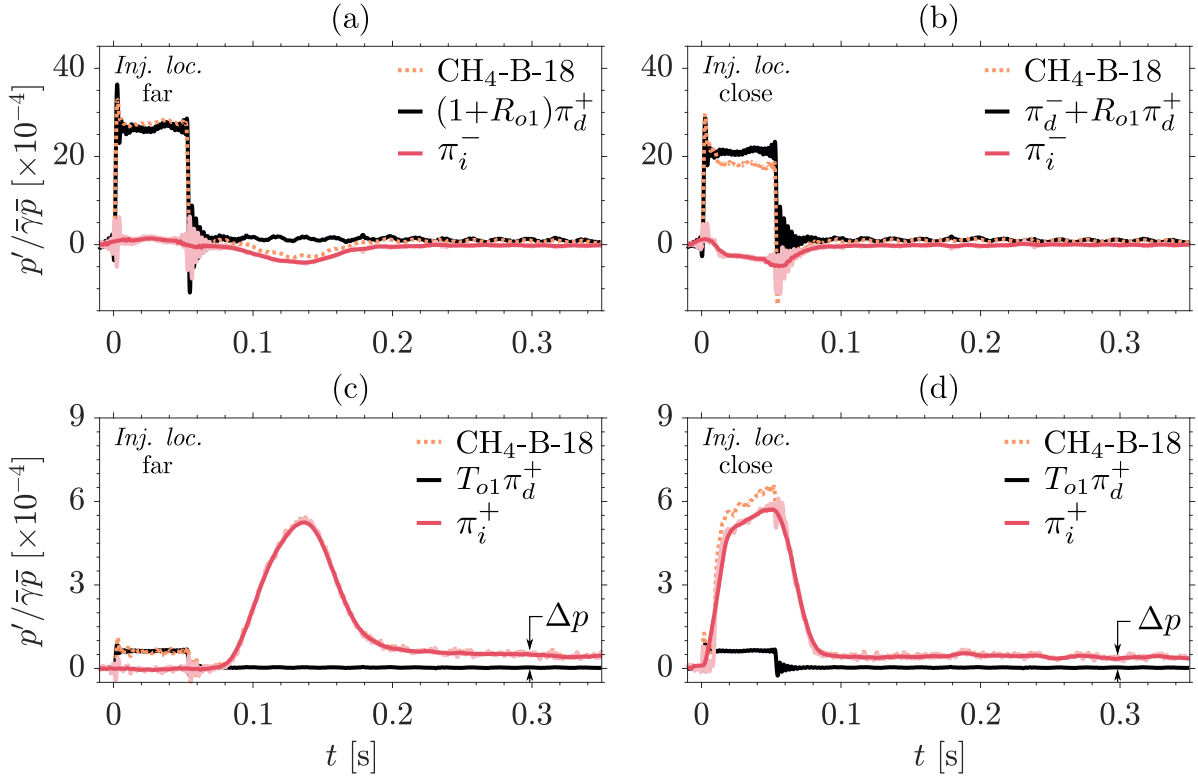


Fig. 5.14 Anechoic subtraction method visualised: test CH₄-B-18 (· · · ·) minus scaled direct noise signal(s) (—). Resultant indirect acoustic waves (—) due to co-flow injection of methane for $\bar{m}/\bar{m}_c=1.1$ are shown: π_i^- for (a) far and (b) close injection locations; π_i^+ for (c) far and (d) close injection locations. A 15 ms moving average filter has been applied to the indirect noise signals.

superpositioning of the direct and indirect noise signals (Figs. 5.14b and 5.14d). The ringing caused by valve dynamics has an effect in the extracted indirect noise signals – it is not fully cancelled out during the subtraction process. This ringing is generally smoothed out by the 15 ms moving average filter used in Fig. 5.14. However, it has a particularly significant effect on π_i^- for the close injection location (Fig. 5.14b). Here the ringing is around the same order of magnitude as π_i^- , whereas for the downstream measurements, it is virtually negligible relative to π_i^+ (as evident in Figs. 5.14c-d).

The resultant π_i^\pm time series for all mass flow rates of air are presented in Fig. 5.15. As expected, the injection location affects the indirect noise signature. For the close location, the signal resembles that of a direct noise pulse (Fig. 5.15b). The signal is slightly distorted as the compositional wave deforms inside the nozzle due to the mean flow gradient³¹⁵. On the other hand, the far injection provides a longer convective length, allowing the compositional wave to disperse and yield signatures that resemble Gaussian pulses (Fig. 5.15a).

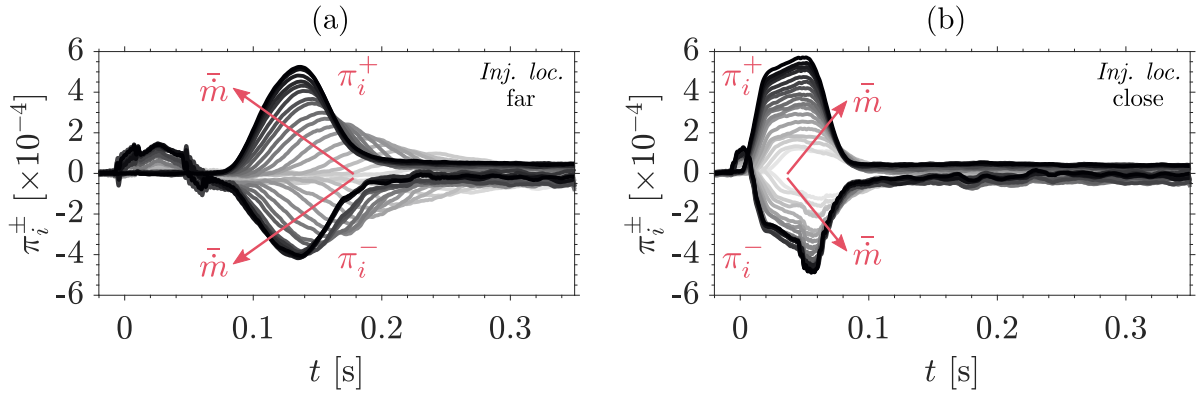


Fig. 5.15 Indirect noise waves obtained via anechoic subtraction: π_i^\pm for the (a) far and (b) close injection locations. A 15 ms moving average filter has been applied to the signals.

The π_i^+ signals for both injection locations are clean and clear of ringing effects from the subtraction method. This is because the noise is an order of magnitude smaller than π_i^+ (Fig. 5.14c-d). In contrast, the π_i^- signals are of the same order of magnitude as the ringing. For the far injection π_i^- (Fig. 5.15a), the direct noise signal is not fully cancelled out. This could be attributed to uncertainties in π_d^+ and/or R_{o1} (see Table 5.2). Since π_d^+ is used to successfully extract π_i^+ , it is unlikely to be the issue.

For the close injection (Fig. 5.15b), the slight differences in the signals' 'valve turn on' ringing (Fig. 5.14b) leads to a misleading positive π_i^- pulse front. Moreover, and as mentioned previously, the 'valve turn off' ringing slightly distorts the shape of the pulse (Fig. 5.14b).

Lastly, for $\bar{m}/\bar{m}_c > 0.5$, the π_i^\pm signals do not return to zero once the compositional inhomogeneity has convected through the nozzle (at least, not within the 0.35 s anechoic acquisition window shown here). Instead, the system's pressure decays to a new, higher mean pressure. This change in pressure Δp is pointed out in Fig. 5.14, and is also visible in Fig. 5.15.

5.4 Reverberating system

5.4.1 Setup and methodology

The CWR is used here without the pseudo-anechoic tubes in the upstream chamber, as done in the work of De Domenico et al.⁶⁴ (Fig. 5.16). As a result, the upstream chamber reverberates (i.e. pressure pulses reflect off both ends, so that the pressure builds up during injection). Downstream of the nozzle, three pseudo-anechoic tubes are used providing an anechoic time of $\tau_a = 0.5$ seconds. As done in §5.3, we identify injection location 1 as the *far* injection location ($L_c = 0.55$ m) and injection location 3 as the *close* injection location ($L_c = 0.11$ m) – see Fig. 5.16. The pressure signals presented are the result of an averaging of 10 pulses, followed by the filtering of the mains frequency (50 Hz) as well as frequencies above 90 Hz. The test cases are outlined in Table 5.1.

5.4.2 Pressure perturbations

The pressure perturbations generated by the co-flow injection of methane or air at two different injection locations are presented here. For the far injection, the convective time $\tau_c = L_c/\bar{u}$ is larger than the pulse duration $t_p = 50$ ms for all flow rates investigated. For this reason, direct and indirect noise are time separated^{62,64}. This was shown in §5.3 and is further confirmed by the Raman measurements presented in §5.7. Owing to this time separation, the air signal can be scaled to match the peak methane signal (more details on this later). All air injection results presented have been scaled accordingly.

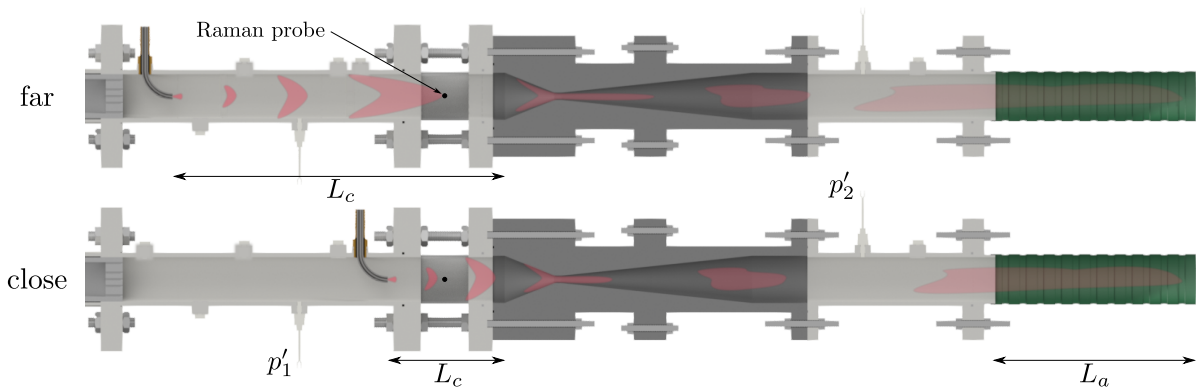


Fig. 5.16 CWR setup for the single pulse injection campaign with far ($L_c = 0.55$ m) and close ($L_c = 0.11$ m) injection locations. The anechoic length is $L_a \simeq 90$ m giving an anechoic time of $\tau_a = 0.5$ s. Pressure perturbations are measured by two transducers (one upstream and one downstream of the nozzle). Dimensions not to scale.

The upstream and downstream methane injection pressure signals are shown in Figs. 5.17 and 5.18 for the far and close injection locations, respectively. Three flow rate conditions are selected and presented as time series in Figs. 5.17 and 5.18 to show the methane and scaled air signals. For both locations and gases, the pulse is injected at $t = 0$ s, generating direct noise for the duration of the pulse ($0 \leq t \leq t_p$). During this

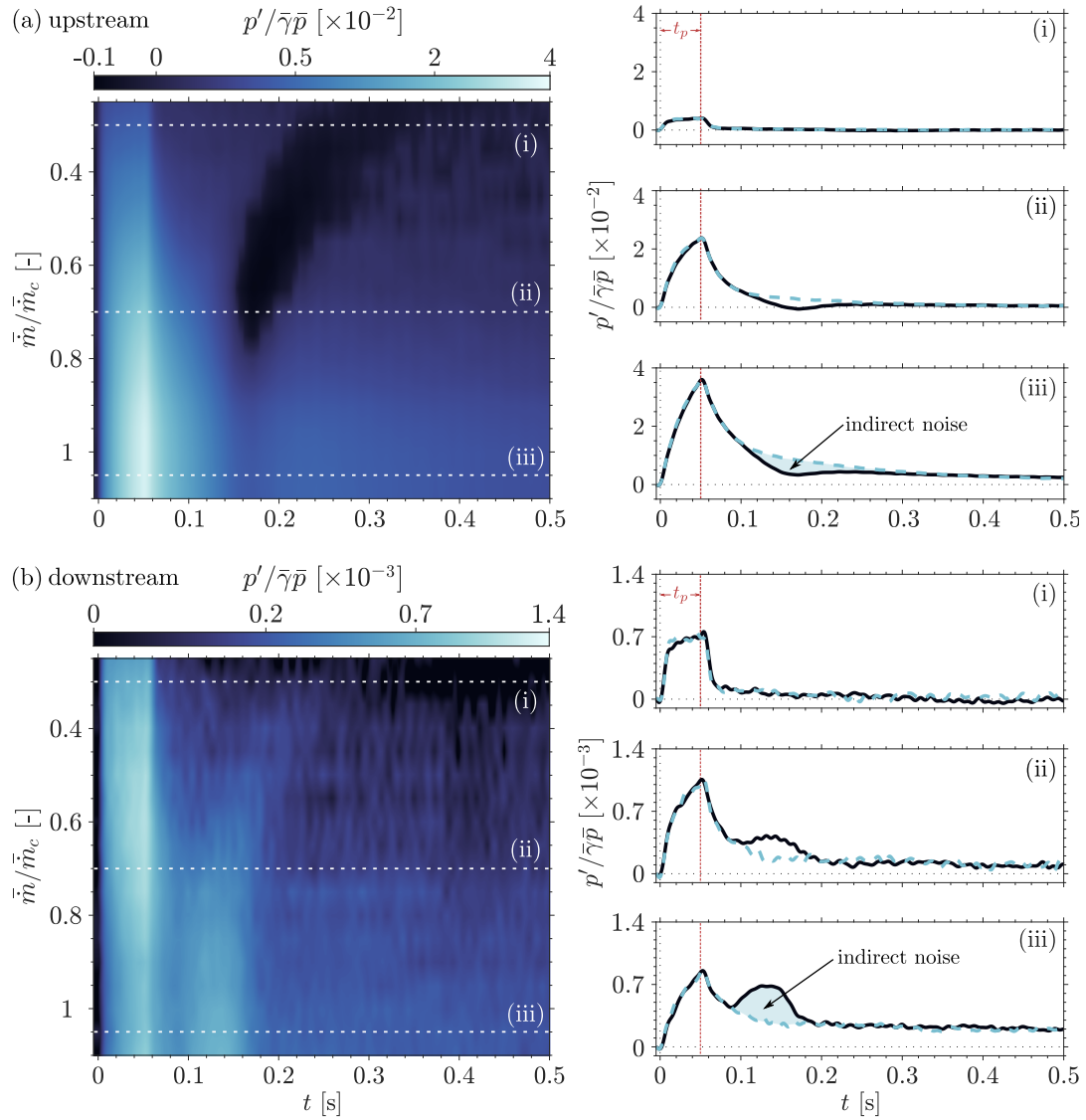


Fig. 5.17 Upstream (a) and downstream (b) pressure perturbations due to injection at the far location. Colourmaps show methane injection perturbations using linear interpolation to map between different mean flow rates. Data is scaled using a power-law relationship ($y = x^\gamma$, where $\gamma = 0.5$) in order to more easily visualise the lower amplitude perturbations; (b,d) three flow rates from the respective colourmaps (i–iii) are selected for the measurement of methane (—) and scaled air (---) injection pressure perturbations.

time, the direct noise inside the chamber builds up owing to reverberation²⁸⁰. The rate of increase in pressure is a function of the injection flow rate (\dot{m}_i), the upstream chamber's length (L_1), and the system's reflection and attenuation coefficients (R_{i1}, R_{o1}, α).

For the far injection of both gases, only direct noise is produced during the pulse duration. The upstream and downstream signals are approximately an order of magnitude different (with the upstream signal being the larger of the two). This is expected as reverberation occurs in the upstream chamber. In the downstream chamber, there is no reverberation. Therefore, the downstream pressure signal is only made up of the noise transmitted from the upstream chamber.

Once the injection is stopped, direct noise generation halts and the pressure waves decay. In the injection of methane, however, indirect noise is produced shortly after the end of the pulse. The upstream-travelling indirect noise is negative, while the downstream-travelling indirect noise is positive. This agrees with indirect noise theory²⁷⁸ and previous experimental results⁶⁴. In the upstream signal, the presence of indirect noise is visible in Fig. 5.17a as a darkening of the blue palette in the colour map, whereas downstream in Fig. 5.17b it is seen as a brightening of the colour map. For signals both upstream and downstream of the nozzle, when increasing the mean mass flow rate, the start time of the respective indirect noise converges to a specific time ($t = 0.09$ s). This is due to the nozzle throat reaching sonic conditions and the upstream bulk velocity plateauing (see Fig. 4.10); this is especially clear when comparing Figs. 5.17b and 5.27a.

For the close injection, direct and indirect noise are no longer time separated, as shown in Fig. 5.18. Indirect noise is now produced before the end of the pulse, interfering destructively upstream and constructively downstream of the nozzle, respectively. The interference effects can be more closely examined by plotting the pressure amplitude at the end of the methane injection pulse ($t = 0.05$ s) for far and close injection locations. This is shown in Fig. 5.19. Upstream, both signals increase with flow rate and reach a plateau at the choking point. In fact, the pressure signals are amplified by an order of magnitude from lowest to largest flow rate as shown in Fig. 5.19a. This is because the acoustic reflection coefficient of the nozzle increases with flow rate⁶³ as described in §5.3.3. Downstream, however, a maximum is reached at around $\bar{m}/\bar{m}_c = 0.6$ as shown in Fig. 5.19b. This is because the nozzle's transmission coefficient decreases with flow rate. At higher flow rates, the increase in transmission loss is greater than the increase in upstream pressure, until we reach the choking point, where both the upstream pressure and the transmission coefficient plateau. Since the direct and indirect noise contributions are time separated for the far injection location, the difference between the far and close

injection amplitudes (Fig. 5.19) is due to indirect noise contributions (i.e. destructive interference upstream and constructive interference downstream).

As mentioned earlier, the time separation in the far injection cases allows us to scale the air results so that the direct noise produced by air and methane is the same. This enables us to extract the reverberated indirect noise p'_i by simply subtracting the scaled

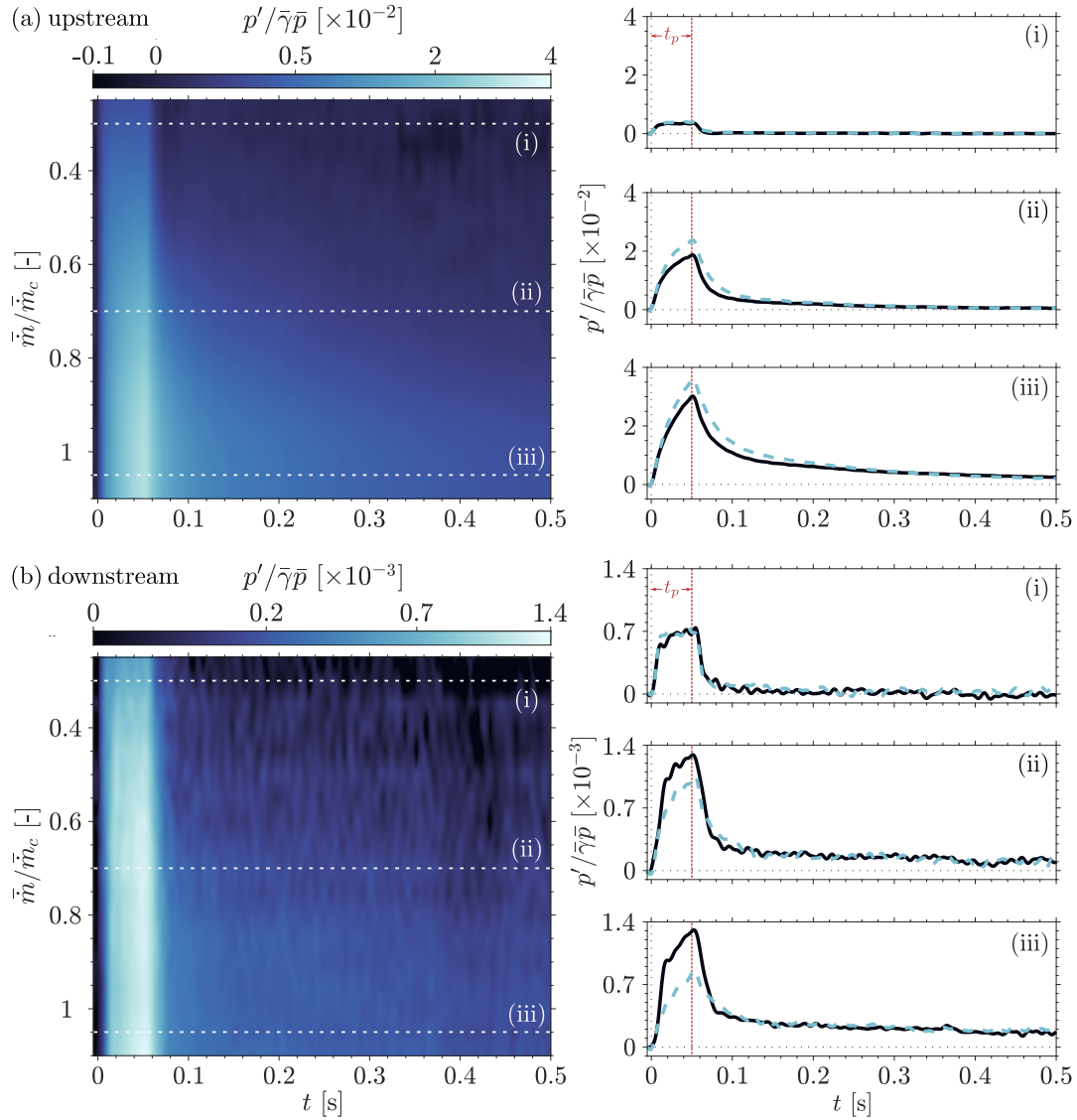


Fig. 5.18 Upstream (a) and downstream (b) pressure perturbations due to injection at the close location. Colourmaps show methane injection perturbations using linear interpolation to map between different mean flow rates. Data is scaled using a power-law relationship ($y = x^\gamma$, where $\gamma = 0.5$) in order to more easily visualise the lower amplitude perturbations; (i-iii) three flow rates from the respective colourmaps are selected for the measurement of methane (—) and scaled air (---) injection pressure perturbations.

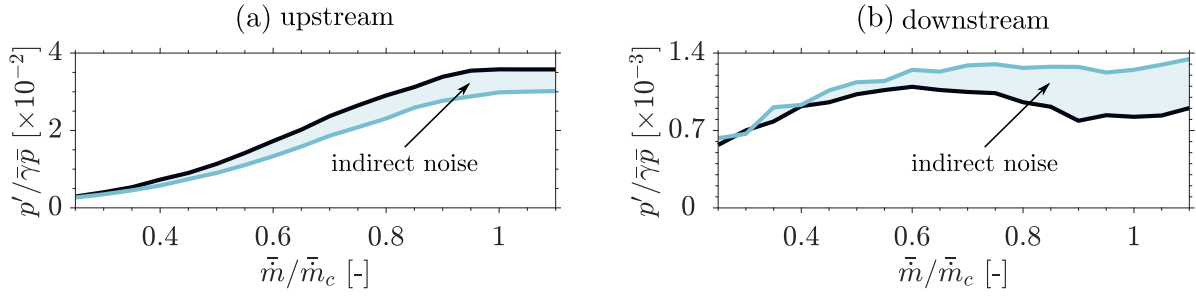


Fig. 5.19 Upstream (a) and downstream (b) pressure perturbations at the end of the pulse ($t = 0.05$ s) due to the co-flow injection of methane at the far (—) and close (—) injection locations as a function of normalised mean flow rate \bar{m}/\bar{m}_c .

air pressure signal (i.e. direct noise p'_d) from the methane pressure signal (i.e. direct plus indirect noise p'), such that $p'_i = p' - p'_d$. Assuming the direct noise generated is independent of injection location, this method can also be applied to the close injection cases⁶⁴. Specifically, the far injection scaled air pressure signals are subtracted from the close injection methane pressure signals. These results are shown in Fig. 5.20.

An initial noise source is identified in the upstream chamber before the compositional wave reaches the nozzle (Fig. 5.20a). As mentioned in §5.3.2, this could be attributed to indirect noise generated as the methane is injected. Downstream of the nozzle, the signal is an order of magnitude smaller than in the upstream section which reverberates. The signal-to-noise ratio in particular is reduced downstream owing to the low acoustic transmission of the nozzle and the highly turbulent nature of the flow accelerating through the throat. Nevertheless, at higher flow rates, indirect noise generation is clear.

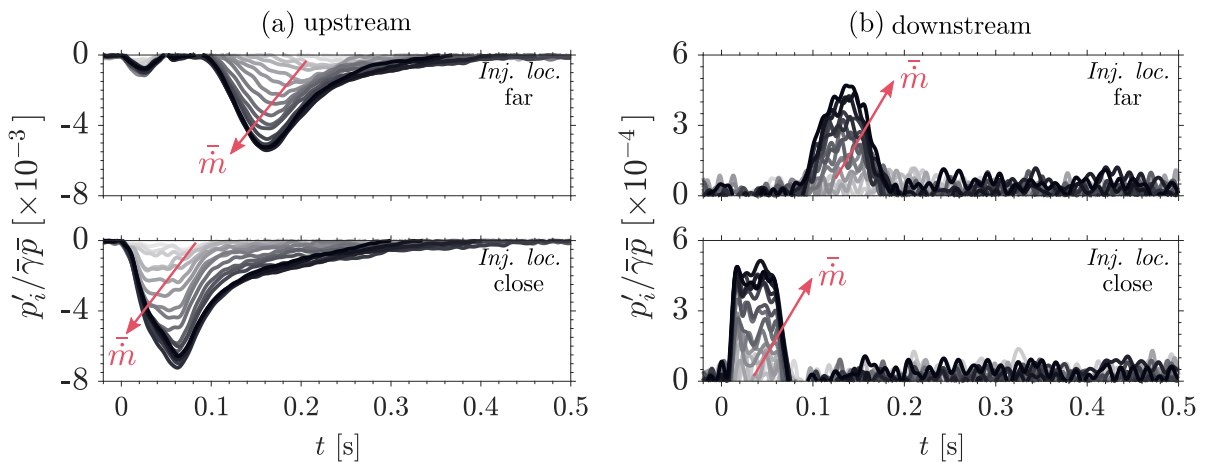


Fig. 5.20 Reverberated indirect noise pressure perturbations obtained by subtracting scaled air signals from methane signals: (a) upstream and (b) downstream of the nozzle.

5.4.3 Dereverberation

In order to quantify the indirect noise waves π_i^\pm , the effects of reverberation need to be removed⁶⁴. Acoustic signals can be dereverberated using system transfer functions^{278,280}. This analysis can be done in the frequency domain using the system properties characterised in §5.3 (i.e. R_{i1} , R_{o1} , T_{o1} , α). We assume that time delays associated with transducer locations are negligible and make use of the fact that we only analyse data within the anechoic acquisition window (i.e. $R_{o2} = 0$). As such, to dereverberate a reverberated, upstream-travelling indirect noise signal $p'_{i,1}/\bar{\gamma}\bar{p}$:

$$\widehat{\pi_i^-} = \frac{\widehat{p'_{i,1}}}{\bar{\gamma}\bar{p}} \left(\frac{1 - R_{i1}R_{o1}e^{-i\omega\tau_1 - 2\alpha L_1}}{1 + R_{i1}} \right). \quad (5.17)$$

Similarly, to dereverberate a reverberated downstream-travelling indirect noise signal $p'_{i,2}/\bar{\gamma}\bar{p}$:

$$\widehat{\pi_i^+} = \frac{\widehat{p'_{i,2}}}{\bar{\gamma}\bar{p}} - \left(\frac{T_{o1}R_{i1}e^{-i\omega\tau_1 - 2\alpha L_1}}{1 + R_{i1}} \right) \frac{\widehat{p'_{i,1}}}{\bar{\gamma}\bar{p}}. \quad (5.18)$$

Note that the upstream travelling indirect noise is an input to this equation as the upstream chamber reverberates and contributes to the downstream signal.

The resulting time series are shown in Fig. 5.21. Similar to the results from the non-reverberating setup, the far injection results demonstrate effects of dispersion. There is evidence of an indirect noise source before the pulse reaches the nozzle (Fig. 5.21a), particularly during the injection period. This could be confirmation that a measurable amount of indirect noise is produced by the co-flow injection process.

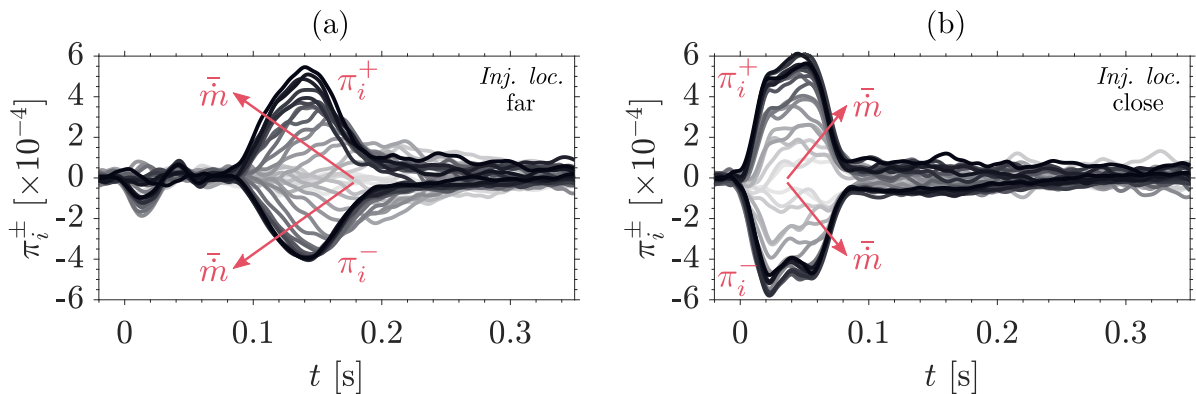


Fig. 5.21 Indirect noise waves obtained via dereverberation: π_i^\pm for the (a) far and (b) close injection locations. A 15 ms moving average filter has been applied to the signals.

5.5 Indirect noise quantification: a comparative study

The resultant indirect noise waves obtained using the two different quantification methods (i.e. anechoic subtraction and dereverberation) are contrasted in Fig. 5.22. A 15 ms moving average filter has been used and the noise measured before the arrival of the pulses has been filtered out for clarity purposes. Positive agreement is found for all cases in terms of signature shape, arrival times, and duration. This is confirmation that the system characterisation and the measurements of the direct noise wave amplitudes are in accordance. Unsurprisingly, the region of clearest difference is π_i^- in the close injection case. This has been discussed in §5.3.4. Admittedly, the anechoic subtraction method produces smoother signals as a result of using more pulses in the averaging (100), comparatively to the reverberated cases (10).

The peak amplitudes are plotted versus normalised mass flow rate in Fig. 5.23. The peak indirect noise generated by the close injection cases is consistently larger than for the far injection cases. This is expected since the compositional wave has more time to disperse in the case of the far injection location. Good overall agreement is found between

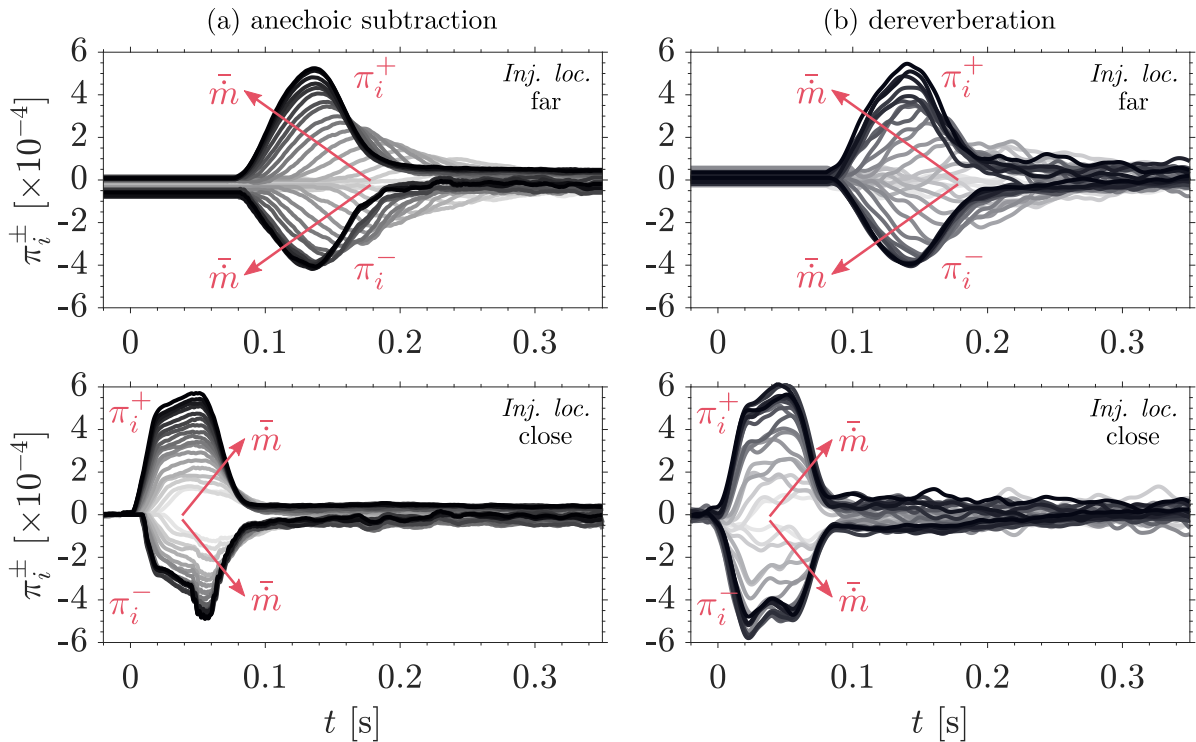


Fig. 5.22 Comparison of indirect wave quantification methods: (a) anechoic subtraction and (b) dereverberation. A 15 ms moving average filter has been used and the subtraction noise appearing before the arrival of the pulses has been filtered out for clarity purposes.

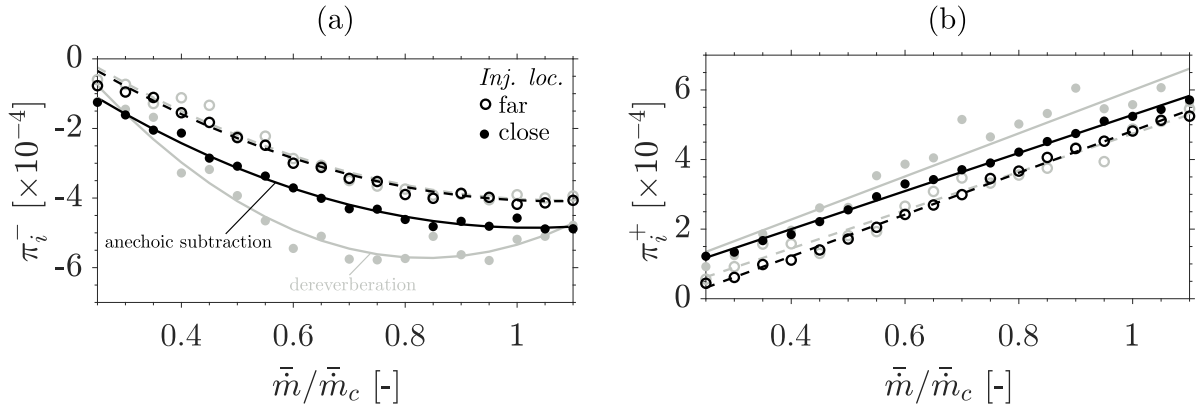


Fig. 5.23 Indirect noise waves: maximum (a) π_i^- and (b) π_i^+ as a function of normalised mass flow rate \bar{m}/\bar{m}_c for far (\circ) and close (\bullet) injection locations. Also included are the best fits for close (—) and far (---) injection results obtained using the anechoic subtraction (—) and dereverberation (—) methods.

dereverberation and anechoic subtraction methods for the far injection case. Qualitatively, the π_i^- signals show the same trend with mass flow rate as the upstream bulk velocity \bar{u} (Fig. 4.10). In other words, they both reach a plateau once the nozzle chokes. This is only not true for the dereverberated π_i^- which peaks at $\bar{m}/\bar{m}_c = 0.75$. The downstream signals π_i^+ show a linear relationship with flow rate. Similar to the upstream π_i^- results, the dereverberated π_i^+ signals for the close injection are larger than for the anechoic subtraction method.

The integral of the perturbations can theoretically help assess whether the same total entropic disturbance has gone through the nozzle for both injection locations. This was not done in the work of De Domenico et al.⁶⁴. However, as mentioned previously in §5.3.4, for $\bar{m}/\bar{m}_c > 0.5$, the π_i^\pm signals do not return to zero. This makes the definition of the limits of integration difficult to organise in a systematic way. For the purpose of this analysis, the integral limits are selected based on the leading and trailing edges of the pulse, on a case by case basis. The same integration limits are used in both the anechoic subtraction and dereverberation methods. The results are plotted in Fig. 5.24 where t_i is defined as the time over which the integral is computed.

Qualitatively, the integral signals have the same trend with flow rate as the signal peaks shown in Fig. 5.23. For π_i^- , the difference in integral is generally greater at higher mean flow rates for both methods. In the case of π_i^+ using the anechoic method, the opposite is true. The average of the close and far integral values is also included in Fig. 5.24. The averages for both measurement methods are in fair agreement with each other. It is assumed that the same mass is being accelerated in all cases.

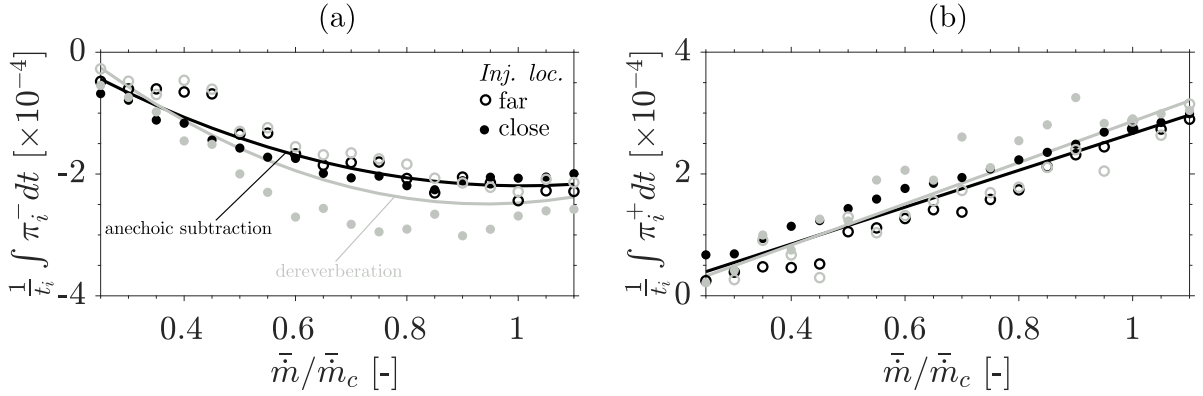


Fig. 5.24 Indirect noise waves: (a) integral of π_i^- with respect to time, and (b) integral of π_i^+ with respect to time as a function of normalised mass flow rate \bar{m}/\bar{m}_c for far (\circ) and close (\bullet) injection locations. Included for visualisation purposes are the average integrals for the anechoic subtraction (—) and dereverberation (---) methods.

Once the compositional wave amplitude ξ has been measured for all the cases, these signals can be used to compute indirect noise transfer functions π_i^\pm/ξ .

5.6 Indirect-to-direct noise ratios

The relative importance of direct and indirect noise has been a matter of longstanding debate in the field⁶⁸. As such, theoretical formulations have been presented to estimate their individual contributions to engine systems.

Assuming a reverberating bicameral system (i.e. two chambers connected by a compact boundary), Rolland²⁷⁸ derived indirect-to-direct noise pressure ratios (i.e. p'_i/p'_d) for the upstream χ_1 and downstream χ_2 chambers:

$$\chi_1 = \frac{p'_{i,1}}{p'_{d,1}} = \frac{|1 + R_{i1}| |R_{o2} T_{i2} \pi_i^+| + |\pi_i^-|}{|1 + R_{o1}| |\pi_d^+| + |R_{i1} \pi_d^-|}, \quad (5.19)$$

$$\chi_2 = \frac{p'_{i,2}}{p'_{d,2}} = \frac{|\pi_i^+| + |R_{i1} T_{o1} \pi_i^-|}{|T_{o1} \pi_d^+| + |T_{o1} R_{i1} \pi_d^-|}. \quad (5.20)$$

The upstream ratio χ_1 is important for the prediction of instabilities (see §1.1.1) whereas the downstream ratio χ_2 helps quantify contributions towards emitted noise (see §1.1.3). For the non-reverberating system presented in §5.3 (i.e. tests CH₄-B), both upstream and downstream boundaries can be considered anechoic (i.e. $R_{i1} = R_{o2} = 0$). In this case, the formulation derived by Rolland²⁷⁸ for the downstream chamber χ_2 simplifies to the ratio presented by Leyko et al.¹⁸⁵ and Durán et al.⁷⁵. For the reverber-

Table 5.3 Summary of indirect-to-direct noise ratios for different cases: fully reverberating bicameral system²⁷⁸, partially non-reverberating bicameral system (i.e. non-reverberating upstream (US) or downstream (DS) chambers with anechoic inlet or outlet, respectively), and fully non-reverberating bicameral system (non-reverberating upstream and downstream chambers with anechoic inlet and outlet).

Ratio	Fully reverberating	Partially or fully non-reverberating		
	$(R_{i1} \neq 0 \ \& \ R_{o2} \neq 0)$	US $(R_{i1} = 0)$	DS (§5.4) $(R_{o2} = 0)$	US & DS (§5.3) $(R_{i1} = R_{o2} = 0)$
χ_1	$\frac{ 1 + R_{i1} R_{o2} T_{i2} \pi_i^+ + \pi_i^- }{ 1 + R_{o1} \pi_d^+ + R_{i1} \pi_d^- }$	$\frac{ R_{o2} T_{i2} \pi_i^+ + \pi_i^- }{ 1 + R_{o1} \pi_d^+ }$	$\frac{ 1 + R_{i1} \pi_i^- }{ 1 + R_{o1} \pi_d^+ + R_{i1} \pi_d^- }$	$\frac{ \pi_i^- }{ 1 + R_{o1} \pi_d^+ }$
χ_2	$\frac{ \pi_i^+ + R_{i1} T_{o1} \pi_i^- }{ T_{o1} \pi_d^+ + R_{i1} T_{o1} \pi_d^- }$	$\frac{ \pi_i^+ }{ T_{o1} \pi_d^+ }$	$\frac{ \pi_i^+ + R_{i1} T_{o1} \pi_i^- }{ T_{o1} \pi_d^+ + R_{i1} T_{o1} \pi_d^- }$	$\frac{ \pi_i^+ }{ T_{o1} \pi_d^+ }$

ating system presented in §5.4, the upstream chamber reverberates, but the downstream boundary is considered anechoic (i.e. $R_{o2} = 0$). The indirect-to-direct noise ratios for all possible reverberating scenarios (with a source in the upstream chamber) are summarised in Table 5.3. The ratios obtained for the two setups employed in this thesis (from §5.3 and §5.4) are presented in Fig. 5.25.

Unsurprisingly, injecting near the nozzle generates the largest indirect-to-direct noise ratios both upstream and downstream of the nozzle. This is because the compositional wave is less dispersed than when injected further away. In the upstream chamber (χ_1), indirect noise is consistently smaller than direct noise, specifically less than 40% of the latter. Moreover, χ_1 is constant across the studied cases, showing no clear trend with air flow rate. In the downstream chamber (χ_2), indirect noise is the same order of magnitude as direct noise for the first few subsonic cases. However, unlike in the upstream chamber, there is a significant dependence on bulk air flow: indirect noise becomes almost an order of magnitude larger than direct noise for the choked cases. We also note that when the inlet is anechoic, the upstream ratio χ_1 decreases relative to when it is not anechoic. The opposite is true in the downstream chamber, where we see that χ_2 is larger when the inlet is anechoic owing to the contribution of the upstream-travelling direct noise wave π_d^- . These conclusions are in line with the analytical work of Mahmoudi et al.²⁰⁸ who estimated that (1) direct noise was dominant upstream of a choked nozzle and (2) indirect noise was dominant downstream of a choked nozzle for a model annular combustor.

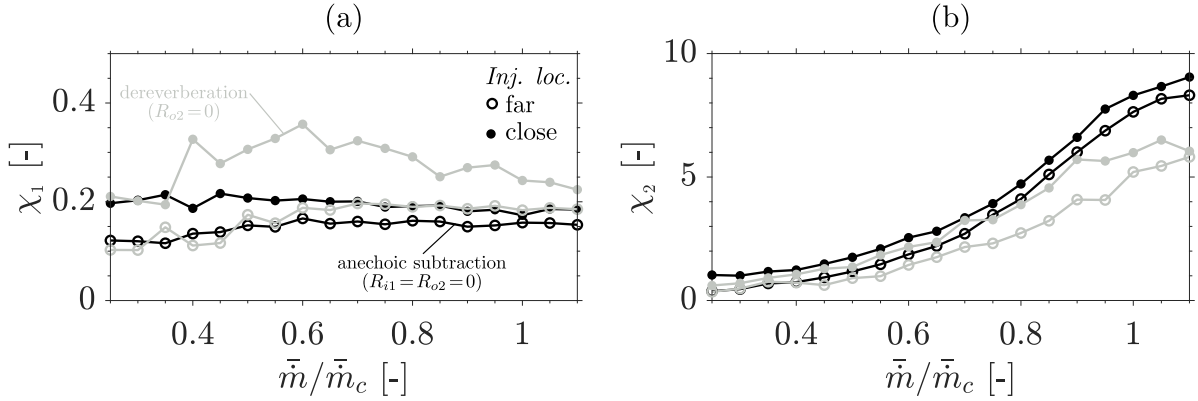


Fig. 5.25 Indirect-to-direct noise ratios for (a) upstream and (b) downstream chambers for far (○) and close (●) injection locations. Included are results obtained via anechoic subtraction (i.e. with anechoic inlet and outlet $R_{i1} = R_{o2} = 0$ condition in §5.3.4 —) and via dereverberation (i.e. with anechoic outlet $R_{o2} = 0$ condition in §5.4.3 —).

5.7 Time-resolved entropic and compositional wave measurement

In §4.3, we presented the Raman technique for measuring methane and nitrogen concentrations. Here we apply the technique for the time-resolved measurement of entropic and compositional wave amplitudes during the transient injection of methane². Firstly, the Raman calibration curves are introduced, and then the injection measurements are presented.

5.7.1 Calibration curves

The calibration method for the Raman measurements was discussed in §4.3.5. As a reminder, during the unsteady injection experiments, we used the nitrogen concentrations to check that the calibrations were consistent. However, it was found that the nitrogen counts were lower or higher than during the original calibration. This was attributed to slight changes in the optical alignment during the setup and quartz etching. Therefore, the total signals had to be re-scaled based on the nitrogen signal obtained on the day, as obtained from the signal after the injection process, specifically once the compositional wave has convected through the probe volume (the method used to obtain the corrected curves is explicitly outlined on page 98). The modified calibration curves are shown in Fig. 5.26.

²The author kindly acknowledges the work of Dr. Lee Weller who collected the Raman data.

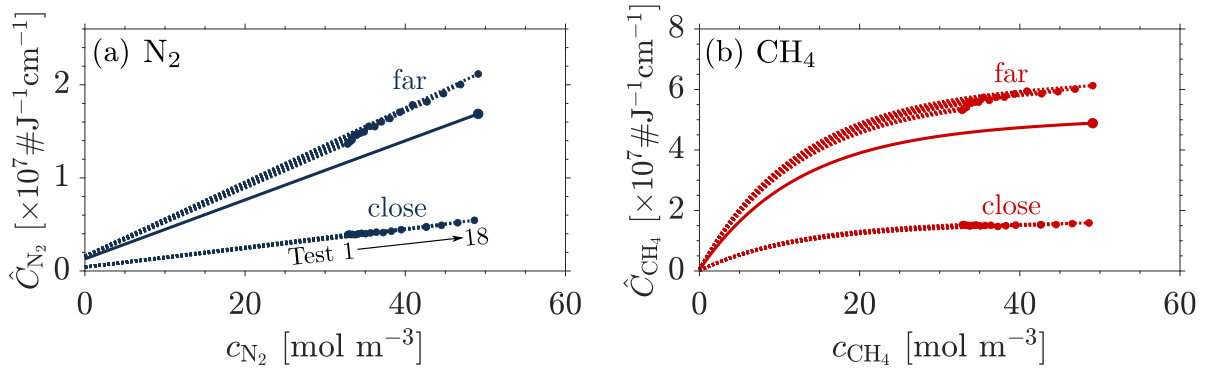


Fig. 5.26 Original calibration curve (—) and corrected calibration curves (.....) used to extract species concentration from the time-resolved integrated counts \hat{C} . The nitrogen counts during the unsteady injection experiments were different than during the original calibration. As a result, two corrected calibration curves are needed (one for each injection campaign) obtained using the methodology described in §4.3.7.

In the case of nitrogen, we see in Fig. 5.26a that with increasing test case (and, therefore, mean pressure – see Table 5.1), the signal maintains its linear dependency on concentration (i.e. for both far and close injection campaigns). We note that, in the case of methane, the error increases with concentration since the calibration curve flattens out above 30 mol m^{-3} , specially so for the close injection case. Measurement errors associated with each test are presented in Appendix B.3.

5.7.2 Results

Figure 5.27 shows the compositional and entropic perturbation amplitudes due to the close and far injections obtained from the Raman signal³. This was run in phase-locked mode with the acoustic measurements for the reverberating system presented in §5.4. Experiments for each injection location were run independently, but the signals have been superimposed for visualisation purposes⁴. Three different flow rates are highlighted in Fig. 5.27b. In comparing the perturbation signatures produced by the injection at the two different locations, three major differences can be identified, particularly in profile, amplitude, and noise levels.

For the close injection case, the probe location is only 62 mm downstream of the injection location. As the convective distance travelled is very short, the pulse is expected

³Changes in the specific entropy due to mean pressure increase are negligible ($< 2\%$) and are, therefore, not considered in the calculation of the entropic wave amplitude (Eq. (2.46)).

⁴Note: an error occurred during test 14 for the close injection case and, unfortunately, this Raman experiment could not be re-run. Consequently, and only for the close injection case, the result for test 15 has been used in place of test 14.

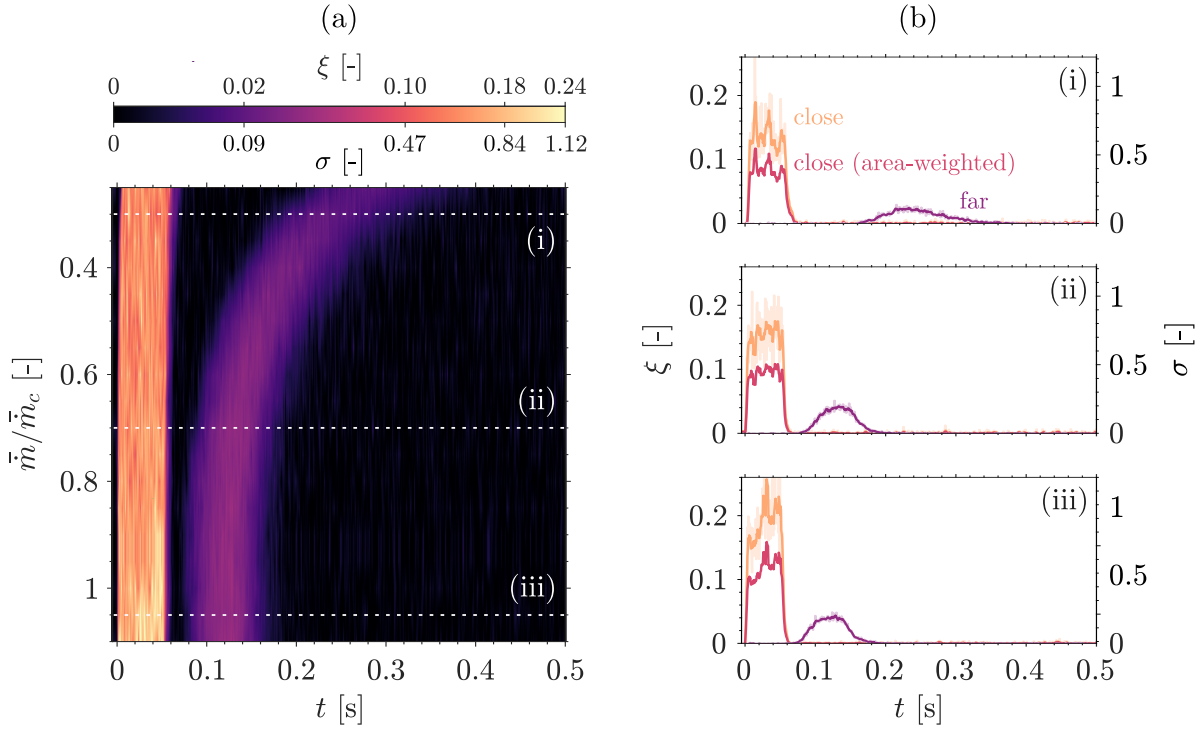


Fig. 5.27 Raman spectroscopy measurements due to injection at (a) close (—) and far (—) locations for all 18 test cases (10 pulse average for each case); experiments for each injection location were run independently, but the signals have been superimposed for visualisation purposes. Colours are mapped for ξ using a power-law relationship ($y = x^\gamma$ where $\gamma = 0.5$) in order to more easily visualise the lower amplitude wave. Linear interpolation is used to map between different mean flow rates in the y-axis; (b) three flow rates from the colourmap are selected to show the changes in signature for different \bar{m}/\bar{m}_c and a five-point (i.e. 3.33 ms) moving average is used; included is the area-weighted result for the close injection case (—).

to have a profile similar to that of the injection pulse excitation signal (i.e. square pulse). This is confirmed by the Raman measurements (Fig. 5.27b). As a result of the proximity of the probe volume to the injection plane, the mean compositional amplitude of the wave may be overestimated by the Raman measurement. The jet diameter at the injection plane is either equal to the inner diameter of the injection pipe (3.4 mm) or smaller (2.5–2.7 mm as estimated in §5.3.2). In Fig. 5.27, we assume an initial injection diameter of 2.5 mm, and use the half-angle of a free jet's turbulent cone ($\theta_{tc} \approx 12^\circ$)^{70,324}. Based on this analysis, the jet requires an approximate mixing length $L_m \approx 90$ mm to fully expand to the duct's wall (Fig. 5.28). Therefore, the jet diameter is estimated to meet the inner wall of the duct approximately 22 mm before the converging section of the nozzle. Furthermore, the area of the injected jet at the probe volume location is estimated to be

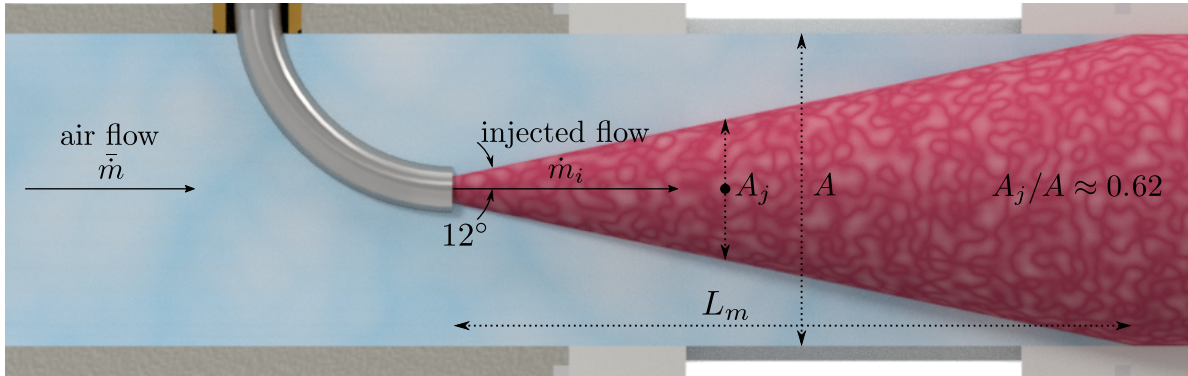


Fig. 5.28 Computer-aided drawing rendering of the injected jet based on the half-angle of a free jet's turbulent cone ($\theta_{tc} \approx 12^\circ$)^{70,324}: for the close injection location, the probed region (●) is located within the mixing length L_m . The ratio of the injection jet area at the probe location A_j to the duct area A is estimated to be approximately 0.62.

approximately 62% of the area of the chamber, as shown in Fig. 5.28. For this reason, an area-weighted disturbance amplitude is included in Fig. 5.27b. Lastly, the high level of noise identified in the close injection result can also be explained by the proximity of the probe volume to the injection location. Since the probed region is estimated to be small relative to the chamber diameter (see Appendix B.1), the Raman measurement is expected to be fairly sensitive to flow perturbations. A shear layer is expected to be generated between the injected methane jet and the surrounding bulk flow of air due to the differences in the respective gas velocities. The shear layer-induced entrainment of air into the methane jet is thought to lead to the large signal fluctuations seen in Fig. 5.27a-b for the close injection location.

For the far injection case, the compositional wave shows evidence of having undergone diffusion and dispersion through the significant reduction in peak amplitude and rounding off of the profile. Furthermore, we see the perturbation is more significantly stretched by the lower bulk air flow rates, as there is more time for mixing to take place relative to the higher bulk flow rates. Lastly, the convective time for each flow rate is identifiable and is in good agreement with the start of indirect noise generation (Fig. 5.22).

The average peak and time-integrated values of the compositional disturbances are shown in Fig. 5.29, where t_i is defined as the time over which the integral is computed. For the purpose of this analysis, the integral limits are selected based on the leading and trailing edges of the pulse, on a case by case basis (as done in §5.5). Note that for each case t_i here is different to the t_i used in §5.5 as the acoustic and compositional waves have different profiles.

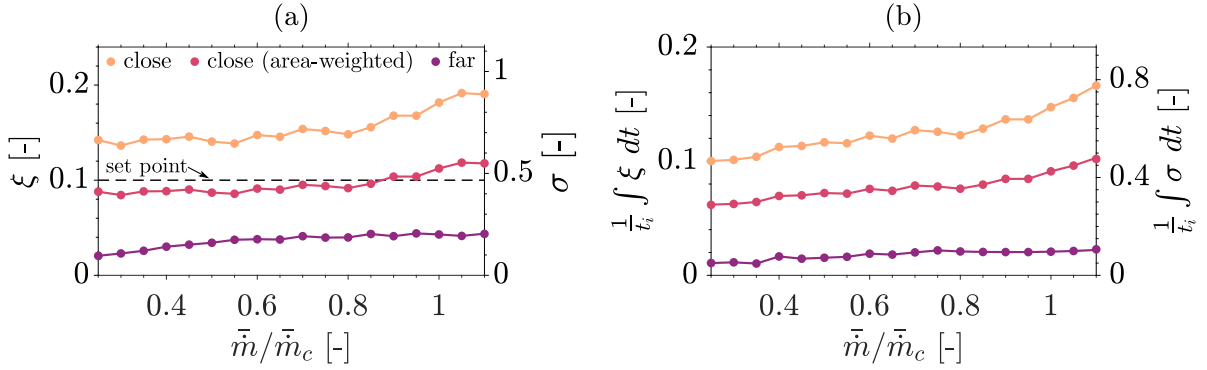


Fig. 5.29 Raman measurements: (a) mean peak compositional amplitude ξ and (b) time-integrated compositional amplitude $\frac{1}{t_i} \int \xi dt$ for close (—) and far (—) injection locations with associated entropic wave amplitude as per Eq. (2.46). Also included is the area-weighted close injection result (—).

With increasing flow rate, the average disturbance amplitude for the close and far injection cases both increase: from 0.14 to 0.19 and 0.02 to 0.04, respectively. It is worth noting that the average standard error for the close and far injection results is 0.007 and 0.002, respectively (see Appendix B.3). The area-weighted results agree favourably with the methane injection mass fraction predicted in §5.3.2 (Fig. 5.7) for the lower bulk flow rates and with the set point (i.e. $Y_i = \dot{m}_i/\bar{m} = 0.1$) for the higher flow rates. Interestingly, we see that for the far injection case, the compositional wave is fully accounted for by using the integral quantity (i.e. quantity is relatively independent of air flow rate). This is an indication that the wave at this location has expanded across the duct and become homogeneous. The same cannot be said for the integral quantity of the close injection results, which, similarly to the average disturbance amplitude, increase moderately with air flow rate. The time-integrated compositional perturbation of the two injection locations (far vs area-weighted close) are, on average, 77% different.

Now that the compositional wave amplitude ξ has been measured for each case, indirect noise transfer functions π_i^\pm/ξ can be calculated.

5.8 Entropic and compositional nozzle transfer functions

The final objective of the model experiment presented is to compute the indirect noise transfer functions π_i^\pm/ξ of the nozzle. Since compositional waves are coupled to entropic waves, π_i^\pm/σ is also computed based on the entropic-compositional coupling term $\Delta s/\bar{c}_p$ as per Eq. (2.46). Three methods of computing π_i^\pm/ξ are contrasted. In particular, we:

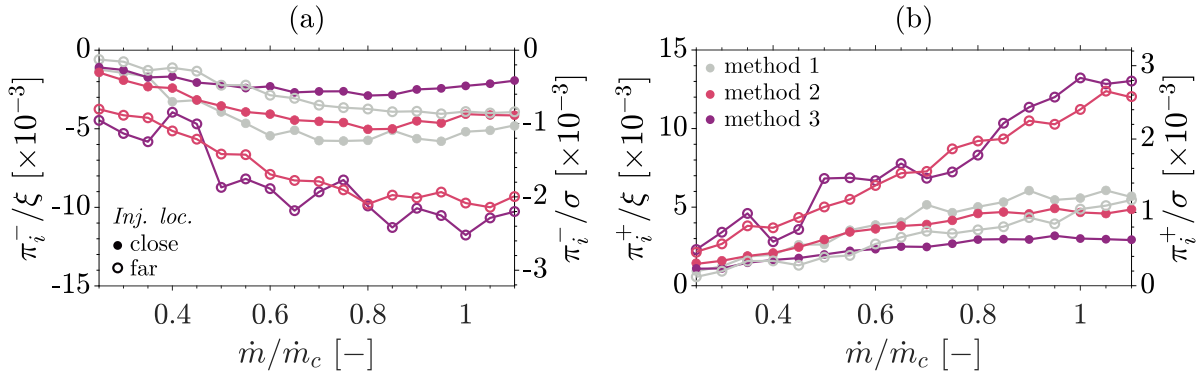


Fig. 5.30 Indirect noise nozzle transfer functions π_i^\pm/ξ (left y -axis) and π_i^\pm/σ (right y -axis) due to injection at close (\bullet) and far (\circ) locations. Contrasted are results using method 1 – proposed by De Domenico et al.⁶⁴ (—), method 2 – using peak quantities (—), and method 3 – using time-integrated quantities (—).

1. use the method presented by De Domenico et al.⁶⁴, where the peak π_i^\pm obtained via dereverberation (Fig. 5.23) is divided by the injection mass fraction $Y_i = \dot{m}_i/\bar{m} = 0.1$ (where \dot{m}_i is measured by the mass flow meter),
2. use the peak π_i^\pm measured in the non-reverberating system (Fig. 5.23) divided by the peak compositional amplitude ξ measured upstream of the nozzle using the Raman technique (Fig. 5.29a),
3. use the time-integrated $\frac{1}{t_i} \int \pi_i^\pm dt$ measured in the non-reverberating system (Fig. 5.24) divided by the time-integrated compositional amplitude $\frac{1}{t_i} \int \xi dt$ measured upstream of the nozzle using the Raman technique (Fig. 5.29b).

For methods 2 and 3, we explicitly assume that the injected flow of methane is the same for the reverberating and non-reverberating systems, so that that the acoustic waves obtained via the anechoic subtraction method can be normalised by the Raman measurements. Additionally, we use the area-weighted result for the close injection transfer functions. The results are shown in Fig. 5.30 – for simplicity, a single y axis label is used.

For both upstream π_i^-/ξ and downstream π_i^+/ξ transfer functions, we see that methods 1 and 2 show good agreement in the case of close injection. In contrast, method 3 (i.e. using time-integrated quantities) yields lower transfer functions (approximately half the value obtained using methods 1 and 2). This could be a symptom that there are issues with the integral limits selected for both the acoustic and the compositional wave measurements.

Further differences are more evident when comparing the results in the case of the far injection. In method 1, we see that far injection yields a smaller transfer function

when compared to close injection – physically this makes sense, as one would expect a more diffused and dispersed compositional wave to produce lower noise. However, methods 2 and 3 demonstrate the opposite trend. Indeed, since both the peak and integral perturbations are smaller in the case of far injection relative to close injection (Fig. 5.29), whereas π_i^\pm remain approximately the same, the transfer functions are much larger (just over twice the value of method 1). This would indicate that the Raman measurement (for the case of the far injection location) is missing a fraction of the compositional disturbance that is unaccounted for. This leads to a false conclusion that the far injection produces a larger amount of indirect noise for the same mass accelerated (as much as approximately five times larger for method 3). In light of these results, we hypothesise that point-wise measurements may not be the ideal measurement method for this type of problem.

The far injection is expected to produce the perturbation that most closely approximates to 1D theory since the long convective length allows the wave to mix with the bulk flow before reaching the probing region²⁷⁶. On the other hand, since the injection process is three-dimensional, the close injection case is expected to deviate from 1D theory the most (although the area-weighted result is employed to counter this issue). Two-dimensional visualisation of the flow field upstream of the nozzle (via planar diagnostics and/or numerical simulations) would aid in better understanding the reason for the conclusions presented here.

5.9 Summary

In this chapter, we presented the measurement of acoustic perturbations due to the low-frequency, single pulse, co-flow injection of air or methane into a low Mach number bulk flow of air. This was done using a model thermoacoustic system (CWR) with reverberating and non-reverberating upstream chambers.

The direct noise measured experimentally was compared to the derived co-flow wave source model. Good agreement was found assuming a 10% error in injection mass fraction and an effective injection diameter that is smaller than the geometric diameter. Moreover, a new method of quantifying indirect noise wave amplitudes in a model system was demonstrated using pseudo-anechoic tubes. This was the first time non-reverberated indirect noise waves were measured.

Two convective lengths were used to investigate the effects of dispersion on the indirect noise generated. The pressure signals due to far injection show clear signs of dispersion, particularly as the signature is Gaussian and has a reduced peak, compared to the

pressure signals due to close injection which resemble a square pulse. Moreover, two methods of quantifying indirect noise were contrasted – in particular, non-reverberated pressure signals using the anechoic subtraction method and dereverberated pressure signals. The non-reverberated results showed good agreement with dereverberated results for the far injection location. For the close injection location, differences are hypothesised to be caused by a valve ringing phenomenon that is present in the non-reverberated results. For both reverberating and non-reverberating upstream chamber CWR setups, direct noise was found to be larger than indirect noise in the upstream chamber. The opposite was found to be true in the downstream chamber.

Additionally, the measurement of local concentration using spontaneous Raman spectroscopy was made in phase-locked mode with the acquisition of pressure for the reverberating system. This demonstrated the viability of running the experimental techniques in phase-locked mode. The time-integrated compositional waves generated by the injection at the two different locations were, on average, 77% different. This was attributed to the fact that, for the case of close injection, the probe volume was located inside the expanding turbulent cone of the injected jet. Two-dimensional diagnostics measurements or numerical simulations would help assess whether this is true. Dispersion effects are clearly captured and the convective time for each flow rate is identifiable and in agreement with the start of indirect noise generation seen in the pressure signals. This reinforces the importance of the simultaneous acquisition of acoustic and species perturbations.

Finally, experimental indirect noise transfer functions were computed using three different methods. Agreement was not found in all cases – in particular, the results falsely suggest that injecting far from the nozzle produces larger transfer functions than injecting close to the nozzle (by up to a factor of five). In light of these results, we hypothesise that point-wise measurements may not be the ideal measurement method for this type of problem. This work highlights the differences that can be found when computing indirect noise transfer functions experimentally using different methods. This is important as it evidences the difficulty in demonstrating full quantitative agreement between theory and experiments.

Chapter 6

Direct & indirect noise experiments II: pulse burst injection

THE pulse burst, co-flow injection of methane into a low Mach number mean flow of air at frequencies of up to 250 Hz is presented. Experiments are carried out using the CWR with a reverberating upstream chamber – subsonic and sonic (choked) conditions are investigated for a convergent-divergent nozzle. Acoustic pressure measurements are made in tandem with spontaneous Raman spectroscopy measurements of the local concentration upstream of the nozzle. Results for two limit cases are shown and a preliminary analysis is presented.

6.1 Motivation and objectives

When the length of a nozzle is small relative to the acoustic perturbation wavelength, its spatial extent is irrelevant to the reflection and refraction processes, and the nozzle is called *acoustically compact*. The dimensionless frequency $He = fL_n/\bar{c}$ is used as a metric for acoustic compactness, where f is the perturbation frequency, L_n is the nozzle length, and c is the speed of sound. When $He \rightarrow 0$, a nozzle is described as compact. As He increases (physically this is equivalent to increasing the frequency of the perturbation and/or increasing the spatial extent of the element), the acoustic wavelength may become of the order of the nozzle length, so that it is no longer a good approximation to assume compactness. Magri et al.^{204,206} demonstrated the effects of non-compactness on the acoustic response of subsonic and supersonic nozzles with a linear velocity profile. With increasing He , the compositional indirect noise is shown to decrease (both upstream and downstream of the nozzle), and both amplitude and phase are substantially affected. However, there is still no experimental evidence to substantiate this.

In this chapter, we present an experimental investigation into the indirect noise generated by the high-frequency injection of compositional inhomogeneities. Specifically, this is done using the co-flow, pulse burst injection of methane at frequencies f_i ranging from 2 to 250 Hz and approximate injection mass fractions Y_i ranging from 4 to 21%. Time-resolved Raman spectroscopy measurements are used to characterise the profile of the disturbances. The overarching goal of this experimental campaign is to present results at more realistic acoustic and compositional forcing frequencies and amplitudes.

The main limitation of some of the reviewed model experiments is the infrasound frequency range at which they operate in order to obtain time separation between direct and indirect noise^{62,277}. When injecting at high frequencies near the nozzle, time separation is no longer possible since direct and indirect noise are generated synchronously. Rolland²⁷⁸ proposed a source identification technique that, in theory, could be used to extract direct and indirect noise amplitudes at any frequency (section V.4.1, page 94). The hypothesis put forward states that, with two pressure measurements upstream of the nozzle (at locations x_{11} and x_{12}) and two measurements downstream of the nozzle (at locations x_{21} and x_{22}), the acoustic source signals could be extracted using the following formulation:

$$\hat{\boldsymbol{\pi}} = \boldsymbol{Z}^{-1}\hat{\boldsymbol{\mathcal{P}}}, \quad (6.1)$$

where $\hat{\boldsymbol{\mathcal{P}}}$ is the vector of the normalised pressure signals:

$$\hat{\boldsymbol{\mathcal{P}}} = \left[\frac{\hat{p}'_{11}}{\bar{\gamma}\bar{p}_1}, \frac{\hat{p}'_{12}}{\bar{\gamma}\bar{p}_1}, \frac{\hat{p}'_{21}}{\bar{\gamma}\bar{p}_2}, \frac{\hat{p}'_{22}}{\bar{\gamma}\bar{p}_2} \right]^T, \quad (6.2)$$

$\hat{\boldsymbol{\pi}}$ is the vector of the acoustic wave amplitudes:

$$\hat{\boldsymbol{\pi}} = \left[\widehat{\pi}_d^+, \widehat{\pi}_d^-, \widehat{\pi}_i^+, \widehat{\pi}_i^- \right]^T, \quad (6.3)$$

and \boldsymbol{Z} is a transfer function matrix which accounts for the reverberation, reflection, transmission, and attenuation effects of the system:

$$\boldsymbol{Z} = \begin{bmatrix} \dot{\mathcal{R}}_1^+(x_{11}, x_{s1}) & \dot{\mathcal{R}}_1^-(x_{11}, x_{s1}) & 0 & \dot{\mathcal{R}}_1^-(x_{11}, L_1) \\ \dot{\mathcal{R}}_1^+(x_{12}, x_{s1}) & \dot{\mathcal{R}}_1^-(x_{12}, x_{s1}) & 0 & \dot{\mathcal{R}}_1^-(x_{12}, L_1) \\ \dot{\mathcal{T}}_1^+(L_1, x_{s1})\dot{\mathcal{R}}_2^+(x_{21}, 0) & \dot{\mathcal{T}}_1^-(L_1, x_{s1})\dot{\mathcal{R}}_2^+(x_{21}, 0) & \dot{\mathcal{R}}_2^+(x_{21}, 0) & \dot{\mathcal{T}}_1^-(L_1, L_1)\dot{\mathcal{R}}_2^+(x_{21}, 0) \\ \dot{\mathcal{T}}_1^+(L_1, x_{s1})\dot{\mathcal{R}}_2^+(x_{22}, 0) & \dot{\mathcal{T}}_1^-(L_1, x_{s1})\dot{\mathcal{R}}_2^+(x_{22}, 0) & \dot{\mathcal{R}}_2^+(x_{22}, 0) & \dot{\mathcal{T}}_1^-(L_1, L_1)\dot{\mathcal{R}}_2^+(x_{22}, 0) \end{bmatrix}. \quad (6.4)$$

This has been simplified assuming the outlet of the system is anechoic ($R_{o2} = 0$). The author kindly re-directs the reader to the reference for the full derivation of this matrix system¹. The relevant transfer functions also simplify to:

$$\dot{\mathcal{R}}_1^+ = \frac{R_{i1}R_{o1}e^{i\omega(\tau_{p1}+\tau_1)-\alpha(l_{p1}+2L_1)} + R_{o1}e^{-i\omega\tau_{q1}-\alpha l_{q1}}}{1 - R_{i1}R_{o1}e^{-i\omega\tau_1-2\alpha L_1}}, \quad (6.5)$$

$$\dot{\mathcal{R}}_1^- = \frac{e^{-i\omega\tau_{r1}-\alpha l_{r1}} + R_{i1}e^{-i\omega\tau_{s1}-\alpha l_{s1}}}{1 - R_{i1}R_{o1}e^{-i\omega\tau_1-2\alpha L_1}}, \quad (6.6)$$

$$\dot{\mathcal{R}}_2^+ = e^{-i\omega\tau_{p2}-\alpha l_{p2}}, \quad (6.7)$$

$$\dot{\mathcal{T}}_1^+ = \frac{T_{o1}e^{i\omega\tau_{p1}-\alpha l_{p1}}}{1 - R_{i1}R_{o1}e^{i\omega\tau_1-2\alpha L_1}}, \quad (6.8)$$

$$\dot{\mathcal{T}}_1^- = \frac{T_{o1}R_{i1}e^{i\omega\tau_{s1}-\alpha l_{s1}}}{1 - R_{i1}R_{o1}e^{i\omega\tau_1-2\alpha L_1}}, \quad (6.9)$$

where L_1 is the upstream chamber length, $\tau_1 = 2L_1/\bar{c}$ is the upstream round-trip time delay, and τ_p , τ_q , τ_r , and τ_s are the time delays between sources and transducers. The time delays for $\dot{\mathcal{T}}_1^+$ and $\dot{\mathcal{T}}_1^-$ are evaluated at the outlet of the first chamber.

This method requires the characterisation of the system properties (R_{o1} , T_{o1} , R_{i1} , α) as a function of frequency and flow rate. As a result, this chapter is divided as follows. Firstly, the test cases are outlined. Secondly, the methods used to characterise the acoustic boundaries are described and results are presented. Thirdly, the pressure perturbations due to the co-flow injection of methane are shown along with the Raman measurements. Lastly, preliminary source identification results are presented and discussed.

¹Note that the matrix system has been corrected here as it was wrongly typed out in the original reference²⁷⁹.

6.2 Test cases

Dowling and Mahmoudi⁶⁸ showed that combustor noise for a turbojet engine at approach conditions has a peak output noise level between 100 Hz and 300 Hz (Fig. 1.4). As such, a range of injection frequencies in that region ($2 \leq f_i \leq 250$ Hz) is investigated. Additionally, engine-representative perturbations can be as large as 40% of the mean flow average conditions¹⁷³. Consequently, a range of injection mass fractions (estimated to be $4 \leq Y_i \leq 21\%$) is investigated.

The pulse bursts are triggered by a $t_p = 2$ ms square pulse signal. For the higher frequencies, the nozzle length is comparable to the wavelength of the disturbances ($He_{\max} = 0.22$), therefore the effects of acoustic non-compactness on indirect noise

Table 6.1 Experimental test conditions: injection frequency f_i , maximum estimated Helmholtz number He , primary mass flow rate \bar{m} , estimated injection mass fraction of methane Y_i , estimated injected mass flow of methane \dot{m}_i , and number of pulses during anechoic window.

Case	f_i [Hz]	$He = f_i L_n / \bar{c}$ [$\times 10^{-3}$]	\bar{m} [g s ⁻¹]	Y_i [%]	\dot{m}_i [g s ⁻¹]	No. pulses [-]
A1-6	2	1.8	6 – 11	4	0.24 – 0.44	2
B1-6	10	8.8	6 – 11	4	0.24 – 0.44	7
C1-6	30	26.0	6 – 11	4	0.24 – 0.44	21
D1-6	60	53.0	6 – 11	4	0.24 – 0.44	42
E1-6	100	88.0	6 – 11	8	0.48 – 0.88	70
F1-6	125	110.0	6 – 11	8	0.48 – 0.88	88
G1			6	17	1.02	
G2			7	15	0.90	
G3	187.5	170.0	8	13	0.78	132
G4			9	11	0.66	
G5			10	10	0.60	
G6			11	9	0.54	
H1			6	21	1.26	
H2			7	18	1.08	
H3	250	220.0	8	16	0.96	175
H4			9	14	0.84	
H5			10	13	0.78	
H6			11	12	0.72	

generation should be present^{204,206}. At each frequency, six mean flow rates \bar{m} are investigated: 6 g s⁻¹ to 11 g s⁻¹ in 1 g s⁻¹ increments. As noted in §4.2.6, the nozzle chokes at 10 g s⁻¹, therefore four of the cases have subsonic nozzle flow conditions, and two have sonic (choked) conditions. Table 6.1 summarises the test conditions.

6.3 High frequency system characterisation

In order to implement the source identification technique (as per Eq. (6.1)), the acoustic response of the convergent-divergent nozzle and the perforated plate geometries needs to be characterised as a function of frequency and air flow rate. This is done using a numerical framework which combines RANS and Linearised Navier Stokes–Equations (LNSE) methods, where the former is used to converge on a velocity field which is fed into the LNSE solver to compute the acoustic response of the geometries (details on this later). The results for the perforated plate are compared to experimental multi-microphone method measurements which are used to validate the numerical results.

6.3.1 Experiments: multi-microphone method

The multi-microphone method is a popular technique whereby the reflection coefficient of a boundary can be obtained from the measurement of acoustic fluctuations at two or more locations^{24,41,162,294}. The theory and experimental methodology employed are described in this subsection.

Theory

The propagation of sound through a cylindrical flow duct with subsonic mean flow is not an elementary problem. Nonetheless, and as noted by Åbom and Bodén², it can be simplified for a cylindrical setup which is long and straight, with rigid walls under the low-frequency assumption. The low-frequency analysis is possible when the frequencies of interest are below the cut-off frequency f_c defined as:

$$f_c = \frac{1.84\bar{c}}{\pi d} \sqrt{1 - \bar{M}^2}. \quad (6.10)$$

In this case, all modes other than the plane-wave mode are evanescent and their amplitudes decay exponentially²⁷⁴.

Under the assumptions outlined above, the acoustic pressure measured at any location can be described by the sum of the incident and reflected pressure waves, as shown in

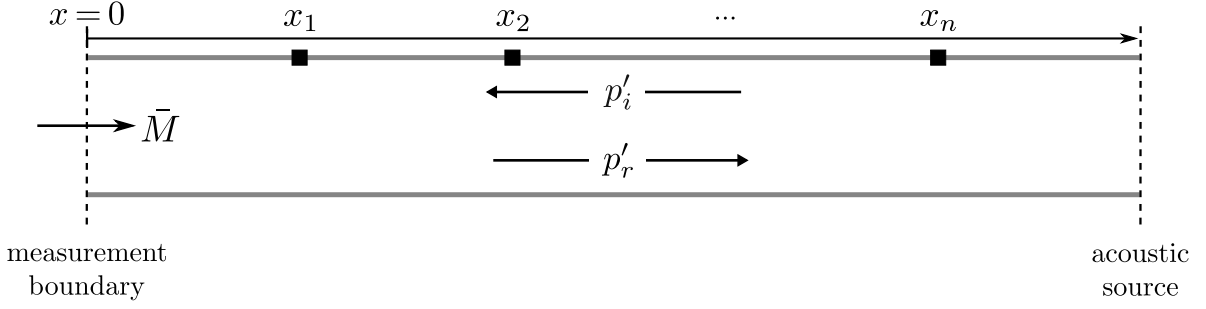


Fig. 6.1 Acoustic pressure field $p' = p'_i + p'_r$ in a cylindrical flow duct with low Mach number mean flow \bar{M} .

Fig. 6.1:

$$p'(x, t) = p'_i(x, t) + p'_r(x, t), \quad (6.11)$$

where

$$p'_i(x, t) = p^- e^{i(\omega t + k^- x)}, \quad p'_r(x, t) = p^+ e^{i(\omega t - k^+ x)}, \quad (6.12)$$

and p^\pm are the acoustic wave amplitudes, and $k^\pm = 2\pi f/\bar{c}(1 \pm \bar{M})$ are the wavenumbers which account for the effects of low Mach number flow. Here it is assumed that the acoustic propagation is non-attenuated ($\alpha = 0$) and non-dispersive, where effects due to heat conduction, viscosity, and sound and flow field interactions are also neglected². Note that the incident wave is defined as negative owing to the fact that the direction of flow is chosen to be positive (as shown in Figs. 6.1 and 6.2).

In the frequency domain, the sound field waves can be written as:

$$\hat{p}_i(x, \omega) = \hat{p}^- e^{ik^- x}, \quad \hat{p}_r(x, \omega) = \hat{p}^+ e^{-ik^+ x}, \quad (6.13)$$

where the Fourier transform of the acoustic spectra is $\hat{p}(x, \omega) = \int_{-\infty}^{\infty} p'(x, t) e^{-i\omega t} dt$. We can now define the reflection coefficient as the ratio of the reflected and incident amplitudes, such that:

$$R(x) = \frac{\hat{p}_r}{\hat{p}_i} = \frac{\hat{p}^+ e^{-ik^+ x}}{\hat{p}^- e^{ik^- x}}. \quad (6.14)$$

Re-writing Eq. (6.11) in the frequency domain for the pressure measured at two transducer locations gives:

$$\begin{aligned} \hat{p}_1 &= \hat{p}^- e^{ik^- x_1} + \hat{p}^+ e^{-ik^+ x_1}, \\ \hat{p}_2 &= \hat{p}^- e^{ik^- x_2} + \hat{p}^+ e^{-ik^+ x_2}. \end{aligned} \quad (6.15)$$

We can do this for n transducers and formulate the problem as a system of equations $\mathbf{Ax} = \mathbf{b}$, where:

$$\mathbf{A} = \begin{pmatrix} e^{ik^-x_1} & e^{-ik^+x_1} \\ e^{ik^-x_2} & e^{-ik^+x_2} \\ \vdots & \vdots \\ e^{ik^-x_n} & e^{-ik^+x_n} \end{pmatrix}, \quad \mathbf{x} = \begin{pmatrix} \hat{p}^- \\ \hat{p}^+ \end{pmatrix}, \quad \mathbf{b} = \begin{pmatrix} \hat{p}_1 \\ \hat{p}_2 \\ \vdots \\ \hat{p}_n \end{pmatrix}, \quad (6.16a-c)$$

which we can solve for \mathbf{x} . When more than two transducers are employed, this becomes an over-constrained problem and can be solved using least-squares method which reduces the error in the calculation^{131,160}.

We can then obtain the reflection coefficient at the measurement boundary of interest by setting $x = 0$ in Eq. (6.14), which yields:

$$R(x = 0) = \frac{\hat{p}^+}{\hat{p}^-}. \quad (6.17)$$

In order to minimise the reflection coefficient's sensitivity to errors in the measured data, Åbom and Bodén² proposed that the transducer separation Δx should be dictated by the following limits:

$$0.1\pi < \frac{k\Delta x}{(1 - M^2)} < 0.8\pi. \quad (6.18)$$

For low Mach number flows, we assume $\bar{M}^2 \approx 0$ and re-formulate Eq. (6.18) in terms of wavelength:

$$\frac{1}{20}\lambda < \Delta x < \frac{2}{5}\lambda. \quad (6.19)$$

Åbom and Bodén² further suggest that the lowest sensitivity to error is found around:

$$\Delta x = \frac{1}{4}\lambda. \quad (6.20)$$

Setup and methodology

An acoustic characterisation campaign is undertaken to calculate the reflection coefficient of the perforated plate as a function of the frequency and bias flow (i.e. air mass flow rate). An experimental set-up using an *impedance tube* test rig is presented, similar to ones presented in literature^{19,308,339}.

A modified version of the modular CWR setup is employed. Notably, the test rig consists of a piston that is terminated by a perforated plate (see §4.2.1). The downstream surface of the plate is defined as $x = 0$. The rig is terminated by a convergent-divergent

nozzle (see §4.2.2) – this is done to ensure the reflection coefficient is computed at the same experimental conditions (in specific, the mean pressure) as the injection experiments. Two Monacor KU-516 horn drivers are used to provide the acoustic excitation. These were modified in order to withstand the pressure increase. In particular, each horn driver was removed from its original diecast housing and put into a pressure-sealed metal casing, which included a pressure equalisation tube, as shown in Fig. 6.2. The horn drivers are located at the axial center of a duct that is added to the CWR setup, in between the pressure measurement sections and the nozzle. They are driven by an IMG Stageline STA-500 amplifier which has a maximum rated power of 600 W and operational frequency range of 10–20,000 Hz¹⁵⁵. The flow downstream of the perforated plate is turbulent (as described in §4.2.6) and, therefore, the nominal flow noise is expected to be large. For this reason, the drivers are positioned opposite each other, and at the same axial location, in order to increase the signal-to-noise ratio. To further maximise the acoustic excitation level and focus the output power from the horn drivers, the study is undertaken at discrete frequencies using swept sinusoidal excitation⁷. The frequency range of interest is

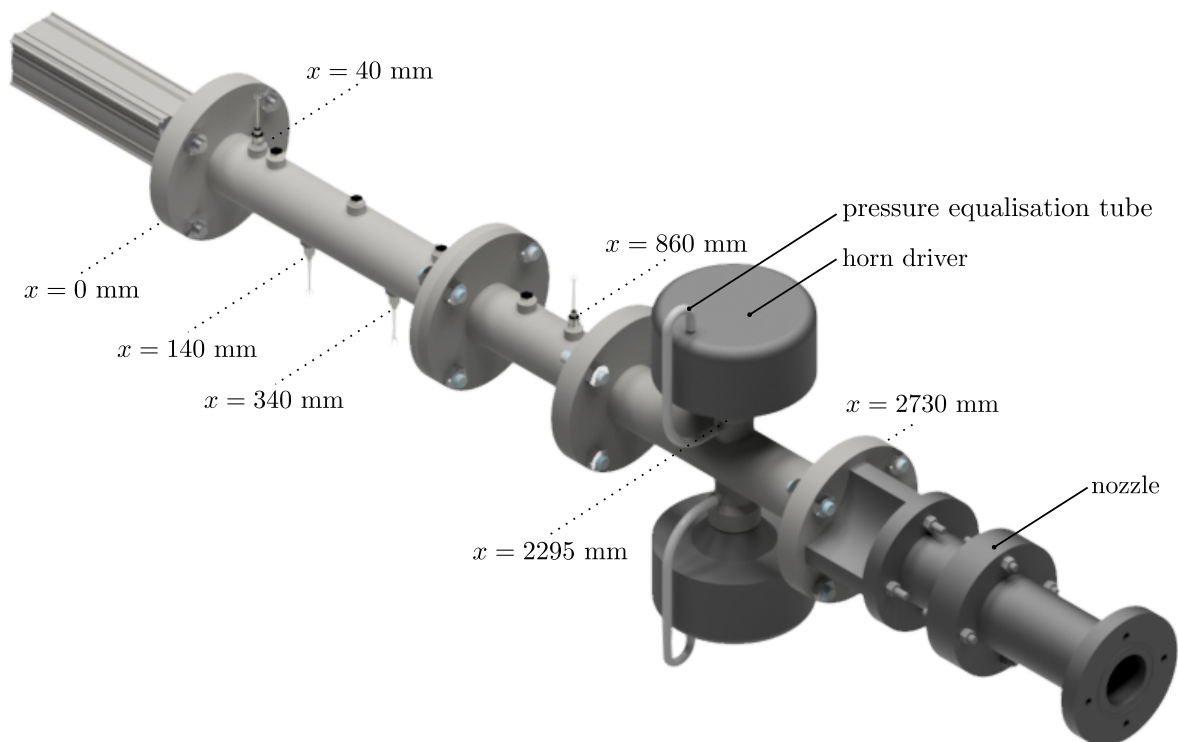


Fig. 6.2 Modified CWR setup used to characterise the inlet (perforated plate) reflection coefficient R_{i1} via the multi-microphone method: sinusoidal excitation is provided by two horn drivers and pressure perturbations are measured using the four pressure transducers highlighted. Lengths not to scale.

$60 \leq f \leq 1000$ Hz. This is below the cut-off frequency $f_c \simeq 5025$ Hz for the propagation of non-planar acoustic modes for the duct². Of particular interest was the computation of the reflection coefficient at the pulse burst injection frequencies (see Table 6.1) and their harmonics. The 28 frequencies studied captured up to at least the 5th harmonic of the pulse burst frequencies studied in this chapter. This frequency sweep was repeated for 7 different mean mass flow rates of air (0, 6, 7, 8, 9, 10 and 11 g s⁻¹). For the latter two cases, the nozzle downstream of the perforated plate is choked.

Four flush-mounted Kulite piezoresistive pressure transducers (as described in §4.2.5) are used to perform the acoustic wave decomposition using the multi-microphone method whereby the over-determined system of equations, described by Eq. (6.16), is solved using the least-squares method. The relative transducer separations are 100 mm, 200 mm, 300 mm, 520 mm, 720 mm and 820 mm, allowing for the computation of the reflection coefficient for the frequency range investigated as per Eq. (6.19)³. A distance of at least 10D (400 mm) is recommended between the transducers and the horn drivers in order to avoid non-linearities and ensure the planar wave condition is met^{24,271}. For the experimental campaign presented here, this separation is at least 35D (1435 mm).

Each test case was computed from an acquisition window of 100 s sampled at 10 kHz. All cases had controlled excitation pressure amplitudes such that the pressure perturbations measured at the transducer locations fell within the small perturbation theory assumption (i.e. <5% of mean pressure).

6.3.2 Numerical investigation: RANS/LNSE

In order to predict the acoustic scattering matrix of both geometries in the linear regime, a hybrid approach is employed: first, the steady-state flow field is computed using the RANS formulation and, subsequently, the linear perturbations around this state are solved for with the fully compressible LNSE⁴.

²Longitudinal resonances could be present in the flow duct due to the highly reflective boundaries (i.e. the perforated plate and the nozzle)¹⁷⁶.

³Focusing on the two frequency limit cases: for $f = 60$ Hz (lowest frequency), the transducer separation should be $286 < \Delta x < 2290$ mm; for $f = 1000$ Hz (highest frequency), the transducer separation should be $17 < \Delta x < 140$ mm.

⁴The author kindly acknowledges that this numerical work was done by Kah Joon Yong (RANS) and Maximilian Meindl (LNSE) as part of a collaboration with Prof. Wolfgang Polifke's group at Technische Universität München (TUM). The description of the numerical setups was written with their assistance and the data is presented here with their consent.

RANS

As of the time of completion of this thesis, only the nozzle simulations have been computed and, therefore, the numerical setup refers only to the nozzle case.

The mean fields are computed using the RANS formulation with the k - ω SST turbulence model²²⁴. The mass flow rates are specified at the inlet as a Dirichlet boundary condition for the velocity. At the outlet, the mean pressure measured experimentally is specified for the pressure boundary condition. A 1/8th geometry is used to minimise computational costs, and, as a result, a periodic boundary condition is employed. A no slip boundary condition is used at the wall. Lastly, wall functions are used for the turbulent kinetic energy k , turbulent dissipation rate ω , and turbulent viscosity ν_t .

For the three lowest mass flow rates (6, 7, and 8 g s⁻¹), the nozzle flow is subsonic and steady state flow is observed. As such, the compressible steady state solver *rhoSimpleFoam* is used. At higher mass flow rates (9, 10, and 11 g s⁻¹), the nozzle flow reaches transonic/sonic conditions. For these cases, the compressible transient solver *sonicFoam* is used. The upstream mean pressure measured experimentally is compared with the simulated results for validation purposes. We accept a maximum relative error of 10%.

LNSE

The LNSE are solved in the frequency domain for a given set of discrete frequencies. At each frequency, the perturbed flow field is computed for upstream acoustic forcing. Characteristic non-reflective boundary conditions at the inlet and outlet ensure free propagation of all outgoing waves (i.e. acoustic waves are not reflected). The forcing is superimposed on top of the characteristic boundary conditions and imposes a real-valued acoustic wave with unity amplitude normal to the respective boundary. The coefficients of the scattering matrix are retrieved by measurement of the spatially averaged acoustic waves exiting the computational domain normal to the inflow and outflow. With this approach, the coefficients T_{o1} and R_{o1} can be determined with upstream forcing. The boundary conditions at all other boundaries are chosen as the linearised equivalent of the RANS boundary conditions. Further details about the method can be found in Meindl et al.²²³ and a description of the numerical approach can be found in Meindl et al.²²².

The frequency band up to 1,000 Hz is investigated in 10 Hz steps. All computations were run on a machine with 128 GB RAM, employing 6 CPUs. Solving for one perturbed flow field at a given frequency takes approximately 10 minutes for the nozzle and 25 minutes for the perforated plate case. LNSE results were obtained for one perforated plate case (no bias flow, $\bar{m} = 0$ g s⁻¹) and for all nozzle flow rate cases ($\bar{m}/\bar{m}_c = 0.6$ –1.1).

6.3.3 Results

The acoustic results are presented, and, for one case, comparisons are made between experimental and numerical data. The RANS mean fields are not shown here.

Validation case: perforated plate

The impedance of perforated plate geometries has been a source of various analytical, numerical and experimental studies. It has been shown to be dependent on many variables, including - but not limited to - forcing frequency, forcing amplitude, plate porosity, hole diameter, spacing between holes, plate thickness, pressure drop across plate, and bias flow^{19,161}. Usually employed as part of a liner configuration for their damping properties^{120,147,285}, here the perforated plate has been used to maximise the reflection coefficient at the inlet when a mid-to-high Mach number bias flow is passing through it. Investigations for perforated plates tend to assume low Mach number flows^{19,136}. As a result, for higher Mach number bias flows, comparisons between numerical predictions and experiments are useful²⁹¹.

Figure 6.3 provides an initial comparison between experimental and numerical data for the case of no bias flow (i.e. $\bar{m} = 0 \text{ g s}^{-1}$). As expected, the lower frequencies are more prone to experimental error since the transducer separation is less than optimal (i.e. $\Delta x = 1/4\lambda$). However, overall agreement in the magnitude improves with increasing frequency. The opposite is true for the phase. At frequencies below 300 Hz, the experiments and numerical data describe a compact (i.e. zero phase shift) boundary. However, with increasing frequency, the phase shift becomes more pronounced for the numerical results (reaching $\pi/2$ rads at 1000 Hz), whereas experimental data remains fairly constantly near and around 0 rads. Any mismatch between the results could be due to not having an anechoic termination (i.e. to reduce error due to resonances¹⁶²).

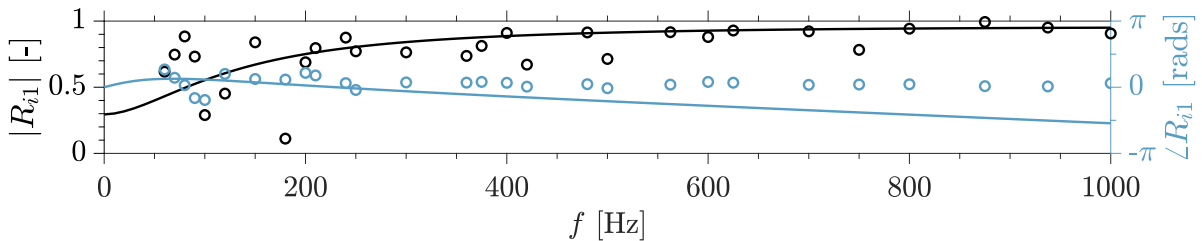


Fig. 6.3 Reflection coefficient for perforated plate inlet as a function of frequency f for no bias flow ($\bar{m} = 0 \text{ g s}^{-1}$): experimental magnitude $|R_{i1}|$ (○) and phase $\angle R_{i1}$ (○), and numerical magnitude $|R_{i1}|$ (—) and phase $\angle R_{i1}$ (—) computed using the LNSE method (numerical data courtesy of Kah Joon Yong and Maximilian Meindl).

Additionally, using more transducers and equally distanced separation might have also increased accuracy¹⁶⁰. The full 100 s acquisition window was used to compute the reflection coefficients – further data analysis should be done using shorter time windows to see if and how this affects the experimental results.

Further comparisons between experimental and numerical data for the case of a perforated plate with bias flow is not currently possible since mean flow simulations for the geometry have not yet been started. However, this will be done in the near future and will provide more fruitful grounds for discussion. For now, we can provide a preliminary discussion by looking at the experimental data shown in Fig. 6.4.

Experimental results show that the perforated plate demonstrates compact behaviour throughout the frequency range studied (i.e. phase is near zero). With increased flow rate, the reflection coefficient magnitude increases throughout the spectrum, but only slightly. In particular, across the flow rate and frequency range investigated, the magnitude ranges from 0.84 to 0.96, meaning it is a highly reflective boundary across the investigated flow regime.

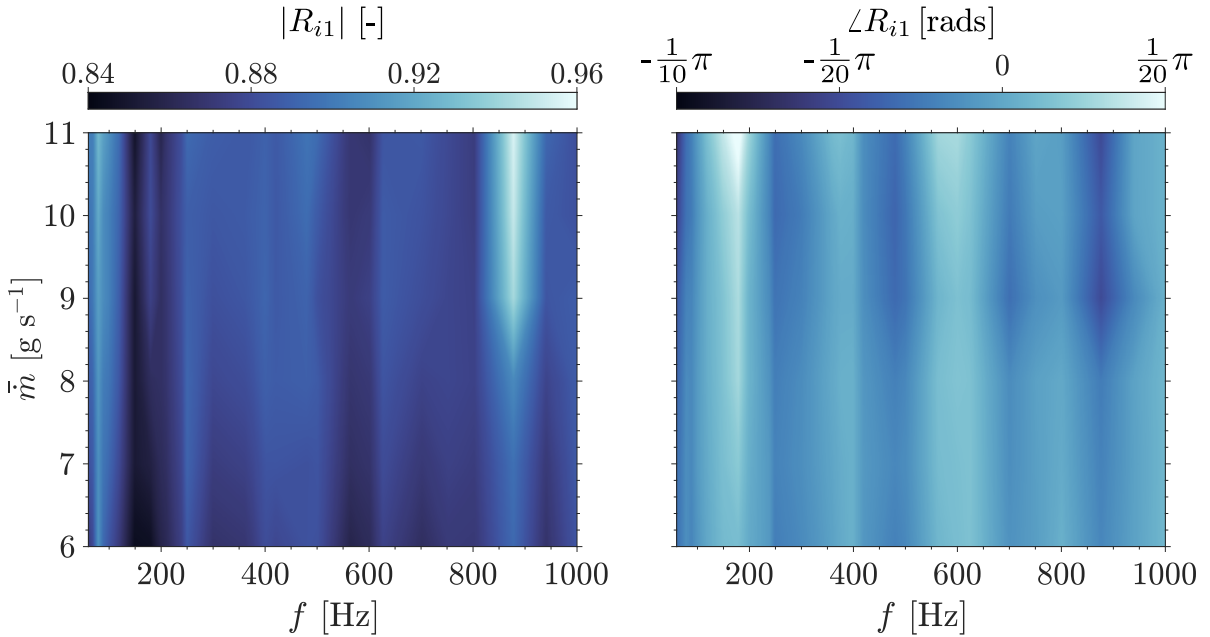


Fig. 6.4 Reflection coefficient for perforated plate inlet as a function of frequency f and flow rate \bar{m} measured using multi-microphone method: magnitude $|R|$ (left) and phase $\angle R$ (right).

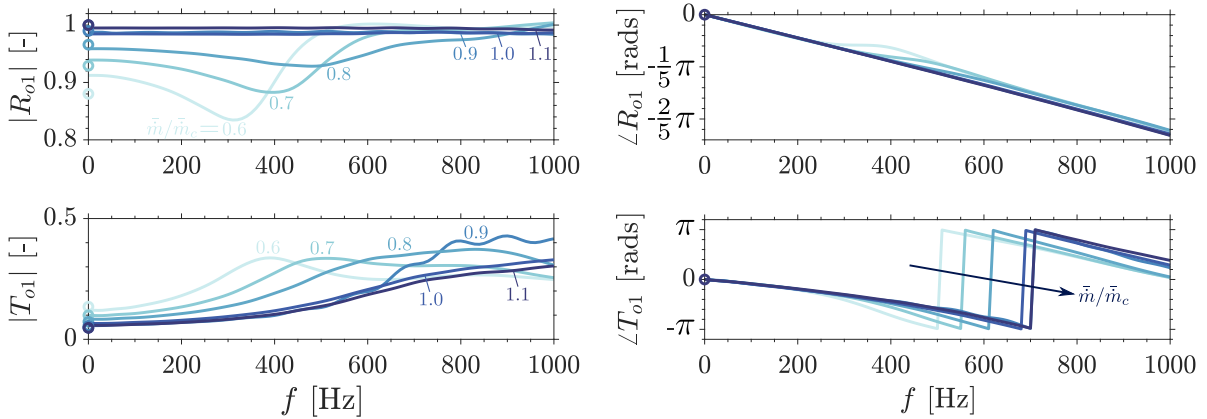


Fig. 6.5 Upstream reflection R_{o1} and transmission T_{o1} coefficients for the convergent-divergent nozzle obtained using a hybrid RANS/LNSE approach (numerical data courtesy of Kah Joon Yong and Maximilian Meindl). Experimental data obtained in §5.3.3 for zero-frequency case (i.e. acoustically compact $He = 0$) is also included for comparison (○).

Convergent-divergent nozzle

The LNSE results for the convergent divergent nozzle are shown in Fig. 6.5 with the flow rate normalised by the nozzle's choking flow rate $\bar{m}_c = 10 \text{ g s}^{-1}$. We see that with increasing flow rate, the upstream reflection coefficient R_{o1} generally increases, approaching unity for the transonic ($\bar{m}/\bar{m}_c = 0.9$) and choked ($\bar{m}/\bar{m}_c = 1.0$ and 1.1) test cases across the frequency spectrum. For the subsonic cases ($\bar{m}/\bar{m}_c = 0.6, 0.7,$ and 0.8), the reflected wave decreases in amplitude until a specific frequency is reached (300 Hz, 400 Hz, and 500 Hz, respectively). Above this frequency, the reflection coefficient increases with frequency until 1000 Hz. A linear decrease in phase shift is seen with increasing frequency for all flow rates. Good agreement is found in the zero-frequency limit with experimental data obtained in §5.3.3.

The upstream transmission coefficient T_{o1} generally increases with frequency, and reduces with flow rate. For the subsonic ($\bar{m}/\bar{m}_c = 0.6, 0.7,$ and 0.8) and transonic ($\bar{m}/\bar{m}_c = 0.9$) cases, a peak transmission coefficient is found around 400 Hz, 500 Hz, 850 Hz, and 900 Hz, respectively. For the two choked test cases ($\bar{m}/\bar{m}_c = 1.0$ and 1.1), the transmission increases monotonically with frequency for the frequency range investigated. Positive agreement is found in the zero-frequency limit with experimental data obtained in §5.3.3.

A more detailed discussion will be possible when the velocity field data is available for analysis.

6.4 Reverberating system

6.4.1 Setup and methodology

The CWR is used here without pseudo-anechoic tubes in the upstream chamber. As a result, the upstream chamber reverberates. Downstream of the nozzle, four pseudo-anechoic tubes are used, providing an anechoic time of $\tau_a = 0.7$ seconds. Methane is injected in the close injection location ($L_c = 0.11$ m) as shown in Fig. 6.6. The pressure signals presented are the result of an averaging of 10 pulse bursts, followed by the filtering of the mains frequency (50 Hz). The test cases are outlined in Table 6.1.

6.4.2 Pressure perturbations

The pressure signals for the pulse burst injection of methane for four of the eight cases are shown in Fig. 6.7. Measurements made with two transducers upstream and two transducers downstream of the nozzle are presented for the anechoic window ($\tau_a = 0.7$ s).

For the subsonic flow case ($\bar{m}/\bar{m}_c = 0.6$), the 10 Hz acoustic pulse decays before the subsequent pulse is injected. The increase in pressure build up from subsonic, $\bar{m}/\bar{m}_c = 0.6$ (Fig. 6.7a) to choked $\bar{m}/\bar{m}_c = 1.1$ (Fig. 6.7b) nozzle flow is due to the increase in the reflection coefficients (perforated plate and nozzle) with flow rate, as shown in Figs. 6.4 and 6.5. Indeed, as seen in §5, the low frequency increase in pressure is caused by reverberation. The higher frequency content is superimposed on top of this low frequency signal (see §6.6).

We see a maximum change in pressure of approximately 18% in the upstream chamber in the case of the choked nozzle for $f_i = 250$ Hz. Due to the low transmission coefficient of the nozzle, the downstream pressure signals are an order of magnitude smaller than the upstream signal, as seen in the single pulse experiments (§5).

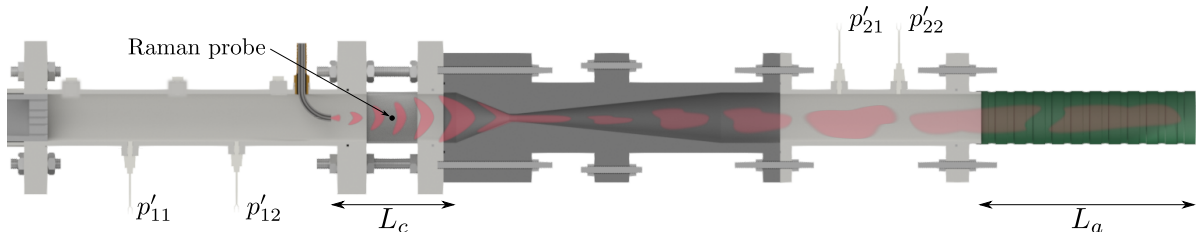


Fig. 6.6 CWR setup for the pulse burst injection campaign using the close injection location ($L_c = 0.11$ m). The anechoic length is $L_a \simeq 120$ m giving an anechoic time of $t_a = 0.7$ s. Pressure fluctuations measured by four transducers (two upstream and downstream of the nozzle, respectively). Dimensions not to scale.

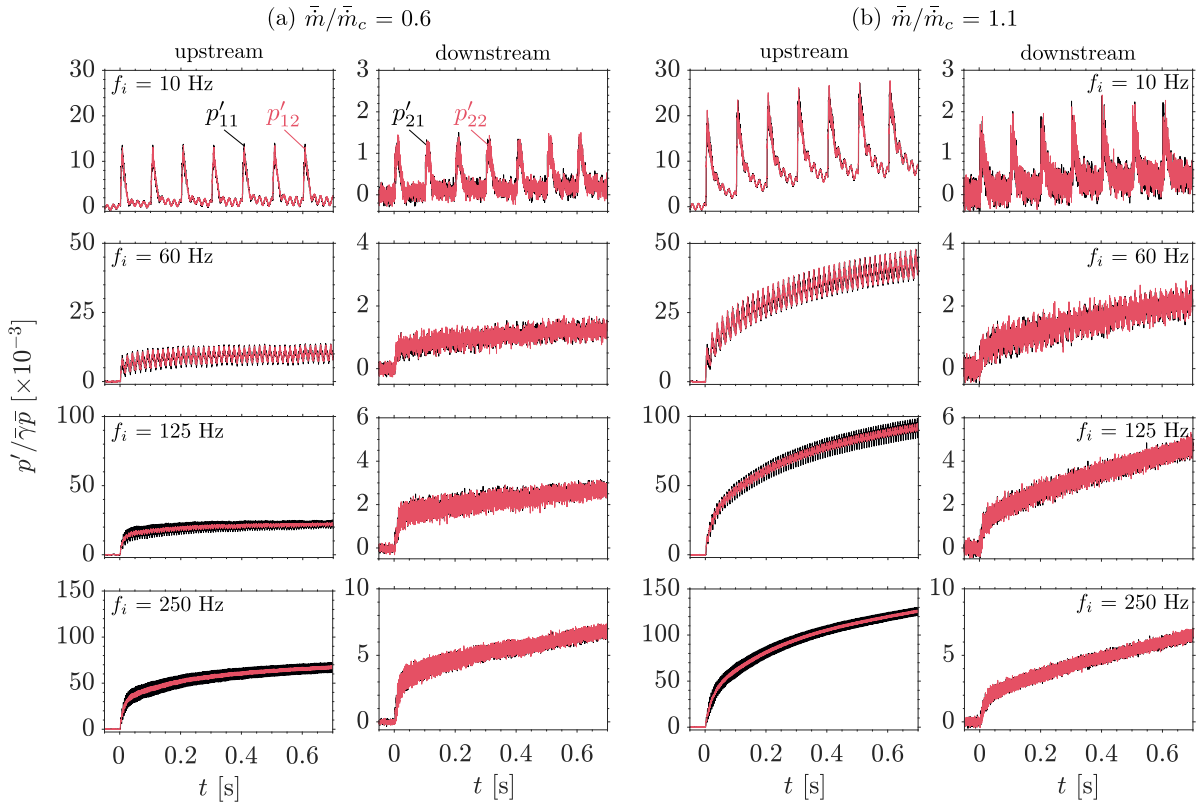


Fig. 6.7 Acoustic pressure perturbations measured by the two upstream (p'_{11} — and p'_{12} —) and downstream (p'_{21} — and p'_{22} —) transducers due to the co-flow injection of methane at frequency f_i for two mean flow rate limit cases: (a) $\bar{m}/\bar{m}_c = 0.6$ (subsonic nozzle) and (b) $\bar{m}/\bar{m}_c = 1.1$ (sonic/choked nozzle). Anechoic window $\tau_a = 0.7$ s is shown.

Since we are injecting methane close to the nozzle, indirect noise is generated synchronously to direct noise. As such, time separation is not possible and the pressure traces are a result of constructive/destructive interference between both sources. As a result of this, we can not identify indirect noise in the time series as was done in §5.4.2 for the far injection case.

6.5 Time-resolved entropic and compositional wave measurement

In §4.3, we presented the Raman technique for measuring methane and nitrogen concentrations. Here we apply the technique for the time-resolved measurement of entropic and compositional wave amplitudes during the transient pulse burst injection of methane⁵.

⁵The author kindly acknowledges the work of Dr. Lee Weller who collected the Raman data.

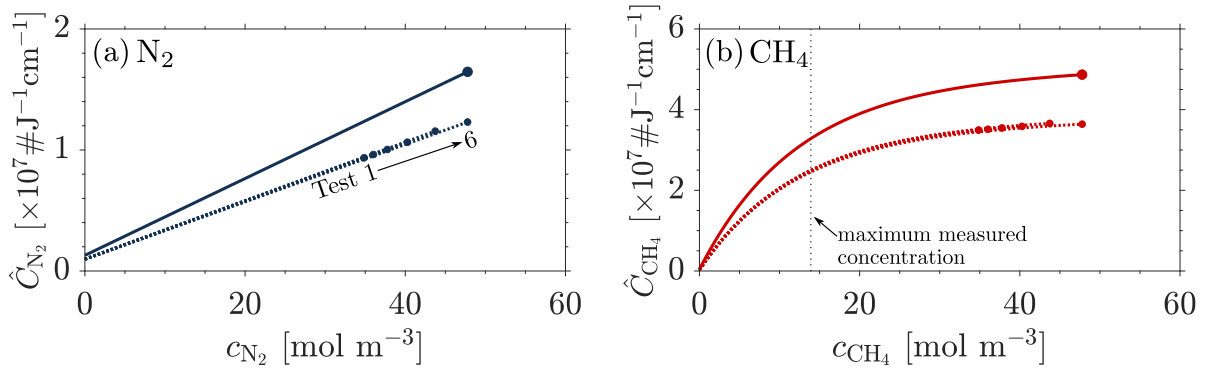


Fig. 6.8 Original calibration curve (—) and corrected calibration curves (.....) used to extract species concentration from the time-resolved integrated counts \hat{C} . The nitrogen counts during the unsteady injection experiments were different than during the original calibration. As a result, a corrected calibration curve is needed obtained using the methodology described in §4.3.7. The 2 Hz injection case is used to calibrate all the Raman experiments in this chapter.

Firstly, the Raman calibration curves are introduced, and then the injection measurements are presented.

6.5.1 Calibration curves

The calibration method for the Raman measurements was discussed in §4.3.5. As seen in the single pulse experiments presented in §5.7, it was found that the nitrogen counts were lower than during the original calibration. This was attributed to slight changes in the optical alignment during the setup and quartz etching. An assumption was made that all total signals had to be re-scaled based on the nitrogen signal obtained on the day (the method used to obtain the corrected curves is explicitly outlined on page 98). In particular, the 2 Hz injection case is used to calibrate all other injection frequency experiments in this chapter. The modified calibration curves are shown in Fig. 6.8.

In the case of nitrogen (Fig. 6.8a), we see that with increasing test case (and, therefore, mean pressure – see Table 6.1), the signal maintains its linear dependency on concentration. In the case of methane (Fig. 6.8b), the error increases with concentration. Note that the maximum measured concentration for the pulse burst injection cases is 14 mol m^{-3} . Measurement errors associated with each test case are presented in Appendix B.3.

6.5.2 Results

Figure 5.27 shows the compositional and entropic perturbation amplitudes due to the close injection of methane⁶. Only the first 0.7 seconds of the Raman data is presented as this is the anechoic window τ_a for the acoustic setup. Two flow rates are presented in Fig. 6.9. Specifically one subsonic ($\bar{m}/\bar{m}_c = 0.6$) and one choked ($\bar{m}/\bar{m}_c = 1.1$). The area-weighted analysis presented in §5.7 is not repeated here.

In comparing the perturbation signatures produced by the injection at different frequencies, two major differences can be identified, particularly in profile (i.e. pulse width) and amplitude. For both 10 Hz and 60 Hz injection frequencies, the measured compositional perturbation ξ is generally between 2 and 4%. This is expected since the estimated injection mass fraction is approximately 4% (Table 6.1). At higher frequencies (125 Hz and 250 Hz), we notice that the baseline is no longer zero. In fact, in the first

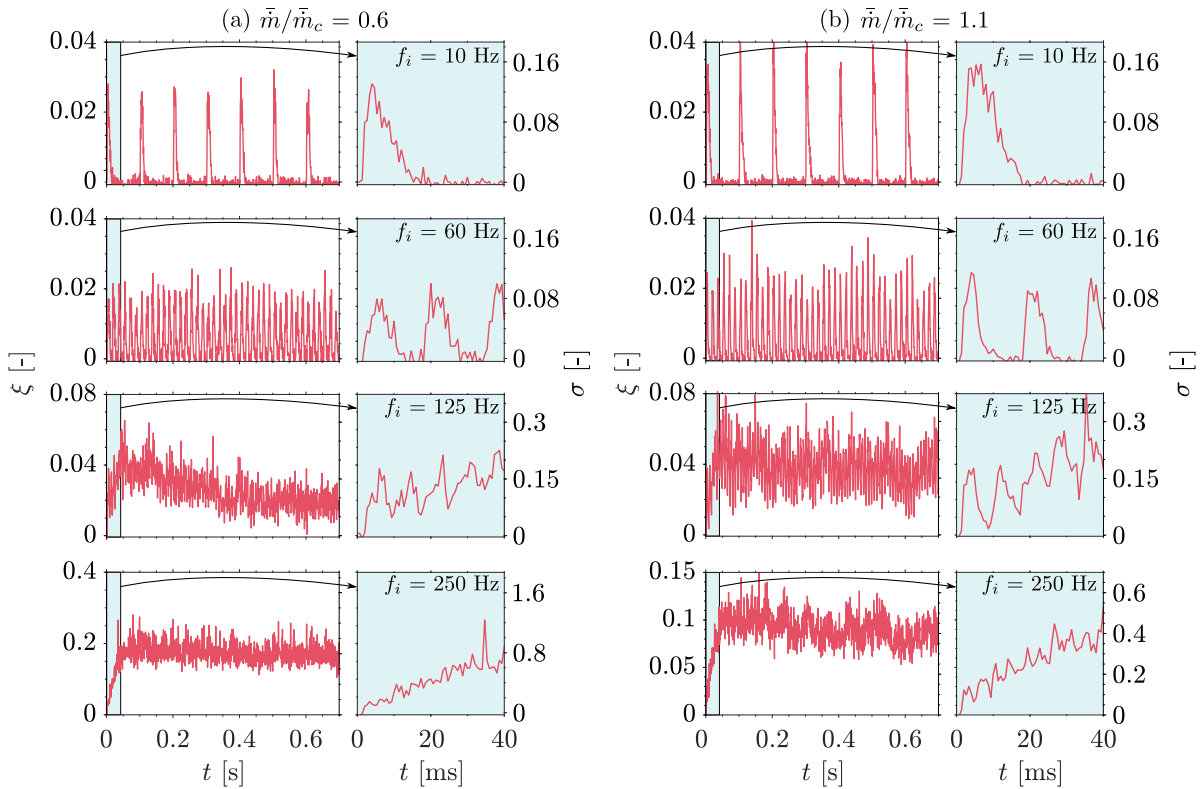


Fig. 6.9 Raman measurements – compositional ξ and entropic σ wave amplitudes due to the co-flow injection of methane at frequency f_i for two mean flow rate limit cases (a) $\bar{m}/\bar{m}_c = 0.6$ (subsonic nozzle) and (b) $\bar{m}/\bar{m}_c = 1.1$ (sonic/choked nozzle). Anechoic window $\tau_a = 0.7$ s is shown with the first 40 ms highlighted in blue.

⁶Changes in specific entropy due to mean pressure increase are negligible ($< 3\%$) and are, therefore, not considered in the calculation of the entropic wave amplitude (Eq. (2.46)).

50 ms, this baseline increases to $\xi = 0.04$ for $f_i = 125$ Hz (for both flow rates), and to $\xi = 0.2$ and $\xi = 0.1$ for $f_i = 250$ Hz (for subsonic and sonic flow rates, respectively). The reason for this is unknown. We hypothesise that a recirculation bubble is produced upstream of the nozzle acceleration region. Numerical simulations and/or 2D species measurements would help assess the cause of this feature.

Lastly, we note that the pulse width decreases with increasing injection frequency. Specifically, from 20 ms at $f_i = 10$ Hz to approximately 2 ms at $f_i = 250$ Hz. Indeed, the pulse width seems to be consistent for $\bar{m}/\bar{m}_c = 0.6$ and $\bar{m}/\bar{m}_c = 1.1$. This means the valve has a response that is independent of mean flow rate \bar{m} (and, therefore, mean pressure \bar{p}), but dependent on injection frequency f_i .

6.6 Frequency content

Of particular importance to the problem, is ensuring the nozzle is being forced at the desired frequency. One way to assess this, is to look at the frequency content of both the Raman and acoustic pressure signals.

The single-side spectrum of the fast Fourier transforms of both signals for the anechoic acquisition window $\tau_a = 0.7$ s is shown in Figs. 6.10 and 6.11 for the subsonic and sonic limit cases, respectively. Note that the mains frequency 50 Hz has been filtered out from the pressure signal (as outlined in §4.2.5) and that the Raman FFT frequency band is limited to 750 Hz since the sampling frequency is 1500 Hz.

In general, the amplitude of the forced frequency signal increases with flow rate, both in the acoustic and Raman measurements (by comparing Figs. 6.10 and 6.11). There are two exceptions, namely the downstream pressure signals for 10 Hz and 250 Hz. The compositional forcing is generally not monotonic. As a result, we note that in the pressure signals we identify that forcing frequency harmonics are also excited, and can sometimes exceed the amplitude of the forcing frequency itself. This is specifically true in the upstream and downstream pressure signals for 125 Hz injection, and in the downstream pressure signal for 60 Hz injection.

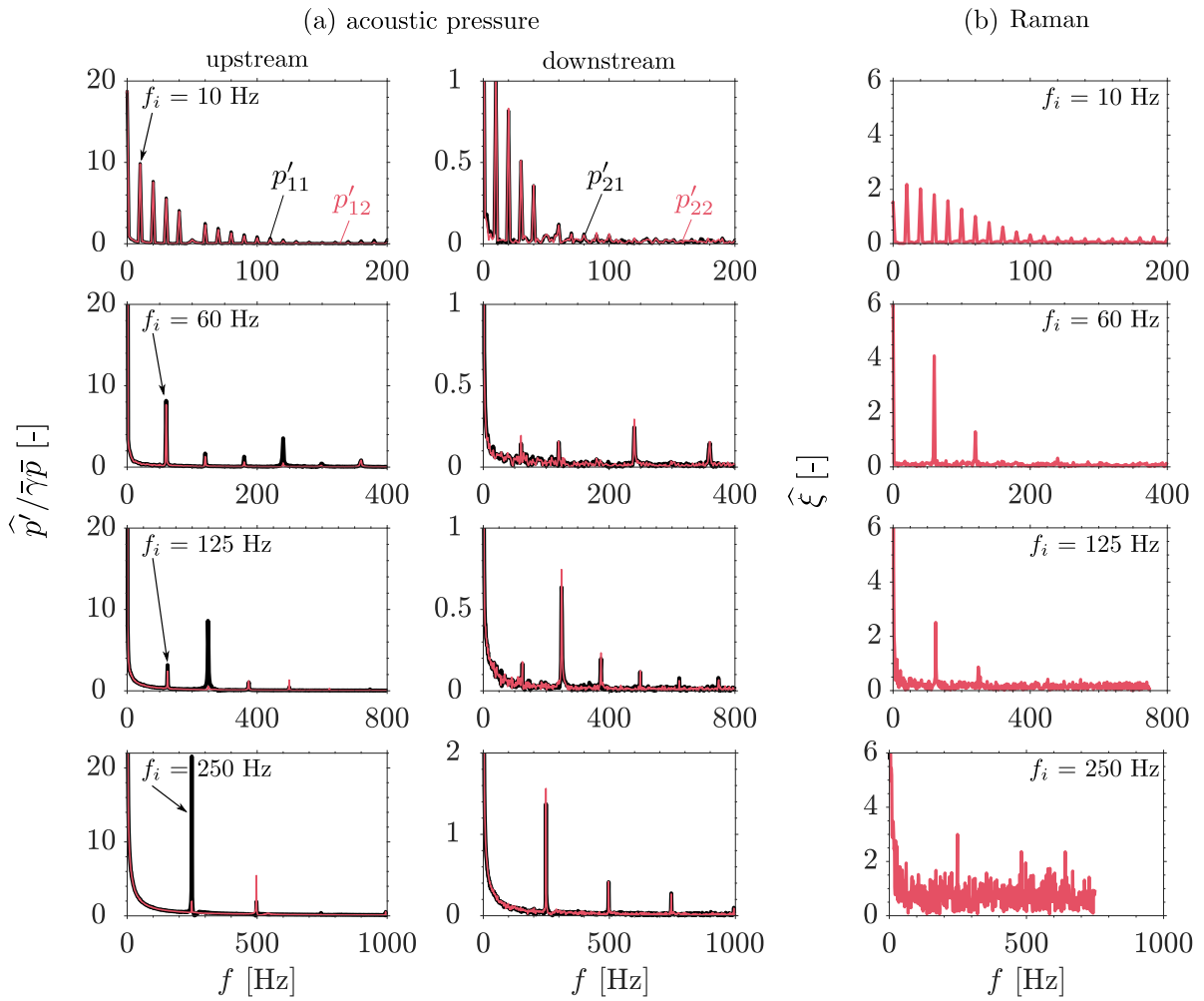


Fig. 6.10 FFT magnitude for normalised air mass flow rate $\bar{m}/\bar{m}_c = 0.6$ (subsonic nozzle): (a) acoustic pressure signals of the two upstream (p'_{11} — and p'_{12} —) and downstream (p'_{21} — and p'_{22} —) transducers; (b) compositional wave amplitude ξ due to methane injection. Signals cut at 0.7 s (anechoic time τ_a).

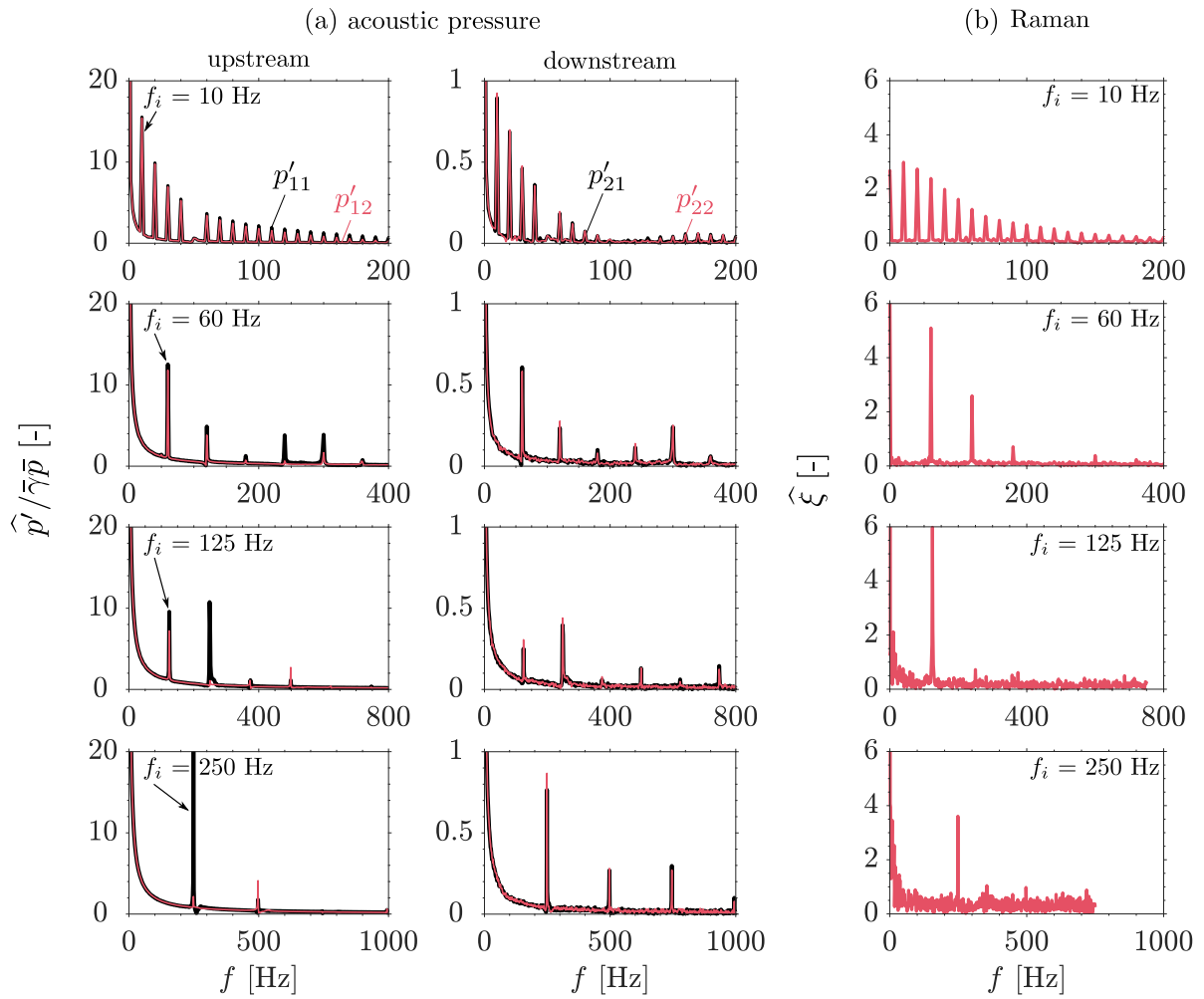


Fig. 6.11 FFT magnitude for normalised air mass flow rate $\bar{m}/\bar{m}_c = 1.1$ (sonic/choked nozzle): (a) acoustic pressure signals of the two upstream (p'_{11} — and p'_{12} —) and downstream (p'_{21} — and p'_{22} —) transducers; (b) compositional wave amplitude ξ due to methane injection. Signals cut at 0.7 s (anechoic time τ_a).

6.7 Source identification

In order to complete the characterisation of the system transfer function \mathcal{Z} in Eq. (6.1), the acoustic attenuation α needs to be characterised as a function of frequency. With pulses this short in duration ($t_p = 2$ ms), it is difficult to implement the experimental method used in §5.3.3. As a result, we need to use theoretical models from literature.

The Stokes-Kirchoff classic attenuation equation^{170,304} predicts the acoustic attenuation of a plane wave due to viscous dissipation and heat conduction as a function of frequency:

$$\alpha_{sk} = \frac{\pi^2 f^2 \mu}{\rho c^3} \left[\frac{4}{3} + \frac{\gamma - 1}{Pr} \right] \quad (6.21)$$

where $Pr = \mu c_p / \kappa$ is the Prandtl number²⁵⁹.

Preliminary analysis

We apply the source identification method to the pressure results presented in §6.4.2. In particular, we use the experimentally-acquired reflection coefficient for the perforated plate and the numerically-acquired reflection and transmissions coefficients for the nozzle (presented in §6.3.3). Frequencies above 1000 Hz have been filtered out since this is the maximum frequency of the characterisation studies. It is important to note that the matrix \mathcal{Z} is close to singular. As a result, Eq. (6.1) is solved at discrete frequencies using the minimum norm least-squares function in MATLAB (which minimises both $\|Ax - b\|$ and $\|x\|$). The results for a subsonic and a choked case are presented in Figs. 6.12 and 6.13, respectively.

We firstly focus our attention on the 10 Hz pulse burst. At this frequency, we expect results similar to that of the single pulse experiments in §5. In other words, we expect to see three particular features: firstly, $\pi_d^+ > \pi_d^-$; secondly that π_i^- is negative; and lastly, that π_i^+ is positive. Figures 6.12a and 6.12b show the resultant waves for this particular case. Looking at the results, we identify two issues:

- π_d^+ is slightly smaller in magnitude than π_d^- : we have demonstrated experimentally (§5.3.2) and theoretically (§2.2.3) that π_d^+ is larger than π_d^- . Furthermore, the end of both π_d^+ and π_d^- signals is negative.
- π_i^- is positive: experimental results^{64,277,278} (§5.5) and theoretical predictions have demonstrated that π_i^- should be negative in amplitude; here it is positive and equal to π_d^\pm in amplitude and shape. As seen in the π_d^\pm signals, the end of the pulse is negative. The fact that π_d^\pm and π_i^- are essentially the same, could indicate that the

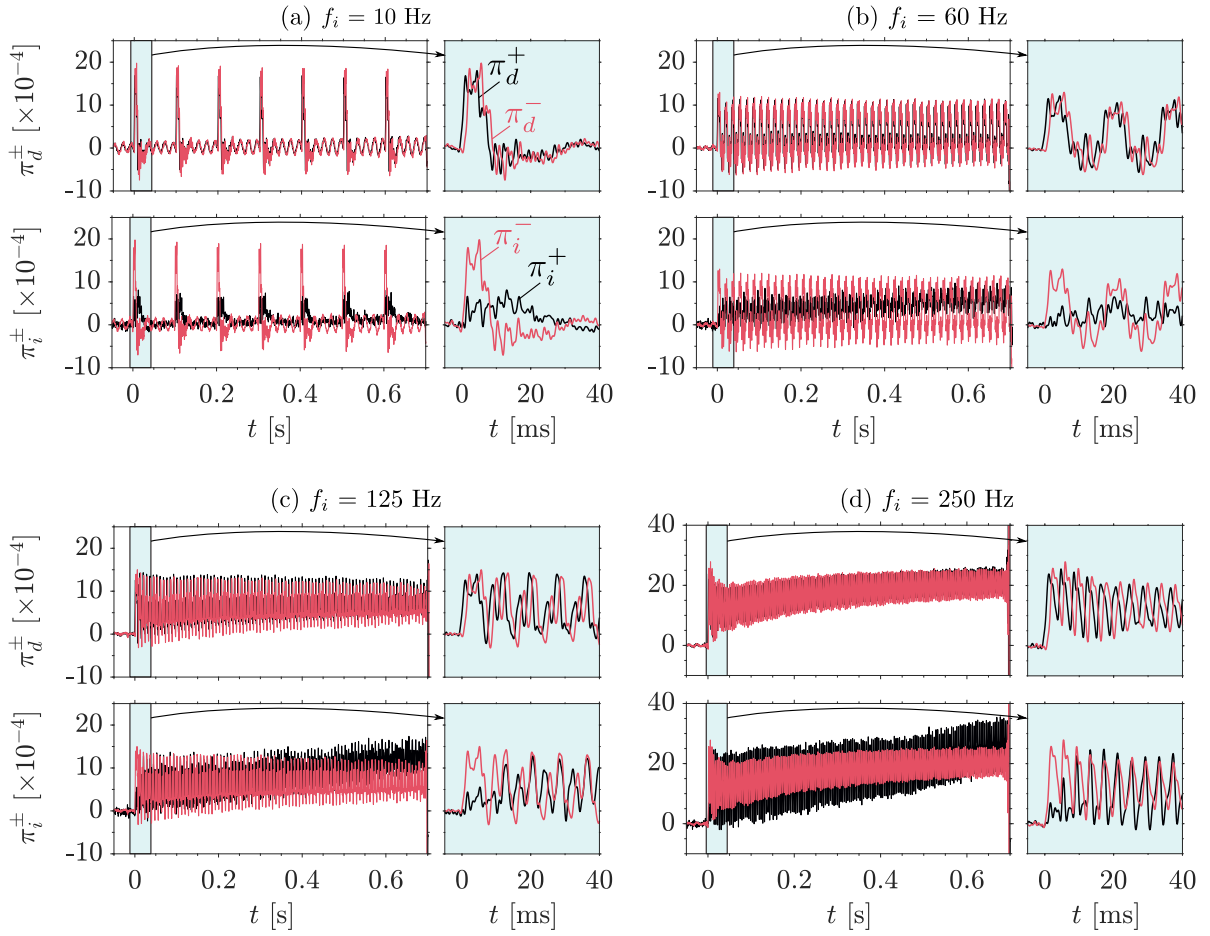


Fig. 6.12 Source identification: extracting acoustic wave sources (π_d^\pm, π_i^\pm) from reverberated pressure signals for pulse burst injection frequencies f_i for $\bar{m}/\bar{m}_c = 0.6$ (subsonic nozzle). Included are the downstream-travelling waves π_d^+, π_i^+ (—) and the upstream-travelling waves π_d^-, π_i^- (---). Anechoic window $\tau_a = 0.7$ s is shown with the first 40 ms highlighted in blue.

system is unable to distinguish between the three waves in the upstream chamber and, instead, outputs the sum of all three waves (i.e. $\pi_d^- + \pi_d^+ + \pi_i^-$).

Despite these two issues, there are three features which are encouraging:

- π_i^+ is positive and the shape is as expected – specifically, the acoustic shape shows signs of dispersion relative to the other three waves,
- the FFTs of the acoustic waves still have content at the injection frequency (not shown here),
- the acoustic pulse widths agree reasonably well with the pulse width measured by the Raman system (presented in §6.5.2).

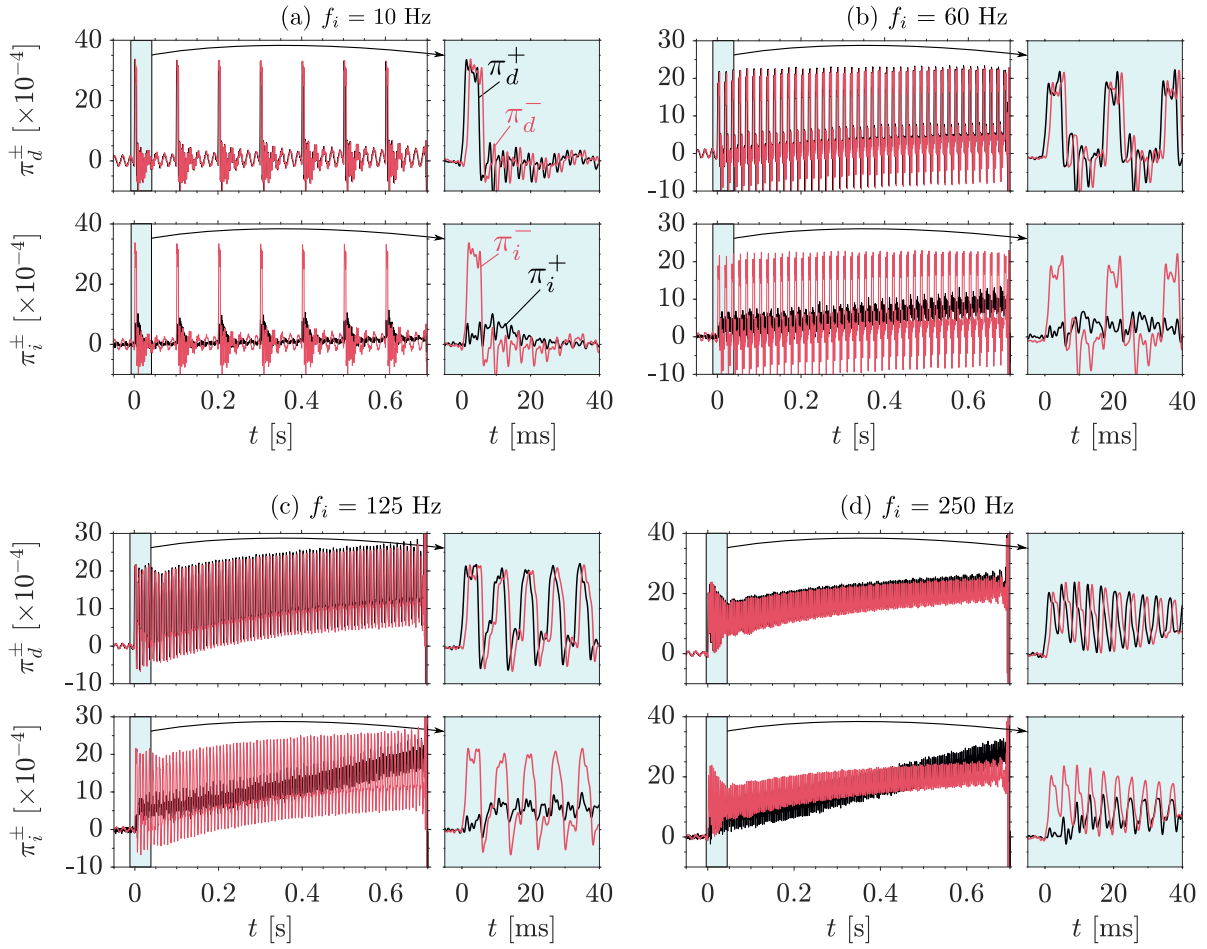


Fig. 6.13 Source identification: extracting acoustic wave sources (π_d^\pm , π_i^\pm) from reverberated pressure signals for pulse burst injection frequencies f_i for $\bar{m}/\bar{m}_c = 1.1$ (sonic/choked nozzle). Included are the downstream-travelling waves π_d^+ , π_i^+ (—) and the upstream-travelling waves π_d^- , π_i^- (—). Anechoic window $\tau_a = 0.7$ s is shown with the first 40 ms highlighted in blue.

These conclusions also hold true for other frequency case results, as shown in Figs. 6.12b-d and 6.13b-d.

The features identified in the results could be caused by a few different things. Firstly, there could be errors in the reflection coefficient of the perforated plate. We must wait for the numerical RANS/LNSE results to see whether they agree with the experimental data or not. Secondly, there are still unanswered questions regarding the acoustic attenuation α . We note that the measured acoustic attenuation α for the low-frequency experiments in §5.3.3 is two orders of magnitude larger than the one predicted by the Stokes-Kirchoff equation (6.21). For instance, for a frequency of 125 Hz and assuming room temperature conditions for air, $\alpha_{sk} = 2.2 \times 10^{-7} \text{ m}^{-1}$. Identifying the reason

for this discrepancy, as well as completing a sensitivity analysis of the acoustic waves to the input α , should both be future objectives. Lastly, and more importantly, the transfer function matrix \mathcal{Z} is ill-conditioned. Using the minimum norm least-squares solution may not be the right approach for the problem. Although not shown, using the Moore-Penrose Pseudoinverse²⁵⁴ resulted in the same results. Further investigation into matrix regularisation with application to this particular problem is needed. It may also be important to note that the transfer function matrix \mathcal{Z} is set up with two measurements in the upstream chamber which are both made upstream of the injection source. Future acoustic measurements should be taken both upstream and downstream of the injection region in the upstream chamber, so that rows 1 and 2 in Eq. (6.4) are different. We hypothesise that this may provide the system with more information in order to accurately separate and solve for the acoustic waves. Additionally, with more transducer measurements, the resultant waves could be more accurately computed via the least-squares method, therefore future work should employ as many transducers upstream and downstream of the nozzle as possible.

6.8 Summary

In this chapter, we identified that experiments have yet to validate or refute theoretical predictions for compositional indirect noise in the non-compact regime^{204,206}. As such, we presented the measurement of acoustic and compositional perturbations due to the pulse burst, co-flow injection of methane into a low Mach number bulk flow of air. This was done at frequencies ranging from 2 Hz to 250 Hz, a frequency band at which combustion noise is a significant contributor in realistic engines at approach conditions⁶⁸ and at which non-compact effects are expected to be present for the nozzle geometry investigated. Experiments were run at subsonic and sonic (choked) nozzle flow conditions.

The compositional wave amplitudes were characterised at each frequency and flow rate using spontaneous Raman spectroscopy. For the lower injection frequencies, the disturbances are separated in time. However, at the higher frequencies they merge, while still maintaining their frequency content. Numerical simulations modelling the injection would help assess the reason for this feature.

A source identification method proposed by Rolland²⁷⁸ was introduced which theoretically allows for the extraction of the acoustic wave amplitudes from reverberated pressure signals. Key variables that need to be characterised as a function of frequency and flow rate were identified, namely the inlet perforated plate and the outlet nozzle reflection and transmission coefficients. Using the multi-microphone method technique,

experimental reflection coefficient results were obtained for the inlet for different bias flow rates and frequencies. Numerical results obtained using a hybrid RANS/LNSE approach were presented for the zero bias flow case for the inlet plate – numerical results for the cases where there is bias flow will be produced in the near future. Additionally, numerical results for the outlet nozzle were presented for all flow rates of interest. Preliminary results from the source identification technique were presented, demonstrating features which suggest that the acoustic sources were not fully recovered. As a result, the amount of direct and indirect noise generated by each pulse burst frequency case could not be quantified. These features may be attributed to a couple of reasons. Firstly, there is a lack of clarity regarding the accuracy of the perforated plate reflection coefficient R_{i1} , and the attenuation coefficient α as a function of frequency and flow rate. Numerical results of the acoustic response of the perforated plate for different bias flows will soon be available to validate or refute the experimental measurements. A sensitivity analysis on the effect of α on the transfer function matrix \mathcal{Z} (and, therefore, on the acoustic wave amplitude results) should also be undertaken. Moreover, a reasoning for the difference between the analytical predictions for attenuation and the measured low-frequency attenuation should be put forth. Secondly, the transfer function matrix \mathcal{Z} is ill-conditioned. Future work should focus on better understanding matrix regularisation methods and applying it appropriately to the problem presented here. Lastly, it is advised that, in future experiments looking to implement the source identification technique proposed by Rolland²⁷⁸, measurements be taken both upstream and downstream of the source in the upstream chamber. Moreover, maximising the number of transducers used would make the problem over-constrained and allow for error reduction by solving the system via least-squares method.

Chapter 7

Final remarks

IN this chapter, the main findings of the thesis are summarised, and recommendations for future work are given.

7.1 Conclusions

Combustion-generated sound is often broken down into two categories: direct and indirect noise. Direct noise is caused by the unsteady heat release rate of a flame, while indirect noise is caused by the interaction of flow inhomogeneities, such as temperature and composition, with mean flow gradients. Indirect noise generation is affected by the convection, diffusion, dispersion, and heat transfer processes that precede the acceleration. Moreover, the identification, separation, and quantification of direct and indirect noise contributions in real engines are still important and unresolved issues in the field. Ideally, these problems would be studied in reacting flow systems. However, this is difficult due to the harsh temperature and pressure conditions inside real engines as well as the high correlation between direct and indirect noise. For these reasons, model setups have been employed to mimic the fundamental thermoacoustic principals that drive combustion noise generation.

The objective of this thesis was to further the understanding of the mechanisms that govern the generation, mixing, and convection of entropic and compositional inhomogeneities in the context of direct and indirect noise generation. This was done through a combination of numerical, analytical, and experimental studies, all of which made use of entropic and compositional sound and source measurements in model setups.

7.1.1 Numerical simulations

In §3, the URANS formulation was employed to model past experiments undertaken using the Cambridge Wave Generator model setup^{62,65}. Specifically, low-frequency flow perturbations were generated by heat addition or cross-flow injection of argon or helium into an open-ended flow duct with a mean flow of air. Numerical predictions for the unsteady entropic and compositional waves generated were compared to experimental results obtained via intrusive and non-intrusive methods. Although the flows investigated were in the transitional and turbulent regimes ($2500 < Re < 8100$), the scalars convected in similar ways and showed good agreement with experimental measurements. Heat transfer at the walls was found to be a key variable in the convection of temperature perturbations. For the compositional perturbation results, different sampling methodologies were contrasted. In the case of helium injection, in particular, it was found that the planar symmetry assumption led to an overestimation of the amplitude of the convected wave at the first probed location, but agreement was found at probes further downstream. Numerical investigations on entropic and compositional perturbations have previously made use of higher-fidelity approaches, such as LES^{18,104,233,347} or DNS^{39,236}. However

this work demonstrates that URANS simulations can provide fair accuracy at reduced costs for the purposes of modelling experiments in model setups^{98,238}. This work informed the design of a new model setup, particularly as it highlighted two important issues. Firstly, by demonstrating that a compositional perturbation is preferred as an unsteady source over a temperature perturbation (i.e. heat addition). Since mass is constant for non-porous walls, wall boundary conditions are not a source of error when running numerical simulations; unlike in the case of heat addition where the wall temperature boundary condition was shown to have a significant effect on the transport of temperature perturbations. Additionally, it is easier to generate a larger entropic source when using compositional disturbances²⁷⁸. By choosing a gas with a much larger or smaller specific entropy than air, a more significant entropic source can be produced via gas injection than heat addition (as shown in Table 2.2). Secondly, by demonstrating that even for small cross-flow momentum flux ratios, the resulting transverse jet would hit the opposite side of the duct. This may affect the frequency content of the disturbance when injecting at higher frequencies. Since we wanted to control the frequency at which the nozzle is forced (ideally via symmetric injection), the gas injection system was adjusted accordingly.

7.1.2 Phase-locked measurement of acoustic & compositional waves

A new model thermoacoustic system – the Canonical Wave Rig – was introduced in §4. It was designed for the purpose of quantifying direct and indirect noise under simplified, well-controlled conditions. Symmetric injection of gases was possible via a centreline, co-flow injection system which was designed to operate over a wide range of injection frequencies. The canonical waves generated were controlled via the gas injected: air injection produced acoustic waves, while methane injection produced acoustic, entropic, and compositional waves. The gases were injected into a low Mach number mean flow of air ($0.005 \leq \bar{M}_1 \leq 0.014$). All of the test cases investigated were in the turbulent regime ($4300 \leq Re \leq 19,000$) and mean pressures of up to 150 kPa were attained. The CWR has a visualisation section which allowed for the measurement of the local concentration upstream of the nozzle. For this purpose, a spontaneous Raman spectroscopy technique was presented. Potential factors affecting the Raman signal were investigated and calibration curves were obtained. A linear dependence between concentration and counts was identified for nitrogen, whereas a non-linear dependence was identified for methane. Both molecules were tracked concurrently in unsteady injection experiments. As such, the calibration curves could be used to extract time-resolved measurements

of local species concentration at 1.5 kHz. Prior to this work, model experiments had measured compositional perturbations⁶⁵ and composition-generated acoustics⁶⁴, but not simultaneously (i.e. in phase-locked mode) as presented in this thesis. In §5 and §6, direct and indirect noise experiments were carried out using the CWR.

Single pulse experiments

In §5, the measurement of acoustic perturbations due to the low-frequency, single pulse, co-flow injection of air or methane into a low Mach number mean flow of air was presented. Since the injection was done in the infrasound frequency range (i.e. < 1 Hz), these experiments are considered to be in the compact limit (i.e. $He \approx 0$), where it is assumed that the spatial extent of the nozzle does not affect the acoustics. Experiments were run at subsonic and sonic (choked) nozzle flow conditions, with reverberating and non-reverberating upstream chambers. Using the non-reverberating system, two contributions can be highlighted. Firstly, the direct noise produced by a co-flowing jet was quantified and compared with theoretical predictions obtained from the co-flow model derived in §2. Good agreement was found assuming a 10% error in injection mass fraction and an effective injection diameter that is smaller than the geometric diameter. Secondly, through the characterisation of the acoustic properties of the system in the low-frequency limit, an anechoic subtraction method was introduced which allowed for the measurement of non-reverberated indirect noise waves for the first time. These were contrasted with indirect noise waves obtained via dereverberation. Two convective lengths were used to investigate the effects of dispersion on the indirect noise generated. The pressure signals generated due to far injection show clear signs of dispersion, particularly as the signature is Gaussian and has a reduced peak, compared to the pressure signals due to close injection which resemble a square pulse. Moreover, since the relative contributions of direct and indirect noise in engine systems is still an ongoing question in the field, these were quantified for the case of these low-frequency studies using the CWR. Specifically, direct noise was found to be larger than indirect noise in the upstream chamber. The opposite was found to be true in the downstream chamber. Furthermore, the methane mass fraction was measured upstream of the nozzle using spontaneous Raman spectroscopy. This was done in phase-locked mode with the acquisition of pressure perturbations for the setup with the reverberating upstream chamber, demonstrating the viability of the method. The importance of the simultaneous acquisition of acoustic and species perturbations is underscored, as it allows for the confirmation that the convective time delay of the disturbance agrees with the start of indirect noise generation. Lastly, experimental transfer functions were obtained and contrasted using three methods. The

results falsely suggest that injecting far from the nozzle produces larger transfer functions than injecting close to the nozzle (by up to a factor of five). This evidences the difficulty in demonstrating full quantitative agreement between theory and experiments⁶⁴.

Pulse burst experiments

Magri et al.^{204,206} demonstrated the effects of non-compactness on the acoustic response of nozzles. In particular, with increasing He (i.e. by increasing the nozzle length or perturbation frequency), the compositional indirect noise was shown to decrease. However, there is still no experimental evidence to prove or refute this. An experimental campaign aiming to provide experimental evidence is presented in §6. In particular, through the measurement of acoustic perturbations due to the pulse burst, co-flow injection of methane into a low Mach number mean flow of air. These experiments were run using the CWR with a reverberating upstream chamber. Frequencies ranging from 2 Hz to 250 Hz were investigated for subsonic and sonic (choked) nozzle flow conditions. This is a frequency band at which combustion noise is a significant contributor in realistic engines at approach conditions⁶⁸ and at which non-compact effects are expected to be present for the nozzle geometry investigated. Since for the two highest injection frequencies the perturbations are above 10%, non-linear effects are also likely to be present. The compositional wave amplitudes were characterised upstream of the nozzle at each frequency and flow rate using spontaneous Raman spectroscopy – this was done in phase-locked mode with the acquisition of pressure perturbations. For the higher frequencies, the compositional waves were not time-separated. However, by analysing the frequency content of the Raman measurements, we confirmed that the nozzle was excited at the desired forcing frequencies in all cases. A frequency-domain source identification method proposed by Rolland²⁷⁸ was introduced which theoretically allows for the extraction of the acoustic wave amplitudes from reverberated pressure signals. Reflection and transmission coefficients were characterised experimentally and numerically as a function of frequency and flow rate. Preliminary results from the source identification technique demonstrated features which suggest the acoustic wave sources are not correctly extracted. This is hypothesised to be primarily due to the transfer function matrix \mathcal{Z} , however, this requires further verification. As a result, the amount of direct and indirect noise generated by these experiments could not be quantified.

7.2 Future work

7.2.1 Data analysis

With regards to the new datasets that have been presented in this thesis, further work can be proposed.

Compact nozzle transfer functions

The experimental nozzle transfer functions π_i/ξ presented in §5 can be compared to the theoretical predictions using the non-isentropic compositional indirect noise model of De Domenico et al.⁶⁴ and the isentropic noise model of Magri et al.²⁰⁷ (as done in the work of De Domenico et al.⁶⁴). The comparison between the different transfer functions extraction methods and the analytical models will be a fruitful source of discussion.

Acoustic non-compactness

With regards to studying nozzle non-compactness effects using the pulse burst experiments, future work should firstly focus on the application of matrix regularisation methods to the source identification problem presented in §6. Secondly, the experimental results for the reflection coefficient of the perforated plate need to be compared to numerical results obtained from the hybrid RANS/LNSE approach. Thirdly, a sensitivity analysis on the effect of the attenuation α on the transfer function matrix \mathcal{Z} (and, therefore, on the acoustic wave amplitude results) should be undertaken. Lastly, a reasoning for the difference between the analytical predictions for attenuation and the measured low-frequency attenuation should be put forth. Once these have been completed, the lower frequency pulse bursts can be used to verify that the output waves are physically meaningful since we know the acoustic signals should be similar to those presented in §5.

7.2.2 Numerical simulations

Acoustic characterisation: geometry scattering matrices

We currently have an ongoing collaboration with Prof. Polifke's group at TUM with the goal of fully characterising the scattering matrices for the perforated plate and the convergent-divergent nozzle geometries as a function of mass flow rate and frequency. The conclusion of this work will be important as it will inform the data analysis of the experimental data, as well as allow for the accurate characterisation of boundary

conditions which could be used as inputs to acoustically-resolved numerical simulations of the unsteady injection experiments.

Direct & indirect noise

Following on from the numerical simulations presented in §3, the logical next step would be to run acoustically-resolved URANS²³⁸ or fully compressible LES²³³ simulations of the experiments presented in §5 and §6 with appropriate acoustic boundary conditions in order to resolve the direct and indirect noise contributions. This would also aid in understanding the mixing and convection processes of the injected compositional disturbance, before being accelerated by the nozzle. The simulations would also allow for the numerical computation of indirect noise transfer functions, providing another result for comparison with experiments and theory.

Injection flow

It would also be useful to model the methane flow inside the injection tube in order to understand whether the effective injection diameter is reduced owing to the elbow geometry (as hypothesised in §5). The velocity field at the outlet plane of the injection tube could then be used as an input (i.e. source term) in the direct and indirect noise simulations. This work could be done using lower-fidelity simulations (e.g. URANS).

Multiphysics

The injection flow (via the injection tube) and direct and indirect noise simulations could potentially be modelled all at once using a multiphysics software (e.g. COMSOL). This may be a more costly computation, however, the effect of the injection tube on the mean flow would be considered and the physics of the injected flow would be captured. Computational costs could be saved by avoiding the modelling of the perforated plate through the use of the acoustic characterisation results – in other words, the scattering matrix of the perforated plate could be used as an inlet boundary condition. An anechoic boundary condition could be implemented at the outlet of the second chamber through use of a non-reflective boundary condition or by implementing a Perfectly Matched Layer (PML).

7.2.3 Experimental studies

Diagnostics

In light of the conclusions of §5, it would be insightful to have simultaneous velocity and species measurements (preferably in 2D) upstream of the nozzle in the CWR setup. Techniques such as PLIF and PIV would be able to provide planar data^{79,202,287,348}. The additional information acquired (when compared to the 0D measurement using Raman) would help us better understand the injection and convection processes. Specifically, we would have a measurement of the mean flow velocity in the main chamber and of the injection velocity of the gas. This would give us a better understanding of how the co-flow jet expands across the duct and how the convection processes affect the compositional wave before reaching the nozzle. These results could then be compared directly to numerical simulations.

Acoustic non-compactness

If the experiments presented in §6 are repeated and analysed using the source identification method proposed by Rolland²⁷⁸, then acoustic measurements should be made both upstream and downstream of the injection location in the upstream chamber, so that rows 1 and 2 in Eq. (6.4) are not the same. We hypothesised in §6.7 that this may provide the system with more information to accurately separate and solve for the acoustic wave sources. Additionally, with more transducer measurements, the resultant waves could be more accurately computed via the least-squares method. For this reason, future work should have as many transducers upstream and downstream of the nozzle and of the injection location as possible. We would recommend these experiments be done in phase-locked mode with the 2D velocity and species measurements suggested above.

Effect of system's resonant frequency

The CWR was designed with an inlet piston that can extend the upstream chamber length by up to 1.6 m. Although unused in the experiments presented in this thesis, it could be employed in future pulse burst studies. The upstream chamber length could be changed discretely prior to tests for a systematic study³⁰⁰, or continuously during a test³⁵² to see the effects that changing the resonant frequency of the system has on direct and indirect noise generation at the different pulse burst frequencies.

Towards realistic test conditions

The big picture goal in the thermoacoustics field is to be able to identify, separate, and quantify direct and indirect noise contributions in reacting flow setups. As pointed out by Dowling and Mahmoudi⁶⁸, aero-engine combustors are typically annular. As such, entropic and compositional noise studies using model annular combustor geometries would be most relevant to realistic engine systems. In such systems, accurate measurement of unsteady scalars is difficult owing to the high temperature and pressures. Techniques such as LIGS⁶⁰ show promise in the accurate measurement of temperature and compositional perturbations in such harsh conditions. However, before moving to reacting flow cases, there could be one more route. As noted in §4.2.6, the experiments presented in this thesis are limited in terms of mean pressures \bar{p} and Reynolds numbers Re , falling short of realistic engine conditions. Running these simplified indirect noise experiments at higher Reynolds numbers and mean pressures (e.g. using a wind-tunnel facility) would be a good stepping stone before running flame experiments. In such a setup, it would be interesting to measure the acoustic response of linear and non-linear compositional inhomogeneities impinging upon nozzles, as well as other terminations (e.g. nozzle guide vanes and turbine blade rows) using multiple pressure measurements upstream and downstream of the acceleration region. As previously noted, simultaneous measurement of velocity and species would be beneficial when running these experiments too.

7.2.4 Analytical modelling

In this thesis, we made a small contribution to the analytical modelling of direct noise by extending a compact wave source model to consider the injection of a co-flowing jet. Although this thesis only references indirect noise models, some suggestions for future work in the analytical modelling of indirect noise generation are included here. A review of the analytical modelling of indirect noise was presented in §2.2.1. To the author's knowledge, there are still a few gaps to be filled in terms of the one-dimensional analytical modelling of acceleration regions subjected to acoustic, entropic, compositional, and vortical perturbations – see Table 7.1. There are currently no models for acoustically compact or non-compact isentropic geometries subjected to non-linear compositional perturbations. Likewise, there are no models for non-isentropic geometries subjected to linear or non-linear vortical perturbations. Also missing is the analytical predictions of acoustically non-compact, non-isentropic geometries subjected to any linear or non-linear disturbance type. In addition to subsonic nozzle flows, it is also relevant to consider nozzle flows which are supersonic (with and without shocks in the downstream section).

Additionally, there are many other interesting applications of the non-isentropic theory of De Domenico et al.^{63,64}. For example, Giauque et al.¹⁰³ optimised a nozzle shape to minimise/maximise indirect noise for an isentropic nozzle subjected to entropic perturbations. It would be interesting to re-run this optimisation routine to see how the optimised nozzle shape differs when non-isentropic losses are considered. Further extending this optimisation routine to all disturbance types would be an intriguing addition to current literature and would help inform the design of nozzles.

Table 7.1 Summary of one-dimensional models for acoustically compact or non-compact, isentropic or non-isentropic regions of flow acceleration subject to linear or non-linear acoustic π , entropic σ , compositional ξ , or vortical Ω perturbations. The first published journal papers are referenced; for full list of works, see the literature review presented in §2.2.1. Empty table cells represent gaps in current literature.

		Compact		Non-compact	
		Isentropic	Non-isentropic	Isentropic	Non-isentropic
Linear	π	Tsien ³²⁷	De Domenico et al. ⁶³	Zinn et al. ³⁵⁷	
	σ	Marble and Candel ²¹³	De Domenico et al. ⁶³	Marble and Candel ²¹³	
	ξ	Magri et al. ²⁰⁷	De Domenico et al. ⁶⁴	Magri et al. ²⁰⁶	
	Ω	Cumpsty and Marble ⁵⁶		Stow et al. ³⁰⁵	
Non-linear	π	Moase et al. ²³²			
	σ	Huet and Giauque ¹⁴⁵			
	ξ				
	Ω				

References

- [1] Abbe, E. (1873). Beiträge zur Theorie des Mikroskops und der mikroskopischen Wahrnehmung. *Archiv für Mikroskopische Anatomie*, 9(1):413–468.
- [2] Åbom, M. and Bodén, H. (1988). Error analysis of two-microphone measurements in ducts with flow. *The Journal of the Acoustical Society of America*, 83(6):2429–2438.
- [3] Aguilar, J. G. and Juniper, M. P. (2020). Thermoacoustic stabilization of a longitudinal combustor using adjoint methods. *Physical Review Fluids*, 5(8):083902.
- [4] Air Transport Action Group (2010). Beginner’s Guide to Aviation Efficiency.
- [5] Air Transport Action Group (2017). Beginner’s Guide to Sustainable Aviation Fuel.
- [6] Air Transport Action Group (2020). Facts & Figures.
- [7] Allam, S. and Bodén, H. (2005). Methods for accurate determination of acoustic two-port data in flow ducts. In *12th International Congress on Sound and Vibration 2005, ICSV 2005*, volume 3, pages 2319–2326.
- [8] Anderson, D. (1975). Effects of Equivalence Ratio and Dwell Time on Exhaust Emissions From an Experimental Premixing Prevaporizing Burner. *American Society of Mechanical Engineers (Paper)*, (75 -GT-69).
- [9] Andor (2015). Shamrock 303i Datasheet.
- [10] Andor (2020). iXon Ultra EMCCD Specifications.
- [11] Bach, T., Huet, M., Watson, R., Spence, S., and Mahmoudi, Y. (2021). Effect of Film Cooling on Entropy Noise Generation in a Stator Blade Row. *AIAA Journal*, pages 1–16.
- [12] Bake, F., Gaetani, P., Persico, G., Neuhaus, L., and Knobloch, K. (2016). Indirect Noise Generation in a High Pressure Turbine Stage. In *22nd AIAA/CEAS Aeroacoustics Conference*, pages 1–12, Reston, Virginia. American Institute of Aeronautics and Astronautics.
- [13] Bake, F., Michel, U., and Roehle, I. (2007a). Fundamental Mechanism of Entropy Noise in Aero-Engines: Experimental Investigation. In *Volume 6: Turbo Expo 2007, Parts A and B*, volume 130, pages 1445–1453. ASME.

- [14] Bake, F., Michel, U., and Roehle, I. (2007b). Investigation of Entropy Noise in Aero-Engine Combustors. *Journal of Engineering for Gas Turbines and Power*, 129(2):370–376.
- [15] Bake, F., Michel, U., Rohle, I., Richter, C., Thiele, F., Liu, M., and Noll, B. (2005). Indirect combustion noise generation in gas turbines. *11th AIAA/CEAS Aeroacoustics Conference*, (23-25 May):1–13.
- [16] Bake, F., Richter, C., Mühlbauer, B., Kings, N., Röhle, I., Thiele, F., and Noll, B. (2009). The Entropy Wave Generator (EWG): A reference case on entropy noise. *Journal of Sound and Vibration*, 326(3-5):574–598.
- [17] Basner, M., Babisch, W., Davis, A., Brink, M., Clark, C., Janssen, S., and Stansfeld, S. (2014). Auditory and non-auditory effects of noise on health. *The Lancet*, 383(9925):1325–1332.
- [18] Becerril, C., Moreau, S., Bauerheim, M., Gicquel, L., and Poinso, T. (2016). Numerical investigation of combustion noise: The Entropy Wave Generator. In *22nd AIAA/CEAS Aeroacoustics Conference*, pages 1–18, Reston, Virginia. American Institute of Aeronautics and Astronautics.
- [19] Bellucci, V., Flohr, P., and Paschereit, C. O. (2004). Numerical and Experimental Study of Acoustic Damping Generated by Perforated Screens. *AIAA Journal*, 42(8):1543–1549.
- [20] Bergman, T., Lavine, A., Incropera, F., and DeWitt, D. (2011). *Fundamentals of Heat and Mass Transfer*. Wiley.
- [21] Beutel, M. E., Jünger, C., Klein, E. M., Wild, P., Lackner, K., Blettner, M., Binder, H., Michal, M., Wiltink, J., Brähler, E., and Münzel, T. (2016). Noise Annoyance Is Associated with Depression and Anxiety in the General Population - The Contribution of Aircraft Noise. *PLOS ONE*, 11(5):e0155357.
- [22] Bicchi, M., Pinelli, L., Marconcini, M., Gaetani, P., and Persico, G. (2019). Numerical study of a high-pressure turbine stage with inlet distortions. In *AIP Conference Proceedings*, volume 2191.
- [23] Bluemner, R., Paschereit, C. O., and Oberleithner, K. (2019). Generation and transport of equivalence ratio fluctuations in an acoustically forced swirl burner. *Combustion and Flame*, 209:99–116.
- [24] Bodén, H. and Åbom, M. (1986). Influence of errors on the two-microphone method for measuring acoustic properties in ducts. *The Journal of the Acoustical Society of America*, 79(2):541–549.
- [25] Bohn, M. (1976). *Noise produced by the interaction of acoustic waves and entropy waves with high-speed nozzle flows*. PhD thesis, Caltech.
- [26] Bonciolini, G. and Noiray, N. (2018). Synchronization of Thermoacoustic Modes in Sequential Combustors. In *Proceedings of ASME Turbo Expo 2018: Turbomachinery Technical Conference and Exposition*, pages 1–10.

- [27] Bonciolini, G. and Noiray, N. (2019). Synchronization of Thermoacoustic Modes in Sequential Combustors. *Journal of Engineering for Gas Turbines and Power*, 141(3):1–9.
- [28] Bowman, C. T. (1992). Control of combustion-generated nitrogen oxide emissions: Technology driven by regulation. *Symposium (International) on Combustion*, 24(1):859–878.
- [29] Bragg, S. L. (1963). Combustion Noise. *Journal of the Institute of Fuel*, 36:12–16.
- [30] Bragg, W. H. and Bragg, W. L. (1913). The Reflection of X-rays by Crystals. *Proceedings of the Royal Society A: Mathematical, Physical and Engineering Sciences*, 88(605):428–438.
- [31] Bushell, K. (1971). A survey of low velocity and coaxial jet noise with application to prediction. *Journal of Sound and Vibration*, 17(2):271–282.
- [32] Busseti, A. (2018). *An experimental and numerical investigation on the propagation of compositional waves*. MSc. Thesis, Università di Genova.
- [33] Cadusch, P. J., Hlaing, M. M., Wade, S. A., McArthur, S. L., and Stoddart, P. R. (2013). Improved methods for fluorescence background subtraction from Raman spectra. *Journal of Raman Spectroscopy*, 44(11):1587–1595.
- [34] Candel, S., Durox, D., Ducruix, S., Birbaud, A.-L., Noiray, N., and Schuller, T. (2009). Flame Dynamics and Combustion Noise: Progress and Challenges. *International Journal of Aeroacoustics*, 8(1):1–56.
- [35] Candel, S. M. (1972). *Analytical studies of some acoustic problems of jet engines*. PhD thesis, California Institute of Technology.
- [36] Ceci, A., Gojon, R., and Mihaescu, M. (2021). Computational analysis of the indirect combustion noise generation mechanism in a nozzle guided vane in transonic operating conditions. *Journal of Sound and Vibration*, 496:115851.
- [37] Chapman, S. and Cowling, T. G. (1970). *The Mathematical Theory of Non-Uniform Gases*. Cambridge University Press.
- [38] Chiu, H. and Summerfield, M. (1974). Theory of combustion noise. *Acta Astronautica*, 1(7-8):967–984.
- [39] Christodoulou, L., Karimi, N., Cammarano, A., Paul, M., and Navarro-Martinez, S. (2020). State prediction of an entropy wave advecting through a turbulent channel flow. *Journal of Fluid Mechanics*, 882:A8.
- [40] Chu, B. T. and Kováshay, L. S. G. (1957). Non-linear interactions in a viscous heat-conducting compressible gas. *Journal of Fluid Mechanics*, 3:494–514.
- [41] Chung, J. Y. and Blaser, D. A. (1980). Transfer function method of measuring in-duct acoustic properties. I. Theory. *The Journal of the Acoustical Society of America*, 68(3):907–913.

- [42] Clapeyron, B. P. E. (1834). Mémoire sur la puissance motrice de la chaleur. *Journal de l'École polytechnique*, 14(23):153–190.
- [43] Coppinger, R. (2009). SpaceShip Two rocket motor testing revealed. *FlightGlobal*.
- [44] Correa, S. M. (1998). Power generation and aeropropulsion gas turbines: From combustion science to combustion technology. *Symposium (International) on Combustion*, 27(2):1793–1807.
- [45] Corrsin, S. (1947). Extended applications of the hot-wire anemometer. *Review of Scientific Instruments*, 18(7):469–471.
- [46] Crighton, D., Dowling, A. P., Williams, J. F., Heckl, M., and Leppington, F. (1992). *Modern Methods in Analytical Acoustics: Lecture Notes*.
- [47] Crocco, L. (1953). Supercritical Gaseous Discharge with High Frequency Oscillations. *Aerotechnica*, 33(1):46–53.
- [48] Crocco, L. (1969). Research on combustion instability in liquid propellant rockets. *Symposium (International) on Combustion*, 12(1):85–99.
- [49] Crocco, L. and Cheng, S. (1956). *Theory of Combustion Instability in Liquid Propellant Rocket Motors*. Butterworths Scientific Publications, London.
- [50] Crocco, L. and Sirignano, W. A. (1967). Behavior of Supercritical Nozzles under Three-Dimensional Oscillatory Conditions. *AGARDograph No. 117*.
- [51] Cuadra, E. (1967). Acoustic Wave Generation by Entropy Discontinuities Flowing Past an Area Change. *The Journal of the Acoustical Society of America*, 42(4):725–732.
- [52] Culick, F. E. C. (1988). Combustion Instabilities in Liquid-Fueled Propulsion Systems - An Overview. In *AGARD Conference Proceedings No. 450*.
- [53] Culick, F. E. C. (2006). Unsteady Motions in Combustion Chambers for Propulsion Systems. *AGARDograph, NATO/RTO-AG-AVT-039*.
- [54] Cumpsty, N. (1979). Jet engine combustion noise: Pressure, entropy and vorticity perturbations produced by unsteady combustion or heat addition. *Journal of Sound and Vibration*, 66(4):527–544.
- [55] Cumpsty, N. A. and Marble, F. E. (1977a). Core noise from gas turbine exhausts. *Journal of Sound and Vibration*, 54(2):297–309.
- [56] Cumpsty, N. A. and Marble, F. E. (1977b). The Interaction of Entropy Fluctuations with Turbine Blade Rows; A Mechanism of Turbojet Engine Noise. *Proceedings of the Royal Society A: Mathematical, Physical and Engineering Sciences*, 357(1690):323–344.
- [57] Danichkin, S. A., Eliseev, A. A., Popova, T. N., Ravodina, O. V., and Stenina, V. V. (1981). Raman scattering parameters for gas molecules (survey). *Journal of Applied Spectroscopy*, 35(4):1057–1066.
- [58] Davidson, M. J. and Wang, H. J. (2002). Strongly advected jet in coflow. *Journal of Hydraulic Engineering*, 128(8):742–752.

- [59] Dawson, V. P. (2004). *Ideas into Hardware: A History of the Rocket Engine Test Facility at the NASA Glenn Research Center*.
- [60] De Domenico, F. (2019). *Behaviour of accelerating entropy spots*. PhD thesis, University of Cambridge.
- [61] De Domenico, F., Rolland, E., and Hochgreb, S. (2017a). Measurements of the Effect of Boundary Conditions on Upstream and Downstream Noise Arising From Entropy Spots. In *Proceedings of ASME Turbo Expo 2017: Turbomachinery Technical Conference and Exposition*, pages 1–13.
- [62] De Domenico, F., Rolland, E. O., and Hochgreb, S. (2017b). Detection of direct and indirect noise generated by synthetic hot spots in a duct. *Journal of Sound and Vibration*, 394:220–236.
- [63] De Domenico, F., Rolland, E. O., and Hochgreb, S. (2019a). A generalised model for acoustic and entropic transfer function of nozzles with losses. *Journal of Sound and Vibration*, 440:212–230.
- [64] De Domenico, F., Rolland, E. O., Rodrigues, J., Magri, L., and Hochgreb, S. (2021). Compositional and entropy indirect noise generated in subsonic non-isentropic nozzles. *Journal of Fluid Mechanics*, 910:A5.
- [65] De Domenico, F., Shah, P., Lowe, S. M., Fan, L., Ewart, P., Williams, B. A. O., and Hochgreb, S. (2019b). High Frequency Measurement of Temperature and Composition Spots With LITGS. *Journal of Engineering for Gas Turbines and Power*, 141(3).
- [66] Dieing, T., Hollricher, O., and Toporski, J. (2011). *Confocal Raman Microscopy*.
- [67] Dowling, A. P. (1995). The calculation of thermoacoustic instabilities. *Journal of Sound and Vibration*, 180(4):557–581.
- [68] Dowling, A. P. and Mahmoudi, Y. (2015). Combustion noise. *Proceedings of the Combustion Institute*, 35(1):65–100.
- [69] Dowling, A. P. and Stow, S. R. (2003). Acoustic Analysis of Gas Turbine Combustors. *Journal of Propulsion and Power*, 19(5):751–764.
- [70] Dowling, D. R. and Dimotakis, P. E. (1990). Similarity of the concentration field of gas-phase turbulent jets. *Journal of Fluid Mechanics*, 218:109–141.
- [71] Downs, A. J., Staveley, L. A. K., and Long, D. A. (1995). *Essays in Structural Chemistry*. Springer US, Boston, MA.
- [72] Dunn-Rankin, D. and Therkelsen, P. (2016). *Lean Combustion: Technology and Control*.
- [73] Durán, I. and Moreau, S. (2013). Solution of the Quasi One-Dimensional Linearized Euler Equations using Flow Invariants and the Magnus Expansion. *Journal of Fluid Mechanics*, 723:190–231.
- [74] Durán, I., Moreau, S., Nicoud, F., Livebardon, T., Bouty, E., and Poinot, T. (2014). Combustion Noise in Modern Aero-Engines. *Aerospace Lab Journal*, (7):1–11.

- [75] Durán, I., Moreau, S., and Poinso, T. (2013). Analytical and Numerical Study of Combustion Noise Through a Subsonic Nozzle. *AIAA Journal*, 51(1):42–52.
- [76] Durán, I. and Morgans, A. S. (2015). On the reflection and transmission of circumferential waves through nozzles. *Journal of Fluid Mechanics*, 773:137–153.
- [77] Dutta, P., Saha, S. K., Nandi, N., and Pal, N. (2016). Numerical study on flow separation in 90° pipe bend under high Reynolds number by k- ϵ modelling. *Engineering Science and Technology, an International Journal*, 19(2):904–910.
- [78] Eckstein, J., Freitag, E., Hirsch, C., and Sattelmayer, T. (2006). Experimental Study on the Role of Entropy Waves in Low-Frequency Oscillations in a RQL Combustor. *Journal of Engineering for Gas Turbines and Power*, 128(2):264.
- [79] Ehn, A., Zhu, J., Li, X., and Kiefer, J. (2017). Advanced Laser-Based Techniques for Gas-Phase Diagnostics in Combustion and Aerospace Engineering. *Applied Spectroscopy*, 71(3):341–366.
- [80] Emanuelli, A. (2019). *Numerical simulation and modelling of entropy noise in nozzle and turbine stator flows*. PhD thesis, Université Paris-Saclay.
- [81] EMEP/EEA (2019). Air pollutant emission inventory guidebook.
- [82] Emmanuelli, A., Zheng, J., Huet, M., Giauque, A., Le Garrec, T., and Ducruix, S. (2020). Description and application of a 2D-axisymmetric model for entropy noise in nozzle flows. *Journal of Sound and Vibration*, page 115163.
- [83] Emmanuelli, A. B., Huet, M., Le Garrec, T., and Ducruix, S. (2018). Study of Entropy Noise through a 2D Stator using CAA. *2018 AIAA/CEAS Aeroacoustics Conference*.
- [84] Eriksson, C., Rosenlund, M., Pershagen, G., Hilding, A., Östenson, C.-G., and Bluhm, G. (2007). Aircraft Noise and Incidence of Hypertension. *Epidemiology*, 18(6):716–721.
- [85] Eroglu, A., Flohr, P., Brunner, P., and Hellat, J. (2009). Combustor Design for Low Emissions and Long Lifetime Requirements. In *Volume 2: Combustion, Fuels and Emissions*, volume 2, pages 435–444. ASMEDC.
- [86] European Commission (2011). Flightpath 2050 Europe’s vision for aviation: Report of the high level group on aviation research.
- [87] European Union Aviation Safety Agency (2019). European Aviation Environmental Report.
- [88] Fattahi, A., Hosseinalipour, S., Karimi, N., Saboohi, Z., and Ommi, F. (2019). On the response of a lean-premixed hydrogen combustor to acoustic and dissipative-dispersive entropy waves. *Energy*, 180.
- [89] Fattahi, A., Hosseinalipour, S. M., and Karimi, N. (2017). On the dissipation and dispersion of entropy waves in heat transferring channel flows. *Physics of Fluids*, 29(8).

- [90] Feitelberg, A. S. and Lacey, M. A. (1998). The GE Rich-Quench-Lean Gas Turbine Combustor. *Journal of Engineering for Gas Turbines and Power*, 120(3):1–11.
- [91] Fenner, W. R., Hyatt, H. A., Kellam, J. M., and Porto, S. P. S. (1973). Raman cross section of some simple gases. *Journal of the Optical Society of America*, 63(1):73.
- [92] Fric, T. F. and Roshko, A. (1994). Vortical structure in the wake of a transverse jet. *Journal of Fluid Mechanics*, 279(1):1–47.
- [93] Friedlingstein, P., O’Sullivan, M., Jones, M. W., Andrew, R. M., Hauck, J., Olsen, A., Peters, G. P., Peters, W., Pongratz, J., Sitch, S., Le Quéré, C., Canadell, J. G., Ciais, P., Jackson, R. B., Alin, S., Aragão, L. E. O. C., Arneeth, A., Arora, V., Bates, N. R., Becker, M., Benoit-Cattin, A., Bittig, H. C., Bopp, L., Bultan, S., Chandra, N., Chevallier, F., Chini, L. P., Evans, W., Florentie, L., Forster, P. M., Gasser, T., Gehlen, M., Gilfillan, D., Gkritzalis, T., Gregor, L., Gruber, N., Harris, I., Hartung, K., Haverd, V., Houghton, R. A., Ilyina, T., Jain, A. K., Joetzjer, E., Kadono, K., Kato, E., Kitidis, V., Korsbakken, J. I., Landschützer, P., Lefèvre, N., Lenton, A., Lienert, S., Liu, Z., Lombardozzi, D., Marland, G., Metzl, N., Munro, D. R., Nabel, J. E. M. S., Nakaoka, S.-I., Niwa, Y., O’Brien, K., Ono, T., Palmer, P. I., Pierrot, D., Poulter, B., Resplandy, L., Robertson, E., Rödenbeck, C., Schwinger, J., Séférian, R., Skjelvan, I., Smith, A. J. P., Sutton, A. J., Tanhua, T., Tans, P. P., Tian, H., Tilbrook, B., van der Werf, G., Vuichard, N., Walker, A. P., Wanninkhof, R., Watson, A. J., Willis, D., Wiltshire, A. J., Yuan, W., Yue, X., and Zaehle, S. (2019). Global Carbon Budget 2019. *Earth System Science Data*, 11:1783–1838.
- [94] Friedlingstein, P., O’Sullivan, M., Jones, M. W., Andrew, R. M., Hauck, J., Olsen, A., Peters, G. P., Peters, W., Pongratz, J., Sitch, S., Le Quéré, C., Canadell, J. G., Ciais, P., Jackson, R. B., Alin, S., Aragão, L. E. O. C., Arneeth, A., Arora, V., Bates, N. R., Becker, M., Benoit-Cattin, A., Bittig, H. C., Bopp, L., Bultan, S., Chandra, N., Chevallier, F., Chini, L. P., Evans, W., Florentie, L., Forster, P. M., Gasser, T., Gehlen, M., Gilfillan, D., Gkritzalis, T., Gregor, L., Gruber, N., Harris, I., Hartung, K., Haverd, V., Houghton, R. A., Ilyina, T., Jain, A. K., Joetzjer, E., Kadono, K., Kato, E., Kitidis, V., Korsbakken, J. I., Landschützer, P., Lefèvre, N., Lenton, A., Lienert, S., Liu, Z., Lombardozzi, D., Marland, G., Metzl, N., Munro, D. R., Nabel, J. E. M. S., Nakaoka, S.-I., Niwa, Y., O’Brien, K., Ono, T., Palmer, P. I., Pierrot, D., Poulter, B., Resplandy, L., Robertson, E., Rödenbeck, C., Schwinger, J., Séférian, R., Skjelvan, I., Smith, A. J. P., Sutton, A. J., Tanhua, T., Tans, P. P., Tian, H., Tilbrook, B., van der Werf, G., Vuichard, N., Walker, A. P., Wanninkhof, R., Watson, A. J., Willis, D., Wiltshire, A. J., Yuan, W., Yue, X., and Zaehle, S. (2020). Global Carbon Budget 2020. *Earth System Science Data*, 12(4):3269–3340.
- [95] Gaetani, P. and Persico, G. (2017). Hot Streak Evolution in an Axial HP Turbine Stage. *International Journal of Turbomachinery, Propulsion and Power*, 2(2):6.
- [96] Gaetani, P. and Persico, G. (2019). Transport of Entropy Waves Within a High Pressure Turbine Stage. *Journal of Turbomachinery*, 141(3):031006.
- [97] Gaetani, P., Persico, G., Pinelli, L., Marconcini, M., and Pacciani, R. (2019). Computational and Experimental Study of Hot Streak Transport Within the First Stage of a Gas Turbine. In *Volume 2A: Turbomachinery*. American Society of Mechanical Engineers.

- [98] Gaetani, P., Persico, G., Pinelli, L., Marconcini, M., and Pacciani, R. (2020). Computational and experimental study of hot streak transport within the first stage of a gas turbine. *Journal of Turbomachinery*, pages 1–18.
- [99] Gaetani, P., Persico, G., Spinelli, A., Sandu, C., and Niculescu, F. (2015). Entropy wave generator for indirect combustion noise experiments in a high-pressure turbine. In *The 11th European Turbomachinery Conference, March 2015, Madrid, Spain.*, pages 1–13, Madrid.
- [100] Galeazzo, F. C. C., Donnert, G., Cárdenas, C., Sedlmaier, J., Habisreuther, P., Zarzalis, N., Beck, C., and Krebs, W. (2013). Computational modeling of turbulent mixing in a jet in crossflow. *International Journal of Heat and Fluid Flow*, 41:55–65.
- [101] Gerend, R. P., Kamasaka, H. P., and Roundhill, J. P. (1973). Core engine noise. In *AIAA Aerocoustics Conference*.
- [102] Giauque, A., Huet, M., and Clero, F. (2012). Analytical Analysis of Indirect Combustion Noise in Subcritical Nozzles. *Journal of Engineering for Gas Turbines and Power*, 134(11):111202.
- [103] Giauque, A., Huet, M., Clero, F., Ducruix, S., and Richecoeur, F. (2013). Thermoacoustic Shape Optimization of a Subsonic Nozzle. *Journal of Engineering for Gas Turbines and Power*, 135(10):102601.
- [104] Giusti, A., Magri, L., and Zedda, M. (2019). Flow Inhomogeneities in a Realistic Aeronautical Gas-Turbine Combustor: Formation, Evolution, and Indirect Noise. *Journal of Engineering for Gas Turbines and Power*, 141(1):011502.
- [105] Giusti, A., Worth, N. A., Mastorakos, E., and Dowling, A. P. (2017). Experimental and Numerical Investigation into the Propagation of Entropy Waves. *AIAA Journal*, 55(2):446–458.
- [106] Goh, C. S. and Morgans, A. S. (2011). Phase prediction of the response of choked nozzles to entropy and acoustic disturbances. *Journal of Sound and Vibration*, 330(21):5184–5198.
- [107] Goh, C. S. and Morgans, A. S. (2013). The Influence of Entropy Waves on the Thermoacoustic Stability of a Model Combustor. *Combustion Science and Technology*, 185:249–268.
- [108] Goodwin, D. G., Moffat, H. K., and Speth, R. L. (2017). Cantera: An object-oriented software toolkit for chemical kinetics, thermodynamics, and transport processes (Version 2.3.0).
- [109] Grande, E. (1974). Exhaust noise field generated in the JT8D core engine—noise floor presented by the internal noise sources. *The Journal of the Acoustical Society of America*, 55(1):30–34.
- [110] Green, K. B., Pasternack, B. S., and Shore, R. E. (1982). Effects of Aircraft Noise on Reading Ability of School-Age Children. *Archives of Environmental Health: An International Journal*, 37(1):141–145.

- [111] Guzmán-Iñigo, J. G., Baddoo, P. J., Ayton, L. J., and Morgans, A. S. (2019). Noise generated by entropic and compositional inhomogeneities interacting with a cascade of airfoils. In *25th AIAA/CEAS Aeroacoustics Conference*, pages 1–11, Reston, Virginia. American Institute of Aeronautics and Astronautics.
- [112] Hajjaligol, N. and Mazaheri, K. (2020). The dissipation and dispersion of the entropy wave caused by a turbulent lean premixed flame in a combustor. *Applied Thermal Engineering*, 165(112900).
- [113] Hansell, A. L., Blangiardo, M., Fortunato, L., Floud, S., de Hoogh, K., Fecht, D., Ghosh, R. E., Laszlo, H. E., Pearson, C., Beale, L., Beevers, S., Gulliver, J., Best, N., Richardson, S., and Elliott, P. (2013). Aircraft noise and cardiovascular disease near Heathrow airport in London: small area study. *British Medical Journal*, 347:9–12.
- [114] Harrabin, R. (2021). Climate change: Carbon emission promises "put Earth on red alert". *BBC News*.
- [115] Harrje, D. T. (1972). Liquid propellant rocket combustion instability. Technical report.
- [116] Hassan, H. A. (1974). Scaling of combustion-generated noise. *Journal of Fluid Mechanics*, 66(3):445–453.
- [117] Hazle, M. A., Mehicic, M., Gardiner, D. J., and Graves, P. R. (1989). *Practical Raman Spectroscopy*, volume 1. Springer Berlin Heidelberg, Berlin, Heidelberg.
- [118] Hernández, Y. and Galarreta, B. C. (2019). Noble Metal-Based Plasmonic Nanoparticles for SERS Imaging and Photothermal Therapy. In *Nanomaterials for Magnetic and Optical Hyperthermia Applications*, pages 83–109. Elsevier.
- [119] Herschel, A. S. (1874). Vibrations of Air Produced by Heat. *Nature*, 10(247):233–235.
- [120] Heuwinkel, C., Enghardt, L., and Röhle, I. (2007). Experimental investigation of the acoustic damping of perforated liners with bias flow. *13th AIAA/CEAS Aeroacoustics Conference (28th AIAA Aeroacoustics Conference)*.
- [121] Hield, P. A. and Brear, M. J. (2008). Comparison of Open and Choked Premixed Combustor Exits During Thermoacoustic Limit Cycle. *AIAA Journal*, 46(2):517–526.
- [122] Higgins, B. (1802). On the sound produced by a current of hydrogen gas passing through a tube. *Journal of Natural Philosophy, Chemistry, and the Arts*, 1:129–131.
- [123] Hill, P. G. and Peterson, C. R. (1992). *Mechanics and Thermodynamics of Propulsion*, volume 280.
- [124] Hilpert, R. (1933). Wärmeabgabe von geheizten Drähten und Rohren im Luftstrom. *Forschung auf dem Gebiete des Ingenieurwesens*, 4(5):215–224.
- [125] Hippler, M. (2015). Cavity-Enhanced Raman Spectroscopy of Natural Gas with Optical Feedback cw-Diode Lasers. *Analytical Chemistry*, 87(15):7803–7809.

- [126] Hirschberg, L., Hulshoff, S. J., and Bake, F. (2020). Sound Production due to Swirl-Nozzle Interaction: Model-Based Analysis of Experiments. In *AIAA AVIATION 2020 FORUM*, pages 1–23, Reston, Virginia. American Institute of Aeronautics and Astronautics.
- [127] HM Government (2020). Energy White Paper: Powering our Net Zero Future.
- [128] Hoch, R. and Hawkins, R. (1973). Recent studies into Concorde noise reduction. In *AGARD Conference Proceedings, Noise Mechanisms, Paper 19*.
- [129] Hochgreb, S., Dennis, D., Ayranci, I., Bainbridge, W., and Cant, S. (2013). Forced and self-excited instabilities from lean premixed, liquid-fuelled aeroengine injectors at high pressures and temperatures. *Proceedings of the ASME Turbo Expo*, 1 B.
- [130] Hollinger, P. (2021). Rolls-Royce to put engine development ‘on ice’ until new jet unveiled. *Financial Times*.
- [131] Holmberg, A., Åbom, M., and Bodén, H. (2011). Accurate experimental two-port analysis of flow generated sound. *Journal of Sound and Vibration*, 330(26):6336–6354.
- [132] Horn, G. and Thring, M. W. (1956). Angle of Spread of Free Jets. *Nature*, 178(4526):205–206.
- [133] Hosseinalipour, S., Fattahi, A., Khalili, H., Tootoonchian, F., and Karimi, N. (2020a). Experimental investigation of entropy waves’ evolution for understanding of indirect combustion noise in gas turbine combustors. *Energy*, 195(116978).
- [134] Hosseinalipour, S., Rahmani, E., Fattahi, A., and Karimi, N. (2020b). Experimental investigation of the hydrodynamic effects upon convecting entropy waves in nozzle flows. *Aerospace Science and Technology*, 107(106301).
- [135] Hosseinalipour, S. M., Fattahi, A., and Karimi, N. (2016). Analytical investigation of non-adiabatic effects on the dynamics of sound reflection and transmission in a combustor. *Applied Thermal Engineering*, 98(5).
- [136] Howe, M. S. (1979). On the Theory of Unsteady High Reynolds Number Flow Through a Circular Aperture. *Proceedings of the Royal Society A: Mathematical, Physical and Engineering Sciences*, 366(1725):205–223.
- [137] Howe, M. S. (2010). Indirect combustion noise. *Journal of Fluid Mechanics*, 659(2010):267–288.
- [138] Howe, M. S. and Liu, J. T. C. (1977). The generation of sound by vorticity waves in swirling duct flows. *Journal of Fluid Mechanics*, 81(2):369–383.
- [139] Hsu, A. T., He, G., and Guo, Y. (2000). Unsteady Simulation of a Jet-in-crossflow. *International Journal of Computational Fluid Dynamics*, 14(1):41–53.
- [140] Hu, K., Fang, Y., Zheng, Y., Wang, G., and Moreau, S. (2020). Numerical Investigation of Influence of Entropy Wave on the Acoustic and Wall Heat Transfer Characteristics of a High-Pressure Turbine Guide Vane. *Acoustics*, 2(3):524–538.

- [141] Huet, M. (2016). Nonlinear indirect combustion noise for compact supercritical nozzle flows. *Journal of Sound and Vibration*, 374:211–227.
- [142] Huet, M. (2018). Budgets of Disturbances Energy for Nozzle Flows at Subsonic and Choked Regimes. *Journal of Engineering for Gas Turbines and Power*, 140(11):112602.
- [143] Huet, M., Bertier, N., Mazur, M., Kings, N., Tao, W., Richecoeur, F., Lapeyre, C., and Poinot, T. (2016). Recent Improvements in Combustion Noise Investigation: from the Combustion Chamber to Nozzle Flow. *Aerospace Lab Journal*, (11):10.
- [144] Huet, M., Emmanuelli, A., and Ducruix, S. (2021). Influence of viscosity on entropy noise generation through a nozzle. *Journal of Sound and Vibration*, 510(May):116293.
- [145] Huet, M. and Giauque, A. (2013). A nonlinear model for indirect combustion noise through a compact nozzle. *Journal of Fluid Mechanics*, 733:268–301.
- [146] Hughes, I. G. and Hase, T. P. A. (2010). *Measurements and their Uncertainties: A Practical Guide to Modern Error Analysis*.
- [147] Hughes, I. J. and Dowling, A. P. (1990). The absorption of sound by perforated linings. *Journal of Fluid Mechanics*, 218:299–335.
- [148] Hultgren, L. and Miles, J. (2009). Noise-Source Separation Using Internal and Far-Field Sensors for a Full-Scale Turbofan Engine. In *15th AIAA/CEAS Aeroacoustics Conference (30th AIAA Aeroacoustics Conference)*, Reston, Virginia. American Institute of Aeronautics and Astronautics.
- [149] Hultgren, L. S. (2011). Core Noise: Implications Of Emerging N+3 Designs & Acoustic Technology Needs. In *Acoustics Technical Working Group*.
- [150] Hurle, I. R., Price, R. B., Sugden, T. M., and Thomas, A. (1968). Sound emission from open turbulent premixed flames. *Proceedings of the Royal Society of London. Series A. Mathematical and Physical Sciences*, 303(1475):409–427.
- [151] Hygge, S., Evans, G. W., and Bullinger, M. (2002). A Prospective Study of Some Effects of Aircraft Noise on Cognitive Performance in Schoolchildren. *Psychological Science*, 13(5):469–474.
- [152] IATA (2020). 20 Year Passenger Forecast.
- [153] ICAO (2018). Long-Term Traffic Forecasts (Passenger and Cargo).
- [154] Ihme, M. (2017). Combustion and Engine-Core Noise. *Annual Review of Fluid Mechanics*, 49(1):277–310.
- [155] IMG Stageline (2016). STA-500 Stereo PA amplifier - Technical specifications.
- [156] Ising, H. and Kruppa, B. (2004). Health effects caused by noise: Evidence in the literature from the past 25 years. *Noise and Health*, 6(22).
- [157] ISO (2018). ISO/FDIS 15552 Pneumatic fluid power — Cylinders with detachable mountings, 1 000 kPa (10 bar) series, bores from 32 mm to 320 mm — Basic, mounting and accessories dimensions.

- [158] Ivanova, E. M., Noll, B. E., and Aigner, M. (2011). Computational Modeling of Turbulent Mixing of a Transverse Jet. *Journal of Engineering for Gas Turbines and Power*, 133(2).
- [159] Jammu, K. S., John, G. E. S., and Welsh, H. L. (1966). Pressure Broadening of the Rotational Raman Lines of Some Simple Gases. *Canadian Journal of Physics*, 44(4):797–814.
- [160] Jang, S.-h. and Ih, J.-g. (1998). On the multiple microphone method for measuring in-duct acoustic properties in the presence of mean flow. *The Journal of the Acoustical Society of America*, 103(3):1520–1526.
- [161] Jing, X. and Sun, X. (2000). Effect of Plate Thickness on Impedance of Perforated Plates with Bias Flow. *AIAA Journal*, 38(9):1573–1578.
- [162] Johnston, J. P. and Schmidt, W. E. (1978). Measurement of acoustic reflection from an obstruction in a pipe with flow. *The Journal of the Acoustical Society of America*, 63(5):1455–1460.
- [163] Jones, R. R., Hooper, D. C., Zhang, L., Wolverson, D., and Valev, V. K. (2019). Raman Techniques: Fundamentals and Frontiers. *Nanoscale Research Letters*, 14(1):231.
- [164] Juniper, M. P. and Sujith, R. I. (2018). Sensitivity and Nonlinearity of Thermoacoustic Oscillations. *Annual Review of Fluid Mechanics*, 50:661–689.
- [165] Kather, V., Lückoff, F., O. Paschereit, C., and Oberleithner, K. (2021). Interaction of equivalence ratio fluctuations and flow fluctuations in acoustically forced swirl flames. *International Journal of Spray and Combustion Dynamics*.
- [166] Keller, J. J. (1995). Thermoacoustic oscillations in combustion chambers of gas turbines. *AIAA Journal*, 33(12):2280–2287.
- [167] Kings, N. (2015). *Indirect Combustion Noise: Experimental Investigation of the Vortex Sound Generation in Nozzle Flows*. PhD thesis.
- [168] Kings, N. and Bake, F. (2010). Indirect Combustion Noise: Noise Generation by Accelerated Vorticity in a Nozzle Flow. *International Journal of Spray and Combustion Dynamics*, 2(3):253–266.
- [169] Kings, N., Tao, W., Scoufflaire, P., Richecoeur, F., and Ducruix, S. (2016). Experimental and Numerical Investigation of Direct and Indirect Combustion Noise Contributions in a Lean Premixed Laboratory Swirled Combustor. In *Volume 4B: Combustion, Fuels and Emissions*, pages 1–12. American Society of Mechanical Engineers.
- [170] Kirchhoff, G. R. (1868). Ueber den Einfluss der Wärmeleitung in einem Gase auf die Schallbewegung. *Annalen der Physik und Chemie*, 134(6):177–193.
- [171] Knobloch, K., Lahiri, C., Enghardt, L., Bake, F., and Peitsch, D. (2011). Hot-Acoustic-Testrig (HAT): A Unique Facility for Thermoacoustic Research. In *ASME Turbo Expo 2011: Turbine Technical Conference and Exposition*, pages 1023–1032. ASME.

- [172] Knobloch, K., Neuhaus, L., Bake, F., Gaetani, P., and Persico, G. (2016). Experimental Assessment of Noise Generation and Transmission in a High-Pressure Transonic Turbine Stage. In *ASME Turbo Expo 2016: Turbine Technical Conference and Exposition*.
- [173] Knobloch, K., Neuhaus, L., Bake, F., Gaetani, P., and Persico, G. (2017). Experimental Assessment of Noise Generation and Transmission in a High-Pressure Transonic Turbine Stage. *Journal of Turbomachinery*, 139(10).
- [174] Knobloch, K., Werner, T., and Bake, F. (2015a). Entropy Noise Generation and Reduction in a Heated Nozzle Flow. In *21st AIAA/CEAS Aeroacoustics Conference*, number June, pages 1–13, Reston, Virginia. American Institute of Aeronautics and Astronautics.
- [175] Knobloch, K., Werner, T., and Bake, F. (2015b). Noise Generation in Hot Nozzle Flow. In *Volume 2B: Turbomachinery*, pages 1–14. American Society of Mechanical Engineers.
- [176] Laffay, P., Moreau, S., Jacob, M. C., and Regnard, J. (2020). Experimental investigation of the noise radiated by a ducted air flow discharge through diaphragms and perforated plates. *Journal of Sound and Vibration*, 472:115177.
- [177] Launder, B. and Spalding, D. (1974). The numerical computation of turbulent flows. *Computer Methods in Applied Mechanics and Engineering*, 3(2):269–289.
- [178] Law, C. K. (2006). *Combustion Physics*. Cambridge University Press, Cambridge.
- [179] Leconte, J. (1858). On the influence of musical sounds on the flame of a jet of coal-gas. *The London, Edinburgh, and Dublin Philosophical Magazine and Journal of Science*, 15(99):235–239.
- [180] Lee, D. S., Fahey, D. W., Skowron, A., Allen, M. R., Burkhardt, U., Chen, Q., Doherty, S. J., Freeman, S., Forster, P. M., Fuglestvedt, J., Gettelman, A., De León, R. R., Lim, L. L., Lund, M. T., Millar, R. J., Owen, B., Penner, J. E., Pitari, G., Prather, M. J., Sausen, R., and Wilcox, L. J. (2021). The contribution of global aviation to anthropogenic climate forcing for 2000 to 2018. *Atmospheric Environment*, 244.
- [181] Leyko, M., Durán, I., Moreau, S., Nicoud, F., and Poinso, T. (2014). Simulation and modelling of the waves transmission and generation in a stator blade row in a combustion-noise framework. *Journal of Sound and Vibration*, 333(23):6090–6106.
- [182] Leyko, M., Moreau, S., Nicoud, F., and Poinso, T. (2011). Numerical and analytical modelling of entropy noise in a supersonic nozzle with a shock. *Journal of Sound and Vibration*, 330(16):3944–3958.
- [183] Leyko, M., Nicoud, F., Moreau, S., and Poinso, T. (2008). Numerical and analytical investigation of the indirect noise in a nozzle. In *Center for Turbulence Research, Proceedings of the Summer Program*.

- [184] Leyko, M., Nicoud, F., Moreau, S., and Poinso, T. (2009a). Numerical and analytical investigation of the indirect combustion noise in a nozzle. *Comptes Rendus Mécanique*, 337(6-7):415–425.
- [185] Leyko, M., Nicoud, F., and Poinso, T. (2009b). Comparison of Direct and Indirect Combustion Noise Mechanisms in a Model Combustor. *AIAA Journal*, 47(11):2709–2716.
- [186] Liam Goodes (Andor - Oxford Instruments) (2021). Andor iXon Ultra-888. private communication.
- [187] Lieuwen, T. (2001). Theoretical investigation of unsteady flow interactions with a premixed planar flame. *Journal of Fluid Mechanics*, 435:289–303.
- [188] Lieuwen, T. and Zinn, B. T. (1998). The role of equivalence ratio oscillations in driving combustion instabilities in low NO_x gas turbines. *Symposium (International) on Combustion*, 27(2):1809–1816.
- [189] Lieuwen, T. C. (2012). *Unsteady Combustor Physics*. Cambridge University Press, Cambridge.
- [190] Lieuwen, T. C. and Zinn, B. T. (2005). *Combustion Instabilities in Gas Turbine Engines: Operational Experience, Fundamental Mechanisms and Modeling*.
- [191] Lighthill, M. J. (1952). On sound generated aerodynamically I. General theory. *Proceedings of the Royal Society of London. Series A. Mathematical and Physical Sciences*, 211(1107):564–587.
- [192] Lighthill, M. J. (1953). On the energy scattered from the interaction of turbulence with sound or shock waves. *Mathematical Proceedings of the Cambridge Philosophical Society*, 49(3):531–551.
- [193] Lighthill, M. J. (1954). On sound generated aerodynamically II. Turbulence as a source of sound. *Proceedings of the Royal Society of London. Series A. Mathematical and Physical Sciences*, 222(1148):1–32.
- [194] Litron Lasers Ltd. (2010). High repetition rate lasers for high speed imaging applications: the LDY300 PIV series.
- [195] Litron Lasers Ltd. (2015). LDY303 PIV - 527nm Litron Lasers Test Sheet.
- [196] Liu, Z., Ciais, P., Deng, Z., Lei, R., Davis, S. J., Feng, S., Zheng, B., Cui, D., Dou, X., Zhu, B., Guo, R., Ke, P., Sun, T., Lu, C., He, P., Wang, Y., Yue, X., Wang, Y., Lei, Y., Zhou, H., Cai, Z., Wu, Y., Guo, R., Han, T., Xue, J., Boucher, O., Boucher, E., Chevallier, F., Tanaka, K., Wei, Y., Zhong, H., Kang, C., Zhang, N., Chen, B., Xi, F., Liu, M., Bréon, F.-M., Lu, Y., Zhang, Q., Guan, D., Gong, P., Kammen, D. M., He, K., and Schellnhuber, H. J. (2020). Near-real-time monitoring of global CO₂ emissions reveals the effects of the COVID-19 pandemic. *Nature Communications*, 11(1):5172.
- [197] Lord Rayleigh, F. (1878). The Explanation of Certain Acoustical Phenomena. *Nature*, 18(455):319–321.

- [198] Lord Rayleigh, F. (1879). XXXI. Investigations in optics, with special reference to the spectroscope. *The London, Edinburgh, and Dublin Philosophical Magazine and Journal of Science*, 8(49):261–274.
- [199] Lord Rayleigh, F. (1894). *The Theory of Sound. Volume I*. Macmillan and Co, London, 2nd edition.
- [200] Lord Rayleigh, F. (1896). *The Theory of Sound. Volume II*. Macmillan and Co, London, 2nd edition.
- [201] Lourier, J.-M., Huber, A., Noll, B., and Aigner, M. (2014). Numerical Analysis of Indirect Combustion Noise Generation Within a Subsonic Nozzle. *AIAA Journal*, 52(10):2114–2126.
- [202] Lozano, A., Yip, B., and Hanson, R. K. (1992). Acetone: a tracer for concentration measurements in gaseous flows by planar laser-induced fluorescence. *Experiments in Fluids*, 13(6):369–376.
- [203] Magnus, W. (1954). On the exponential solution of differential equations for a linear operator. *Communications on Pure and Applied Mathematics*, 7(4):649–673.
- [204] Magri, L. (2017). On indirect noise in multicomponent nozzle flows. *Journal of Fluid Mechanics*, 828(R2):1–13.
- [205] Magri, L., O’Brien, J., and Ihme, M. (2016a). Compositional inhomogeneities as a source of indirect noise in subsonic and supersonic nozzles. *Center for Turbulence Research, Annual Research Briefs 2016*, pages 235–246.
- [206] Magri, L., O’Brien, J., and Ihme, M. (2018). Effects of Nozzle Helmholtz Number on Indirect Combustion Noise by Compositional Perturbations. *Journal of Engineering for Gas Turbines and Power*, 140(3).
- [207] Magri, L., O’Brien, J., and Ihme, M. (2016b). Compositional inhomogeneities as a source of indirect combustion noise. *Journal of Fluid Mechanics*, 799(R4):R4.
- [208] Mahmoudi, Y., Dowling, A. P., and Stow, S. R. (2017). Acoustic and Entropy Waves in Nozzles in Combustion Noise Framework. *AIAA Journal*, 55(7):2369–2381.
- [209] Malhotra, A. and Kang, S. (1984). Turbulent Prandtl number in circular pipes. *International Journal of Heat and Mass Transfer*, 27(11):2158–2161.
- [210] Mangiarotty, R. (1971). The reduction of aircraft engine fan-compressor noise using acoustic linings. *Journal of Sound and Vibration*, 18(4):565–576.
- [211] Mani, R. (1981). Low-frequency sound propagation in a quasi-one-dimensional flow. *Journal of Fluid Mechanics*, 104:81–92.
- [212] Marble, F. E. (1975). Response of a nozzle to an entropy disturbance: example of thermodynamically unsteady aerodynamics. *Unsteady Aerodynamics*, 2(699):1–19.
- [213] Marble, F. E. and Candel, S. (1977). Acoustic disturbance from gas non-uniformities convected through a nozzle. *Journal of Sound and Vibration*, 55(2):225–243.

- [214] Mark J. Riches (Managing Director - Invisible Vision Ltd.) (2020). UVi 1850-10-S20 Camera Intensifier. private communication.
- [215] Mathews, D. C. and Peracchio, A. A. (1974). Progress in core engine and turbine noise technology. In *6th AIAA Aircraft Design, Flight Test and Operation Meeting, AIAA Paper No. 74-988*.
- [216] Mazur, M., Tao, W., Scoufflaire, P., Richecoeur, F., and Ducruix, S. (2015). Experimental and Analytical Study of the Acoustic Properties of a Gas Turbine Model Combustor With a Choked Nozzle. In *Volume 4B: Combustion, Fuels and Emissions*, pages 1–10. American Society of Mechanical Engineers.
- [217] Mazur, M. A. (2017). *Etude expérimentale du bruit de combustion dans un foyer de type aéronautique*. PhD thesis, Université Paris-Saclay.
- [218] McCreery, R. L. (2001). Raman Spectroscopy for Chemical Analysis. *Measurement Science and Technology*, 12(5):653–654.
- [219] McCullough, D. (2016). *The Wright Brothers*. Simon & Schuster.
- [220] McEligot, D. and Taylor, M. (1996). The turbulent Prandtl number in the near-wall region for low-Prandtl-number gas mixtures. *International Journal of Heat and Mass Transfer*, 39(6):1287–1295.
- [221] McSweeney, R. and Tandon, A. (2020). Global Carbon Project: Coronavirus causes ‘record fall’ in fossil-fuel emissions in 2020.
- [222] Meindl, M., Albayrak, A., and Polifke, W. (2020). A state-space formulation of a discontinuous Galerkin method for thermoacoustic stability analysis. *Journal of Sound and Vibration*, 481:115431.
- [223] Meindl, M., Merk, M., Fritz, F., and Polifke, W. (2019). Determination of Acoustic Scattering Matrices from Linearized Compressible Flow Equations with Application to Thermoacoustic Stability Analysis. *Journal of Theoretical and Computational Acoustics*, 27(03):1–27.
- [224] Menter, F. R. (1994). Two-equation eddy-viscosity turbulence models for engineering applications. *AIAA Journal*, 32(8):1598–1605.
- [225] Miedema, H. M. and Oudshoorn, C. G. (2001). Annoyance from transportation noise: relationships with exposure metrics DNL and DENL and their confidence intervals. *Environmental Health Perspectives*, 109(4):409–416.
- [226] Miles, J. H. (2009). Time Delay Analysis of Turbofan Engine Direct and Indirect Combustion Noise Sources. *Journal of Propulsion and Power*, 25(1):218–227.
- [227] Miles, J. H. (2010a). Core Noise Diagnostics of Turbofan Engine Noise Using Correlation and Coherence Functions. *Journal of Propulsion and Power*, 26(2):303–316.
- [228] Miles, J. H. (2010b). Separating Direct and Indirect Turbofan Engine Combustion Noise Using the Correlation Function. *Journal of Propulsion and Power*, 26(5):1144–1152.

- [229] Miles, J. H. (2011). Estimation of signal coherence threshold and concealed spectral lines applied to detection of turbofan engine combustion noise. *The Journal of the Acoustical Society of America*, 129(5):3068–3081.
- [230] Miles, J. H. (2012). Spatial correlation in the ambient core noise field of a turbofan engine. *The Journal of the Acoustical Society of America*, 131(6):4625–4639.
- [231] Mishra, A. and Bodony, D. J. (2013). Evaluation of actuator disk theory for predicting indirect combustion noise. *Journal of Sound and Vibration*, 332(4):821–838.
- [232] Moase, W. H., Brear, M. J., and Manzie, C. (2007). The forced response of choked nozzles and supersonic diffusers. *Journal of Fluid Mechanics*, 585:281–304.
- [233] Moreau, S., Becerril, C., and Gicquel, L. Y. (2018). Large-Eddy-simulation prediction of indirect combustion noise in the entropy wave generator experiment. *International Journal of Spray and Combustion Dynamics*, 10(2):154–168.
- [234] Morfey, C. L. (1973). Amplification of aerodynamic noise by convected flow inhomogeneities. *Journal of Sound and Vibration*, 31(4):391–397.
- [235] Morgans, A. S. and Durán, I. (2016). Entropy noise: A review of theory, progress and challenges. *International Journal of Spray and Combustion Dynamics*, 8(4):285–298.
- [236] Morgans, A. S., Goh, C. S., and Dahan, J. A. (2013). The dissipation and shear dispersion of entropy waves in combustor thermoacoustics. *Journal of Fluid Mechanics*, 733(R2).
- [237] Motheau, E., Nicoud, F., Mery, Y., and Poinsot, T. (2013). Analysis and Modelling of Entropy Modes in a Realistic Aeronautical Gas Turbine. *Volume 1A: Combustion, Fuels and Emissions*, 135(September 2013):V01AT04A009.
- [238] Mühlbauer, B., Noll, B., and Aigner, M. (2009). Numerical Investigation of the Fundamental Mechanism for Entropy Noise Generation in Aero-Engines. *Acta Acustica united with Acustica*, 95(3):470–478.
- [239] Mühlbauer, B., Widenhorn, A., Liu, M., Noll, B., and Aigner, M. (2007). Fundamental mechanism of entropy noise in aero-engines: numerical simulation. *Proceedings of ASME Turbo Expo 2007: Power for Land, Sea and Air*, pages 1–10.
- [240] Mullikin, J. C., van Vliet, L. J., Netten, H., Boddeke, F. R., van der Feltz, G., and Young, I. T. (1994). Methods for CCD camera characterization. In Titus, H. C. and Waks, A., editors, *IEEE Transactions on Electron Devices*, volume 50, pages 73–84, San Jose, CA.
- [241] Münzel, T., Schmidt, F. P., Steven, S., Herzog, J., Daiber, A., and Sørensen, M. (2018). Environmental Noise and the Cardiovascular System. *Journal of the American College of Cardiology*, 71(6):688–697.
- [242] Muthukrishnan, M., Strahle, W. C., and Neale, D. H. (1978). Separation of Hydrodynamic, Entropy, and Combustion Noise in a Gas Turbine Combustor. *AIAA Journal*, 16(4):320–327.

- [243] NASA Glenn Research Center (1999). Making Future Commercial Aircraft Quieter. Technical report.
- [244] National Academy of Engineering (2010). *Technology for a Quieter America*. National Academies Press, Washington, D.C.
- [245] Noiray, N., Durox, D., Schuller, T., and Candel, S. (2009). Mode Conversion in Acoustically Modulated Confined Jets. *AIAA Journal*, 47(9):2053–2062.
- [246] O’Brien, J. D. and Ihme, M. (2017). Species Dependency of the Compositional Indirect Noise Mechanism. In *Proceedings of ASME Turbo Expo 2017: Turbomachinery Technical Conference and Exposition*.
- [247] Oefelein, J. C. and Yang, V. (1993). Comprehensive Review of Liquid-Propellant Combustion Instabilities in F-1 Engines. *Journal of Propulsion and Power*, 9(5):657–677.
- [248] Ono, A., Kimura, N., Kamide, H., and Tobita, A. (2011). Influence of elbow curvature on flow structure at elbow outlet under high Reynolds number condition. *Nuclear Engineering and Design*, 241(11):4409–4419.
- [249] Oyediran, A., Darling, D., and Radhakrishnan, K. (1995). Review of Combustion-Acoustic Instabilities. In *31st Joint Propulsion Conference and Exhibit*, page 16.
- [250] Panczer, G., De Ligny, D., Mendoza, C., Gaft, M., Seydoux-Guillaume, A.-M., and Wang, X. (2012). Raman and fluorescence. In *Raman spectroscopy applied to Earth sciences and cultural heritage*, volume 12, pages 61–82. European Mineralogical Union and the Mineralogical Society of Great Britain & Ireland.
- [251] Papadogiannis, D., Wang, G., Moreau, S., Duchaine, F., Gicquel, L., and Nicoud, F. (2016). Assessment of the Indirect Combustion Noise Generated in a Transonic High-Pressure Turbine Stage. *Journal of Engineering for Gas Turbines and Power*, 138(4):261–270.
- [252] Paschereit, C. O., Gutmark, E., and Weisenstein, W. (1998). Structure and Control of Thermoacoustic Instabilities in a Gas-turbine Combustor. *Combustion Science and Technology*, 138(1-6):213–232.
- [253] Penney, C. M., Goldman, L. M., and Lapp, M. (1972). Raman Scattering Cross Sections. *Nature Physical Science*, 235(58):110–112.
- [254] Penrose, R. (1955). A generalized inverse for matrices. *Mathematical Proceedings of the Cambridge Philosophical Society*, 51(3):406–413.
- [255] Persico, G., Gaetani, P., and Spinelli, A. (2017). Assessment of synthetic entropy waves for indirect combustion noise experiments in gas turbines. *Experimental Thermal and Fluid Science*.
- [256] Petrov, D. (2018). Raman spectrum of methane in nitrogen, carbon dioxide, hydrogen, ethane, and propane environments. *Spectrochimica Acta Part A: Molecular and Biomolecular Spectroscopy*, 191:573–578.

- [257] Petrov, D. V., Matrosov, I. I., Sedinkin, D. O., and Zaripov, A. R. (2018). Raman Spectra of Nitrogen, Carbon Dioxide, and Hydrogen in a Methane Environment. *Optics and Spectroscopy*, 124(1):8–12.
- [258] Pickett, G. F. (1975). Core engine noise due to turbine fluctuations convecting through turbine blade rows. *AIAA 2nd Aeroacoustics Conference, Hampton, VA, March 24-26*, pages 589–608.
- [259] Pierce, A. D. (2019). *Acoustics: An Introduction to Its Physical Principles and Applications*. Springer.
- [260] Poinso, T. (2017). Prediction and control of combustion instabilities in real engines. *Proceedings of the Combustion Institute*, 36(1):1–28.
- [261] Poinso, T. and Veynante, D. (2005). *Theoretical and Numerical Combustion*. R.T. Edwards, second edition.
- [262] Polifke, W., Paschereit, C. O., and Paschereit, K. (2001). Constructive and Destructive Interference of Acoustic and Entropy Waves in a Premixed Combustor with a Choked Exit. *The International Journal of Acoustics and Vibration*, 6(3):135–146.
- [263] Pope, S. B. (2000). *Turbulent Flows*. Cambridge University Press.
- [264] Povey, T., Chana, K. S., Jones, T. V., and Hurrion, J. (2007). The Effect of Hot-Streaks on HP Vane Surface and Endwall Heat Transfer: An Experimental and Numerical Study. *Journal of Turbomachinery*, 129(1):32–43.
- [265] Powell, A. (1990). Some Aspects of Aeroacoustics: From Rayleigh Until Today. *Journal of Vibration and Acoustics*, 112(2):145–159.
- [266] Prashanth, P., Speth, R. L., Eastham, S. D., Sabnis, J. S., and Barrett, S. R. H. (2021). Post-combustion emissions control in aero-gas turbine engines. *Energy & Environmental Science*, 14(2):916–930.
- [267] Putnam, A. A. (1971). *Combustion-driven oscillations in industry*. Elsevier, New York.
- [268] Putnam, A. A. and Dennis, W. R. (1956). Survey of Organ-Pipe Oscillations in Combustion Systems. *Journal of the Acoustical Society of America*, 28(2):246–259.
- [269] Raman, C. V. (1928). A new radiation. *Indian Journal of Physics*, 2:387–398.
- [270] Raman, C. V. and Krishnan, K. S. (1928). A New Type of Secondary Radiation. *Nature*, 121:501–502.
- [271] Rämmal, H. and Abom, M. (2009). Experimental Determination of Sound Transmission in Turbo-Compressors. In *SAE 2017 Noise and Vibration Conference and Exhibition*, volume 4970.

- [272] Rausch, A., Fischer, A., Konle, H., Gaertlein, A., Nitsch, S., Knobloch, K., Bake, F., and Rohle, I. (2011). Measurements of Density Pulsations in the Outlet Nozzle of a Combustion Chamber by Rayleigh-Scattering Searching Entropy Waves. *Journal of Engineering for Gas Turbines and Power*, 133(March):1–9.
- [273] Reynolds, O. (1883). An experimental investigation of the circumstances which determine whether the motion of water shall be direct or sinuous, and of the law of resistance in parallel channels. *Philosophical Transactions of the Royal Society of London*, 174:935–982.
- [274] Rienstra, S. W. and Hirschberg, A. (2019). *An Introduction to Acoustics*.
- [275] Ritchie, H. (2020). Climate change and flying: what share of global CO₂ emissions come from aviation? *Our World in Data*.
- [276] Rodrigues, J., Busseti, A., and Hochgreb, S. (2020). Numerical investigation on the generation, mixing and convection of entropic and compositional waves in a flow duct. *Journal of Sound and Vibration*, 472(115155).
- [277] Rolland, E., De Domenico, F., and Hochgreb, S. (2018). Direct and indirect noise generated by entropic and compositional inhomogeneities. *Journal of Engineering for Gas Turbines and Power*, 140(8):1–12.
- [278] Rolland, E. O. (2017). *Sound produced by entropic and compositional inhomogeneities*. PhD thesis, University of Cambridge.
- [279] Rolland, E. O. (2021). Source identification technique. private communication.
- [280] Rolland, E. O., De Domenico, F., and Hochgreb, S. (2017). Theory and application of reverberated direct and indirect noise. *Journal of Fluid Mechanics*, 819:435–464.
- [281] Rolls-Royce (2015). *The Jet Engine*. Wiley.
- [282] Ron, E. (2015). *Entropy noise*. PhD thesis, Oxford University.
- [283] Ron, E. and Chana, K. (2017). Comparison of Large Eddy Simulation and Unsteady Reynolds-Averaged Navier–Stokes for Evaluation of Entropy Noise. *Journal of Fluids Engineering*, 139(11).
- [284] Rosfjord, T. J. and Padget, F. C. (2001). Experimental Assessment of the Emissions Control Potential of a Rich/Quench/Lean Combustor for High Speed Civil Transport Aircraft Engines. *NASA CR—2001-210613*.
- [285] Rupp, J., Carrotte, J., and MacQuisten, M. (2012). The use of perforated damping liners in aero gas turbine combustion systems. *Journal of Engineering for Gas Turbines and Power*, 134(7).
- [286] Rüttinger, S., Buschmann, V., Krämer, B., Erdmann, R., Macdonald, R., and Koberling, F. (2007). Determination of the confocal volume for quantitative fluorescence correlation spectroscopy. In Wilson, T. and Periasamy, A., editors, *Confocal, Multiphoton, and Nonlinear Microscopic Imaging III*, volume 6630.

- [287] Sadanandan, R., Stöhr, M., and Meier, W. (2008). Simultaneous OH-PLIF and PIV measurements in a gas turbine model combustor. *Applied Physics B: Lasers and Optics*, 90(3-4):609–618.
- [288] Salikuddin, M. (1990). Acoustic behavior of orifice plates and perforated plates with reference to low-frequency sound absorption. *Journal of Sound and Vibration*, 139(3):361–381.
- [289] Sattelmayer, T. (2003). Influence of the Combustor Aerodynamics on Combustion Instabilities From Equivalence Ratio Fluctuations. *Journal of Engineering for Gas Turbines and Power*, 125(1):11–19.
- [290] Schemel, C., Thiele, F., Bake, F., Lehmann, B., and Michel, U. (2004). Sound Generation in the Outlet Section of Gas Turbine Combustion Chambers. In *10th AIAA/CEAS Aeroacoustics Conference*, pages 1–10.
- [291] Schulze, M., Wagner, M., and Sattelmayer, T. (2016). Linearized Euler Equations for the Determination of Scattering Matrices for Orifice and Perforated Plate Configurations in the High Mach Number Regime. *Aerospace*, 3(4):33.
- [292] Seeger, T., Kiefer, J., Weikl, M. C., Leipertz, A., and Kozlov, D. N. (2006). Time-resolved measurement of the local equivalence ratio in a gaseous propane injection process using laser-induced gratings. *Optics Express*, 14(26):12994.
- [293] Semlitsch, B., Hynes, T., Langella, I., Swaminathan, N., and Dowling, A. P. (2019). Entropy and Vorticity Wave Generation in Realistic Gas Turbine Combustors. *Journal of Propulsion and Power*, pages 1–11.
- [294] Seybert, A. F. and Ross, D. F. (1977). Experimental determination of acoustic properties using a two-microphone random-excitation technique. *Journal of the Acoustical Society of America*, 61(5):1362–1370.
- [295] Shao, C., Maeda, K., and Ihme, M. (2021). Analysis of core-noise contributions in a realistic gas-turbine combustor operated near lean blow-out. *Proceedings of the Combustion Institute*, 38(4):6203–6211.
- [296] Sinai, Y. L. (1980). The generation of combustion noise by chemical inhomogeneities in steady, low-Mach-number duct flows. *Journal of Fluid Mechanics*, 99(2):383–397.
- [297] Smekal, A. (1923). Zur Quantentheorie der Streuung und Dispersion. *Naturwissenschaften*, 11:873–875.
- [298] Smith, E. and Dent, G. (2004). *Modern Raman Spectroscopy - A Practical Approach*, volume 36. John Wiley & Sons, Ltd, Chichester, UK.
- [299] Smith, M. J. T. (1989). *Aircraft Noise*. Cambridge University Press.
- [300] Smith, R., Ellis, M., Xia, G., Sankaran, V., Anderson, W., and Merkle, C. L. (2008). Computational Investigation of Acoustics and Instabilities in a Longitudinal-Mode Rocket Combustor. *AIAA Journal*, 46(11):2659–2673.

- [301] Stansbury, E. J., Crawford, M. F., and Welsh, H. L. (1953). Determination of Rates of Change of Polarizability from Raman and Rayleigh Intensities. *Canadian Journal of Physics*, 31(6):954–961.
- [302] Stansfeld, S. A. (2015). Noise effects on health in the context of air pollution exposure. *International Journal of Environmental Research and Public Health*, 12(10):12735–12760.
- [303] Stansfeld, S. A. and Matheson, M. P. (2003). Noise pollution: non-auditory effects on health. *British Medical Bulletin*, 68(1):243–257.
- [304] Stokes, G. G. (1845). On the Theories of the Internal Friction of Fluids in Motion, and of the Equilibrium and Motion of Elastic Solids. *Transactions of the Cambridge Philosophical Society*, 8(22):287–319.
- [305] Stow, S. R., Dowling, A. P., and Hynes, T. P. (2002). Reflection of circumferential modes in a choked nozzle. *Journal of Fluid Mechanics*, 467:215–239.
- [306] Strahle, W. C. (1971). On combustion generated noise. *Journal of Fluid Mechanics*, 49(2):399–414.
- [307] Strahle, W. C. (1978). Combustion noise. *Progress in Energy and Combustion Science*, 4(3):157–176.
- [308] Su, J., Rupp, J., Garmory, A., and Carrotte, J. (2015). Measurements and computational fluid dynamics predictions of the acoustic impedance of orifices. *Journal of Sound and Vibration*, 352:174–191.
- [309] Sujith, R. I., Juniper, M. P., and Schmid, P. J. (2016). Non-normality and nonlinearity in thermoacoustic instabilities. *International Journal of Spray and Combustion Dynamics*, 8(2):119–146.
- [310] Sutherland, W. (1893). The viscosity of gases and molecular force. *Philosophical Magazine Series 5*, 36(223):507–531.
- [311] Sutton, G. and Biblarz, O. (2001). *Rocket Propulsion Elements*. Wiley, 7 edition.
- [312] Swaminathan, N., Xu, G., Dowling, A. P., and Balachandran, R. (2011). Heat release rate correlation and combustion noise in premixed flames. *Journal of Fluid Mechanics*, 681:80–115.
- [313] Tam, C. K. (2015). The Spectral Shape of Combustion Noise. *International Journal of Aeroacoustics*, 14(3-4):431–456.
- [314] Tam, C. K. and Parrish, S. A. (2015). Noise of high-performance aircraft at afterburner. *Journal of Sound and Vibration*, 352:103–128.
- [315] Tam, C. K. and Parrish, S. A. (2018). The physical processes of indirect combustion noise generation. *International Journal of Aeroacoustics*, 17(1-2):22–35.
- [316] Tam, C. K., Parrish, S. A., Xu, J., and Schuster, B. (2013). Indirect combustion noise of auxiliary power units. *Journal of Sound and Vibration*, 332(17):4004–4020.

- [317] Tam, C. K. W., Bake, F., Hultgren, L. S., and Poinso, T. (2019). Aircraft noise generation and assessment. *CEAS Aeronautical Journal*.
- [318] Tam, C. K. W. and Parrish, S. A. (2014). On the Generation of Indirect Combustion Noise. *20th AIAA/CEAS Aeroacoustics Conference, 2014*, (June).
- [319] Tao, W., Mazur, M., Huet, M., and Richecoeur, F. (2016). Indirect Combustion Noise Contributions in a Gas Turbine Model Combustor with a Choked Nozzle. *Combustion Science and Technology*, 188(4-5):793–804.
- [320] Tao, W., Schuller, T., Huet, M., and Richecoeur, F. (2017). Coherent entropy induced and acoustic noise separation in compact nozzles. *Journal of Sound and Vibration*, 394:237–255.
- [321] Thomas, A. and Williams, G. T. (1966). Flame noise: sound emission from spark-ignited bubbles of combustible gas. *Proceedings of the Royal Society A*, 294(449).
- [322] Thomas, R. H., Guo, Y., Berton, J., and Fernandez, H. (2017). Aircraft Noise Reduction Technology Roadmap Toward Achieving The NASA 2035 Goal. In *23rd AIAA/CEAS Aeroacoustics Conference*, number June, pages 1–26, Reston, Virginia. American Institute of Aeronautics and Astronautics.
- [323] Tkatchenko, I., Kornev, N., Jahnke, S., Steffen, G., and Hassel, E. (2007). Performances of LES and RANS Models for Simulation of Complex Flows in a Coaxial Jet Mixer. *Flow, Turbulence and Combustion*, 78(2):111–127.
- [324] Tollmien, W. (1926). Berechnung turbulenter Ausbreitungsvorgänge. *ZAMM - Journal of Applied Mathematics and Mechanics / Zeitschrift für Angewandte Mathematik und Mechanik*, 6(6):468–478.
- [325] Tominaga, Y. and Stathopoulos, T. (2007). Turbulent Schmidt numbers for CFD analysis with various types of flowfield. *Atmospheric Environment*, 41(37):8091–8099.
- [326] Tsien, H. S. (1952a). Servo-Stabilization of Combustion in Rocket Motors. *Journal of the American Rocket Society*, (September-October):704–719.
- [327] Tsien, H. S. (1952b). The Transfer Functions of Rocket Nozzles. *Journal of the American Rocket Society*, pages 650–660.
- [328] Tyndall, J. (1857). LXIII. On the sounds produced by the combustion of gases in tubes. *The London, Edinburgh, and Dublin Philosophical Magazine and Journal of Science*, 13(89):473–479.
- [329] Ullrich, W. C., Bake, F., Kings, N., and Sattelmayer, T. (2015). Numerical Investigation of Indirect Noise Generation by Accelerated Vorticity. In *21st AIAA/CEAS Aeroacoustics Conference*, Reston, Virginia. American Institute of Aeronautics and Astronautics.
- [330] Ullrich, W. C., Gikadi, J., Jörg, C., and Sattelmayer, T. (2014). Acoustic-entropy coupling behavior and acoustic scattering properties of a Laval nozzle. In *20th AIAA/CEAS Aeroacoustics Conference*, number June, Reston, Virginia. American Institute of Aeronautics and Astronautics.

- [331] Wang, G., Liu, X., Wang, S., Li, L., and Qi, F. (2019). Experimental investigation of entropy waves generated from acoustically excited premixed swirling flame. *Combustion and Flame*, 204:85–102.
- [332] Wang, J., Ge, N., and Sheng, C. (2016). Analysis of swirling flow effects on the characteristics of unsteady hot-streak migration. *Chinese Journal of Aeronautics*, 29(6):1469–1476.
- [333] Wassmer, D., Pause, F., Schuermans, B., Paschereit, C. O., and Moeck, J. P. (2017a). An Onion Peeling Reconstruction of the Spatial Characteristics of Entropy Waves in a Model Gas Turbine Combustor. *Proceedings of ASME Turbo Expo 2017: Turbomachinery Technical Conference and Exposition*, pages 2017–64717.
- [334] Wassmer, D., Schuermans, B., Paschereit, C. O., and Moeck, J. P. (2017b). An Acoustic Time-of-Flight Approach for Unsteady Temperature Measurements: Characterization of Entropy Waves in a Model Gas Turbine Combustor. *Journal of Engineering for Gas Turbines and Power*, 139(April):1–8.
- [335] Wassmer, D., Schuermans, B., Paschereit, C. O., and Moeck, J. P. (2017c). Measurement and modeling of the generation and the transport of entropy waves in a model gas turbine combustor. *International Journal of Spray and Combustion Dynamics*, 9(4):299–309.
- [336] Way, J. and Libby, P. A. (1970). Hot-wire probes for measuring velocity and concentration in helium and air mixtures. *AIAA Journal*, 8(5):976–978.
- [337] Weber, A. (1979). *Topics in Current Physics: Raman Spectroscopy of Gases and Liquids*.
- [338] Weilenmann, M., Doll, U., Bombach, R., Blondé, A., Ebi, D., Xiong, Y., and Noiray, N. (2021). Linear and nonlinear entropy-wave response of technically-premixed jet-flames-array and swirled flame to acoustic forcing. *Proceedings of the Combustion Institute*, 38(4):6135–6143.
- [339] Weilenmann, M. and Noiray, N. (2021). Experiments on sound reflection and production by choked nozzle flows subject to acoustic and entropy waves. *Journal of Sound and Vibration*, 492(115799).
- [340] Weilenmann, M., Xiong, Y., Bothien, M., and Noiray, N. (2019a). Background-Oriented Schlieren of Fuel Jet Flapping Under Thermoacoustic Oscillations in a Sequential Combustor. *Journal of Engineering for Gas Turbines and Power*, 141(1).
- [341] Weilenmann, M., Xiong, Y., and Noiray, N. (2019b). Background-oriented schlieren of entropy waves advected in straight duct. In *Proceedings of the 23rd International Congress on Acoustics*, pages 5607–5614.
- [342] Weilenmann, M., Xiong, Y., and Noiray, N. (2020). On the dispersion of entropy waves in turbulent flows. *Journal of Fluid Mechanics*, 903(R1).
- [343] White, F. M. (2006). *Viscous Fluid Flow*. McGraw-Hill, 3rd edition.

- [344] Williams, F. A. (1985). *Combustion theory: the fundamental theory of chemically reacting flow systems*. Benjamin/Cummings Publishing Company, Inc, 2nd edition.
- [345] Williams, J. F. and Howe, M. S. (1975). The generation of sound by density inhomogeneities in low Mach number nozzle flows. *Journal of Fluid Mechanics*, 70(3):605–622.
- [346] Wolf, D. E. (2008). What is the Confocal Volume?
- [347] Xia, Y., Durán, I., Morgans, A. S., and Han, X. (2018). Dispersion of Entropy Perturbations Transporting through an Industrial Gas Turbine Combustor. *Flow, Turbulence and Combustion*, 100(2):481–502.
- [348] Xing, F., Huang, Y., Zhao, M., and Zhao, J. (2016). The Brief Introduction of Different Laser Diagnostics Methods Used in Aeroengine Combustion Research. *Journal of Sensors*, 2016:1–13.
- [349] Yang, D., Guzmán-Iñigo, J., and Morgans, A. S. (2020). Sound generation by entropy perturbations passing through a sudden flow expansion. *Journal of Fluid Mechanics*, 905:R2.
- [350] Yeddula, S. R. and Morgans, A. S. (2021). A semi-analytical solution for acoustic wave propagation in varying area ducts with mean flow. *Journal of Sound and Vibration*, 492:115770.
- [351] Younes, K. and Hickey, J.-P. (2018). Indirect noise prediction in compound, multi-stream nozzle flows. *Journal of Sound and Vibration*.
- [352] Yu, Y., O’Hara, L., Sisco, J., and Anderson, W. (2009). Experimental Study of High-Frequency Combustion Instability in a Continuously Variable Resonance Combustor (CVRC). In *47th AIAA Aerospace Sciences Meeting including The New Horizons Forum and Aerospace Exposition*, number January, pages 1–12, Reston, Virginia. American Institute of Aeronautics and Astronautics.
- [353] Zaman, K. B. M. Q., Bridges, J. E., and Huff, D. L. (2012). Evolution from ‘Tabs’ to ‘Chevron Technology’ - a Review (NASA Glenn Research Center). *Proceedings of the 13th Asian Congress of Fluid Mechanics 17–21 December 2010, Dhaka, Bangladesh*, 11(1):27–48.
- [354] Zhao, D., Lu, Z., Zhao, H., Li, X., Wang, B., and Liu, P. (2018). A review of active control approaches in stabilizing combustion systems in aerospace industry. *Progress in Aerospace Sciences*, 97(January):35–60.
- [355] Zheng, J., Huet, M., Giauque, A., and Ducruix, S. (2015). A 2D-axisymmetric analytical model for the estimation of indirect combustion noise in nozzle flows. In *21st AIAA/CEAS Aeroacoustics Conference*, number June, pages 1–14.
- [356] Zhu, Z., Mühlbacher, D., Morana, M., Koppe, M., Scharber, M. C., Waller, D., Dennler, G., Brabec, C. J., Petrova-Koch, V., Hezel, R., and Goetzberger, A. (2012). *Raman Imaging: Techniques and Applications*, volume 168 of *Springer Series in Optical Sciences*. Springer Berlin Heidelberg, Berlin, Heidelberg.

-
- [357] Zinn, B. T., Bell, W. A., Daniel, B. R., Smith Jr., A. J., and Smith, A. J. (1973). Experimental determination of three-dimensional liquid rocket nozzle admittances. *AIAA Journal*, 11(3):267–272.
- [358] Zinn, B. T. and Powell, E. A. (1971). Nonlinear combustion instability in liquid-propellant rocket engines. *Symposium (International) on Combustion*, 13(1):491–503.
- [359] Zukoski, E. E. and Auerbach, J. M. (1976). Experiments Concerning the Response of Supersonic Nozzles to Fluctuating Inlet Conditions. *Journal of Engineering for Power*, 98(1).

Appendix A

Derivations

THIS appendix serves to explicitly present the full derivations for some of the expressions used in the main text of this thesis. In particular, the entropic wave amplitude and the general compact wave source formulation.

A.1 Entropic wave amplitude

We start with the enthalpy formulation $H \equiv U + pV$, one of the four fundamental equations of chemical thermodynamics:

$$dH = TdS + Vdp + \sum_{i=1}^N \mu_i dN_i. \quad (\text{A.1})$$

By dividing through by the mass M of the closed element, we obtain the Gibbs' equation for a calorically perfect multi-component gas (also known as the fundamental thermodynamic relation) expressed in terms of specific enthalpy³⁴⁴:

$$dh = Tds + vdp + \sum_{i=1}^N \frac{\mu_i}{W_i} dY_i, \quad (\text{A.2})$$

where s is the specific entropy, μ_i is the chemical potential of species i , and W is the molecular weight of species i . As shown explicitly by Williams³⁴⁴, the last term in Eq. (A.2) is derived as follows:

$$\begin{aligned} dN_i/M &= d(N_i/M), \\ &= d[(N_i/N)/(M/N)], \\ &= d(X_i/\bar{W}), \\ &= d(Y_i/W_i), \\ &= dY_i/W_i, \end{aligned} \quad (\text{A.3})$$

where $N \equiv \sum_{i=1}^N N_i$ is the total number of moles in this closed element, $\bar{W} \equiv M/N = \sum_{i=1}^N X_i W_i = \left(\sum_{i=1}^N Y_i/W_i \right)^{-1}$ is the average molecular weight.

Since $h = c_p T$:

$$\begin{aligned} dh &= d(c_p T), \\ &= \bar{T} dc_p + \bar{c}_p dT. \end{aligned} \quad (\text{A.4})$$

Substituting this into Eq. (A.2), knowing that $v = 1/\rho$ and employing the linear perturbation theory notation (i.e. $d\alpha = \alpha'$):

$$\bar{T}c'_p + \bar{c}_p T' = \bar{T}s' + \frac{p'}{\bar{\rho}} + \sum_{n=1}^N \frac{\mu_i}{W_i} dY_i. \quad (\text{A.5})$$

Dividing by $\bar{c}_p \bar{T}$:

$$\frac{c'_p}{\bar{c}_p} + \frac{T'}{\bar{T}} = \frac{s'}{\bar{c}_p} + \frac{p'}{\bar{\rho} \bar{c}_p \bar{T}} + \frac{1}{\bar{c}_p \bar{T}} \sum_{n=1}^N \frac{\mu_i}{W_i} dY_i, \quad (\text{A.6})$$

and re-arranging:

$$\frac{s'}{\bar{c}_p} = \frac{c'_p}{\bar{c}_p} + \frac{T'}{\bar{T}} - \frac{p'}{\bar{\rho} \bar{c}_p \bar{T}} - \frac{1}{\bar{c}_p \bar{T}} \sum_{n=1}^N \frac{\mu_i}{W_i} dY_i. \quad (\text{A.7})$$

Linearising the equation of state, we obtain three useful formulations:

$$\left. \begin{aligned} p' &= \bar{\rho} \bar{R} T' + \rho' \bar{R} \bar{T} + \bar{\rho} R' \bar{T}, \\ \bar{p} &= \bar{\rho} \bar{R} \bar{T}, \\ p'/\bar{p} &= \rho'/\bar{\rho} + R'/\bar{R} + T'/\bar{T}. \end{aligned} \right\} \quad (\text{A.8})$$

In terms of temperature:

$$\frac{T'}{\bar{T}} = \frac{p'}{\bar{p}} - \frac{\rho'}{\bar{\rho}} - \frac{R'}{\bar{R}}. \quad (\text{A.9})$$

We also know that:

$$\bar{c}_p = \frac{\bar{\gamma}}{\bar{\gamma} - 1} \bar{R}. \quad (\text{A.10})$$

Inputting this into Eq. (A.7), using $\bar{p} = \bar{\rho} \bar{R} \bar{T}$:

$$\begin{aligned} \frac{s'}{\bar{c}_p} &= \frac{c'_p}{\bar{c}_p} + \frac{p'}{\bar{p}} - \frac{\rho'}{\bar{\rho}} - \frac{R'}{\bar{R}} - \left(\frac{\bar{\gamma} - 1}{\bar{\gamma}} \right) \frac{p'}{\bar{p}} - \frac{1}{\bar{c}_p \bar{T}} \sum_{i=1}^N \frac{\mu_i}{W_i} dY_i, \\ &= \frac{p'}{\bar{p}} \left(1 - \left(\frac{\bar{\gamma} - 1}{\bar{\gamma}} \right) \right) + \frac{c'_p}{\bar{c}_p} - \frac{\rho'}{\bar{\rho}} - \frac{R'}{\bar{R}} - \frac{1}{\bar{c}_p \bar{T}} \sum_{i=1}^N \frac{\mu_i}{W_i} dY_i, \\ &= \frac{p'}{\bar{p}} \left(\frac{\bar{\gamma} - \bar{\gamma} + 1}{\bar{\gamma}} \right) + \frac{c'_p}{\bar{c}_p} - \frac{\rho'}{\bar{\rho}} - \frac{R'}{\bar{R}} - \frac{1}{\bar{c}_p \bar{T}} \sum_{i=1}^N \frac{\mu_i}{W_i} dY_i. \end{aligned} \quad (\text{A.11})$$

Therefore,

$$\sigma \equiv \frac{s'}{\bar{c}_p} = \frac{p'}{\bar{\gamma} \bar{p}} + \frac{c'_p}{\bar{c}_p} - \frac{\rho'}{\bar{\rho}} - \frac{R'}{\bar{R}} - \frac{1}{\bar{c}_p \bar{T}} \sum_{i=1}^N \frac{\mu_i}{W_i} dY_i. \quad (\text{A.12})$$

We can now define the chemical potential function Ψ and heat-capacity factor \aleph ²⁰⁴:

$$\Psi = \frac{1}{c_p T} \sum_{i=1}^N \left(\frac{\mu_i}{W_i} \right) \frac{dY_i}{dZ}, \quad (\text{A.13})$$

$$\aleph = \frac{R'}{R} - \frac{c'_p}{c_p} = \sum_{i=1}^N \left(\frac{1}{R} \frac{dR}{dY_i} - \frac{1}{c_p} \frac{dc_p}{dY_i} \right) \frac{dY_i}{dZ}, \quad (\text{A.14})$$

such that⁶⁴:

$$\sigma = \frac{p'}{\bar{\gamma}\bar{p}} - \frac{\rho'}{\bar{\rho}} - (\bar{\aleph} + \bar{\Psi})\xi. \quad (\text{A.15})$$

As explicitly done by Magri²⁰⁴, we use the 1st order homogeneity of Gibbs' energy:

$$\mu_i = W_i g_i, \quad (\text{A.16})$$

where g is the specific Gibbs' energy²⁰⁴:

$$g = h - Ts. \quad (\text{A.17})$$

We can further simplify Eq. (A.15) since we are dealing with a non reacting, binary gas mixture due to the injection of a gas i . All species are expressed in terms of mixture fraction, such that $Y_i = Y_i(Z)$, and $dY_i = (dY_i/dZ)dZ$ ³⁴⁴:

$$\begin{aligned} dZ &= Y_i, \\ \frac{dY_i}{dZ} &= 1, \\ \frac{dY_{\text{air}}}{dZ} &= \frac{d(1 - Y_i)}{dZ} = -1. \end{aligned} \quad (\text{A.18})$$

Applying these definitions, along with Eq. (A.16), to Eq. (A.13):

$$\begin{aligned} \Psi &= \frac{1}{c_p T} \left(\frac{\mu_i}{W_i} - \frac{\mu_{\text{air}}}{W_{\text{air}}} \right), \\ &= \frac{1}{(c_{p,i} Y_i + c_{p,\text{air}}(1 - Y_i)) (T_i Y_i + T_{\text{air}}(1 - Y_i))} \left(\frac{W_i g_i}{W_i} - \frac{W_{\text{air}} g_{\text{air}}}{W_{\text{air}}} \right), \\ &= \frac{1}{(c_{p,i} Y_i + c_{p,\text{air}}(1 - Y_i)) (T_i Y_i + T_{\text{air}}(1 - Y_i))} \left[(h_i - T_i s_i) - (h_{\text{air}} - T_{\text{air}} s_{\text{air}}) \right]. \end{aligned} \quad (\text{A.19})$$

For $Y_i \ll 1$, we can assume $(\)_{\text{air}} = (\)$ and neglect terms multiplied by Y_i . Knowing that $h = c_p T$, then:

$$\bar{\Psi} = \frac{1}{\bar{c}_p \bar{T}} \left[(c_{p,i} T_i - T_i s_i) - (\bar{c}_p \bar{T} - \bar{T} \bar{s}) \right].$$

Assuming the temperature of the perturbation is the same as the mean flow temperature ($T_i = \bar{T}$):

$$\bar{\Psi} = \frac{1}{\bar{c}_p} \left[(c_{p,i} - s_i) - (\bar{c}_p - \bar{s}) \right],$$

$$\boxed{\bar{\Psi} = \frac{c_{p,i} - \bar{c}_p}{\bar{c}_p} - \frac{s_i - \bar{s}}{\bar{c}_p}}. \quad (\text{A.20})$$

Similarly, for the heat-capacity factor:

$$\aleph = \frac{R'}{R} - \frac{c'_p}{c_p},$$

where

$$R_i = \frac{\mathcal{R}_u}{W_i}, \quad R_{\text{air}} = \frac{\mathcal{R}_u}{W_{\text{air}}},$$

and

$$R = \mathcal{R}_u \sum_{i=1}^N \frac{Y_i}{W_i}.$$

Therefore:

$$\begin{aligned} \frac{R'}{R} &= \frac{\left(\frac{\mathcal{R}_u}{W_i}\right) - \left(\frac{\mathcal{R}_u}{W_{\text{air}}}\right)}{\left(\frac{\mathcal{R}_u}{W_i}\right) Y_i + \left(\frac{\mathcal{R}_u}{W_{\text{air}}}\right) (1 - Y_i)}, \\ &= \frac{\left(\frac{\mathcal{R}_u W_{\text{air}}}{W_i W_{\text{air}}}\right) - \left(\frac{\mathcal{R}_u W_i}{W_i W_{\text{air}}}\right)}{\left(\frac{\mathcal{R}_u W_{\text{air}}}{W_i W_{\text{air}}}\right) Y_i + \left(\frac{\mathcal{R}_u W_i}{W_i W_{\text{air}}}\right) (1 - Y_i)}, \\ &= \frac{\left(\frac{\mathcal{R}_u W_{\text{air}} - \mathcal{R}_u W_i}{W_i W_{\text{air}}}\right)}{\left(\frac{\mathcal{R}_u W_{\text{air}} Y_i + \mathcal{R}_u W_i (1 - Y_i)}{W_i W_{\text{air}}}\right)}, \\ \frac{R'}{R} &= \frac{W_{\text{air}} - W_i}{W_{\text{air}} Y_i + W_i (1 - Y_i)}. \end{aligned}$$

Equation (A.14) then becomes:

$$\aleph = \frac{W_{\text{air}} - W_i}{W_{\text{air}} Y_i + W_i (1 - Y_i)} - \frac{c_{p,i} - c_{p,\text{air}}}{c_{p,i} Y_i + c_{p,\text{air}} (1 - Y_i)}. \quad (\text{A.21})$$

For $Y_i \ll 1$, we can assume $(\)_{\text{air}} = (\bar{\ })$ and neglect terms multiplied by Y_i :

$$\boxed{\bar{\aleph} = \frac{\bar{W} - W_i}{W_i} - \frac{c_{p,i} - \bar{c}_p}{\bar{c}_p}}. \quad (\text{A.22})$$

Using Eqs. (A.20) and (A.22) in Eq. (A.15):

$$\sigma = \frac{p'}{\bar{\gamma}\bar{p}} - \frac{\rho'}{\bar{\rho}} - \left(\frac{W_i - \bar{W}}{W_i} - \frac{c_{p,i} - \bar{c}_p}{\bar{c}_p} + \frac{c_{p,i} - \bar{c}_p}{\bar{c}_p} - \frac{s_i - \bar{s}}{\bar{c}_p} \right) \xi,$$

$$\boxed{\sigma = \frac{p'}{\bar{\gamma}\bar{p}} - \frac{\rho'}{\bar{\rho}} - \left(\frac{W_i - \bar{W}}{W_i} - \frac{s_i - \bar{s}}{\bar{c}_p} \right) \xi.} \quad (\text{A.23})$$

A.2 Compact wave source

The Navier-Stokes equations can be simplified for an inviscid flow, without volumetric heating, viscous forces, heat conduction, shear forces, and external forces. These are called the three-dimensional compressible Euler equations and are written as:

$$\frac{\partial \mathbf{U}}{\partial t} + \frac{\partial \mathbf{F}_x}{\partial x} + \frac{\partial \mathbf{F}_y}{\partial y} + \frac{\partial \mathbf{F}_z}{\partial z} = \phi', \quad (\text{A.24})$$

where:

$$\mathbf{U} = \begin{bmatrix} \rho \\ \rho u_x \\ \rho u_y \\ \rho u_z \\ \rho e_t \end{bmatrix}, \quad \mathbf{F}_x = \begin{bmatrix} \rho u_x \\ \rho u_x^2 + p \\ \rho u_y u_x \\ \rho u_z u_x \\ (\rho e_t + p)u_x \end{bmatrix}, \quad \mathbf{F}_y = \begin{bmatrix} \rho u_y \\ \rho u_x u_y \\ \rho u_y^2 + p \\ \rho u_z u_y \\ (\rho e_t + p)u_y \end{bmatrix}, \quad \mathbf{F}_z = \begin{bmatrix} \rho u_z \\ \rho u_x u_z \\ \rho u_y u_z \\ \rho u_z^2 + p \\ (\rho e_t + p)u_z \end{bmatrix}, \quad (\text{A.25})$$

and the source term vector is:

$$\phi' = [\phi'_m, \phi'_{M_x}, \phi'_{M_y}, \phi'_{M_z}, \phi'_e]^T. \quad (\text{A.26})$$

where we define the total specific energy $e_t = e + e_k$, which is made up of the specific internal energy $e = c_v T$ and specific kinetic energy $e_k = 1/2 u^2$. The first row of the vectors in (A.25) represents mass conservation (continuity), the second to fourth represent momentum conservation in the three axial directions, and the fifth row represents energy conservation.

For a one-dimensional ($u_y = u_z = \phi'_{M_y} = \phi'_{M_z} = 0$), steady-state ($\partial/\partial t = 0$) analysis, we can simplify Eq. (A.24) into the following mass, momentum, and energy equations, and relate them to their respective added fluxes $\phi'_m, \phi'_M, \phi'_e$:

$$\frac{d}{dx}(\rho u) = \phi'_m, \quad (\text{A.27})$$

$$\frac{d}{dx}(\rho u^2 + p) = \phi'_M, \quad (\text{A.28})$$

$$\frac{d}{dx}((\rho e_t + p)u) = \phi'_e, \quad (\text{A.29})$$

where $\phi_M = \phi_{M_x}$. We can re-formulate (A.29) by inputting the definition for total specific energy e_t :

$$\frac{d}{dx} \left(\rho u c_v T + \frac{1}{2} \rho u^3 + p u \right) = \phi'_e, \quad (\text{A.30})$$

or

$$\frac{d}{dx} \left(\rho u c_p T + \frac{1}{2} \rho u^3 \right) = \phi'_e. \quad (\text{A.31})$$

The one-dimensional, steady Euler equations above, along with an additional compositional addition ϕ'_Z , can be formulated as jump conditions across a compact discontinuity:

$$\left. \begin{aligned} \left[(\rho u)' \right]_0^1 &= \phi'_m, \\ \left[(p + \rho u^2)' \right]_0^1 &= \phi'_M, \\ \left[\left(\rho u \left(c_p T + \frac{1}{2} u^2 \right) \right)' \right]_0^1 &= \phi'_e, \\ \left[Z' \right]_0^1 &= \phi'_Z. \end{aligned} \right\} \quad (\text{A.32})$$

The notation $[\cdot]_0^1$ denotes the difference in flow properties between the upstream [1] and downstream [0] sections of the compact wave source (i.e. $[\cdot]_0^1 = [\cdot]_1 - [\cdot]_0$).

A.2.1 Linearisation and normalisation

The linearisation and normalisation of the mass, momentum, and energy equations are outlined here.

Applying the linearisation procedure to each flow variable, we get:

$$\left. \begin{aligned} \left[(\bar{\rho} + \rho')(\bar{u} + u') \right]_0^1 &= \phi'_m, \\ \left[(\bar{p} + p') + (\bar{\rho} + \rho')(\bar{u} + u')^2 \right]_0^1 &= \phi'_M, \\ \left[(\bar{\rho} + \rho')(\bar{u} + u')(\bar{c}_p + c'_p)(\bar{T} + T') + \frac{1}{2}(\bar{\rho} + \rho')(\bar{u} + u')^3 \right]_0^1 &= \phi'_e. \end{aligned} \right\} \quad (\text{A.33})$$

The fluxes are assumed to be small, such that the mean variables are constant before and after the discontinuity. Terms with second-order fluctuations or higher are cancelled out; only the terms with one first-order fluctuation remain.

Mass

From Eq. (A.33):

$$\begin{aligned}\phi'_m &= (\bar{\rho} + \rho')(\bar{u} + u') - \bar{\rho}\bar{u}, \\ \phi'_m &= \rho'\bar{u} + \bar{\rho}u'.\end{aligned}\tag{A.34}$$

One can obtain the normalised mass flux φ'_m by dividing Eq. (A.34) through by $\bar{\rho}\bar{u}$:

$$\begin{aligned}\varphi'_m &= \frac{\rho'\bar{u}}{\bar{\rho}\bar{u}} + \frac{\bar{\rho}u'}{\bar{\rho}\bar{u}}, \\ \varphi'_m &= \frac{\rho'}{\bar{\rho}} + \frac{\bar{c}u'}{\bar{c}\bar{u}}, \\ \varphi'_m &= \frac{\rho'}{\bar{\rho}} + \frac{\bar{c}}{\bar{u}} \frac{u'}{\bar{c}},\end{aligned}$$

$$\boxed{\varphi'_m = \left(\frac{\rho'}{\bar{\rho}}\right) + \frac{1}{M} \left(\frac{u'}{\bar{c}}\right)}.\tag{A.35}$$

Momentum

From Eq. (A.33):

$$\begin{aligned}\phi'_M &= (\bar{p} + p') + (\bar{\rho} + \rho')(\bar{u} + u')^2 - (\bar{p} + \bar{\rho}\bar{u}^2), \\ \phi'_M &= p' + \rho'\bar{u}^2 + 2\bar{\rho}\bar{u}u'.\end{aligned}\tag{A.36}$$

One can obtain the normalised momentum flux φ'_M by dividing Eq. (A.36) through by $\bar{\rho}\bar{u}^2$:

$$\begin{aligned}\varphi'_M &= \frac{p'}{\bar{\rho}\bar{u}^2} + \frac{\rho'\bar{u}^2}{\bar{\rho}\bar{u}^2} + 2\frac{\bar{\rho}\bar{u}u'}{\bar{\rho}\bar{u}^2}, \\ \varphi'_M &= \frac{p'}{\bar{\rho}\bar{u}^2} + \frac{\rho'}{\bar{\rho}} + 2\frac{u'}{\bar{u}}, \\ \varphi'_M &= \frac{p'}{\frac{\bar{p}}{RT}M^2\bar{c}^2} + \frac{\rho'}{\bar{\rho}} + \frac{2}{M} \frac{u'}{\bar{c}}, \\ \varphi'_M &= \frac{p'}{\frac{\bar{p}}{RT}M^2\bar{\gamma}RT} + \frac{\rho'}{\bar{\rho}} + \frac{2}{M} \frac{u'}{\bar{c}},\end{aligned}$$

$$\boxed{\varphi'_M = \frac{1}{M^2} \left(\frac{p'}{\bar{\gamma}\bar{p}}\right) + \left(\frac{\rho'}{\bar{\rho}}\right) + \frac{2}{M} \left(\frac{u'}{\bar{c}}\right)}.\tag{A.37}$$

Energy

Since there are more terms here, the linearisation of the energy term in Eq. (A.33) is shown in full:

$$\begin{aligned}\phi'_e &= (\bar{\rho} + \rho')(\bar{u} + u')(\bar{c}_p + c'_p)(\bar{T} + T') + \frac{1}{2}(\bar{\rho} + \rho')(\bar{u} + u')^3 - (\bar{\rho}\bar{u}\bar{c}_p\bar{T} + \frac{1}{2}\bar{\rho}\bar{u}^3), \\ \phi'_e &= \bar{\rho}\bar{u}\bar{c}_p T' + \bar{\rho}\bar{u}c'_p\bar{T} + \bar{\rho}u'\bar{c}_p\bar{T} + \rho'\bar{u}\bar{c}_p\bar{T} + \frac{1}{2}(3\bar{\rho}\bar{u}^2u' + \rho'\bar{u}^3).\end{aligned}$$

Re-arranging,

$$\phi'_e = \bar{c}_p\bar{T}(\rho'\bar{u} + \bar{\rho}u') + \bar{\rho}\bar{u}(\bar{c}_p T' + c'_p\bar{T} + \frac{3}{2}\bar{u}u') + \frac{1}{2}\rho'\bar{u}^3. \quad (\text{A.38})$$

One can obtain the normalised energy flux φ'_e by dividing Eq. (A.38) through by $\bar{\rho}\bar{u}\bar{c}_p\bar{T}_t$, where the total temperature is defined as $\bar{T}_t = \bar{T}(1 + \frac{\gamma-1}{2}\bar{M}^2)$:

$$\begin{aligned}\varphi'_e &= \frac{\rho'\bar{u}\bar{c}_p\bar{T}}{\bar{\rho}\bar{u}\bar{c}_p\bar{T}_t} + \frac{\bar{\rho}u'\bar{c}_p\bar{T}}{\bar{\rho}\bar{u}\bar{c}_p\bar{T}_t} + \frac{\bar{\rho}\bar{u}c'_p\bar{T}}{\bar{\rho}\bar{u}\bar{c}_p\bar{T}_t} + \frac{\bar{\rho}\bar{u}\bar{c}_p T'}{\bar{\rho}\bar{u}\bar{c}_p\bar{T}_t} + \frac{3}{2}\frac{\bar{\rho}\bar{u}^2u'}{\bar{\rho}\bar{u}\bar{c}_p\bar{T}_t} + \frac{1}{2}\frac{\rho'\bar{u}^3}{\bar{\rho}\bar{u}\bar{c}_p\bar{T}_t}, \\ \varphi'_e &= \frac{\rho'}{\bar{\rho}}\frac{\bar{T}}{\bar{T}_t} + \frac{u'}{\bar{u}}\frac{\bar{T}}{\bar{T}_t} + \frac{c'_p}{\bar{c}_p}\frac{\bar{T}}{\bar{T}_t} + T'\frac{1}{\bar{T}_t} + \frac{3}{2}\frac{\bar{u}u'}{\bar{c}_p}\frac{1}{\bar{T}_t} + \frac{1}{2}\frac{\rho'}{\bar{\rho}}\frac{\bar{u}^2}{\bar{c}_p}\frac{1}{\bar{T}_t}, \\ \varphi'_e &= \frac{\bar{T}}{\bar{T}_t}\left(\frac{\rho'}{\bar{\rho}} + \frac{u'}{\bar{u}} + \frac{c'_p}{\bar{c}_p} + \frac{T'}{\bar{T}} + \frac{3}{2}\frac{1}{\bar{c}_p}\frac{\bar{u}u'}{\bar{T}} + \frac{1}{2}\frac{1}{\bar{c}_p}\frac{\rho'}{\bar{\rho}}\frac{\bar{u}^2}{\bar{T}}\right), \\ \varphi'_e &= \frac{\bar{T}}{\bar{T}_t}\left(\frac{\rho'}{\bar{\rho}} + \frac{1}{\bar{M}}\frac{u'}{\bar{c}} + \frac{c'_p}{\bar{c}_p} + \frac{T'}{\bar{T}} + \frac{3}{2}\frac{(\bar{\gamma}-1)}{\bar{\gamma}\bar{R}}\frac{\bar{u}u'}{\bar{T}} + \frac{1}{2}\frac{(\bar{\gamma}-1)}{\bar{\gamma}\bar{R}}\frac{\rho'}{\bar{\rho}}\frac{\bar{M}^2\bar{\gamma}\bar{R}\bar{T}}{\bar{T}}\right), \\ \varphi'_e &= \frac{\bar{T}}{\bar{T}_t}\left(\frac{\rho'}{\bar{\rho}} + \frac{1}{\bar{M}}\frac{u'}{\bar{c}} + \frac{c'_p}{\bar{c}_p} + \frac{T'}{\bar{T}} + \frac{3(\bar{\gamma}-1)}{2}\bar{M}\bar{c}\frac{u'}{\bar{c}^2} + \frac{(\bar{\gamma}-1)}{2}\bar{M}^2\frac{\rho'}{\bar{\rho}}\right), \\ \varphi'_e &= \frac{\bar{T}}{\bar{T}_t}\left(\frac{1}{\bar{M}}\frac{u'}{\bar{c}}\left(1 + \frac{(\bar{\gamma}-1)}{2}\bar{M}^2\right) + \frac{1}{\bar{M}}(\bar{\gamma}-1)\bar{M}^2\frac{u'}{\bar{c}} + \frac{c'_p}{\bar{c}_p} + \frac{T'}{\bar{T}} + \frac{\rho'}{\bar{\rho}}\left(1 + \frac{(\bar{\gamma}-1)}{2}\bar{M}^2\right)\right), \\ \varphi'_e &= \frac{\rho'}{\bar{\rho}} + \frac{1}{\bar{M}}\frac{u'}{\bar{c}} + \frac{\bar{T}}{\bar{T}_t}\left((\bar{\gamma}-1)\bar{M}\frac{u'}{\bar{c}} + \frac{c'_p}{\bar{c}_p} + \frac{p'}{\bar{p}} - \frac{\rho'}{\bar{\rho}} - \frac{R'}{\bar{R}}\right).\end{aligned}$$

Using Eq. (A.14), we finally arrive at:

$$\boxed{\varphi'_e = \left(\frac{\rho'}{\bar{\rho}}\right) + \frac{1}{\bar{M}}\left(\frac{u'}{\bar{c}}\right) + \frac{1}{1 + \frac{\bar{\gamma}-1}{2}\bar{M}^2}\left(\bar{\gamma}\frac{p'}{\bar{\gamma}\bar{p}} - \frac{\rho'}{\bar{\rho}} + (\bar{\gamma}-1)\bar{M}\frac{u'}{\bar{c}} - \bar{\aleph}\xi\right)}. \quad (\text{A.39})$$

A.2.2 Resulting jump conditions

Using Eqs. (A.35), (A.37) and (A.39), the normalised version of Eq. (A.32) is:

$$\left. \begin{aligned} \left[\left(\frac{\rho'}{\bar{\rho}} \right) + \frac{1}{\bar{M}} \left(\frac{u'}{\bar{c}} \right) \right]_0^1 &= \varphi'_m, \\ \left[\frac{1}{\bar{M}^2} \left(\frac{p'}{\bar{\gamma}\bar{p}} \right) + \left(\frac{\rho'}{\bar{\rho}} \right) + \frac{2}{\bar{M}} \left(\frac{u'}{\bar{c}} \right) \right]_0^1 &= \varphi'_M, \\ \left[\left(\frac{\rho'}{\bar{\rho}} \right) + \frac{1}{\bar{M}} \left(\frac{u'}{\bar{c}} \right) + \frac{1}{1 + \frac{\bar{\gamma}-1}{2}\bar{M}^2} \left(\bar{\gamma} \frac{p'}{\bar{\gamma}\bar{p}} - \frac{\rho'}{\bar{\rho}} + (\bar{\gamma}-1)\bar{M} \frac{u'}{\bar{c}} - \bar{\aleph}\xi \right) \right]_0^1 &= \varphi'_e, \\ [Z']_0^1 &= \varphi'_Z, \end{aligned} \right\} \quad (\text{A.40})$$

where \bar{M} is the Mach number, and φ'_m , φ'_M , φ'_e and φ'_Z are the normalised changes in mass, momentum, energy, and mixture fraction:

$$\varphi'_m = \frac{\phi'_m}{\bar{\rho}\bar{u}}, \quad \varphi'_M = \frac{\phi'_M}{\bar{\rho}\bar{u}^2}, \quad \varphi'_e = \frac{\phi'_e}{\bar{\rho}\bar{u}\bar{c}\bar{T}_t}, \quad \varphi'_Z = \phi'_Z. \quad (\text{A.41a-d})$$

Equation (A.40) can be decomposed by using the wave amplitudes defined in Eqs. (2.23) and (A.15):

$$\left. \begin{aligned} \sigma &= \frac{p'}{\bar{\gamma}\bar{p}} - \frac{\rho'}{\bar{\rho}} - (\bar{\Psi} + \bar{\aleph})\xi, \\ \frac{\rho'}{\bar{\rho}} &= \frac{p'}{\bar{\gamma}\bar{p}} - \sigma - (\bar{\Psi} + \bar{\aleph})\xi, \\ \frac{p'}{\bar{\gamma}\bar{p}} &= \pi^+ + \pi^-, \\ \frac{u'}{\bar{c}} &= \pi^+ - \pi^-, \\ Z' &= \xi. \end{aligned} \right\} \quad (\text{A.42})$$

Using Eq. (A.42) in Eq. (A.40):

$$\left. \begin{aligned}
 & \left[\left(\pi^+ + \pi^- - \sigma - (\bar{\Psi} + \bar{\aleph})\xi \right) + \frac{1}{\bar{M}} (\pi^+ - \pi^-) \right]_0^1 = \varphi'_m, \\
 & \left[\frac{1}{\bar{M}^2} (\pi^+ + \pi^-) + \left(\pi^+ + \pi^- - \sigma - (\bar{\Psi} + \bar{\aleph})\xi \right) + \frac{2}{\bar{M}} (\pi^+ - \pi^-) \right]_0^1 = \varphi'_M, \\
 & \left[\left(\pi^+ + \pi^- - \sigma - (\bar{\Psi} + \bar{\aleph})\xi \right) + \frac{1}{\bar{M}} (\pi^+ - \pi^-) + \right. \\
 & \quad \left. \frac{1}{1 + \frac{\bar{\gamma}-1}{2}\bar{M}^2} \left(\bar{\gamma}(\pi^+ + \pi^-) - \left((\pi^+ + \pi^-) - \sigma - (\bar{\Psi} + \bar{\aleph})\xi \right) + \right. \right. \\
 & \quad \quad \left. \left. (\bar{\gamma} - 1)\bar{M}(\pi^+ - \pi^-) - \bar{\aleph}\xi \right) \right]_0^1 = \varphi'_e, \\
 & \quad \quad \quad [\xi]_0^1 = \varphi'_Z.
 \end{aligned} \right\} \quad (\text{A.43})$$

Re-arranging and combining terms related to the respective disturbance amplitudes:

$$\left. \begin{aligned}
 & \left[\left(1 + \frac{1}{\bar{M}} \right) \pi^+ + \left(1 - \frac{1}{\bar{M}} \right) \pi^- - \sigma - (\bar{\Psi} + \bar{\aleph})\xi \right]_0^1 = \varphi'_m, \\
 & \left[\left(1 + \frac{1}{\bar{M}^2} + \frac{2}{\bar{M}} \right) \pi^+ + \left(1 + \frac{1}{\bar{M}^2} - \frac{2}{\bar{M}} \right) \pi^- - \sigma - (\bar{\Psi} + \bar{\aleph})\xi \right]_0^1 = \varphi'_M, \\
 & \left[\left(1 + \frac{1}{\bar{M}} + \frac{(\bar{\gamma} - 1)(1 + \bar{M})}{1 + \frac{\bar{\gamma}-1}{2}\bar{M}^2} \right) \pi^+ + \left(1 - \frac{1}{\bar{M}} + \frac{(\bar{\gamma} - 1)(1 - \bar{M})}{1 + \frac{\bar{\gamma}-1}{2}\bar{M}^2} \right) \pi^- - \right. \\
 & \quad \left. \left(\frac{1}{1 + \frac{\bar{\gamma}-1}{2}\bar{M}^2} - 1 \right) \sigma + \left(\frac{\bar{\Psi}}{1 + \frac{\bar{\gamma}-1}{2}\bar{M}^2} - (\bar{\Psi} + \bar{\aleph}) \right) \xi \right]_0^1 = \varphi'_e, \\
 & \quad \quad \quad [\xi]_0^1 = \varphi'_Z.
 \end{aligned} \right\} \quad (\text{A.44})$$

The jump conditions across the compact wave source of Eq. (A.44) can be recast in matrix form⁶⁴:

$$[\mathbf{X}\mathbf{w}]_0^1 = \boldsymbol{\varphi}', \quad (\text{A.45})$$

where \mathbf{X} is the matrix of normalised flow fluctuations:

$$\mathbf{X} = \begin{bmatrix} 1 + \frac{1}{\bar{M}} & 1 - \frac{1}{\bar{M}} & -1 & -(\bar{\Psi} + \bar{\aleph}) \\ \left(1 + \frac{1}{\bar{M}}\right)^2 & \left(1 - \frac{1}{\bar{M}}\right)^2 & -1 & -(\bar{\Psi} + \bar{\aleph}) \\ 1 + \frac{1}{\bar{M}} + \frac{(\bar{\gamma} - 1)(1 + \bar{M})}{1 + \frac{\bar{\gamma} - 1}{2}\bar{M}^2} & 1 - \frac{1}{\bar{M}} + \frac{(\bar{\gamma} - 1)(1 - \bar{M})}{1 + \frac{\bar{\gamma} - 1}{2}\bar{M}^2} & \frac{1}{1 + \frac{\bar{\gamma} - 1}{2}\bar{M}^2} - 1 & \frac{\bar{\Psi}}{1 + \frac{\bar{\gamma} - 1}{2}\bar{M}^2} - (\bar{\Psi} + \bar{\aleph}) \\ 0 & 0 & 0 & 1 \end{bmatrix}, \quad (\text{A.46})$$

\mathbf{w} is the vector of wave amplitudes:

$$\mathbf{w} = [\pi^+, \pi^-, \sigma, \xi]^T, \quad (\text{A.47})$$

and $\boldsymbol{\varphi}'$ is the vector of the normalised source terms:

$$\boldsymbol{\varphi}' = [\varphi'_m, \varphi'_M, \varphi'_e, \varphi'_\xi]^T. \quad (\text{A.48})$$

Equation (A.45) can be manipulated to obtain the outgoing waves relative to the wave source:

$$\begin{bmatrix} \pi_1^+ \\ \pi_0^- \\ \sigma_1 \\ \xi_1 \end{bmatrix} = \begin{bmatrix} \pi_0^+ \\ \pi_1^- \\ \sigma_0 \\ \xi_0 \end{bmatrix} + \begin{bmatrix} \frac{1}{2} \frac{(\bar{\gamma} - 1)\bar{M}^3 - \bar{M}^2}{\bar{M} + 1} & \frac{1}{2} \frac{\bar{M}^2 - (\bar{\gamma} - 1)\bar{M}^3}{\bar{M} + 1} & \frac{1}{2} \frac{\bar{M} + \frac{(\bar{\gamma} - 1)\bar{M}^3}{2}}{\bar{M} + 1} & \frac{1}{2} \frac{\bar{\aleph}}{\bar{M} + 1} \frac{\bar{M}}{1 + \bar{M}} \\ \frac{1}{2} \frac{(1 - \bar{\gamma})\bar{M}^3 - \bar{M}^2}{\bar{M} - 1} & \frac{1}{2} \frac{\bar{M}^2 + (\bar{\gamma} - 1)\bar{M}^3}{\bar{M} - 1} & \frac{1}{2} \frac{(1 - \bar{\gamma})\bar{M}^3 - \bar{M}}{\bar{M} - 1} & \frac{1}{2} \frac{\bar{\aleph}}{\bar{M} - 1} \frac{\bar{M}}{1 - \bar{M}} \\ \frac{1}{2}(\bar{\gamma} - 1)\bar{M}^2 - 1 & (1 - \bar{\gamma})\bar{M}^2 & \frac{1}{2}(\bar{\gamma} - 1)\bar{M}^2 + 1 & -\bar{\Psi} \\ 0 & 0 & 0 & 1 \end{bmatrix} \begin{bmatrix} \varphi'_m \\ \varphi'_M \\ \varphi'_e \\ \varphi'_\xi \end{bmatrix}. \quad (\text{A.49})$$

Since we assume there are no incoming waves (i.e. $\pi_0^+ = \pi_1^- = \sigma_0 = \xi_0 = 0$)²⁷⁸, we can solve for the outgoing waves (i.e. $\pi_d^+ = \pi_1^+$, $\pi_d^- = \pi_0^-$, $\sigma = \sigma_1$ and $\xi = \xi_1$):

$$\left. \begin{aligned} \frac{1}{2} \left(\frac{\bar{M} + \frac{(\bar{\gamma}-1)\bar{M}^3}{2}}{1+\bar{M}} \right) \varphi'_e - \frac{1}{2} \left(\frac{\bar{M}^2 - \frac{(\bar{\gamma}-1)\bar{M}^3}{2}}{1+\bar{M}} \right) \varphi'_m + \frac{1}{2} \left(\frac{\bar{M}^2 - (\bar{\gamma}-1)\bar{M}^3}{1+\bar{M}} \right) \varphi'_M + \frac{1}{2} \left(\bar{\aleph} \frac{\bar{M}}{1+\bar{M}} \right) \varphi'_Z &= \pi_d^+, \\ \frac{1}{2} \left(\frac{\bar{M} - \frac{(\bar{\gamma}-1)\bar{M}^3}{2}}{1-\bar{M}} \right) \varphi'_e + \frac{1}{2} \left(\frac{\bar{M}^2 + \frac{(\bar{\gamma}-1)\bar{M}^3}{2}}{1-\bar{M}} \right) \varphi'_m - \frac{1}{2} \left(\frac{\bar{M}^2 + (\bar{\gamma}-1)\bar{M}^3}{1-\bar{M}} \right) \varphi'_M + \frac{1}{2} \left(\bar{\aleph} \frac{\bar{M}}{1-\bar{M}} \right) \varphi'_Z &= \pi_d^-, \\ \left(\frac{(\bar{\gamma}-1)}{2} \bar{M}^2 + 1 \right) \varphi'_e - \left(\frac{(1-\bar{\gamma})}{2} \bar{M}^2 + 1 \right) \varphi'_m + ((1-\bar{\gamma}) \bar{M}^2) \varphi'_M - \bar{\Psi} \varphi'_Z &= \sigma, \\ \varphi'_Z &= \xi. \end{aligned} \right\} \quad (\text{A.50})$$

Considering a low Mach number mean flow ($M \ll 1$), \bar{M}^3 terms can be neglected. Re-arranging:

$$\left. \begin{aligned} \frac{1}{2} \left(\frac{\bar{M}}{1+\bar{M}} \right) (\varphi'_e + \bar{\aleph} \varphi'_Z) + \frac{1}{2} \left(\frac{\bar{M}^2}{1+\bar{M}} \right) (\varphi'_M - \varphi'_m) &= \pi_d^+, \\ \frac{1}{2} \left(\frac{\bar{M}}{1-\bar{M}} \right) (\varphi'_e + \bar{\aleph} \varphi'_Z) - \frac{1}{2} \left(\frac{\bar{M}^2}{1-\bar{M}} \right) (\varphi'_M - \varphi'_m) &= \pi_d^-, \\ (\varphi'_e - \varphi'_m) + \frac{(\bar{\gamma}-1)}{2} \bar{M}^2 (\varphi'_m - 2\varphi'_M + \varphi'_e) - \bar{\Psi} \varphi'_Z &= \sigma, \\ \varphi'_Z &= \xi. \end{aligned} \right\} \quad (\text{A.51})$$

Appendix B

Additional details on Raman spectroscopy

THIS appendix serves three purposes. Firstly, to present the equations describing the probe volume for a confocal Raman setup. Estimated values for the probe and illuminated volumes of the spontaneous Raman spectroscopy technique presented in §4, and used in §5 and §6, are reported. Secondly, to present the full calibration dataset and the proportionalities of the Stokes signal with varying mass fraction, intensifier gains, and mean pressure. Lastly, to provide an estimate of the measurement errors associated with the experiments presented in §5 and §6.

B.1 Probe volume

B.1.1 Confocal theory

In order to understand the spatial resolution of the diagnostic technique, it is important to estimate the probe volume of the setup. In a confocal setup, the in-focus volume is known as the confocal volume, V_{con} . As mentioned in §4.3.2, only Stoke-shifted Raman photons are expected to pass through the notch filter, before being focused through a pinhole aperture in the conjugate image plane. The size of the aperture is such that only the central part of the focus can pass through for detection. Any light which does not come from the focal plane will not be transmitted through the pinhole⁶⁶.

The confocal volume V_{con} is given by:

$$V_{\text{con}} = \pi^{3/2} \kappa \omega_0^3, \quad (\text{B.1})$$

where ω_0 is the $1/e^2$ beam radius (13.5% of maximum) in the x - y plane given by:

$$\omega_0 = \frac{2f\lambda_l}{\pi d} = \frac{\lambda_l}{\pi \text{NA}}, \quad (\text{B.2})$$

where f is the focal length, d is the beam diameter at the lens, and λ_l is the laser pulse wavelength²⁸⁶. The numerical aperture is given by Abbe's formula, $\text{NA} = d/2f$ ¹. The geometric factor κ describes the eccentricity of the confocal volume and is given by the ratio of the optical resolution in the z direction and x - y plane.

The resolution in the x - y plane is given by the Rayleigh criterion¹⁹⁸:

$$\delta_{xy} = \frac{0.61\lambda_l}{\text{NA}}, \quad (\text{B.3})$$

where $\delta_{xy} = \delta_x = \delta_y$. The resolution in the z -axis is given by:

$$\delta_z = \frac{2n\lambda_l}{\text{NA}^2}, \quad (\text{B.4})$$

where n is the refractive index³⁴⁶.

The perfect diffraction-limited value of κ is given by:

$$\kappa = \frac{2.33n}{\text{NA}}. \quad (\text{B.5})$$

The diffraction-limited confocal volume is given by:

$$V_{\text{con}} = \frac{2.33}{\pi^{3/2}} \frac{n\lambda_l^3}{\text{NA}^4}. \quad (\text{B.6})$$

Lastly, the illumination volume V_{ill} is defined as the beam volume from the imaging lens to the focus point. Assuming a spherically Gaussian beam, this volume is cone-shaped, such that:

$$V_{\text{ill}} = \frac{1}{6} \pi d^2 f. \quad (\text{B.7})$$

B.1.2 Limit cases

For the optical setup used in the CWR, $\lambda_l = 527$ nm (set by the laser), $n = 1$ (for air) and $f = 100$ mm. Assuming a spherically Gaussian beam, the volume will have an oblate ellipsoid shape (as shown in Fig. 4.13c). The beam diameter is expected to be 5 mm¹⁹⁴, however, the actual diameter may stray from this due to optical component imperfection and degradation³⁵⁶. In fact, during the alignment procedure, it was clear that the beam was slightly elongated in the y direction. This inevitably affects the confocal volume shape.

We assume the beam diameter is $d = 5 \pm 2$ mm and, as such, calculate the confocal volume assuming the beam is perfectly circular for $d = 3$ mm, $d = 5$ mm, and $d = 7$ mm. The dimensions for the probe and illuminated volume have been estimated for the three cases and are presented in Table B.1. In reality, the confocal probe volume and resolution across all three axes are expected to lie somewhere between the two limit cases.

Table B.1 Raman spectroscopy setup: beam diameter d , numerical aperture NA, resolution in x - y plane δ_{xy} , resolution in z plane δ_z , confocal volume V_{con} , and illumination volume V_{ill} .

d [mm]	NA [-]	δ_{xy} [μm]	δ_z [mm]	V_{con} [$\times 10^{-4}$ mm ³]	V_{ill} [$\times 10^3$ mm ³]
3	0.015	21.4	4.7	12.1	0.5
5	0.025	12.9	1.7	1.6	1.3
7	0.035	9.2	0.9	0.4	2.6

B.2 Full calibration dataset

Calibration of the experimental setup was done by varying the methane mass fraction Y_{CH_4} (0–100%), intensifier gain G (35–70%) and mean pressure \bar{p} (1–1.5 bar) for a total of 144 test cases. The integrated counts $\bar{C}_{S'}$ for each test case are shown in Fig. B.1 (cases where the camera has saturated are not shown). The figure has a normalised x-axis where EM is the intensifier’s electron multiplication factor and c is the molar concentration. The intensifier’s electron multiplication factor is $\text{EM} = 15$ which has a non-linear dependency due to the behaviour of the intensifier’s MCPs (see §4.3.4). For each test condition, the error associated with the measurement of the integrated counts \bar{C} is computed by taking the standard deviation of the single-shot integrated counts for a series of 1450 shots (an example of test case variability is shown in Fig. 4.14). This value accounts for all the measurable fluctuations in the system. Error bars are included in Fig. B.1 presenting the standard deviation ($\pm 1\sigma$) in the signal for each test case. The shot-to-shot signal variation is larger for nitrogen than for methane.

The data shows a fit which follows a power-law $y = \beta x^\eta$ where β and η are constants specific to each molecule which are solved for via minimisation of the residual sum of squares ($\beta_{\text{CH}_4} = 4289 \pm 1$, $\eta_{\text{CH}_4} = 0.77 \pm 0.02$, $\beta_{\text{N}_2} = 673 \pm 2$, $\eta_{\text{N}_2} = 0.79 \pm 0.04$). The

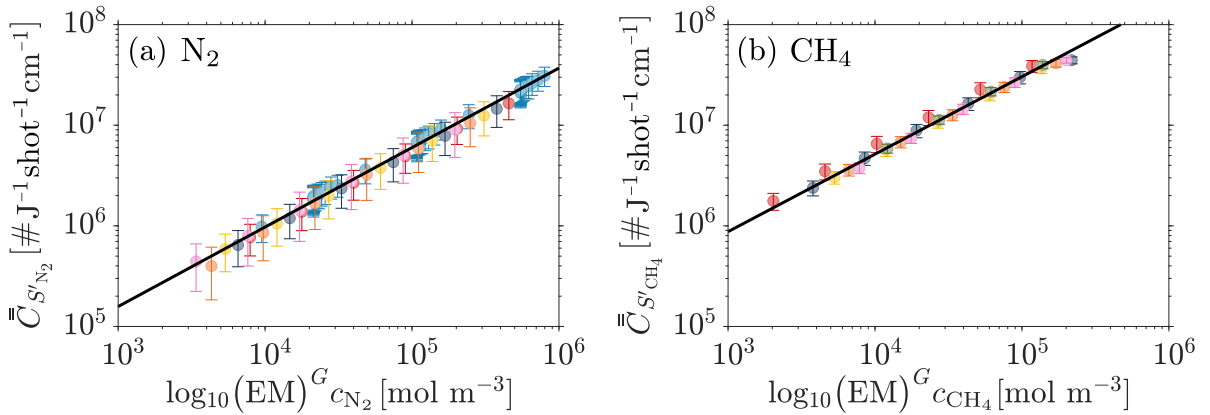


Fig. B.1 Calibration curves for (a) N_2 and (b) CH_4 shows data points for calibration test cases using different mean pressures \bar{p} (1.0–1.5 bar), intensifier gains G (35–70%) and methane mass fractions Y_{CH_4} (● 0%, ● 10%, ● 20%, ● 30%, ● 40%, ● 50%, ● 100%). Error bars show the standard deviation ($\pm 1\sigma$) in the signal for each test case. The region of operation is presented (cases where camera has saturated are not shown) where $\text{EM} = 15$ is the intensifier’s electron multiplication factor and c_i is the molar concentration of the respective molecule. Lines of best fit (—) use the power-law $y = \beta x^\eta$ where β and η are constants calculated via the sum of squared residuals method for each gas ($\beta_{\text{CH}_4} = 4289 \pm 1$, $\eta_{\text{CH}_4} = 0.77 \pm 0.02$, $\beta_{\text{N}_2} = 673 \pm 2$, $\eta_{\text{N}_2} = 0.79 \pm 0.04$).

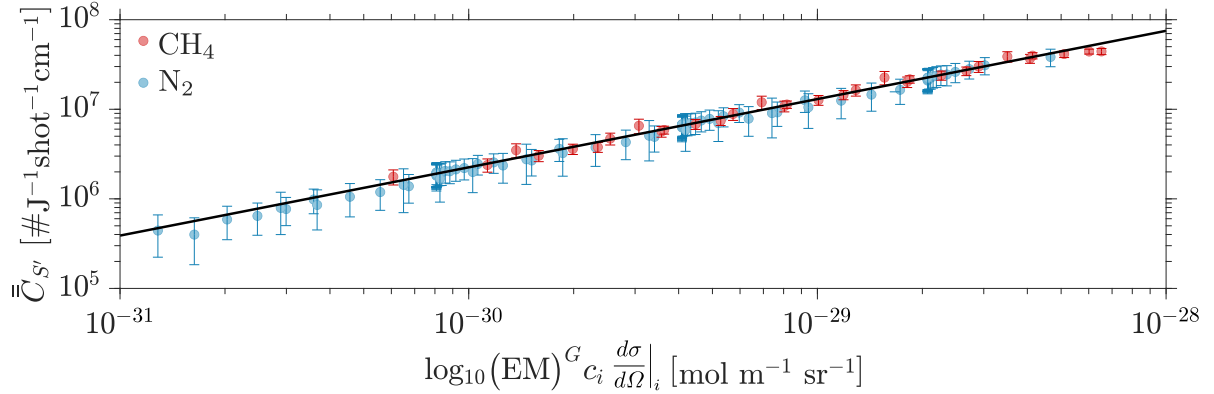


Fig. B.2 Integrated counts for N_2 (●) and CH_4 (●) versus normalised x-axis where $EM = 15$ is the intensifier's electron multiplication factor, G is the intensifier gain, c_i is the molar concentration and $d\sigma/d\Omega|_i$ is the differential Raman scattering cross section of the respective molecule. Error bars show the standard deviation ($\pm 1\sigma$) in the signal for each test case. The region of operation is presented (cases where camera has saturated are not shown). Data follows a power-law $y = \beta x^\eta$ where β and η are constants calculated via the sum of squared residuals method ($\beta = 1.63 \times 10^{29}$, $\eta = 0.76$) along with the ratio of differential Raman scattering cross section between the two molecules, which is estimated to be $\frac{d\sigma}{d\Omega}|_{CH_4} / \frac{d\sigma}{d\Omega}|_{N_2} = 7.9$. This agrees with literature^{57,91,253}.

errors on the slope was determined using the method of weighted least-squares fit for a heteroscedastic data set (equations 6.3 to 6.7 in Hughes and Hase¹⁴⁶).

There is a factor 6.4 difference in the power-law slopes for each molecule. Since the power of the scattered light is directly proportional to the differential Raman scattering cross-section $d\sigma/d\Omega$ as per Eq. (4.7), the difference in slope can be, to first order, attributed to the ratio between the molecules' differential Raman scattering cross-sections. From literature, we assume $d\sigma/d\Omega|_{N_2} = 3.79 \times 10^{-35} \text{ m}^2 \text{ sr}^{-1}$ ^{91,253,301}, and the curves fall along the same line as shown in Fig. B.2. Using a least-squares method¹, a differential Raman scattering cross-section ratio of 7.9 is computed which agrees with literature's estimates of 7.1 ± 1 ^{57,91,253}.

Figure B.3 shows the range of SBR measured for the calibration test cases (cases where the camera has saturated are not shown). The maximum SBR measured for the molecules investigated was 3.8 for N_2 and 7.6 for CH_4 .

¹The author kindly acknowledges the work of Dr. Lee Weller who computed the fits shown in Figs. B.1 and B.2.

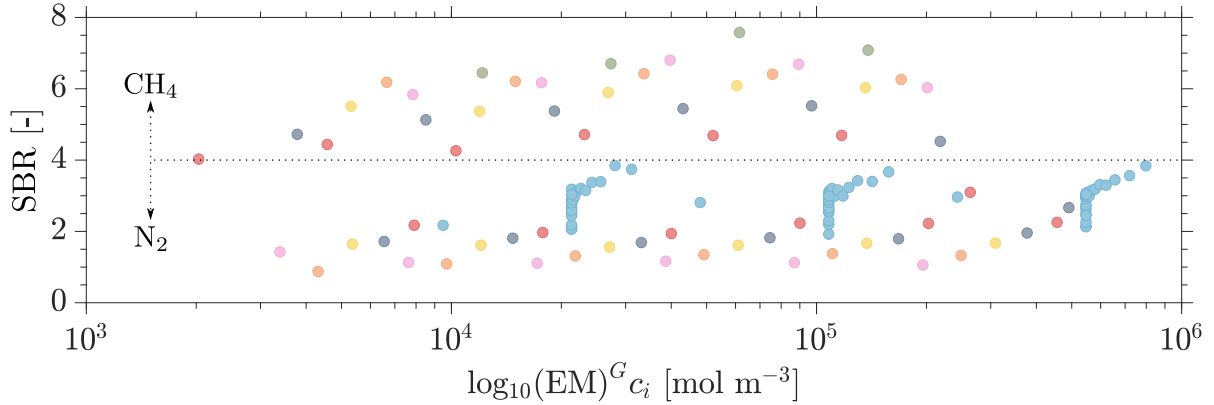


Fig. B.3 Signal-to-background ratio (SBR) for N_2 and CH_4 : calibration test cases are shown here (cases where the camera has saturated are not shown) with different mean pressures \bar{p} (1.0–1.5 bar), intensifier gains G (35–70%) and methane mass fractions Y_{CH_4} (● 0%, ● 10%, ● 20%, ● 30%, ● 40%, ● 50%, ● 100%). For cases shown, $\text{SBR}_{\text{CH}_4} > 4$ and $\text{SBR}_{\text{N}_2} < 4$.

B.3 Error analysis

The error in the Raman measurement can be assessed by looking at the total mole fraction across the anechoic windows of the respective experimental campaigns – this is expected to be unity. Additionally, we can propagate forward the standard deviation and standard errors of the time-resolved integrated counts by using Eqs. (4.15) and (4.16). The mean standard deviation $\bar{\sigma}$ and mean standard error $\bar{\sigma}_{\bar{x}}$ of the measured compositional wave amplitude ξ are then computed across the respective anechoic time windows. These results are presented in Fig. B.4.

For the single pulse experiments (Fig. B.4a), both close and far injection cases show a mean total mole fraction \bar{X}_{tot} near one. We note that during the convection of the compositional wave through the probe volume, the total molar fraction deviates from one (as shown in Fig. 4.26). This is accepted as the measurement error. Looking at $\bar{\sigma}$ and $\bar{\sigma}_{\bar{x}}$, we note that larger errors are present for the close injection case due to the fact that the error in the methane measurement increases with concentration, as per Eq. 4.16. A maximum of $\bar{\sigma} = 3.5 \times 10^{-2}$ and $\bar{\sigma}_{\bar{x}} = 0.8 \times 10^{-2}$ is estimated for the close injection cases, and $\bar{\sigma} = 0.8 \times 10^{-2}$ and $\bar{\sigma}_{\bar{x}} = 0.2 \times 10^{-2}$ is estimated for the far injection cases.

In the pulse burst experiments (Fig. B.4b), there are more compositional waves convecting through the probe volume during the anechoic window than in the single pulse experiments. Since the 2 Hz case is used to correct the calibration curve, it naturally shows the best agreement with $\bar{X}_{\text{tot}} = 1$ for all flow rates. Generally, with increasing frequency, \bar{X}_{tot} decreases. A particular jump is seen from 100 Hz to 187.5 Hz and 250 Hz

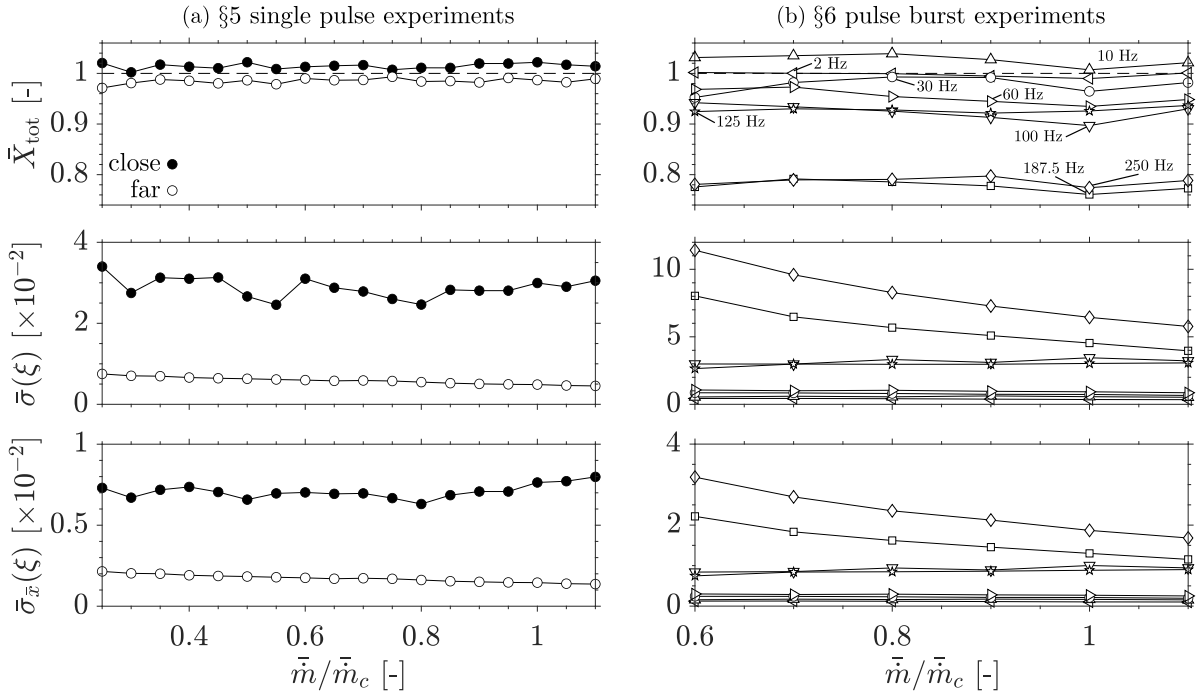


Fig. B.4 Error analysis for (a) single pulse and (b) pulse burst experiments: (top) mean total mole fraction \bar{X}_{tot} computed across the anechoic window; (middle) mean standard deviation $\bar{\sigma}$ of compositional wave amplitude ξ computed across the anechoic window – calculated by propagating forward the standard deviation of the time-resolved integrated counts \hat{C} ; (bottom) mean standard error $\bar{\sigma}_{\bar{x}}$ of compositional wave amplitude ξ computed across the anechoic window – calculated by propagating forward the standard error of the time-resolved integrated counts \hat{C} .

– this is attributed to the fact that the latter two experiments were run on a separate day to the first six experiments (2 Hz to 125 Hz). Similar to the single pulse experiments, we note that larger $\bar{\sigma}$ and $\bar{\sigma}_{\bar{x}}$ are present for the cases where a larger injection mass fraction is used (see Table 6.1). Once more, this is due to the fact that the error in the methane measurement increases with concentration, as per Eq. 4.16.

